ENGINEERING HIGH-AFFINITY SUPRAMOLECULAR POLYMERS FOR ANTIBODY CAPTURE AND PURIFICATION

by

Yi Li

A dissertation submitted to Johns Hopkins University in conformity with the
requirements for the degree of Doctor of Philosophy

Baltimore, Maryland

July 2020

Abstract

Monoclonal antibodies (mAbs) have received considerable attention over the past three decades for the treatment of many diseases. With the significant titer improvement in cell culture processes, the mAb capture step using protein A chromatography has become one of the major downstream bottlenecks due to limited resin capacity and high production cost. As such, affinity precipitation has been increasingly explored as a promising alternative to purify mAbs and other therapeutic proteins. Despite recent advances in new affinity precipitants, challenges still remain in achieving high capture efficiency and complete removal of the precipitants. Supramolecular polymers formed by self-assembly of peptides and peptide derivatives are attractive biomaterials due to their inherent biodegradability and biocompatibility and have been widely explored for use in regenerative medicine, drug delivery, and disease diagnostics. Importantly, the selective presentation of various bioactive epitopes on a supramolecular substrate enables specific biology interfacing and molecular recognition. Furthermore, the multilevel reversible transitions within a supramolecular system make it uniquely suited for use as effective affinity agents for mAb precipitation and purification.

The aim of this dissertation is to develop peptide-based supramolecular polymers as affinity agents for efficient capture and purification of mAbs. First of all, Z33, a protein A-derived peptide with two α-helical strands, was selected from literature as the mAb binding ligand due to its high binding affinity and short sequence. I discovered that the alkylation strategy plays an important role in preserving the α-helical conformation of the peptides within its supramolecular assemblies. Second, I designed and constructed self-assembling immuno-amphiphiles (IAs) *via* the direct conjugation of the Z33 peptide to linear hydrocarbons. The resulting IAs can effectively associate under physiological conditions into immunofibers (IFs) while preserving their native α-helical conformation and mAb binding affinity. However, the mAb precipitation efficiency was found to be very modest, which was attributed to the steric hindrance among tightly packed ligands that prevents their efficient interactions with mAbs.

Third, to reduce the steric hindrance among Z33 ligands, I developed co-assembled IFs formed by a Z33-containing amphiphile with a rationally designed filler molecule to modulate the distribution of Z33 on IF surfaces. Under optimized conditions, IFs can specifically precipitate mAbs with a yield greater than 99%. I also demonstrated the feasibility of capturing and recovering mAbs from clarified cell culture harvest. Importantly, the added IFs can be easily removed via membrane separation, without introducing new contaminants. However, this system was limited by the high ammonium sulfate concentration necessary to trigger mAb precipitation. Lastly, to minimize the usage of salt, a series of IF building blocks with OEG (or PEG) linkers was designed to optimize the presentation of Z33 on IF surfaces. Results reveal that the mAb-IF interactions could be significantly improved as the linker length increases; however, too long a linker has an adverse impact on the function of the resultant IFs. I demonstrated that the desired IF system was able to precipitate mAbs without the help of additional salt and promising yields were obtained, especially when using a sequential precipitation strategy.

These findings shed important light on the engineering of supramolecular polymers for specific molecular recognition and capture. I envision that the peptide-based supramolecular IF system can be potentially scaled up, serving as an efficient alternative for the purification of mAbs and other proteins of interest.

Advisor

Honggang Cui, Ph.D.

Associate Professor of Chemical & Biomolecular Engineering, Johns Hopkins University

Committee Members

Hai-Quan Mao, Ph.D.

Professor of Materials Science & Engineering, Johns Hopkins University

Efie Kokkoli, Ph.D.

Professor of Chemical & Biomolecular Engineering, Johns Hopkins University

Jamie Spangler, Ph.D.

Assistant Professor of Chemical & Biomolecular Engineering, Johns Hopkins University

Xuankuo Xu, Ph.D.

Senior Principal Scientist, Bristol-Myers Squibb

Acknowledgements

It has been a challenging and inspiring experience, during which I had the great honor to meet with a group of incredible individuals. I genuinely appreciate their guidance and help in the past five years.

I would like to express my deepest gratitude to my advisor Dr. Honggang Cui for the continuous support of my Ph.D. study and research. His broad vision of the research field and insightful guidance always gave me great inspiration and helped me move forward at all stages of my research as well as make my career decisions. I have learned a lot from his research philosophy and skills of scientific communications. His patience, understanding, and encouragement helped me become a more confident researcher and also made the whole lab a creative and collaborative community. Working in Cui lab has been a fantastic journey in the past five years and I am very grateful for this opportunity.

I sincerely appreciate my GBO committee members, Dr. Hai-Quan Mao, Dr. Efie Kokkoli, Dr. Jamie Spangler, Dr. Xuankuo Xu, and Dr. Honggang Cui, not only for their time and patience, but also for their intellectual contributions to my research and this dissertation. I sincerely appreciate their participation and assistance.

During the past five years, I was given many precious opportunities to collaborate with various esteemed people within and outside Hopkins. I would like to sincerely thank our collaborators at Bristol-Myers Squibb, Dr. Xuankuo Xu, Dr. Lye Lin Lock, Jason Mills, for the invaluable bi-weekly discussions and guidance on the project. Their suggestions from an industrial perspective distinctively broaden my views in research, allowing me to have a deeper understanding of the project, a clearer goal, and a more organized project planning. In particular, I would like to thank Dr. Lye Lin Lock for her dedication to this

project that we have been working closely together. I would never forget the countless hours we spent over the phone discussing the project and brainstorming enthusiastically. Without her valuable insights and constructive suggestions, this dissertation would not have been possible.

I appreciate Dr. Arne Schon and Dr. Katherine Tripp for their patient guidance on using ITC, Dr. J. Michael McCaffery and Erin Pryce for their help in TEM and confocal microscope, Dr. Phil Mortimer for his help in mass spectrometry, Dr. Joel Tang and Dr. Ananya Majumdar their help in NMR facilities.

I would like to sincerely thank Dr. Ran Lin for her mentorship in research from fundamental theories to experimental techniques. I am also grateful to our past and current lab members, Dr. Feihu Wang, Dr. Yin Wang, Dr. Lisi Xie, Dr. Hao Su, Dr. Wenbin Dai, Dr. Xuanrong Sun, Dr. Weijie Zhang, Dr. Rami Chakroun, Caleb Anderson, Han Wang, Zongyuan Wang, Qin Fan, David Stern, Maya Monroe, Roxana Mitrut, Weiran Xie, Yuzhu Wang, Ben Ou, Marina Morrow, Yanqi Jiang, for providing incredible help in my research and creating the friendly lab environment in the past five years.

I am truly grateful to all my dearest friends for their continued company and support in my life. I especially want to thank Xiaoqing Hua, Ran Lin, Yumo Wang, Qi Huang, Runchen Zhao, Jianli Zhang, Hong Zhang, Yuzhu Wang, Yuqi Zhang, Yi Li, Danyu Wang for all the incredible moments we have had together. I will always treasure these memories wish you all the best in your future endeavors.

Most importantly, I want to express my most heartfelt gratitude to my parents, for their unconditional love and continuous support to my education and career. A special thanks to my boyfriend, for always being there for me, despite the distance. Life is so beautiful with you.

Dedication

To my beloved family, friends, and people who never stop pursuing their dreams.

Table of Contents

Abstract .... **ii**

Acknowledgements .... **v**

Table of Contents .... **ix**

List of Tables .... **xiii**

List of Figures .... **xiv**

1 Introduction **1**

1.1 Background and Motivation 1

1.2 Downstream Processing Strategies for Purification of Monoclonal Antibodies 3

1.2.1 Overview *3*

1.2.2 Affinity Chromatography *5*

1.2.3 Non-Affinity Chromatography *12*

1.2.4 Membrane Separation *14*

1.3 Recent Advances in the Precipitation of Monoclonal Antibodies 18

1.3.1 Overview *18*

1.3.2 Non-Affinity Precipitation *18*

1.3.3 Affinity Precipitation *24*

1.4 Peptide-Based Supramolecular Polymers 27

1.4.1 The Self-Assembly of Peptide-Based Supramolecular Polymers *27*

1.4.2 Design Principles of Bioactive Peptide Amphiphile Nanofibers *30*

1.4.3 Construction of Peptide-Based Supramolecular Polymers for Antibody Affinity Precipitation and Purification *34*

1.5 Dissertation Overview 37

2 Conformation Preservation of α-Helical Peptides within Supramolecular Filamentous Assemblies **38**

2.1 Overview 38

2.2 Introduction 39

2.3 Experimental Procedures 42

2.3.1 Materials and Molecular Synthesis *42*

2.3.2 Self-Assembly and Transmission Electron Microscopy (TEM) Imaging *43*

2.3.3 Critical Micelle Concentration (CMC) Measurement 44

2.3.4 Circular Dichroism (CD) Spectroscopy 44

2.3.5 Thioflavin T (ThT) Assays 45

2.4 Results and Discussions 45

2.4.1 Molecular Design 45

2.4.2 Molecular Assembly 47

2.4.3 Secondary Structure Measurements 51

2.4.4 Effect of Alkyl Chain Length 58

2.5 Conclusion 73

3 Bioinspired Supramolecular Engineering of Self-Assembling Immunofibers for High Affinity Binding of Immunoglobulin G 75

3.1 Overview 75

3.2 Introduction 76

3.3 Experimental Procedures 79

3.3.1 Materials and Molecular Synthesis 79

3.3.2 Self-Assembly of IAs and TEM Imaging 80

3.3.3 Circular Dichroism (CD) Spectroscopy 81

3.3.4 ITC Experiment 81

3.3.5 Confocal Imaging 82

3.4 Results and Discussions 82

3.4.1 Molecular Design 82

3.4.2 Molecular Assembly and Characterization 86

3.4.3 Binding Affinity Measurements 89

3.4.4 The Universality of the Functional Design of Supramolecular IFs 93

3.4.5 The Direct Visualization of IgG Bound to the Surface of IFs 96

3.5 Conclusion 102

4 Supramolecular Copolymers as Reversible Affinity Precipitants for Selective Capture and Recovery of Monoclonal Antibodies 104

4.1 Overview 104

4.2 Introduction 105

4.3 Experimental Procedures 107

4.3.1 Materials and Molecular Synthesis 107

4.3.2 CMC Measurement *109*
4.3.3 Self-Assembly, Co-Assembly, and TEM Imaging *109*
4.3.4 Cryo TEM *110*
4.3.5 CD Spectroscopy *110*
4.3.6 ITC Experiment *111*
4.3.7 Precipitation of Pure mAb1 and Pure Fc-fusion Protein *111*
4.3.8 Precipitation of IgG (FITC) and mCherry *112*
4.3.9 Resuspension of Pure mAb1 .... *112*
4.3.10 Capture and Recovery of Pure mAbs and mAbs in Clarified Bulk *112*
4.3.11 Size Elusion Chromatography (SEC) *113*
4.4 Results and Discussions 113
4.4.1 Design Principles and Molecular Characterization *113*
4.4.2 Mechanism Studies of Protein Precipitation and Yield Optimization *121*
4.4.3 Selectivity of Co-Assembled IFs *126*
4.4.4 Protein Recovery *129*
4.4.5 Capture and Recovery of mAbs from Cell Culture Harvest *130*
4.5 Conclusion 132

5 Manipulation of Epitope Radial Topography in High-Affinity Supramolecular Polymers for Binding-Triggered Antibody Precipitation 134
5.1 Overview 134
5.2 Introduction 135
5.3 Experimental Procedures 137
5.3.1 Materials and Molecular Synthesis *137*
5.3.2 CMC Measurement *138*
5.3.3 Self-Assembly, Co-Assembly, and TEM Imaging *138*
5.3.4 CD Spectroscopy *139*
5.3.5 ITC Experiment *139*
5.3.6 mAb Precipitation Experiment *140*
5.3.7 Sequential Precipitation and mAb Elution *140*
5.4 Results and Discussions 141
5.4.1 Molecular Design and Characterization *141*
5.4.2 Molecular Assembly and Characterization *145*

5.4.3 Impact of Linker Length and Ligand Selection 149
5.4.4 Optimization of mAb Precipitation under No Salt Conditions 153
5.4.5 Sequential Precipitation and mAb Elution 156
5.5 Conclusion 158

6 Conclusions and Future Work 159
6.1 Conclusions 159
6.2 Future Work... 160

References 162
Curriculum Vitae 176

List of Tables

Table 1-1. *Commonly used affinity ligands for protein purification in affinity chromatography.* 7

Table 1-2. *Commonly used affinity tags for protein purification in affinity chromatography.* 11

Table 2-1. *All the studied IA molecules, their CMC values, and peptide conformation measured at 100 µM.* 63

Table 3-1. *Thermodynamic parameters for binding of Z33-based ligands to IgG1 at 15 °C in PBS at pH 7.4. Data are reported per ligand/Z33.* 90

Table 3-2. *Recalculation of the thermodynamic parameters (per IgG1) for binding of Z33-based ligands to IgG1 at 15 °C in PBS at pH 7.4. Please note K_d, the binding affinity constant, differs when the data are normalized according to IgG1.* 90

Table 5-1. *Summary of ligand molecule design with various linkers.* 142

List of Figures

Figure 1-1. *Schemes of representative methods discussed in this review for purification of therapeutic proteins. Reprinted with permission from ref. 12, Copyright © 2019 Acta Materialia Inc. Published by Elsevier Ltd.* *5*

Figure 1-2. *(**A**) Schematic illustration of similarly sized protein separations through tunable nanoporous block copolymer membrane. (**B**) Regular order of the membrane's surface as shown by SEM. (**C**) Cross-section SEM image showing the thin top layer and the sponge-like bottom layer. (**A**) (**B**) (**C**) were reprinted with permission from ref. 129, Copyright © 2013, American Chemical Society. SEM images of (**D**) 100 nm PS latex beads and (**E**) SIV particles following filtration on Cladophora cellulose membrane. Reprinted with permission from ref. 130, Copyright © 2014, John Wiley and Sons.* *16*

Figure 1-3. *(**A**) Schematic of ELP-tagged split intein purification method. Reprinted from ref. 154. (**B**) Affinity precipitation of mAbs from cell culture with Z-ELP-E2 nanocages. (1) Mix nanocage stock with clarified culture. (2) Spontaneous aggregation through multivalent crosslinking. (3) Wash pellet by suspending in target wash buffer pH>5. (4) Elute by suspending pellet in buffer pH<4. (5) Add salt for selective precipitation of nanocage and collect purified mAb in supernatant. (6) Regenerate nanocage to recycle for future use. Reprinted with permission from ref. 18, Copyright © 2017, John Wiley and Sons.23*

Figure 1-4. *Schematic representation of the self-assembly of peptide-based materials. (**A**) The reversible self-assembly of various peptide motifs. (**B**) Possible non-covalent interactions among peptide-based building blocks, including hydrophobic collapse, van der Waals interactions, hydrogen bonding, π–π stacking, and electrostatic interactions. Adapted with permission from ref. 181 (© 2016 The Authors.)* *29*

Figure 1-5. *(**A**) Molecular structure of a representative PA with four rationally designed chemical entities. (**B**) Molecular graphics illustration of an IKVAV-containing PA molecule and its self-assembly into nanofibers. (**C**) Scanning electron micrograph of the IKVAV nanofiber network formed by adding cell media (DMEM) to the PA aqueous solution. (**D**) The encapsulation and release of biologics using supramolecular PA nanofiber hydrogels. (**A**) (**B**) (**C**) were reprinted with permission from Science (http://www.sciencemag.org) ref.186 (© 2004 AAAS). (**D**) was reprinted with permission from ref. 181 (© 2016 The Authors.)* *31*

Figure 1-6. *Overview of the mAb purification system using supramolecular immunofibers (IFs).* *36*

Figure 2-1. *(**A**) Schematic illustration of the molecular design of Helix1- and Helix2- based peptide amphiphiles via direct alkylation with C16 and 2C8, respectively. These peptide amphiphiles are termed immuno-amphiphiles because of the origin of the protein A-derived peptide Z33 for its specific binding ability to immunoglobulin antibodies. (**B**) Schematic illustration of the self-assembly of the designed IAs into one-dimensional nanostructures* *47*

Figure 2-2. *Representative TEM micrographs of filamentous assemblies formed by the four designed immuno-amphiphiles in aqueous solution, pH 7.4. TEM images of (**A**) Helix1-C16 and (**C**) C16-Helix2 reveal filament morphology with diameters of 9.6±1.3 nm and 12.4 ± 1.7 nm, respectively. TEM images of (**B**) Helix1-2C8 and (**D**) 2C8-Helix2 also relatively shorter filaments with diameters of 11.0±1.4 nm and 9.7±1.3 nm, respectively. Inserts (**A-D**) are higher resolution images illustrating the representative features. All the samples were prepared in water at a concentration of 1 mM at pH 7.4, aged overnight and diluted 10 fold right before TEM sample preparation. All TEM samples were stained with 2 wt% uranyl acetate aqueous solution, a negative contrast agent, to improve imaging resolution. All scale bars: 200 nm.* *49*

Figure 2-3. *Emission spectra of a reporter dye Nile Red upon incubating with (**A**) Helix1-C16, (**B**) C16-Helix2, (**C**) Helix1-2C8, and (**D**) 2C8-Helix2 for determining the critical micelle concentrations (CMCs). All spectra shown here are normalized by the emission maximum. A blue-shift is expected when the IA concentrations exceed the CMC. The CMC range for each IA is boxed in the legend.* *50*

Figure 2-4. *Normalized CD Spectra of 100 μM (**A**) Helix1, Helix1-C16, Helix1-2C8, and (**B**) Helix2, C16-Helix2, 2C8-Helix2 in water, pH 7.4. The spectra show that double-chain alkylated peptides can effectively preserve their native helical conformation, whereas single-chain alkylation led to a transition from helical conformation to β-sheet-bonded assemblies.* 51

Figure 2-5. *Normalized CD Spectra of Helix1, Helix2, and Z33 at 100 μM in water, pH 7.4.* 53

Figure 2-6. *Analysis of CD spectra for Helix1- and Helix2-based IAs. The content of three main secondary structures in (**A**) Helix1-based and (**B**) Helix2-based molecules. The CD data were fit from 200 nm to 240 nm using a linear combination of polylysine basis spectra to determine approximate α-helix, β-sheet, and random coil peptide secondary structure.* 53

Figure 2-7. *Fluorescence of ThT dye with (**A**) Helix1 and Helix1-based and (**B**) Helix2 and Helix2-based immuno-amphiphiles at 100 μM in deionized water, pH 7.4.* 54

Figure 2-8. *Normalized CD Spectra of (**A**) Helix1-2C8 and (**B**) Helix1-C16 at various concentrations in water, pH 7.4. These studies suggest that peptide conjugates within their supramolecular assemblies primarily contribute to the observed CD absorption. Both conjugates appear to be unstructured random coils when concentrations are dropped below their respective CMCs.* 56

Figure 2-9. *Characterization of Helix1-2C12 and 2C12-Helix2. TEM images of (**A**) Helix1-2C12 and (**B**) 2C12-Helix2 display nanofibers morphology with diameters of 15.7 ± 1.4 nm, and 13.4 ± 0.9 nm, respectively. The samples were prepared in deionized water at pH 7.4. (**C**) Normalized CD Spectra of 100 μM Helix1-2C12 and 2C12-Helix2 in water, pH 7.4. Emission spectra of the reporter dye Nile Red when incubated with (**D**) Helix1-2C12 and (**E**) 2C12-Helix2 for determining the CMC values.* 59

Figure 2-10. *Emission spectra of the reporter dye Nile Red when incubated with (**A**) Helix1-C8, (**B**) C8-Helix2 for determining the critical micelle concentration (CMC) values. All spectra shown here are normalized by the emission maximum. There was no detectable peak shift observed even the conjugate concentrations reached 100 μM.* 60

Figure 2-11. *Characterization of different Peptide conjugates. TEM images of (**A**) Helix1-C12 and (**B**) C12-Helix2 display nanofibers morphology with diameters of 12.9 ± 0.9 nm, and 13.9 ± 1.5 nm, respectively. All scale bars: 200 nm. Emission spectra of the reporter dye Nile Red when incubated with (**C**) Helix1-C12 and (**D**) C12-Helix2 for determining the CMC values. Normalized CD spectra of 100 μM (**E**) Helix1, Helix1-C8, Helix1-C12, and Helix1-C16 and (**F**) Helix2, C8-Helix2, C12-Helix2, and C16-Helix2 in water, pH 7.4.* 61

Figure 2-12. *Peptide sequences and chemical structures of Helix1, Helix2, and Z33* 64

Figure 2-13. *Chemical structures of Helix1-C8, Helix1-C12, Helix1-C16, Helix1-2C8, and Helix1-2C12* ... 65

Figure 2-14. *Chemical structures of C8-Helix2, C12-Helix2, C16-Helix2, 2C8-Helix2, and 2C12-Helix2* ... 66

Figure 2-15. *RP-HPLC (**A**) and MALDI-TOF MS (**B**) characterization of Z33. The RP-HPLC spectrum confirms the purity of the product (>99%). The expected mass is 4102.0. The peak at 4103.4 corresponds to $[M+H]^+$.* 67

Figure 2-16. *RP-HPLC (**A**) and MALDI-TOF MS (**B**) characterization of Helix 1. The RP-HPLC spectrum confirms the purity of the product (>99%). The expected mass is 1980.9. The peak at 1982.1 corresponds to $[M+H]^+$.* 67

Figure 2-17. *RP-HPLC (**A**) and MALDI-TOF MS (**B**) characterization of Helix 2. The RP-HPLC spectrum confirms the purity of the product (>99%). The expected mass is 2181.3. The peak at 2182.4 corresponds to $[M+H]^+$.* 68

Figure 2-18. *RP-HPLC (**A**) and MALDI-TOF MS (**B**) characterization of Helix1-C8. The RP-HPLC spectrum confirms the purity of the product (>99%). The expected mass is 2235.1. The peak at 2236.3 corresponds to $[M+H]^+$.* 68

Figure 2-19. *RP-HPLC (**A**) and MALDI-TOF MS (**B**) characterization of C8-Helix2. The RP-HPLC spectrum confirms the purity of the product (>99%). The expected mass is 2265.2. The peak at 2266.3 corresponds to [M+H]$^+$.* 69

Figure 2-20. *RP-HPLC (**A**) and MALDI-TOF MS (**B**) characterization of Helix1-C12. The RP-HPLC spectrum confirms the purity of the product (>99%). The expected mass is 2292.2. The peak at 2293.3 corresponds to [M+H]$^+$.* 69

Figure 2-21. *RP-HPLC (**A**) and MALDI-TOF MS (**B**) characterization of C12-Helix2. The RP-HPLC spectrum confirms the purity of the product (>99%). The expected mass is 2321.2. The peak at 2322.2 corresponds to [M+H]$^+$.* 70

Figure 2-22. *RP-HPLC (**A**) and MALDI-TOF MS (**B**) characterization of Helix1-C16. The RP-HPLC spectrum confirms the purity of the product (>99%). The expected mass is 2248.8. The peak at 2350.4 corresponds to [M+H]$^+$.* 70

Figure 2-23. *RP-HPLC (**A**) and MALDI-TOF MS (**B**) characterization of C16-Helix2. The RP-HPLC spectrum confirms the purity of the product (>99%). The expected mass is 2378.7. The peak at 2380.3 corresponds to [M+H]$^+$.* 71

Figure 2-24. *RP-HPLC (**A**) and MALDI-TOF MS (**B**) characterization of Helix1-2C8. The RP-HPLC spectrum confirms the purity of the product (>99%). The expected mass is 2489.3. The peak at 2490.2 corresponds to [M+H]$^+$.* 71

Figure 2-25. *RP-HPLC (**A**) and MALDI-TOF MS (**B**) characterization of 2C8-Helix2. The RP-HPLC spectrum confirms the purity of the product (>99%). The expected mass is 2520.9. The peak at 2521.7 corresponds to [M+H]$^+$.* 72

Figure 2-26. *RP-HPLC (**A**) and MALDI-TOF MS (**B**) characterization of Helix1-2C12. The RP-HPLC spectrum confirms the purity of the product (>99%). The expected mass is 2603.2. The peak at 2604.1 corresponds to [M+H]$^+$.* 72

Figure 2-27. *RP-HPLC (**A**) and MALDI-TOF MS (**B**) characterization of Helix1-2C12. The RP-HPLC spectrum confirms the purity of the product (>99%). The expected mass is 2603.2. The peak at 2604.1 corresponds to [M+H]$^+$.* 73

Figure 3-1. *(**A**) Schematic illustration of the Z33 peptide binding to Fc-portion of human IgG1. (**B**) The sequences of C12-Z33 and 2C8-Z33. Alkyl groups and Z33 are indicated with the yellow and blue shaded areas, respectively. (**C**) Schematic illustration of the self-assembly of IAs and the binding between IFs and IgG.* 83

Figure 3-2. *Chemical structures of Z33, C12-Z33, 2C8-Z33, and C12-SZ33. The peptide and alkyl chain are shown in blue and yellow, respectively.* 84

Figure 3-3. *RP-HPLC (**A**) and MALDI-TOF MS (**B**) characterization of Z33. The RP-HPLC spectrum confirms the purity of the product (>99%). The expected mass is 4102.0. The peak at 4103.2 corresponds to [M+H]$^+$.* 85

Figure 3-4. *RP-HPLC (**A**) and MALDI-TOF MS (**B**) characterization of C12-Z33. The RP-HPLC spectrum confirms the purity of the product (>99%). The expected mass is 4284.2. The peak at 4285.7 corresponds to [M+H]$^+$.* 85

Figure 3-5. *RP-HPLC (**A**) and MALDI-TOF MS (**B**) characterization of 2C8-Z33. The RP-HPLC spectrum confirms the purity of the product (>99%). The expected mass is 4482.3. The peak at 4483.9 corresponds to [M+H]$^+$.* 85

Figure 3-6. *RP-HPLC (**A**) and MALDI-TOF MS (**B**) characterization of C12-SZ33. The RP-HPLC spectrum confirms the purity of the product (>99%). The expected mass is 4284.2. The peak at 4285.6 corresponds to [M+H]$^+$.* 86

Figure 3-7. *Molecular assembly and nanostructure characterization of IAs. TEM characterization of C12-Z33 at pH 7.4 (**A**, **B**) and 2.8 (**C**, **D**). The TEM samples were prepared at concentration of 100 μM in PBS* *(pH 7.4) and IgG elution buffer (pH 2.8), respectively. The TEM samples were negatively stained with 2 wt% uranyl acetate aqueous solution. (**E**) Normalized CD spectra of Z33 peptide and C12-Z33 at pH 7.4 and 2.8, respectively.* *88*

Figure 3-8. *ITC profiles and binding curves for the stepwise injection of 100 μM C12-Z33 into a solution of 2 μM IgG1 at 15 °C in (**A**) PBS buffer, pH 7.4, and (**C**) IgG elution buffer, pH 2.8. ITC profiles and binding curves for the stepwise injection of 100 μM (**B**) Z33 and (**D**) C12-SZ33 into 2 μM IgG1 in PBS at 15 °C, pH 7.4.* *89*

Figure 3-9. *TEM images of 100 μM (**A**) C12-SZ33 and (**C**) RB-C12-Z33 in PBS, pH 7.4. Both molecules self-assembled into nanofibers with diameters of 11.5 ± 1.5 nm and 13.8 ± 1.8 nm respectively. Normalized CD spectra of 100 μM (**B**) C12-SZ33 and (**D**) RB-C12-Z33 nanofibers in PBS at pH 7.4 showed β-sheet and α-helix conformation, respectively.* *93*

Figure 3-10. *TEM characterization of 2C8-Z33 in (**A**) PBS at pH 7.4 with a diameter of 16.8 ± 1.5 nm and (**B**) IgG elution buffer at pH 2.8 with a diameter of 17.3 ± 1.9 nm. The preparation of TEM sample was similar with that of C12-Z33. (**C**) Normalized CD spectra of 100 μM 2C8-Z33 in PBS at pH 7.4 showed α-helix secondary structures. ITC profiles for the stepwise injection of 100 μM 2C8-Z33 into a solution of 2 μM IgG1 in (**D**) PBS buffer, pH 7.4 and (**E**) IgG elution buffer, pH 2.8.* *95*

Figure 3-11. *TEM images of (**A**, **B**) 100 μM C12-Z33 and (**C**, **D**) 100 μM C12-SZ33 after incubation with IgG-coated Au nanoparticles in PBS, pH 7.4. IgG concentration: 0.33-0.66 μM.* *96*

Figure 3-12. *CMC measurement of C12-Z33. Emission spectra of the reporter dye Nile Red monitored by a Fluorolog fluorometer (Jobin Yvon, Edison, NJ) after incubated with a series of concentrations of C12-Z33. Excitation wavelength was fixed at 560 nm; emission spectra were monitored 580–720 nm. The CMC of C12-Z33 is determined by a blue-shift of the emission maximum, where the transition indicates the dye partitioning into the hydrophobic compartment of assembled nanostructures. All spectra shown here are normalized by the emission maximum. The CMC range for C12-Z33: 2-5 μM.* *98*

Figure 3-13. *Chemical structures of RB-C12-Z33. The peptide, alkyl chain, and Rhodamine B are shown in blue, yellow, and red, respectively.* *99*

Figure 3-14. *RP-HPLC (**A**) and MALDI-TOF MS (**B**) characterization of RB-C12-Z33. The RP-HPLC spectrum confirms the purity of the product (>99%). The expected mass is 4838.5. The peak at 4840.2 corresponds to $[M+H]^+$.* *100*

Figure 3-15. *Confocal fluorescence images of 100 μM RB-C12-Z33 incubated with 2 μM FITC-IgG in PBS (pH 7.4) show co-localization of the fluorescence signal of Rhodamine B with that of the FITC. (**A**) Image of Rhodamine B fluorescence. (**B**) Image of FITC fluorescence. (**C**) Merged image of (**A**) and (**B**). Scale bar: 20 μm.* *100*

Figure 3-16. *Confocal fluorescence images of (**A**) 2 μM FITC-IgG, (**B**) 100 μM RB-C12-Z33, (**C**) 2 μM FITC-IgG incubated with 100 μM C12-Z33, and (**D**) 2 μM FITC-IgG incubated with 100 μM C12-SZ33 in PBS, pH 7.4. All fluorescence images were taken under identical conditions. Compared to the bright fluorescence of FITC-IgG when incubated with RB-C12-Z33, no fluorescent signals were detected or after incubated with C12-SZ33, while comparable fluorescence was observed when incubated with C12-Z33. This showed that FITC-IgG was dispersed well in the PBS buffer or in the presence of C12-SZ33, while the binding to RB-C12-Z33 or C12-Z33 induced the aggregation of FITC-IgG and thus the strong fluorescence. Scale bar: 20 μm.* *101*

Figure 4-1. *The overview of the purification process, design of filler and ligand, and molecular characterization. (**A**) Schematic illustration of the overall mAb purification process using co-assembled IFs. (**B**) Chemical structures and key design components of the filler and ligand molecules. Representative transmission electron microscopy (TEM) images of self-assembled filamentous structures formed by (**C**) filler and (**D**) ligand with a diameter of 7.4 ± 0.6 nm and 14.9 ± 1.5 nm, respectively. Filament diameters are represented as mean ± SD (n = 30). TEM sample was stained with 2 wt % uranyl acetate aqueous solution to improve imaging quality. Scale bars in (**C-D**) are 100 nm. (**E**) Normalized CD spectra of self-assembled filler, self-assembled ligand, and free Z33 peptide. (**F**) ITC profiles and binding curves for the stepwise injection of 100 μM mAb1 into a solution of 40 μM ligand molecule at 25 °C in PBS, pH 7.4...* *115*

Figure 4-2. *Chemical structures of filler (C12-VVEE) and ligand (C12-VVKKGGZ33) molecule. The alkyl chain (C12), VVKK/EE, GG, and Z33 are shown in yellow, blue, green, and black, respectively.* *116*

Figure 4-3. *RP-HPLC (**A**) and MALDI-TOF MS (**B**) characterization of C12-VVEE. The RP-HPLC spectrum confirms the purity of the product (>99%). The expected mass is 655.4. The peak at 678.1 corresponds to $[M+Na]^+$.* *116*

Figure 4-4. *RP-HPLC (**A**) and MALDI-TOF MS (**B**) characterization of C12-VVKKGGZ33. The RP-HPLC spectrum confirms the purity of the product (>99%). The expected mass is 4852.6. The peak at 4853.6 corresponds to $[M+H]^+$.* *117*

Figure 4-5. *mAb1 precipitation after incubation with self-assembled ligand molecule. 20 µM mAb1 was incubated with 50 µM self-assembled ligand molecule and 1 M ammonium sulfate. In the control group, 20 µM mAb1 was incubated with 1 M ammonium sulfate. Both mAb1 control group and self-assembled ligand group showed negligible mAb precipitation. All experiments were performed in triplicate and the data is shown as mean ± standard deviation.* *118*

Figure 4-6. *CMC measurement of (**A**) filler and (**B**) ligand. The CMC ranges are 50-100 µM and 2-5 µM, respectively. Emission spectra of the reporter dye Nile Red monitored by a Fluorolog fluorometer (Jobin Yvon, Edison, NJ) after incubation with a series of concentrations of filler or ligand. Excitation wavelength was fixed at 560 nm; emission spectra were monitored 580-720 nm. The CMC value was determined by a blue-shift of the emission maximum, where the transition indicates the dye partitioning into the hydrophobic compartment of assembled nanostructures. All spectra shown here are normalized by the emission maximum.* *118*

Figure 4-7. *Representative TEM images of supramolecular copolymers formed by filler and ligand molecules at (**A**) 5:1, (**B**) 25:1, and (**C**) 50:1 molar ratios with a diameter of 14.1 ± 0.8 nm, 8.4 ± 0.9 nm, and 7.5 ± 0.9 nm, respectively. Filament diameters are represented as mean ± SD (n = 30). (**D**) CD spectra of co-assembled IFs at different spacer:ligand molar ratios. The spectra were normalized by the concentration of the ligand molecules, showing a transition of the apparent conformation from α-helix to β-sheet with the increase of the spacer:ligand molar ratio. (**E**) Representative TEM image of 50:1 IFs+mAb1. Representative cryo-TEM images of (**F**) 50:1 IFs+mAb1, (**G**) 50:1 IFs, and (**H**) mAb1 in PBS showed the binding between mAb1 and IFs. All TEM sample was stained with 2 wt % uranyl acetate aqueous solution to improve imaging quality. Scale bars are 100 nm.* *120*

Figure 4-8. *Key experimental parameters in the selective capture of mAbs and Fc-fusion proteins. (**A**) Precipitation yields of mAb1 and Fc-fusion protein at different molar ratios of filler:ligand with fixed ligand concentration. (**B**) Schematic illustration of the effect of ligand density in IFs when the ligand concentration is fixed. Precipitation yields of (**C**) filler and (**D**) ligand molecule in co-assembled IFs at different molar ratios of filler:ligand with fixed ligand concentration. Precipitation yields of mAb1 and Fc-fusion protein at different (**E**) molar ratios of ligand:protein with fixed ligand concentration and (**F**) molar ratios of filler:ligand with fixed filler concentration. As a proof of concept, purified mAb1 and Fc-fusion protein were used in (**A**, **C**-**F**). All experiments were performed in triplicate and the data is shown as mean ± standard deviation.* *122*

Figure 4-9. *Precipitation yields of (**A**) filler and (**B**) ligand molecule for 50:1 IFs at various ligand:protein ratios and 1 M ammonium sulfate conditions. The IFs were incubated with mAb1or Fc-fusion protein. All experiments were performed in triplicate and the data is shown as mean ± standard deviation.* *123*

Figure 4-10. *Stability of mAb1 (**A**) and IgG (FITC) (**B**) at various salt concentrations. Proteins were incubated with salt for 30 minutes and centrifuged at 15000 rpm for 15 minutes. All experiments were performed in duplicate and the data is shown as mean ± standard deviation.* *125*

Figure 4-11. *Precipitation yields of (**A**) mAb1 and Fc-fusion protein, (**B**) filler, and (**C**) ligand for 50:1 IFs with 10:1 ligand:protein molar ratio at different salt conditions. All experiments were performed in triplicate and the data is shown as mean ± standard deviation.* *126*

Figure 4-12. *Selectivity of co-assembled IFs in precipitating immunoglobulin G (IgG). (**A**) Photographs and (**B**) fluorescence images of i) PBS, ii) IgG (FITC), iii) mCherry, iv) IgG (FITC)+mCherry, v) IgG (FITC)+IFs, vi) mCherry+IFs, and vii) IgG (FITC)+mCherry+IFs. IgG (FITC) and mCherry were incubated* with 50:1 IFs and 0.75 M ammonium sulfate was used to trigger precipitation. Green precipitates were observed in v) and vii), indicating the precipitation of IgG (FITC). However, the precipitation of mCherry was not observed in vi) and vii), showing high specificity of mAb precipitation by IFs. Fluorescence measurements of supernatant in sample i)-vii) on the (**C**) green and (**D**) red channels. Fluorescence of IgG (FITC) dropped in v) and vii) after incubated with 50:1 IFs, while fluorescence of mCherry remained similar with control groups. 127

Figure 4-13. Supplementary bright field and fluorescence images for **Figure 4-12**: i) PBS; ii) IgG (FITC) control; iii) mCherry control; iv) IgG (FITC)+mCherry control; v) IgG (FITC) +IFs; vi) mCherry+IFs; vii) IgG (FITC)+mCherry+IFs. 128

Figure 4-14. mAb recovery and purification. Resuspension yields of (**A**) mAb1, (**B**) filler, and (**C**) ligand molecules in three resuspension buffers at pH 3.7, pH 7.4, and pH 10.1, respectively. The precipitated samples were 50:1 IFs and mAb1 at 10:1 ligand:protein molar ratio with 1 M ammonium sulfate. (**D**) Precipitation and overall yields of mAb1, filler, and ligand molecules after the incubation of pure mAb1 with 50:1 IFs and 1 M ammonium sulfate. (**E**) Schematic illustration of the process of purifying mAbs from CB using IFs. (**F**) mAb precipitation yields, overall yields, and percentage retention of filler and ligand molecules after the whole purification process for mAb1 CB and mAb2 CB. All experiments were performed in triplicate and the data is shown as mean ± standard deviation. 130

Figure 4-15. SEC spectra of the sample solutions for CB, CB supernatant, and product pool after membrane separation for (**A**) mAb1 and (**B**) mAb2. 131

Figure 5-1. Molecular design of the IF building units with OEG (or PEG) linkers and the formation of IFs for mAb capture. (**A**) Chemical structures of the filler molecule, C12-VVEE, and the ligand molecules, C12-VVKK[Linker]Z33. (**B**) Schematic illustration of the ligand molecule design with various linkers and the effect of linker length on the presentation of Z33 peptide on co-assembled IFs. **(C)** Co-assembly of filler and ligand molecules into supramolecular IFs and four possible states of mAbs in an IF solution: **1**) Two Fc-portions of a mAb bound to two ligands from two different IFs. **2**) Two Fc-portions of a mAb bound to two adjacent ligands from the same IF. **3**) Only one Fc-portion of a mAb bound to one ligand on an IF. **4**) Free mAbs in the solution bound to zero, one, or two monomer ligands that are not assembled in IFs. 142

Figure 5-2. Chemical structures of filler and ligand molecule. The alkyl chain (C12), VVKK/EE, OEG_n, and Z33 are shown in yellow, blue, green, and black, respectively. 143

Figure 5-3. RP-HPLC and MALDI-TOF MS characterization of O4 (**A-B**), O8 (**C-D**), and O12 (**E-F**). 144

Figure 5-4. RP-HPLC and MALDI-TOF MS characterization of O16 (**A-B**), O36 (**C-D**), and P2000 (**E-F**). 144

Figure 5-5. CMC measurement of O4-P2000. Normalized emission spectra of the reporter dye Nile Red monitored by a Fluorolog fluorometer (Jobin Yvon, Edison, NJ) after incubation with a series of concentrations of ligand molecules. Plotting the ratio of intensity at 635 nm (emission maximum of Nile red in a hydrophobic environment) to that at 660 nm (emission maximum of Nile red in an aqueous environment) against the tested concentration indicates the transition that occurs when the concentration exceeds the CMC. The CMC value for each ligand molecule was then determined by the intersection of the two fitting lines. 147

Figure 5-6. Characterization of filler and ligand molecules. Representative TEM images of self-assembled filler and ligand molecules (**A**:C12-VVEE, **B**:O4; **C**:O8; **D**:O12; **E**:O16; **F**:O36; **G**:P2000) in PBS with a diameter of 7.4 ± 0.6 nm, 11.1 ± 0.9 nm, 12.6 ± 1.2 nm, 13.6 ± 1.2 nm, 14.9 ± 1.3 nm, 18.5 ± 1.8 nm, 19.3 ± 2.0 nm, respectively. Diameters are given as mean ± SD (n = 30). Scale bars: 100 nm. (**H**) Normalized CD spectra of self-assembled ligand molecules with different OEG (or PEG) linkers suggest the formation and retention of α-helix secondary structures. 148

Figure 5-7. ITC profiles and binding curves for the stepwise injection of 100 µM mAb1 into 40 µM (**A**) O4, (**B**) O8, (**C**) O12, (**D**) O16 at 25 °C in PBS, pH 7.4. 149

Figure 5-8. Comparison of mAb precipitation performance of IFs with different ligand molecules. mAb precipitation yields for (**A**) 20 µM and (**B**) 40 µM mAb1 incubated with various co-assembled IFs (2.5 mM *filler, 100 μM ligand) under 1 M salt or no salt conditions. Precipitated mAb mass from 100 μL samples of (**C**) 20 μM (0.3 mg) and (**D**) 40 μM (0.6 mg) mAb1 incubated with various 100 IFs (2.5 mM filler, 100 μM ligand) under 1 M salt or no salt conditions. (**E**) Photographs of co-assembled IFs (2.5 mM filler, 100 μM ligand) after mixed with 40 μM mAb for 5 min under 1 M salt or no salt conditions. All experiments were performed in triplicate and the data is shown as mean ± standard deviation*.. *151*

Figure 5-9. *Optimization of mAb precipitation yield. The (**A**) yield and (**B**) mass of mAb precipitation for 100 μL mAb1 at 40 μM (0.6 mg), 80 μM (1.2 mg), and 133 μM (2 mg) incubated with IFs at various O16 concentrations. (**C**) Comparison of mAb precipitation yield for 40 μM mAb1 incubated with optimized IFs (2.5 mM filler, 250 μM O16) at different salt concentrations. (**D**) Proposed mechanism of mAb-IF agglomeration as the ligand concentration increases for a fixed mAb concentration. mAbs at **States 3**, **State 1**, and **State 2** are dominant at low, medium, and high ligand concentrations, respectively. (**E**) Turbidity of 40 μM mAb with optimized IFs (2.5 mM filler, 250 μM O16) in 2 hours. (**F**) The effect of binding time on the mAb precipitation yield for 40 μM mAb1 incubated with optimized IFs (2.5 mM filler, 250 μM O16). All experiments were performed in triplicate and the data is shown as mean ± standard deviation.* *153*

Figure 5-10. *Sequential precipitation and mAb purification. (**A**) Schematic illustration of the mAb purification process using IFs. (**B**) mAb precipitation yield, yield loss at wash step, elution yield for 40 μM and 80 μM pure mAb1 after two sequential precipitations under no salt conditions. All experiments were performed in triplicate and the data is shown as mean ± standard deviation*.. *156*

Figure 5-11. *mAb precipitation yields for 100 μL mAb1 at 10 μM and 20 μM after an incubation with 100 μL IFs at various O16 concentrations. IFs with 200 μM O16 gave the best mAb precipitation yield for both mAb concentrations*... *157*

1 Introduction

1.1 Background and Motivation

mAbs have received considerable attention in the past two decades for the treatment of diseases in oncology, hematology, dermatology, rheumatology, etc.[1-2] The mAb market has rapidly increased in the past five years with market sales exceeding $98 billion in 2017 and predicted sales of $137-200 billion by 2022.[2] The rapidly growing mAb market and the competition from biosimilars have placed an increasing burden on industrial mAb manufacturing.[2-4] Downstream processing is considered one of the most challenging phases of industrial manufacturing of therapeutic proteins, accounting for a large portion of the total production costs. Meanwhile, increasing pressure on downstream processing is due to the significant growth of upstream titers.[5-6] More than tenfold increase in titers has been seen over the past 30 years with an average of 3 g/L, while several new products are reported to reach more than 10 g/L.[5, 7-8] In contrast, improvement of downstream processing lags substantially behind the increase in titers, and downstream costs increase dramatically as the capacity increases.[7] Currently, protein A affinity chromatography dominates the mAb capture step but suffers from limited production capacities and high media cost.[9] Optimization of the mAb capture step or exploration of potential alternatives to chromatography is essential to improve process efficiency and reduce production costs.[6, 10-12]

Affinity precipitation has been increasingly explored as a promising alternative that features high affinity capture as well as reversible soluble-insoluble transitions.[13-14] The precipitation can be triggered either by the ligand-mAb interactions or external stimuli such as temperature, pH, ionic strength, and concentration.[15] To some extent, affinity precipitation can surpass chromatography limitations involved with column size and ligand immobilization;[16] however, it demands high mAb capture selectivity and the complete removal of precipitants. Therefore, rational design of affinity precipitants is key for this technology, which requires at least one segment to specifically capture mAbs and the feature to make the whole system responsively and reversibly soluble. Several biomaterials such as elastin-like polypeptide (ELP) based materials,[17-19] smart polymers,[20] and affinity peptides[21] have been investigated as affinity precipitants for mAb capture and purification. However, concerns remain in capture efficiency and difficulty in removing these biomaterials.

Supramolecular peptide assemblies have been widely explored in the past three decades for applications in drug delivery,[22-30] regenerative medicine,[31-35] and disease diagnostics.[36-38] As molecular building units, peptides are particularly attractive for creating supramolecular materials for biomedical applications due to their inherent biodegradability and biocompatibility, and most importantly, their ability to incorporate a variety of bioactive epitopes for specific biology interfacing.[39-43] Of all the peptide-based assemblies explored thus far, peptide amphiphile nanofibers[44] and protein analogous micelles[45] are the most studied as bioactive materials for diverse biomedical applications. In both cases, the underlying molecular design involves covalent linkage of one or more hydrocarbons/lipids onto either the *N* or *C* terminus of a short peptide to generate self-assembling peptide amphiphiles (PAs). In a typical peptide-based supramolecular system, reversible transitions can occur at multiple length scales,[46] including the intramolecular chain adjustment to adopt various conformations,[47] the intermolecular interactions to assemble into discrete polymeric nanostructures,[40, 48-49] and the inter-particle interactions to percolate into a 3D network (gelation) or to cause macroscopic phase separation (coacervation or precipitation).[50-52]

In this work, I took advantage of the inherent reversible transitions in supramolecular systems to develop peptide-based supramolecular polymers as effective affinity precipitants for selective capture and purification of mAbs. My approach was to incorporate a mAb-binding peptide ligand with high affinity into the molecular building units of the supramolecular system. The design principles of constructing the building units while preserving the conformation of the peptide ligand were first investigated. The supramolecular system created using self-assembly or co-assembly strategy has been thoroughly studied for mAb capture and purification. I believe these results shed important light on the use of supramolecular systems for non-chromatographic purification of mAbs and other protein therapeutics.

1.2 Downstream Processing Strategies for Purification of Monoclonal Antibodies[a]

1.2.1 Overview

Nowadays, downstream processing of therapeutic proteins is facing great challenges created by the rapid increase of the market size and upstream titers, starving for significant improvements or innovations in current downstream unit operations. The emergence of advanced biomaterials has contributed to addressing the downstream

---

[a] Reprinted with permission from Li, Y.; Stern, D.; Lock, L.L.; Mills, J.; Ou, S.-H.; Morrow, M.; Xu, X.; Ghose, S.; Li, Z.J.; Cui, H. Emerging biomaterials for downstream manufacturing of therapeutic proteins, ***Acta Biomaterialia, 2019***, 95, 73-90. Copyright © 2019 Acta Materialia Inc. Published by Elsevier Ltd.

bottleneck by introducing high-performance and cost-effective downstream technologies.[7, 10, 53] Typically, downstream mAb processing involves a sequence of different chromatographic separations, virus inactivation and filtration, and membrane-based separations.[7] After clarifying cell culture harvest, protein A or other affinity-based chromatography is used to capture the target mAb product, followed by a virus inactivation step.[7, 54] Then combinations of polishing chromatography steps, including but not limited to ion exchange chromatography (IEX) and hydrophobic interaction chromatography (HIC), are allowed to further reduce impurity levels by utilizing the differences in physical properties such as charge, hydrophobicity, and molecule size.[7, 11] Finally, a virus filtration step and an ultrafiltration/diafiltration step are performed to ensure viral clearance and to exchange the product into the formulation buffer, respectively.[10, 54] Despite the high media cost and limited loading capacity, affinity chromatography remains the most widely used capture method for large-scale purification.[53] Proteins of interest can be separated from impurities through reversible interactions between the target protein and affinity ligands immobilized on chromatography media. For example, protein A chromatography has been widely used in the purification of mAbs and Fc-fusion proteins.[9] Over the past decades, numerous affinity ligands have been developed to improve the binding capacity, capture efficiency, and ligand stability.[55] Furthermore, affinity tags that are genetically grafted onto target proteins have also gained widespread attention, as these pre-defined affinity pairs are independent of each particular target protein.[56-57] Advances have also been made in developing more efficient chromatography media such as natural or synthetic polymers to achieve higher column performance.[11] To overcome limitations of chromatographic procedures for high cost and demanding operations, continuous efforts have also been made to develop non-chromatographic methods including membrane separations,[58] magnetic separations,[59] and precipitation/phase separations.[60-61] These are promising alternatives to chromatography-based approaches, with advantages including cost-effectiveness and operational simplicity in some applications. Among these non-chromatographic methods, polymer/peptide-based biomaterials have been intensively utilized in the design and construction of membranes, magnetic nanoparticles, and precipitants with high capture efficiency and high selectivity. This section provides an overview of the recent advances in the development and optimization of biomaterials for applications in downstream processing of therapeutic proteins (**Figure 1-1**). Discussions will be focused on chromatography and membrane separation. Approaches currently used in industry and in development will be discussed.

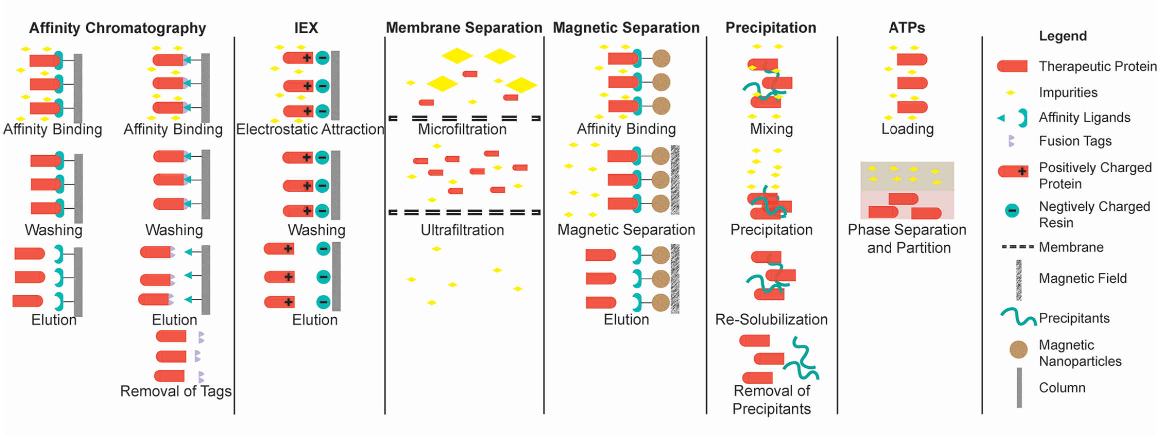

Figure 1-1. Schemes of representative methods discussed in this review for purification of therapeutic proteins. Reprinted with permission from ref. 12, Copyright © 2019 Acta Materialia Inc. Published by Elsevier Ltd.

1.2.2 Affinity Chromatography

Affinity chromatography is the predominant unit operation for large-scale bioprocessing and purification of therapeutic proteins.[55] Despite its high binding specificity to the target protein, affinity chromatography is currently still the downstream productivity bottleneck due to its relatively low resin binding capacity, limited column size amenable to biomanufacturing, and high resin cost.[62] Affinity ligands that are immobilized on the chromatography media can recognize and bind to specific proteins through molecular interactions such as hydrophobic and electrostatic interactions, hydrogen bonding, and van der Waals forces.[55] Important features of an affinity ligand include its high affinity and specificity to the target, stability in various solution conditions, ease of immobilization, and target-binding retention following attachment to the matrix.[63] A myriad of affinity ligands can be used for protein purification depending on the biophysical properties of the target protein. **Table 1-1** shows some of the vast array of affinity ligands that have gained interest over the last several years for applications in the purification of therapeutic proteins.

The majority of ligands currently being used in affinity chromatography are biospecific ligands. They are ligands of biological origin that are derived from natural sources and can bind to specific targets such as bacterial immunoglobulin-binding proteins, antibodies, lectins, and nucleic acids.[55] The most frequently used biospecific ligands for mAb and Fc-fusion protein purification processes are protein A, protein G, and protein L, which are all derived from bacterial cell walls.[55] Many species of antibodies can bind to these ligands, yet, their affinities vary depending on the antibody subclass.[64-65] However, the harsh environment during elution and other conditions at extreme pH and exposure to organic solvents or detergents can denature coupled biospecific molecules, often resulting in ligand leaching.[63] The stability and binding capacity of recombinant protein A affinity resins are constantly being improved. For example, Toyopearl AF-rProtein A-650F, a recombinant protein A affinity resin derived from an immunoglobulin G (IgG)-binding domain, has been optimized to withstand alkaline solutions during cleaning and sanitization procedures and displays higher binding capacities, up to 50-70 mg/mL, yielding eluted antibodies of about 99% purity.[66] Additional resins with high binding capacities and high alkaline stabilities are found in GE Healthcare's MabSelect family, including MabSelect Sure, Sure LX, Sure pcc, and PrismA.[67-69] Within this family of resins, MabSelect Sure pcc and MabSelect PrismA have the highest binding capacities for mAbs and bispecific antibodies, ranging from 58-74 mg/mL. These MabSelect resins are derived from the B domain of protein A, giving them a high binding affinity for various mAbs and Fc-fusion proteins, such as immunoglobulins.[67-69]

Table 1-1. Commonly used affinity ligands for protein purification in affinity chromatography.

Ligand/Family	Affinity Target	Scaffold/Origin	References
Recombinant protein A derived from an IgG-binding domain	IgG, IgM, and Fab fragments	Fc-region (B domain) and Fab-region (D&E) domains of protein A	70
MabSelect Sure, Sure LX, Sure pcc, PrismA	Fc-region of IgG	B domain of protein A	67-69
Camelid VHH	IgA, IgG, various blood factors, and adeno-associated viruses	VHH antibody	71-72
Anti-EGFR Affibody	EGFR receptor	Z domain, modified from B domain of *Staphylococcal* protein A (SpA)	73
Anti-TNF-α Affibody	TNF-α receptor	Z domain, modified from B domain of SpA	73
Anti-idiotypic Affibody	Human epidermal growth factor receptor 2 affibody molecule	Z domain, modified from B domain of SpA	74

Con A	Glycoproteins/carbohydrate residues	Lectin	75
3-aminophenylboronic acid	Glycoproteins/carbohydrate residues	Boronate	76
Repebody	IL-6, lysozyme, Fc fragment of IgG	Variable lymphocyte receptors	66
Ugi and Triazine *de novo* ligands	Glycoproteins, EPO, IgG (Fc and Fab fragments)	protein L (A&C domain), protein G *Streptococcal* protein G (SpG-III domain)	77-80
Short peptide ligands (HWRGWV, HYFKFD, and HFRRHL)	Fc region of IgG	Fc-binding domain of protein A	81-82
Short cyclic peptide ligands (cyclo[Link-M-WFRHY-K])	Fc region of IgG	Fc-binding domain of protein A	83
Cibacron Blue F3GA	Several enzymes and proteins (non-specific)	Reactive dye and protein, EPO	84
Aptamers (e.g. Mapt2.2CS, MaptH1.1CSO, Nonapta5.1)	Variety of small molecules, proteins, membrane-bound receptors, cell surface epitopes	Nucleotide sequences selected from combinatorial libraries (i.e. SELEX)	85-88

Since most biospecific ligands are derived from bacteria, there is a risk of contamination by viruses, DNA, and pyrogens; thus, further purification is essential, which increases the manufacturing and bioprocessing costs. Compared to biospecific ligands, pseudo-biospecific ligands, are more robust, economically feasible, structurally simple, less toxic, and very stable with resistance to punitive sterilization environments. However, pseudo-biospecific ligands are not as selective as biological ligands, and require substantial optimization for each protein to achieve high selectivity, thus limiting their acceptability as a superior purification technique in industry.[63] There are many types of synthetic ligands that can be chemically modified including biomimetic peptoidal, peptidic, and dye-based ligands. Biomimetic peptoidal ligands utilize the physicochemical properties of amino acid residues to interact and bind with the target protein. For example, protein A mimetic peptoidal ligand is commonly used for mAb purification because of its specificity towards the Fc fragment of immunoglobulins. Rational design and synthesis of synthetic ligands like biomimetic triazine and Ugi ligands, known as *de novo* ligands, have already led to successful purification of several proteins at the bench scale.[77-80] Additionally, DNA aptamer affinity ligands have also been developed to selectively purify human plasma-related proteins from various origins.[85]

Affinity tags have also gained widespread attention in the purification of therapeutic proteins. They are comprised of exogenous amino acid sequences with a high affinity for certain biological or chemical ligands. Affinity tags are normally fused to the *N*-terminus or *C*-terminus of a target protein, which allows the protein to be selectively captured and purified using a tag-specific resin via affinity chromatography or other methods.[89] Affinity tags are advantageous to utilize in the downstream processing of protein therapeutics for several reasons. In many instances, the target protein exists as a version with an affinity tag from prior research stages. Furthermore, the high yields of affinity purification make the use of affinity tags economically favorable. Affinity tags can be both beneficial and harmful for the target protein, and are typically removed through the addition of proteolytic enzymes or more recently, through self-cleaving modules that have been developed over the past several years.[90-91]

Table 1-2 shows a multitude of relevant affinity tags commonly used in affinity chromatography for protein purification. His-tags are one of the most prevalent affinity tags used in purification strategies due to their abundance in many different proteins. Additionally, His-tags do not require a specific protein folding conformation to function and have been used to purify soluble membrane proteins stabilized by detergents or lipids, thus demonstrating their robustness.[90, 92-93] Purification of His-tagged proteins is accomplished by using chelated metal ions as affinity ligands that are complexed with an immobilized chelating agent. The target protein is separated through interactions between the imidazole side chain of histidine and the affinity ligands and is purified using immobilized metal affinity chromatography.[94] Another very common epitope tag used for affinity protein purification is the FLAG tag, which consists of a short, hydrophilic octapeptide (DYKDDDDK).[95] The FLAG tag contains an intrinsic enterokinase cleavage site at the *C*-terminus, allowing it to be easily removed from the target protein. Affinity tags present a viable alternative to affinity ligands for enhancing the purification of therapeutic proteins. Over the next several decades, we can expect that the number of affinity tags will continue to rise as newer tags continue to be developed to improve purification strategies for a vast array of therapeutics.

Table 1-2. Commonly used affinity tags for protein purification in affinity chromatography.

Tag	Fusion/Recognition Partner	Function/Purpose	References
His-tag	Metal chelate	Purification under native and denaturing conditions	90, 92-93
GST	GST-fusion protein	Enhances purification and stability with mild elution conditions	96-97
FLAG	M1, M2, M5 mAbs	Calcium-dependent binding reaction for mAb purification	95, 97-98
Hemagglutinin antigen	12 CA5 mAb	Mostly used as a detection tool for recombinant proteins through immunoblotting assays	95, 99
Heme tag	Various peptide motifs	High affinity for specific amino acid sequences found in various proteins (e.g. Az-Hm14 and MBP-Hm16) utilizing coordination chemistry	100
S1*v*1	Various peptide motifs	Multifunctional tag that is a substitute for the His-tag; simultaneously enhances expression, thermostability, and production of recombinant proteins	101
Streptag II, Twin-Strep-tag	Strep-Tactin protein	Matrix modified with streptavidin for improved affinity	102
MBP	Amylose (maltose analog)	Single step purification via cross-linked amylose affinity resin; mild conditions for elution of target fusion protein; effective solubilizing agent	103
Self-cleaving intein	Depends on the affinity tag intein is fused with (eg. chitin binding domain)	Intein can be fused to many different affinity tags to induce self-cleavage and avoid the risk of nonspecific cleavage of tags and target proteins from proteolytic enzymes	104-105

1.2.3 Non-Affinity Chromatography

Non-affinity chromatography is commonly used during the polishing steps in the downstream processing of therapeutic proteins. In a typical platform operation for mAb purification, one or two polishing steps follow a protein A affinity capture step to remove residual host cell protein (HCP), DNA, viruses and other product-related impurities.[106] Unlike affinity chromatography, which relies on the likeness or specificity of an antibody binding to a stationary phase, non-affinity chromatography utilizes charge, hydrophobicity, or molecule size for purification.[106-107] The most frequently used non-affinity chromatographic modes are ion exchange chromatography (IEX), either anion exchange or cation exchange, and hydrophobic interaction chromatography (HIC). Other methods include mixed-mode chromatography (charge and hydrophobicity based separation), size-exclusion chromatography and reverse-phase chromatography. Current IEX resins utilize a cross-linked matrix commonly made of agarose, silica, polymethacrylate, poly(styrene-divinylbenzene) with a functional ligand, such as a sulfonate group (cation exchanger) or a quaternary amine (anion exchanger), to facilitate binding. HIC resins exploit similar support matrices but have hydrophobic ligands such as ethyl, propyl, or benzyl/aromatic groups to enable adsorption. In most cases, non-affinity chromatography is crucial for obtaining high purity in biopharmaceuticals manufacturing.

IEX has served as an essential tool for the separation of biomolecules for decades and remains a frontrunner in impurity-removal steps and charge heterogeneity evaluation.[108] This modality utilizes a charged (negative or positive) stationary phase with immobilized ligands and binds therapeutic proteins under specific solution conditions, particularly pH. With increasing pH, the overall charge of the protein changes from net positive to net negative, with the transition occurring at the isoelectric point (pI), the point of zero net charge.[109] Ion exchangers typically operate in one of two modes: (1) bind-and-elute mode where proteins bind to a resin and impurities are forced out, or (2) flow-through where impurities bind to the resin and the desired protein is allowed to flow through the column.

HIC is exceptional at removing product-related impurities and is an essential tool in downstream mAb purification.[110] HIC works by adsorbing the non-polar sidechains of proteins to hydrophobic ligands on a stationary phase typically in the presence of high salt concentrations and allowing more polar molecules or impurities to pass through. Hydrophilic interaction chromatography (HILIC) works in the opposite manner and utilizes a polar stationary phase with a non-polar mobile phase.[111] Hydrophobic charge-induction chromatography (HCIC) operates similarly but requires no addition of salt to the mobile phase. Desorption is based on electrostatic charge repulsion and is achieved by lowering the pH of the mobile phase.[112] These modalities are effective at removing molecular weight variants (aggregates and fragments) and process related impurities, and are often utilized as polishing steps in the purification of therapeutic proteins.[113] Much like IEX, HIC, HILIC, and HCIC are typically operated in a column format and can suffer from diffusion limitations and fouling. Methods such as grafted resins with novel ligands and bio-based monoliths have been developed to improve the efficiency and robustness of these modalities.[114-115]

Mixed-mode chromatography (MMC) is a new purification method that utilizes more than one form of interaction between the stationary and mobile phases. Mixed-mode resins typically have ligands with multiple functional groups to facilitate hydrophobic interactions, electrostatic interactions, and even hydrogen bonding.[116] MMC resins usually combine ion exchange and hydrophobic interactions to achieve high selectivity and sensitivity.[117] Over the past decade MMC has shown great performance in the separation of mAbs and therapeutic proteins.[54, 118] Some MMC resin types utilize a multimodal ligand with a carboxylic group and an aromatic group to facilitate electrostatic and hydrophobic interactions, respectively. Other commercially available MMC materials contain hydrocarbyl amines or sulphur atoms to enable interactions. A significant benefit to MMC is that protein binding can occur without any feedstock dilution or addition of lyotropic salts.[119] While relatively little ground-breaking work has been done in recent years to incorporate biomaterials into MMC resins for protein purification, this technology is promising in its use as a platform chromatography method.

1.2.4 Membrane Separation

Membrane separation is one of the key systems utilized in therapeutic protein purification and downstream processes, such as depth filtration, ultrafiltration, virus filtration, and sterile filtration. Depth filters are commonly used in downstream processes during the cell culture product harvest and post viral-inactivation step to remove biomass particulates, precipitates, HCP, DNA, and potentially high molecular weight species in some instances.[120-121] Typically, a depth filter is composed of filter aid, binder, and cellulose fiber. The filter's effective protein absorption capacity was evaluated by Khanal *et al*. to gain optimal usage.[58] As conventional depth filters contain naturally-derived diatomaceous earth and potentially beta-glucan leachable material that could affect process variability and endotoxin assays, all-synthetic depth filtration media (e.g., Millistak+® HC

Pro X0SP) has emerged as the alternative to address these challenges and has shown to improve HCP clearance.[122]

Sorting molecular components through optimized and engineered barriers could enhance efficiency and selectivity between the feed and permeate streams.[123] To achieve highly concentrated mAbs intended for a subcutaneous injection, ultrafiltration is the main unit operation on the manufacturing scale. For example, Pall Omega® T-series and Millipore Pellicon® series offer ultrafiltration membranes with different screen channel types, ultra-low protein binding membrane, and different sizes depending on the required scale. However, there are existing challenges associated with this process, such as increased risk of aggregate formation or membrane fouling affecting selectivity and permeability at high protein concentrations.[124-125] Furthermore, physical properties can alter filtration flux and high viscosities can limit operating pressures.[126-127] Various research groups have developed new biomaterials or membrane modifications to enhance the performance of the ultrafiltration unit operation.[128] Membrane surface modifications such as chemical grafting and physical coating post polymer matrix formation provide options for presenting the membrane surface with various functional groups based on specific applications. On the other hand, bulk blending is another approach for membrane modification by which the functional modifiers of interest are added into the membrane casting solution.

Separation of similarly sized proteins has been a challenge due to limited fabrication techniques and biomaterials. In the work reported by Qiu *et al.*, an amphiphilic block co-polymer (PS-b-P4VP) was introduced to self-assemble into a thin layer of densely packed, highly ordered cylindrical channels with uniform pore sizes of ~34 nm and lengths of ~100 nm (**Figure 1-2 A-C**).[129] By customizing the membrane properties with quaternization, the membrane was able to separate similarly sized proteins based on their respective pIs. Additionally, the authors found that other parameters such as molecular shape, mobility, and the hydrophilic-to-hydrophobic ratio of amino acids could also affect the protein transport behavior through the nanopores.[129]

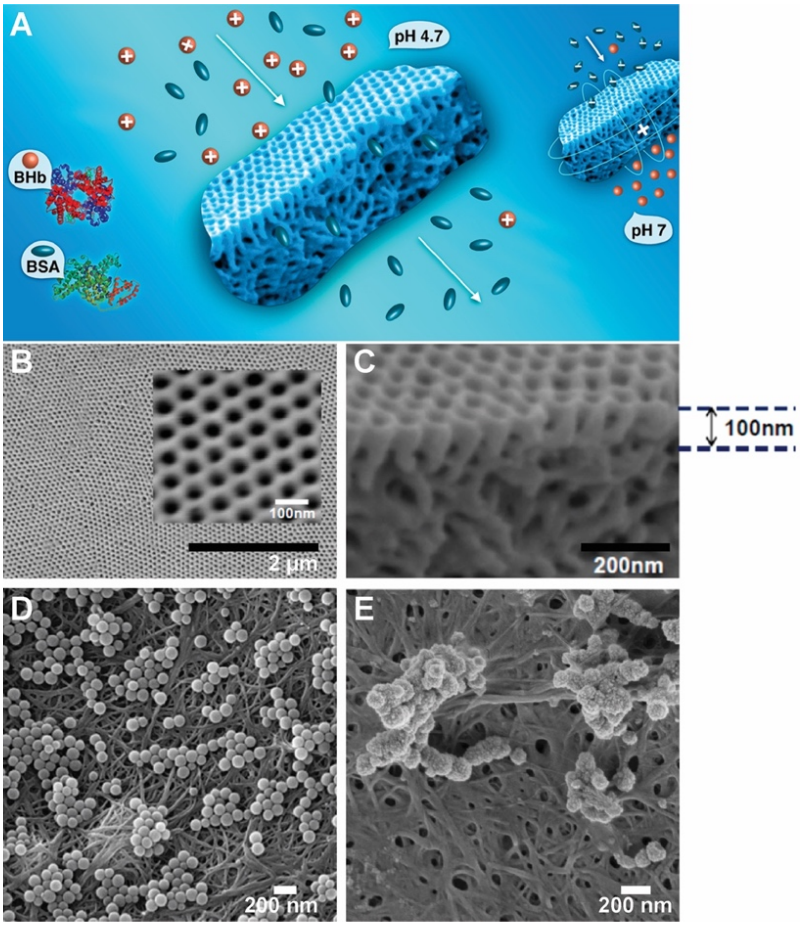

Figure 1-2. (**A**) Schematic illustration of similarly sized protein separations through tunable nanoporous block copolymer membrane. (**B**) Regular order of the membrane's surface as shown by SEM. (**C**) Cross-section SEM image showing the thin top layer and the sponge-like bottom layer. (**A**) (**B**) (**C**) were reprinted with permission from ref. 129, Copyright © 2013, American Chemical Society. SEM images of (**D**) 100 nm PS latex beads and (**E**) SIV particles following filtration on Cladophora cellulose membrane. Reprinted with permission from ref. 130, Copyright © 2014, John Wiley and Sons.

Viral filtration is an expensive operation and generally produced by a synthetic polymer for the biotechnology industry to remove adventitious virus particles from the therapeutic drug product. Metreveli *et al.* described a natural, unmodified nanofibrous polymer-based membrane, utilizing size-exclusion principles, that was able to remove nano-sized virus/particles by ≥ 6.3 log reduction value, which is comparable to industrial filters (**Figure 1-2 D** and **E**).[130] The nanocellulose filter paper had an average pore size of 19 nm and was shown to efficiently filter beads ranging from 30 nm to 500 nm.[130] With the filter's ease of large-scale manufacturing, it showed potential for applications in the industrial sector.

Membranes with nanochannels that feature charged groups can be applied to the purification of biomolecules by allowing the passage of uncharged or oppositely charged solutes, but opposing the passage of co-ions.[131] Sadeghi *et al*. have developed membranes that feature a packed array of self-assembled micelles with carboxylate functional surfaces.[131] The interstices (1-3 nm minimum) serve as charged nanochannels that allow the passage of solutes. The membranes have been shown to effectively retain negatively charged molecules and allow positively charged and neutral molecules to pass through. In filtration experiments, anionic and neutral compounds were separated with water fluxes comparable to existing commercial membranes.[131] These membranes are also manufactured using easier and more scalable methods than other comparable approaches. The self-assembled micelle membranes can be used for processes that involve the separation of charged particles, such as IEX in the processing of therapeutic proteins.

1.3 Recent Advances in the Precipitation of Monoclonal Antibodies[b]

1.3.1 Overview

Protein precipitation has long been developed for protein purification and concentration in both laboratory protein isolation and downstream processing.[132] Ammonium sulfate precipitation is often performed before the chromatography steps to concentrate target proteins and remove impurities based on solubility differences in proteins. However, relying on bulky and expensive centrifuge systems and relatively low selectivity limit its applications in large-scale purification.[11] Nevertheless, methods based on solid-liquid phase separation mechanisms, e.g., crystallization and precipitation, have seen a renaissance in protein purification to achieve high throughput and reduced costs.[13] To overcome the obstacles of current precipitation methods, continuous efforts have been made to develop more advanced precipitants using biomaterials to reduce or avoid the use of column chromatography. Meanwhile, the improvement of membrane filtration techniques will facilitate the wide implementation of the precipitation methods for protein purification.

1.3.2 Non-Affinity Precipitation

1.3.2.1 PEG-Induced Precipitation

Polymers such as polyethylene glycol (PEG) can be used as non-specific precipitants. PEG precipitation has received broad interest in the field of mAb purification because of its simple operation in mild conditions, fast precipitation kinetics, and low cost.

---

[b] Reprinted with permission from Li, Y.; Stern, D.; Lock, L.L.; Mills, J.; Ou, S.-H.; Morrow, M.; Xu, X.; Ghose, S.; Li, Z.J.; Cui, H. Emerging biomaterials for downstream manufacturing of therapeutic proteins, ***Acta Biomaterialia*, *2019***, 95, 73-90. Copyright © 2019 Acta Materialia Inc. Published by Elsevier Ltd.

It was originally found that the logarithm of protein solubility follows a linear relationship with the concentration of PEG and higher molecular weight PEGs show higher precipitation efficiency due to excluded volume effects.[133] Linear PEG4000-6000 of high concentrations were traditionally employed and followed by the exploration of branched PEG to reduce viscosity caused by the large linear PEG chains, although protein precipitation yield can be compromised using branched PEG.[134] Recent studies revealed that the efficiency of PEG precipitant could be further characterized by the hydrodynamic radius of PEG, $r_{h,PEG}$, which takes into account the effects of PEG branching and environmental conditions.[134-135] Conditions such as PEG and protein concentration, pH, ionic strength, and time should be optimized to achieve the best precipitation efficiency.

However, PEG is insufficient at removing product-related high molecular weight impurities.[136] Low selectivity remains the major limitation of this technique. In recent years, the combination of PEG with other precipitation methods has been investigated to improve selectivity and achieve higher yields. For example, Oelmeier *et al.* reported the employment of centrifugal partitioning chromatography (CPC) in combination with PEG precipitation for mAb purification. PEG-driven precipitation was performed in the CPC output stream and results showed that the reduction of HCP was improved from 88 % to 99 % after PEG precipitation while recovering 93% of the target protein after re-solubilization.[137] To address the limitation of PEG precipitation in removing process-/product-related impurities such as DNA and mAb aggregates respectively, the combination of different precipitants, including PEG, caprylic acid, $CaCl_2$, and cold ethanol, were intensively investigated.[136, 138] In a subsequent study, continuous PEG precipitation of different recombinant antibodies was developed with similar performance to that for batch operation.[139] Recently, the integration of PEG precipitation and cation exchange chromatography was demonstrated a feasible alternative to protein A chromatography.[140] Despite the wide application of PEG-induced precipitation, concerns still remain about solubility predictions of target proteins in high protein concentrations, the removal of impurity precipitates and PEGs, and assay interference. Careful investigations and additional validation of results are recommended for the development of PEG-based precipitation conditions.[141-142]

1.3.2.2 Polyelectrolytes-Induced Precipitation

Depending on the pH of the environment, therapeutic proteins or impurities can exhibit charged groups and be precipitated by oppositely charged polyelectrolytes due to electrostatic interactions.[143] Extensive efforts have been made to study the mechanism and influencing factors of precipitating protein-polyelectrolyte complexes.[144-145] Proteins carry positive or negative charges when the solution pH is below or above their pIs, respectively. It provides the opportunity for charge-based precipitation of target proteins or impurities by controlling solution pH condition. Typically, anionic polyelectrolytes including polyvinylsulfonic acid, polyacrylic acid, and polystyrenesulfonic acid are used to precipitate mAbs of basic pIs.[146] Conversely, cationic polyelectrolytes such as polyamines can be used to remove negatively charged impurities such as HCP and DNA.[147] The reversible nature of ionization eases the re-solubilization of the precipitated complex by tuning the solution pH or ionic strength.

Sieberz *et al*. investigated the impact and interactions of various parameters on the separation of a mAb from a model impurity, BSA, using anionic polyelectrolytes. A Design of Experiments (DOE) strategy was utilized to show that all parameters should be optimized simultaneously to account for any significant parameter interactions.[148] In a later study, influencing factors for the precipitation of BSA with cationic polyelectrolytes were investigated and two statistical models were established using DOE.[149] Recently, poly(glutamic acid) (polyE) was utilized to precipitate IgGs in high-concentration solutions. The formation of reversible liquid droplets of the IgG-polyE complex demonstrated an indispensable role in improving precipitation and redissolution yields to nearly 100%.[150] Future studies in polyelectrolytes-induced precipitations require fundamental understanding of more complicated systems involving the prediction of 3D structures of proteins, local charge distributions, and multi-type interactions including hydrophobic interactions, hydrogen bonding, etc.[145]

1.3.2.3 Self-Precipitation with Fusion Tags

As mentioned previously, fusion tags (mostly peptides and proteins) have been widely used to purify target proteins through tag-specific affinity chromatography. As increasing attention has been focused on the development of column-free purification methods, a variety of aggregating tags have been explored to induce the self-precipitation of fusion proteins.[61] Subsequent removal of aggregating tags can be achieved by incorporating a cleavage site or a cleavage tag in favor of chemical cleavage, protease cleavage, or self-cleavage.[89] Mechanisms of how these tags induce the aggregation of proteins can be interpreted by the responsive solubility, high hydrophobicity, and self-assembling behavior of the aggregating tags.

Elastin-like polypeptide (ELP), a representative fusion tag composed of repeating peptides Val-Pro-Gly-Xaa-Gly, where Xaa is any amino acid except for proline, is well-known for its thermally reversible phase transition behavior which has attracted considerable attention in protein purification, drug delivery, and tissue engineering.[151] ELPs in aqueous solutions abruptly aggregate when temperature is raised above the transition temperature (T_t). The pellet can be further redissolved at a temperature below T_t. Meyer and Chilkoti demonstrated for the first time that recombinant proteins can be purified by fusion with thermally-responsive ELP.[151] A large number of subsequent studies have been reported to optimize properties of ELP-fusion proteins such as molecular weight, T_t, and ELP cleavage to achieve better purification performance for various proteins.[152] A self-cleaving ELP tag was designed by Wood and coworkers to purify RNA polymerase and several recombinant proteins with reasonable yield and purity (**Figure 1-3 A**).[153-154] The tagged target protein could be precipitated with a mild temperature shift and resuspended in a cleaving buffer to remove the ELP tag. A subsequent precipitation step was conducted to separate the cleaved tag from the target protein. A recent study built upon this concept and established a high-throughput platform using 24-well plate cultures followed by purification in 96-well plates.[155] It was demonstrated that this high-throughput format showed high well-to-well reproducibility without compromising purity or robustness.[155]

Apart from the thermally responsive ELP, many tags were constructed with high hydrophobicity to promote the aggregation of the target protein. These include proteins such as N^{pro}, Ketosteroid isomerase, 4AaCter and short self-assembling peptides like ELK16 and 18A.[61] For example, recombinant cystatin C was expressed as an insoluble fusion protein with a peptide-tag, 4AaCter, for simple and efficient purification steps. Recently, Xu *et al.* reported recombinant production of influenza hemagglutinin and HIV-1 GP120 antigenic peptides using a cleavable self-aggregating tag comprised of a short self-assembling amphipathic peptide ELK16 (LELELKLKLELELKLK) and an intein molecule. The target proteins were first expressed as insoluble aggregates and released by intein self-cleavage into the soluble fraction with high yield and reasonable purity.[156] In general, using these aggregating tags is a simpler purification method and requires minimal production or processing costs. However, the yield and purity of purified proteins are inferior to that achieved by traditional chromatography methods. Further exploration of more efficient designs of cleavable fusion tags to address co-aggregation of impurities, partial premature cleavage, and incomplete removal of the fusion tags are necessary for more applicable purification systems.

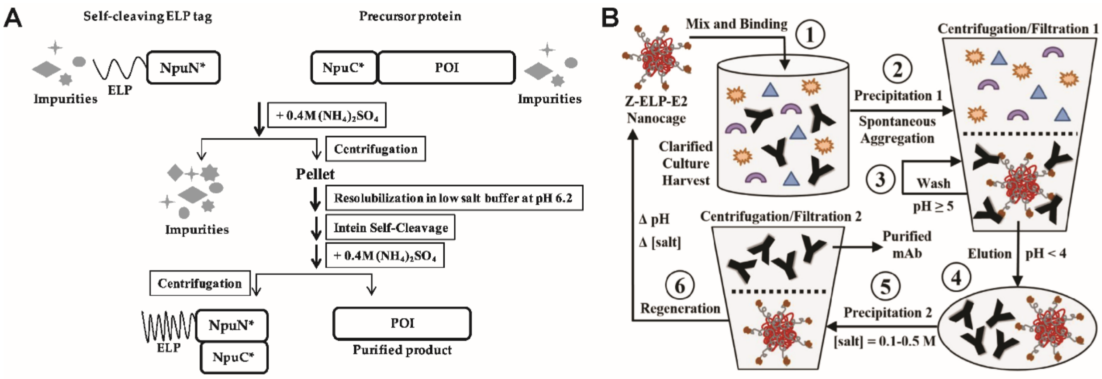

Figure 1-3. (**A**) Schematic of ELP-tagged split intein purification method. Reprinted from ref. 154. (**B**) Affinity precipitation of mAbs from cell culture with Z-ELP-E2 nanocages. (1) Mix nanocage stock with clarified culture. (2) Spontaneous aggregation through multivalent crosslinking. (3) Wash pellet by suspending in target wash buffer pH>5. (4) Elute by suspending pellet in buffer pH<4. (5) Add salt for selective precipitation of nanocage and collect purified mAb in supernatant. (6) Regenerate nanocage to recycle for future use. Reprinted with permission from ref. 18, Copyright © 2017, John Wiley and Sons.

1.3.3 Affinity Precipitation

Affinity precipitation colligates the advantages of both specific capture of affinity ligands/tags and reversible precipitation. It seems contradictory to possess both characteristics simultaneously since affinity binding requires thermodynamic stability while precipitation represents a phase separation behavior. In fact, the precipitation of the affinity precipitant and protein complex are often triggered either by environmental stimuli such as temperature, pH, ionic strength, and concentration after the formation of the complex or by the internal changes in the complex such as crosslinking or aggregation upon the ligand-protein interactions. For the precipitation triggered by external stimuli, the design of affinity precipitants requires one segment to specifically capture target proteins and the other segment to be responsive and reversibly soluble. To render the crosslinking of target protein, a design of one precipitant molecule with multiple ligands is necessary in the case of capturing proteins with more than one binding site. In spite of the strict criteria of affinity precipitants, several types of biomaterials including ELP-based materials, smart polymers, and affinity peptides have been investigated for affinity precipitation.

1.3.3.1 ELP-Mediated Precipitation

As mentioned above, ELP has been employed as a fusion tag for thermally reversible precipitation. A major drawback of this method is the limited availability of the genes coding for fusion construction especially in the case of novel proteins. An alternative method is the creation of an external ELP fused with a binding ligand to capture the target protein and undergo inverse transition cycling. Affinity partners could also be engineered into the target protein and ELP separately in order to customize a binding domain for codable proteins.[157]

Chen and coworkers pioneered the design of a series of ELP-ligand precipitants for mAb affinity precipitation processing.[60, 158-160] The ELP-ligand-protein complex was precipitated at an elevated temperature and/or specific salt concentration at neutral pH. After redissolving the complex, an elution buffer at a lower pH was added to release the target protein. Subsequently, the free ELP-ligands were removed by a second round of thermally triggered precipitation. In addition to the ease of purification and the high efficiency, the avoidance of tag cleavage and favorable reusability property make it a promising method for protein purification.[158]

Recently, ELP fused Z-domain, a shorter synthetic domain derived from the B-domain of protein A, was designed to bypass the lower expression levels previously observed with protein G-fused ELP.[159] High-throughput screening was employed to determine appropriate conditions for the precipitation and elution of mAbs using ELP-Z.[19, 60] Greater than 99% mAb precipitation yields were obtained at ELP-Z:mAb molar ratio of 4:1 with 0.25 M Na_2SO_4 for pure mAbs as well as the mAb harvest mixtures.[60] More than 90% overall yields were achieved in elution buffers with pH up to 4.2.[60] However, the potential denaturation of antibodies at an elevated phase transition temperature and high salt concentration especially in low pH conditions, remain the major concerns for the ELP-Z precipitants. Therefore, exploring new substrates to present antibody-binding ligands at physiological temperature with low/no salt condition is crucial.

Recent progress in creating an ELP-Z functionalized E2 protein nanocage significantly lowered the temperature and salt concentrations due to increased scaffold dimensions and IgG triggered scaffold crosslinking (**Figure 1-3 B**).[18, 160] High-yield isothermal purification of IgG without adding salt was achieved in a simple and nondestructive manner. Similar to ELP-Z, several other binding ligands such as Z33 and lectin were fused with ELP as the affinity precipitants for purification of human antibodies and glycoproteins.[161-162] With more affinity ligands or affinity pairs being identified, ELP-mediated precipitation has substantial potential for the large-scale downstream processing of therapeutic proteins.

1.3.3.2 Peptide-Based Materials and Smart Polymers

In addition to ELP, several peptide-based materials and smart polymers with affinity ligands have been used in affinity precipitation for protein purification. Peptide-based trivalent haptens were designed with the ability to form cyclic complexes with trastuzumab and rituximab.[21] It was demonstrated that the purified antibodies had native levels of binding to the cells.[21] Unlike ELP-based systems, additional precipitation was not required to remove the trivalent haptens. After the dissociation of the trivalent haptens from the target antibody in specific buffers, membrane filtration can be used to remove the trivalent haptens.[21] This is due to the significant size difference between the trivalent haptens and target proteins.[21]

Smart polymers including thermo-responsive polymers, pH-responsive polymers, and reversibly cross-linked polymer networks are often combined with affinity ligands to create effective precipitants.[20, 163-164] In recent work, a pH-responsive copolymer Eudragit® S-100 was linked to protein A ligand for precipitation and elution of IgG at pH 5 and pH 2.5, respectively.[20] It was demonstrated that 89% of IgG was recovered from a protein mixture with a purity greater than 95%. However, special considerations for pH-sensitive protein-ligand interactions are necessary when designing the pH-responsive polymers. Ideally, the critical pH for protein precipitation and elution should be independent. With the abundant monomer types and easily modulated structures, polymer-based materials show enormous potentials in constructing affinity precipitants.

In this section, I discussed the recent advances in affinity or non-affinity precipitation of therapeutic proteins. Affinity precipitation is more favorable than non-affinity precipitation due to its high selectivity, however, more efficient methods to remove precipitants or fusion tags need to be developed and validated. Based on existing studies and prior work, several criteria must be satisfied for a successful and efficient precipitant design. First, the precipitant should not compromise the functionality of the target protein and it should be easily removed from the protein solution. Second, high selectivity and high efficiency are needed for either the precipitation of target proteins or impurities. Third, the precipitation behavior should occur in a well-predicted and well-controlled manner. Fourth, the precipitant could be easily manufactured at a large scale and economically. Finally, the precipitant can be conveniently recycled without causing the loss of protein activity. These criteria should be considered for future improvement and development of precipitants for therapeutic protein purification.

1.4 Peptide-Based Supramolecular Polymers

1.4.1 The Self-Assembly of Peptide-Based Supramolecular Polymers

At the molecular scale, self-assembly is a spontaneous and reversible process when molecular components form ordered structures via non-covalent interactions, presenting a fascinating bottom-up approach to construct complex and hierarchical nanostructures. Supramolecular polymers, formed by self-assembly of monomeric units, represent attractive materials for various biomedical applications including drug delivery, regenerative medicine, and biosensing. Amphiphiles, consisting of both hydrophilic and hydrophobic moieties, are the most common self-assembly building blocks that have been widely explored to mimic biological systems. When dispersed in solvents, amphiphiles such as surfactants, lipids, and amphiphilic block copolymers are able to self-assemble into various supramolecular nanostructures, e.g. micelles, nanofibers, nanotubes, vesicles, etc. As a result of minimizing system free energy to assume a spontaneous interfacial curvature, the solvophilic moieties of the amphiphile preferentially interact with the solvent while the solvophobic moieties tend to pack internally. The final morphology is determined by the balance of multiple non-covalent interactions including hydrophobic attraction, ionic repulsion, the system entropy, van der Waals interaction, as well as some directional interactions such as hydrogen bonding or π–π stacking. Critical micelle concentration (CMC) is an important characteristic for amphiphiles, above which amphiphilic monomers start to self-assemble into ordered structures. Besides, the self-assembly process can be readily tuned by many environmental factors such as pH, ionic strength, temperature, solvents, and co-assembling molecules.

Among the recently developed supramolecular polymers, peptide-based assemblies, formed by self-assembly of synthetic or naturally occurring peptides and their derivatives, are notably fascinating because of their biocompatibility, biodegradability, and low toxicity.[165-167] In particular, one-dimensional (1D) nanostructures (nanofibers, nanotubes, nanowires, nanobelts, etc.) formed by β-sheet-forming peptides via directional, intermolecular hydrogen bonding, have been intensively investigated for use as scaffolding materials in regenerative medicine[31, 41, 44, 168-170] and also as therapeutic and diagnostic carriers in drug delivery[171-178] and molecular imaging.[179-180] With the hierarchically organized structures, peptide-based materials are suitable as building blocks for self-assembly (**Figure 1-4 A**). The diversity of amino acids provides a broad basis for non-covalent interactions including hydrogen bonding (polar amino acids like glutamine), π–π stacking (aromatic amino acids like phenylalanine), hydrophobic collapse (non-polar amino acids like valine), and electrostatic interactions (acidic and basic amino acids like glutamic acid and lysine) (**Figure 1-4 B**).[167] Moreover, the well-established solid-phase peptide synthesis (SPPS) protocols further contribute to the efficient and easy synthesis of peptides by researchers who have not had rigorous chemistry trainings.

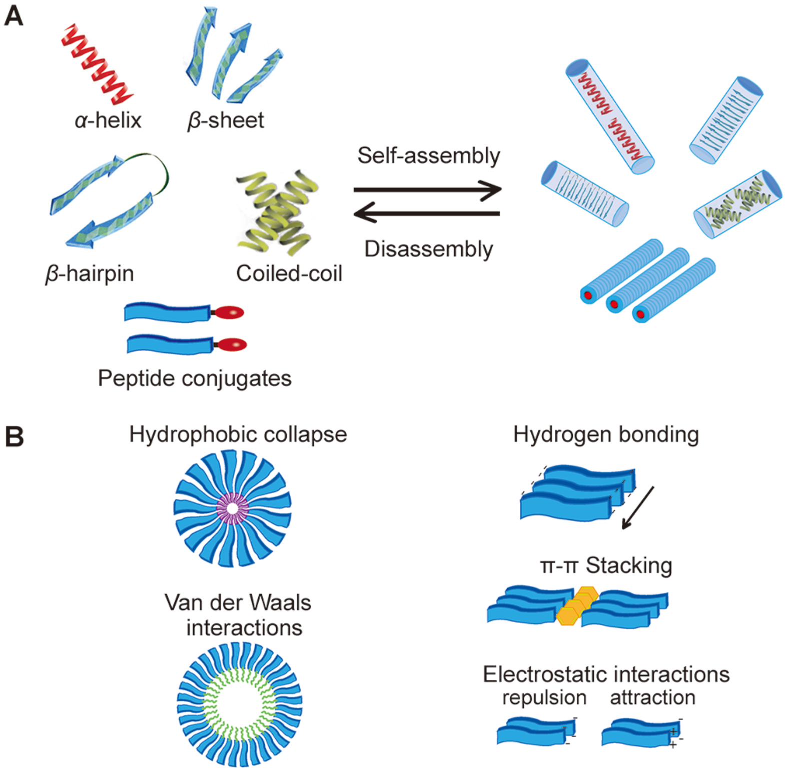

Figure 1-4. Schematic representation of the self-assembly of peptide-based materials. (**A**) The reversible self-assembly of various peptide motifs. (**B**) Possible non-covalent interactions among peptide-based building blocks, including hydrophobic collapse, van der Waals interactions, hydrogen bonding, π–π stacking, and electrostatic interactions. Adapted with permission from ref. 181 (© 2016 The Authors.)

1.4.2 Design Principles of Bioactive Peptide Amphiphile Nanofibers

Of all the peptide-based assemblies explored thus far, peptide amphiphile (PA) nanofibers are the most studied as bioactive materials for diverse biomedical applications. The Stupp laboratory has molecularly developed and crafted a class of PAs by conjugating linear hydrocarbons onto a *β*-sheet-forming sequence that could self-assemble into supramolecular nanofibers under the physiological conditions with hydrocarbons packed in the core of the fibers and peptide segments exposed to the aqueous environment.[31, 41, 44, 182-185] The incorporation of this hydrophobic segment on either the *N*- or *C*- terminus of the intended peptide sequence not only enhances the self-assembly potential of the peptide amphiphile in an aqueous environment, but also enables the specific presentation of enhanced bioactive signals on the resultant assemblies.[186-188] Given that molecular and cellular signaling are highly regulated events, a variety of bioactive epitopes, either naturally occurring peptides or *de novo* designed sequences, have been incorporated into the PA design to enhance their biologically active features for a target application,[31, 41, 172, 183, 186, 189-190] with the respective goal of promoting cell adhesion, proliferation and differentiation, or selectively recognizing particular cells or tissues for disease treatments. Since some of these epitopes must assume an appropriate secondary structure to interact with their molecular target(s), the challenge remains how to retain their bioactive conformation within their respective supramolecular assemblies.[191-192] It has been shown by a number of research laboratories that the solvent property,[193-195] the added hydrophobic segment,[187, 196-199] and the thermal history[197, 200] could all potentially affect the peptide's secondary structures, and consequently, their assembled morphologies.

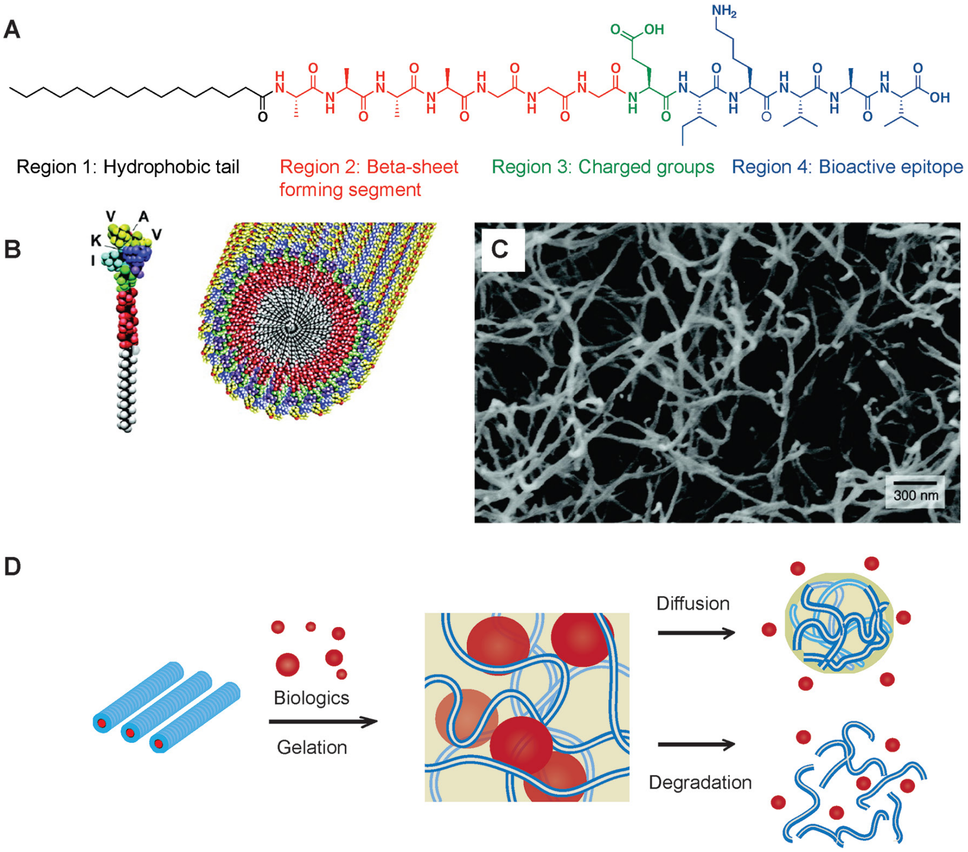

Figure 1-5. (**A**) Molecular structure of a representative PA with four rationally designed chemical entities. (**B**) Molecular graphics illustration of an IKVAV-containing PA molecule and its self-assembly into nanofibers. (**C**) Scanning electron micrograph of the IKVAV nanofiber network formed by adding cell media (DMEM) to the PA aqueous solution. (**D**) The encapsulation and release of biologics using supramolecular PA nanofiber hydrogels. (**A**) (**B**) (**C**) were reprinted with permission from Science (http://www.sciencemag.org) ref.186 (© 2004 AAAS). (**D**) was reprinted with permission from ref. 181 (© 2016 The Authors.)

A typical PA design consists of four structural regions (**Figure 1-5 A**). Region 1 contains a hydrophobic tail, usually an alkyl chain or other hydrophobic components, to enhance the amphiphilicity for self-assembly and enable the presentation of bioactive epitopes on the nanofiber periphery in an aqueous environment. Region 2 is a short peptide sequence with high tendency of forming *β*-sheets via intermolecular hydrogen bonding to direct the formation of 1D nanostructures. This sequence usually contains hydrophobic amino acids (V, A, I, L) and large aromatic residues (F, Y, W). Region 3 includes charged amino acids, such as D, E, K, to promote the solubility of the whole PA molecule and provide the responsive feature to pH or ionic strength for nanofiber growth or gelation. The last region usually represents the functional groups of the PA molecule for various biological purpose. Bioactive epitopes can be incorporated into this region and displayed on the nanofiber surfaces after self-assembly without changing the cylindrical geometry of the nanofibers. In the meanwhile, their conformation and functionality can be potentially maintained at the self-assembled state. In some cases, it may not be necessary to have all four regions in the molecular design. For example, Region 3 can be omitted if there are charged groups in Region 4. **Figure 1-5 A-C** show the design of an IKVAV-containing PA molecule and its self-assembly into nanofibers. The Stupp Lab has shown that the high-density presentation of neurite-promoting laminin epitope IKVAV on peptide amphiphile nanofibers is critical for the selective differentiation of neural progenitor cells into neurons while discouraging the development of astrocytes.[186] In another example, Webber *et al.* investigated bioactive PA nanofibers displaying the RGDS epitope on the surface for therapeutic delivery of bone-marrow mononuclear cells (BMNCs), implying an enhanced biological adhesion.[41] In an effort to modulate immunogenicity of peptide assemblies, Collier and coworkers covalently linked the self-assembling peptide Q11 to an antigen OVA peptide and found that the resultant supramolecular OVA-Q11 nanofibers possess enhanced immunogenicity.[174] This direct placement of bioactive peptide on either *C*- or *N*-terminus of a self-assembling peptide motif has become a popular strategy to create bioactive materials for a specific biomedical application.

Extensive investigations have also been focused on engineering self-assembled PA nanofibers into hydrogels under the physiological condition. Typical nanofibers formed by self-assembled PAs have diameters between 5 nm and 15 nm and lengths on the micrometer scale, and are able to further entangle to form a 3D network as a result of several types of non-covalent interactions among individual nanofibers. In general, the gelation of PA nanofibers could be aided by charged amino acid residues[201] or mediated by metal ions[202] and the network displays unique reversibility and bioresponsibility that most chemically cross-linked hydrogels do not possess. For example, the self-assembly process of charged peptides can be facilitated by tuning the pH or adding salts to reduce the electrostatic repulsions and promote aggregation. The PA hydrogels are able to encapsulate small hydrophobic drugs or large hydrophilic biologics in the inter- or intra-fiber areas and offer a stimuli-triggered and well-controlled release capability (**Figure 1-5 D**). For instance, tubular hydrogels formed by circumferentially aligned peptide amphiphile nanofibers were shown to encapsulate vascular cells and direct cellular organization.[203] Recently, C_{16}-$V_2A_2E_2$-NH_2 PA hydrogels were used as a sonic hedgehog protein delivery system for the treatment of erectile dysfunction, suggesting the PA hydrogels have potentially broad applications as protein vehicles.[204] Tirrell and coworkers designed pH-responsive branched peptide amphiphile composed of histidine and serine amino acids conjugated to a palmitoyl tail.[205] These PA solutions are able to switch from viscoelastic liquids to an injectable tissue scaffold above pH 6.5 as a result of the protonation of histidine. In another study, a PA hydrogel consisting of $C_{16}GSH$ was optimized to have greater utility for peripheral nerve repair compared with a commercially available collagen gel.[206]

1.4.3 Construction of Peptide-Based Supramolecular Polymers for Antibody Affinity Precipitation and Purification

The demand for therapeutic proteins has rapidly grown over recent decades, creating a dramatic shift in the pharmaceutical industry from small molecule drugs to biological macromolecular therapeutics. Therapeutic proteins, mainly consisting of mAbs, Fc fusion proteins, recombinant enzymes, and antibody fragments, are the most rapidly growing field in biopharmaceutical industry.[207-209] In general, therapeutic proteins possess superior properties over small molecule drugs, such as highly specific and diverse functions that are associated with structural complexity and delicacy and that cannot be easily mimicked by synthetic chemistry.[210-211] The largest and fastest growing protein therapeutics in the USA are antibody-related drugs for the treatment of many diseases such as cancer, chronic inflammatory disease, cardiovascular, and infectious diseases.[209] Nowadays, downstream processing of therapeutic antibodies is facing great challenges created by the rapid increase of the market size and upstream titers, starving for significant improvements or innovations in current downstream unit operations for the implementation of more efficient and economical purification methods.

Supramolecular PA assemblies show a great potential as antibody precipitants for antibody capture and purification. First, there have been a variety of peptide-related ligands identified with high mAb binding affinity. Protein A, a protein originally found in the cell wall of staphylococcus aureus, is the most frequently used ligand that specifically binds to the Fc-portion of IgG from most mammalian species, including human.[212-213] It is composed of five homologous domains that fold into a three-helix bundle. The binding occurs at the neutral or mild basic pH and could be disrupted at acidic pH. However, the large size and instability of protein A limit its industrial application, and as such a number of synthetic and minimized domains of protein A have been designed and studied.[214-216] The Z-domain of protein A is the first and most famous synthetic domain with 59 amino acid residues and a dissociation constant (K_d) of ~10 nM when bound to human IgG1.[217-219] To further minimize the Z-domain of protein A, several two-helix derivatives such as Z33 were designed without significantly changing the binding affinity.[214] As the decrease of ligand length, the incorporation of affinity ligands into PAs becomes more facile. However, the way to present these antibody-binding ligands on a PA template is equally essential for ligand-protein interactions and requires elaborate investigations.

Second, the most intriguing properties that favor the use of supramolecular peptide assemblies for antibody precipitation and purification are their dynamic and reversible features. In a typical supramolecular peptide assembly system, reversible transitions can occur at multiple length scales, including the intramolecular chain adjustment to adopt various conformations,[47] the intermolecular interactions to assemble into discrete nanostructures,[40, 49] and the inter-filament interactions to percolate into a 3D network (gelation) or to cause macroscopic phase separation.[50-51] The transitions among different assembly states can be induced by changes in temperature, pH, ionic strength, concentration, or molecular interactions. Among these transitions, the reversible aggregation and macroscopic phase separation of the assemblies, either triggered by ionic strength or inter-filament crosslinking, could enable the reversible precipitation of captured antibodies. The transition between monomeric units and their assembled nanostructures could provide an effective means for their effective removal from the protein product pool through dissociation. Third, PAs are highly customizable to fine-tune their overall nanostructure characteristics as a result of the diversity of amino acids. In particular, charged amino acids and hydrophobic chains can be modified to facilitate the transition between PA monomer, nanofibers, and macroscopic aggregations.

To construct a peptide-based supramolecular polymer system for antibody capture and purification, the strategy is to use the customized PA as molecular building unit, creating antibody-targeting immunofibers (IFs) (**Figure 1-6**). Through non-covalent interactions, PA monomers spontaneously form IFs in aqueous condition with a high density of antibody-binding ligands presented on their surface, serving as the docking station for antibody binding. The precipitation and resuspension of the IFs and captured antibodies can be readily tuned by pH-, salt-, concentration-, or binding-dependent conditions. After the elution of antibody from IFs by adjusting the buffer pH, the dissociated PA monomers building units can be easily removed through membrane separation, maintaining purified antibody at relatively high concentration.

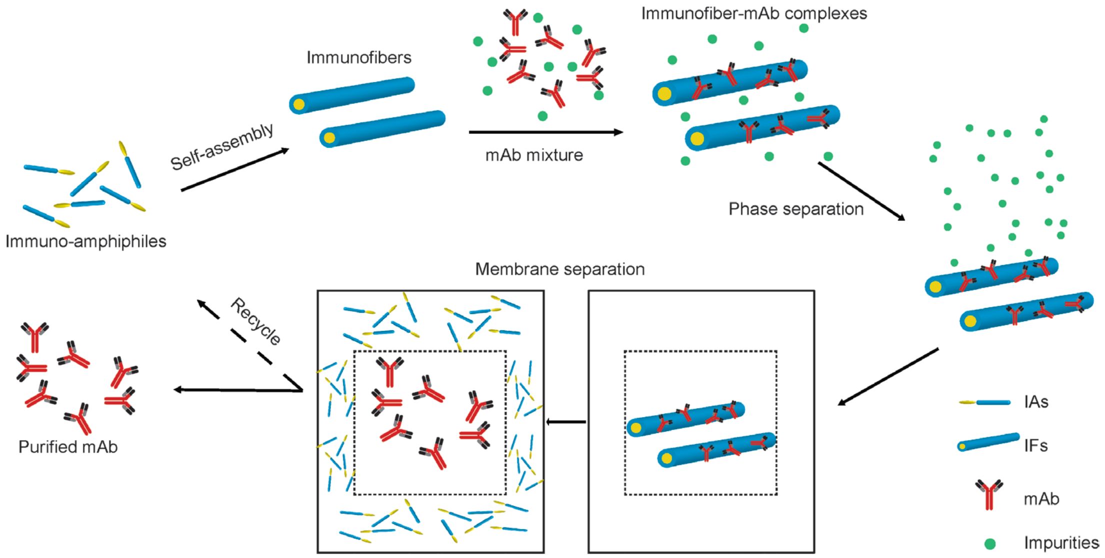

Figure 1-6. Overview of the mAb purification system using supramolecular immunofibers (IFs).

1.5 Dissertation Overview

This dissertation aims to develop a peptide-based supramolecular polymer system for efficient capture and purification of monoclonal antibodies, which could potentially address current limitations in chromatography. The incorporation of a high-affinity mAb-binding ligand into the building units enables the strong mAb binding of the supramolecular system. Moreover, the dynamic property of the supramolecular assemblies enables the reversible mAb precipitation and efficient clearance of the capture agents. This dissertation covers several milestones that has been reached along the way to improving and optimizing the supramolecular polymer design. Chapter 2 investigates the design principles of incorporating α-helical peptide ligands into the supramolecular building units while preserving its conformation. Chapter 3 demonstrates the design and construction of a self-assembly system can specifically bind monoclonal human IgG1 (mAb1). Chapter 4 develops a co-assembly system on the basis of the self-assembly system described in Chapter 3 for successful capture, precipitation, and recovery of mAbs. Chapter 5 explores more advanced designs of the co-assembly system by using oligo ethylene glycol (OEG) linkers to significantly improve the ligand-mAb interactions and achieve a better performance in mAb capture and precipitation. Lastly, Chapter 6 presents the conclusions as well as potential future work to further explore and improve this supramolecular polymer system.

2 Conformation Preservation of α-Helical Peptides within Supramolecular Filamentous Assemblies[c]

2.1 Overview

Hydrogen-bonded β-sheets are the most commonly explored building motifs for creating peptide-based filamentous nanostructures; however, most bioactive epitopes must assume an α-helix conformation to exert their functions. Incorporating α-helical sequences into β-sheet-forming peptides often involves the use of a flexible spacer to alleviate the steric impact of the intermolecular hydrogen bonding on the α-helical conformation. In this context, I report the findings on the alkylation-regulated conformation preservation of α-helical peptides within their filamentous assemblies. I found that the chemical conjugation of two short linear hydrocarbons (octanoic acids, C8) can retain the α-helical conformation of two protein A-derived peptide sequences while effectively driving their assembly into filamentous nanostructures. In contrast, the use of a single palmitoyl tail (C16) of similar hydrophobicity would lead to formation of β-sheet assemblies. My studies further demonstrated that the length of the conjugated hydrocarbon also plays an important role in

---

[c] Reprinted with permission from Li, Y.; Wang, Y.; Ou, S.-H.; Lock, L. L.; Xu, X.; Ghose, S.; Li, Z. J.; Cui, H. Conformation Preservation of Alpha-Helical Peptides within Supramolecular Filamentous Assemblies, ***Biomacromolecules***, **2017**, 18(11), 3611-3620. Copyright © 2017 American Chemical Society.

partially preserving the native α-helical conformation, with longer ones promoting β-sheet formation and short ones stabilizing α-helices to some extent. I believe that these findings offer important guiding principles for the alkylation of self-assembling peptides containing α-helical sequences.

2.2 Introduction

Peptide-based filamentous nanostructures have been exploited for use as scaffolding materials in regenerative medicine[31, 41, 44, 168-170] and also as therapeutic and diagnostic carriers in drug delivery[171-178] and molecular imaging.[179-180] From the perspective of supramolecular materials design, these filamentous nanostructures are often constructed by self-assembly of low-molecular weight peptides or their rationally designed conjugates or derivatives that have high propensity to form intermolecular hydrogen bonding.[45-46, 192, 220-222] Unlike traditional cylindrical micelles that are stabilized by a spontaneous curvature as a result of minimizing system free energy, the one-dimensionality for peptide-based assemblies primarily roots in the formation of directional hydrogel bonds among the chosen β-sheet-forming peptide sequences.[223-224] Of all the peptidic assemblies explored thus far, peptide amphiphile nanofibers[44] and protein analogous micelles[45] are the most studied as bioactive materials for diverse biomedical applications. In both cases, the underlying molecular design involves covalent linkage of one or more hydrocarbons/lipids onto either the *N* or *C* terminus of a short peptide to generate self-assembling peptide amphiphiles (PAs). The incorporation of this hydrophobic segment not only enhances the self-assembly potential of the peptide conjugate in an aqueous environment, but also enables the specific presentation of enhanced bioactive signals on the resultant assemblies.[186-188] For example, the Stupp Lab has shown that the high-density presentation of neurite-promoting laminin epitope IKVAV on peptide amphiphile nanofibers is critical for the selective differentiation of neural progenitor cells into neurons while discouraging the development of astrocytes.[186]

Given that molecular and cellular signaling are highly regulated events, a variety of bioactive epitopes, either naturally occurring peptides or *de novo* designed sequences, have been incorporated into the PA design to enhance their biologically active features for a target application,[31, 41, 172, 183, 186, 189-190] with the respective goal of promoting cell adhesion, proliferation and differentiation, or selectively recognizing particular cells or tissues for disease treatments. Since some of these epitopes must assume an appropriate secondary structure—for the most part an α-helical conformation—to interact with their molecular target(s), the challenge then becomes how to retain their bioactive conformation within their respective supramolecular assemblies.[191-192] It has been shown by a number of research laboratories that the solvent property,[193-195] the added hydrophobic segment,[187, 196-199] and the thermal history[197, 200] could all potentially affect the peptide's secondary structures, and consequently, their assembled morphologies. For α-helical peptides in particular, the Tirrell lab has suggested that confinement and crowdedness within the micellar corona would favor the α-helical conformation, and reported formation of protein analogous micelles with significant α-helicity.[172, 225-228] Recently, it was also found that the linker chemistry[190] and the contour length of the chosen peptide[229] play a critical role in retaining the native peptide conformation within supramolecular nanostructures. Despite important progress, concerns still remain on the structural uncertainty of α-helical peptides upon forming their respective supramolecular assemblies.[224, 230]

In this context, I report the findings on the alkylation-regulated conformation preservation of α-helical peptides within their filamentous assemblies. Although the β-sheet-forming peptide sequences are essential for the formation of one-dimensional nanostructures and have been applied to many peptide-based self-assembling systems for diverse biomedical applications, this work focuses on the strategy of the preservation of the α-helix conformation in the self-assembling nanostructures for the peptide epitopes that must assume an α-helix conformation to exert their functions. I found that the chemical conjugation of two short linear hydrocarbons (octanoic acids, C8) can retain the α-helical conformation of the two protein A-derived peptide sequences while effectively driving their assembly into filamentous nanostructures. In contrast, the use of a single palmitoyl tail (C16) of similar hydrophobicity would lead to formation of β-sheets assemblies. As for single chain alkylation, I further discovered that the length of the conjugated hydrocarbon is crucial for tuning the peptide conformation, in addition to affecting the critical micelle concentration (CMC) and assembled morphologies. α-helical conformation was also observed in the lauric acid (C12) alkylated peptide sequence. Further, increasing the double alkyl chains to 12 carbons can also induce the formation of β-sheets, underscoring the effect of the overall hydrophobicity. Although it is well known that the alkylation can enhance the conformation stability of α-helical peptides,[187, 198] it is rare that such a subtle difference in the number and length of hydrocarbons could lead to dramatic changes in secondary structures from β-sheets to α-helices within filamentous assemblies. I believe these findings provide important insight into the design and construction of supramolecular filaments containing α-helical peptides.

2.3 Experimental Procedures

2.3.1 Materials and Molecular Synthesis

All Fmoc amino acids and resins were purchased from Advanced Automated Peptide Protein Technologies (Louisville, KY), and Fmoc-Lys(Fmoc) were obtained from Novabiochem (San Diego, CA). All other reagents were obtained from VWR (Radnor, PA) and used as received without further purification.

Peptide conjugates were synthesized using similar methods. All the peptide sequences were synthesized on the Focus XC automatic peptide synthesizer (AAPPTEC, Louisville, KY) using standard 9-fluorenylmethoxycarbonyl (Fmoc) solid phase synthesis protocols. Alkyl chains were then manually coupled at the *N*-terminus of the peptide or the side chain of lysine (K) to produce different peptide conjugates, and shaken overnight at room temperature. Fmoc deprotections were performed using a 20% 4-methylpiperidine in DMF solution for 10 minutes, repeated once. In all cases, reactions were tested using the ninhydrin test (Anaspec Inc., Fremont, CA) for free amines. Completed Peptide conjugates were cleaved from the solid support using a mixture of TFA/TIS/H2O in a ratio of

92.5:5:2.5 for 2.5 hours. Excess TFA was removed by rotary evaporation and cold diethyl ether was added to precipitate the crude peptide. By centrifugation method, precipitated peptide and diethyl ether were separated at 6000 rpm for 3 minutes. Peptides were washed 2 more times with diethyl ether and the solution was removed by centrifugation.

The peptide conjugates were purified by preparative RP-HPLC using a Varian Polymeric Column (PLRP-S, 100 Å, 10 µm, 150 × 25 mm) at 25 °C on a Varian ProStar Model 325 preparative HPLC (Agilent Technologies, Santa Clara, CA) equipped with a fraction collector. A water/acetonitrile gradient containing 0.1% v/v TFA was used as eluent at a flow rate of 20 mL/min. The absorbance peak was monitored at 220 nm for peptide segments. The crude materials were dissolved in 20 mL of 0.1% aqueous TFA, and each purification run was carried out with a 10 mL injection. Collected fractions were analyzed by MALDI-ToF (BrukerAutoflex III MALDI-ToF instrument, Billerica, MA) and those containing the desired product were lyophilized (FreeZone -105 °C 4.5 L freeze dryer, Labconco, Kansas City, MO) and stored at -30 °C.

2.3.2 Self-Assembly and Transmission Electron Microscopy (TEM) Imaging

Peptide conjugates of 1 mM concentration were pretreated with hexafluoroisopropanol (HFIP), a good solvent for the peptide conjugates, to eliminate any pre-existing nanostructures that could be possibly formed during the synthesis, purification and lyophilization process. HFIP were then removed via rotatory evaporation, followed by subsequent addition of deionized water to reach a final concentration of 1 mM. Sodium hydroxide was used to tune the pH of the solution to 7.4. After aged overnight at room temperature, 10 μL of 10-fold diluted sample was spotted on a carbon film copper grid with 400 square mesh (from EMS: Electron Microscopy Sciences) and the excess was removed with filter paper to leave a thin film of sample on the grid. After letting the sample dry for 5 minutes, 10 μL of 2% uranyl acetate was added to the sample grid, and the excess was removed after 30 seconds. All samples were dried for at least 3 hours before TEM imaging.

2.3.3 Critical Micelle Concentration (CMC) Measurement

The CMC of the peptide conjugates was determined by incubating these molecules at various concentrations with a certain amount of Nile Red.[231-232] The stock solution of Nile Red was initially prepared by dissolving the dye in acetone at 50 μM. 10 μL stock solution was loaded into several centrifuge tubes, where the solvent evaporates under room temperature to yield the dry mass of Nile Red. Various concentrations of the peptide solutions were prepared in deionized water, and then identical volume was added into the centrifuge tubes containing dry Nile Red and aged overnight. Fluorescent spectra of Nile Red were then monitored by a Fluorolog fluorometer (Jobin Yvon, Edison, NJ) with fixed excitation wavelength at 560 nm; emission spectra were monitored 580–720 nm. The CMC of peptide conjugates is determined by a blue-shift of the emission maximum, whereas this transition occurs as the incubated peptides exceed their CMC values.

2.3.4 Circular Dichroism (CD) Spectroscopy

The CD experiments of self-assembled samples were conducted on a Jasco J-710 spectropolarimeter (JASCO, Easton, MD) using a 1 mm path length quartz UV-Vis absorption cell (ThermoFisher Scientific, Pittsburgh, PA) at 25°C. The samples were instantly diluted from the 1 mM stock solution to 100 μM in deionized water at pH 7.4 prior to the experiment. Using the average of three scans, the spectra were collected in the wavelength range of 190–280 nm. A background spectrum of the solvent was acquired and subtracted from the sample spectrum. The collected data was normalized with respect to the sample concentration. A curve was fit for each IA molecule using a linear combination of polylysine basis spectra to estimate the content of α-helix, β-sheet, and random coil peptide secondary structure.

2.3.5 Thioflavin T (ThT) Assays

A ThT stock solution was prepared in deionized water at 50 μM. 100 μM Peptide conjugates were vortexed and incubated with an identical volume of ThT stock solution for 1 h. The fluorescence intensity was then measured by a Fluorolog fluorometer (Jobin Yvon, Edison, NJ) with excitation at 440 nm (slit width 5 nm) and emission at 482 nm (slit width 10 nm).

2.4 Results and Discussions

2.4.1 Molecular Design

The protein A-derived peptide, Z33 (FNMQQQRRFYEALHD-PNLNEEQRNAKIKSIRDD) contains two α-helical strands as the core binding motifs for immunoglobulin G (IgG).[214, 233] Considering the complexity and possible complication factors in working with this long sequence, I decided to investigate the impact of alkylation on each of the individual helical strand. Also given that proline is a known disrupter for α-

helix, I decided to separate the two helices between the aspartic acid residue (**D)** and the proline residue (**P)** to obtain Helix1 (FNMQQQRRFYEALHD) and Helix2 (PNLNEEQRNAKIKSIRDD). As such, two series of peptide amphiphiles, termed here immuno-amphiphile (IAs) due to the origin of Z33 peptide for immunoglobulin binding, were constructed using each helical sequence. The alkyl chains are conjugated onto the *C*-terminus of the Helix1 but to the *N*-terminus of Helix2 (**Figure 2-1 A**). The reason I chose to conjugate alkyl tails on the different termini of the two helical peptides was to mimic the relative position between Helix1 and Helix2 shown in the Z33 peptide. Under aqueous conditions, Helix1- and Helix2-based IAs are expected to associate into supramolecular assemblies with the hydrophobic segment trapped in the core and the peptides facing towards the aqueous environment (**Figure 2-1 B**). All the molecules studied here were synthesized using solid-phase peptide synthesis methods, and then purified with RP-HPLC. The purity and expected molecular masses of the synthesized compounds were confirmed using analytical HPLC and mass spectrometry, respectively.

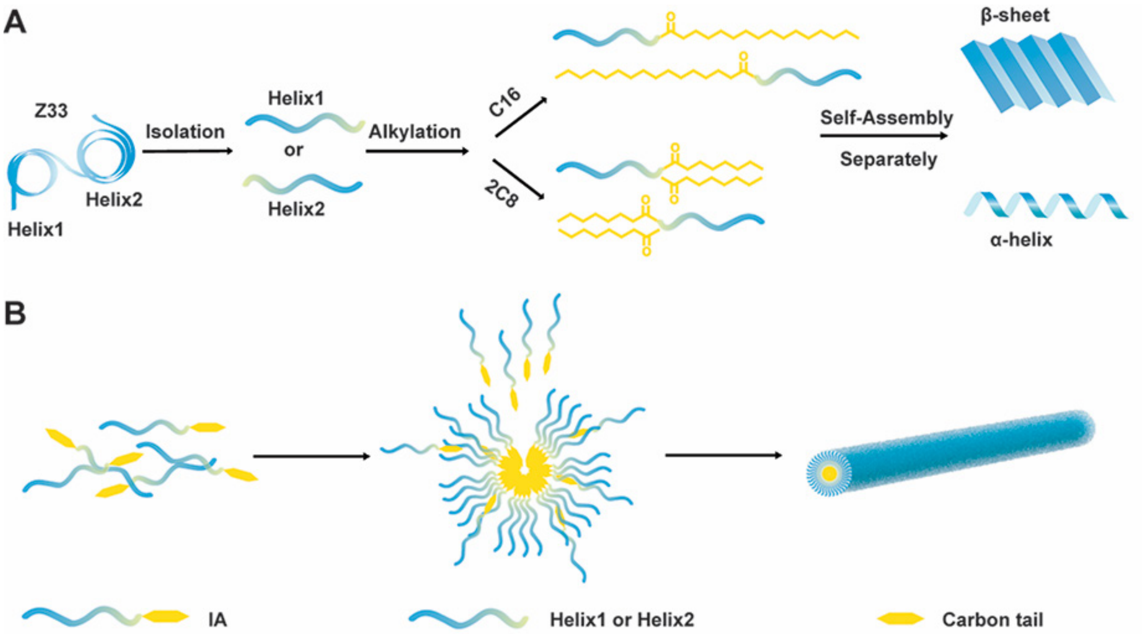

Figure 2-1. (**A**) Schematic illustration of the molecular design of Helix1- and Helix2-based peptide amphiphiles via direct alkylation with C16 and 2C8, respectively. These peptide amphiphiles are termed immuno-amphiphiles because of the origin of the protein A-derived peptide Z33 for its specific binding ability to immunoglobulin antibodies. (**B**) Schematic illustration of the self-assembly of the designed IAs into one-dimensional nanostructures.

2.4.2 Molecular Assembly

All the synthesized peptide conjugates were first pretreated with Hexafluoro-2-propanol (HFIP) to eliminate any pre-existing nanostructures that could be possibly formed during the synthesis, purification and lyophilization process. HFIP were then removed *via* rotatory evaporation, followed by subsequent addition of deionized water to reach a final concentration of 1 mM. After aging overnight, TEM was utilized to visualize the assembled morphologies (**Figure 2-2**). **Figure 2-2 A** and **C** are representative TEM micrographs, revealing that single-chain alkylated peptides, both Helix1-C16 and C16-Helix2, self-assembled into filamentous structures with a diameter of 9.6 ± 1.3 nm and 12.4 ± 1.7 nm, respectively. Two or more of these filaments were occasionally observed to intertwine into bundled structures of larger diameters. The lengths of the observed filaments are very polydisperse but on tens of micrometer scale. For double-chain alkylation with octonoic acid (C8), filamentous assemblies were also found for both Helix1-2C8 and 2C8-Helix2 under the same conditions (**Figure 2-2 B** and **D**). However, these filaments are relatively shorter, also appearing more polydisperse in length. In addition, variations in the diameter were observed, with smallest filaments possessing a diameter of 11.0±1.4 nm for Helix1-2C8 filaments and of 9.7±1.3 nm for Helix2-2C8 filaments. It is very likely that those of larger diameters are hierarchical structures formed by intertwining and bundling of smaller ones (*vide infra*).

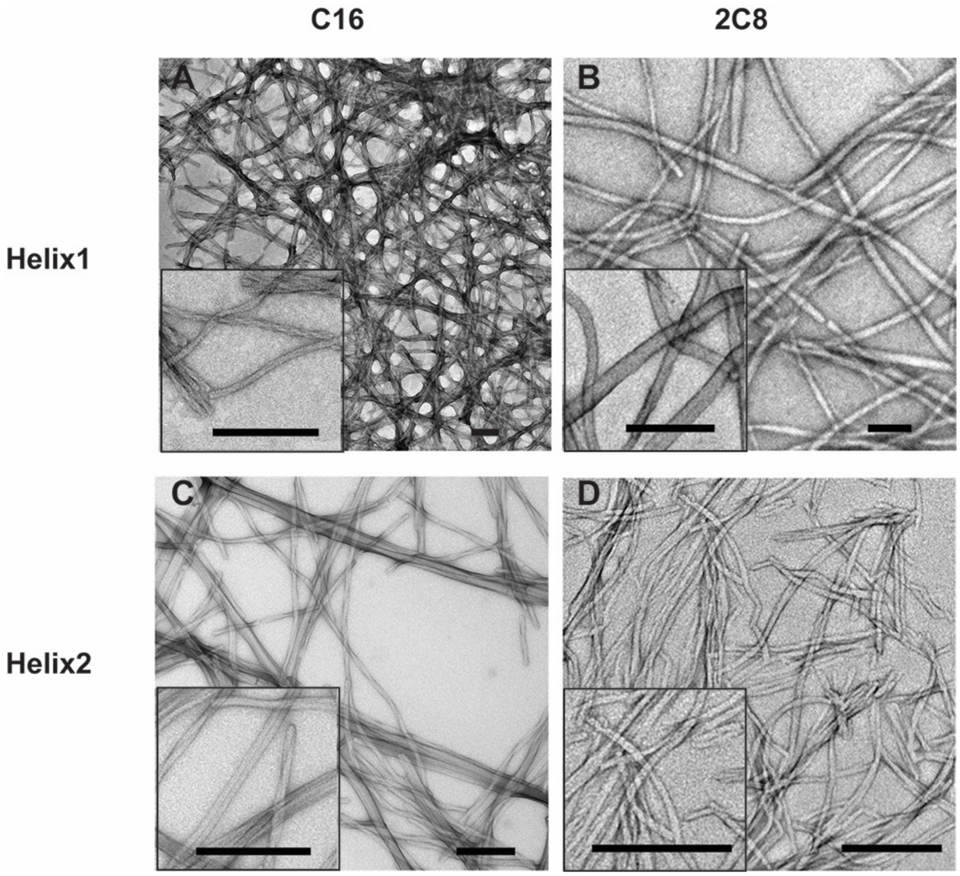

Figure 2-2. Representative TEM micrographs of filamentous assemblies formed by the four designed immuno-amphiphiles in aqueous solution, pH 7.4. TEM images of (**A**) Helix1-C16 and (**C**) C16-Helix2 reveal filament morphology with diameters of 9.6±1.3 nm and 12.4 ± 1.7 nm, respectively. TEM images of (**B**) Helix1-2C8 and (**D**) 2C8-Helix2 also relatively shorter filaments with diameters of 11.0±1.4 nm and 9.7±1.3 nm, respectively. Inserts (**A-D**) are higher resolution images illustrating the representative features. All the samples were prepared in water at a concentration of 1 mM at pH 7.4, aged overnight and diluted 10 fold right before TEM sample preparation. All TEM samples were stained with 2 wt% uranyl acetate aqueous solution, a negative contrast agent, to improve imaging resolution. All scale bars: 200 nm.

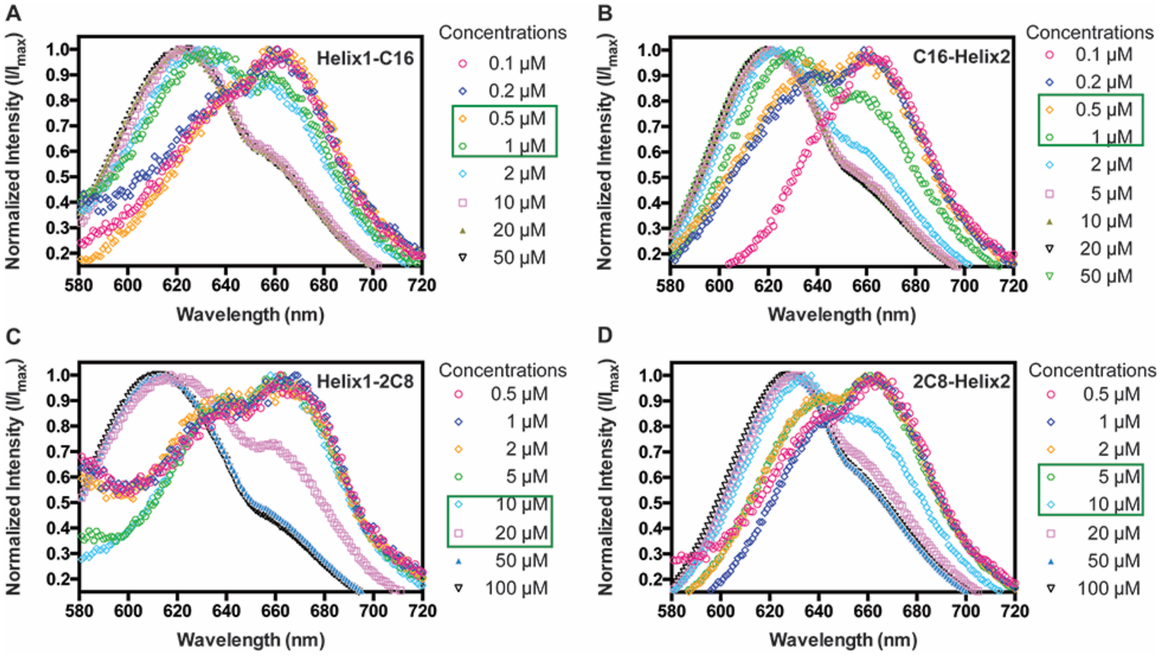

Figure 2-3. Emission spectra of a reporter dye Nile Red upon incubating with (**A**) Helix1-C16, (**B**) C16-Helix2, (**C**) Helix1-2C8, and (**D**) 2C8-Helix2 for determining the critical micelle concentrations (CMCs). All spectra shown here are normalized by the emission maximum. A blue-shift is expected when the IA concentrations exceed the CMC. The CMC range for each IA is boxed in the legend.

To understand the assembly differences between single-chain and double-chain alkylated peptides, I conducted further experiments to evaluate their critical micelle concentrations (CMCs) as well as secondary structures in supramolecular assemblies. The CMCs were measured using a Nile Red assay. Nile Red is a lipophilic dye that fluoresces depending on solvent polarity and local environment. When incubated with various concentrations of self-assembling IAs in aqueous solution, Nile Red prefers to partition into the hydrophobic domains if there exist any supramolecular assemblies. The CMC value can be determined when a blue-shift of the emission maximum started to occur.

Figure 2-3 A shows a plot of Nile Red fluorescence intensity versus emission wavelengths for a series of Helix1-C16 aqueous solutions of various concentrations. The maximum emission peaked at 660 nm at low peptide concentrations up to 0.5 µM. At 1 µM, this peak was blue-shifted to 635 nm, suggesting formation of micellar structures. Similarly, CMC values for C16-Helix2, Helix1-2C8, and 2C8-Helix2 can be observed as 0.5-1µM, 10-20 µM, and 5-10 µM from **Figure 2-3 B-D**, respectively. Although two C8 alkyl chains carry a similar number of carbon atoms to that of one single C16 alkyl chain, I found that double-chain alkylated peptides exhibit consistently higher CMCs compared to the single-chain alkylated ones. This likely arises from the differences in packing order among the hydrophobic segments and also the secondary structure that the peptides assume. In addition, 2C8-Helix2 shows a stronger tendency for aggregation than Helix1-2C8, likely due to the fact that Helix2 contains residues of bearing opposite charges.

2.4.3 Secondary Structure Measurements

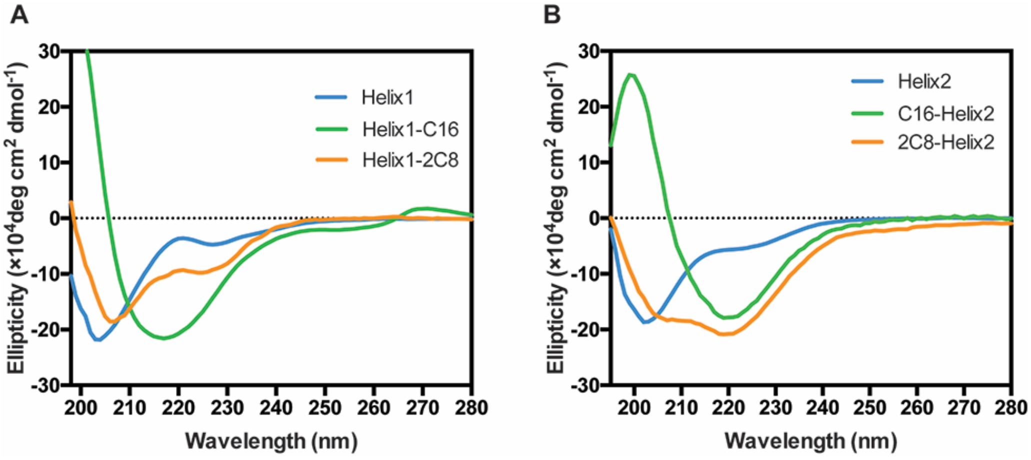

Figure 2-4. Normalized CD Spectra of 100 µM (**A**) Helix1, Helix1-C16, Helix1-2C8, and (**B**) Helix2, C16-Helix2, 2C8-Helix2 in water, pH 7.4. The spectra show that double-chain

alkylated peptides can effectively preserve their native helical conformation, whereas single-chain alkylation led to a transition from helical conformation to β-sheet-bonded assemblies.

Next, circular dichroism (CD) spectroscopy was used to study the aqueous solutions of peptide assemblies to understand the molecular packing within their self-assembled structures. As shown in **Figure 2-4**, the unconjugated, free peptides of Helix1 and Helix2 display typical CD absorption of random coils, indicating a loss of the α-helical structures (**Figure 2-5**). This is not unexpected since it is well known that isolation from the parent Z33 sequence may disrupt the mutual dependence for stability between the two helices.[214] Helix1-C16 and C16-Helix2 assemblies exhibit strong negative signals at around 218 nm and a positive signal between 190 nm-200 nm, suggesting the formation of β-sheet secondary structures. The β-sheet conformation plays an important role in promoting the formation of one-dimensional nanostructures.[223, 234] In contrast, it was found that both Helix1-2C8 and 2C8-Helix2 assumed typical α-helix secondary structure within their respective filamentous assemblies, as evidenced by the two negative signals at around 225 nm (n-π^* transition) and 208 nm (π-π^* transition). These CD spectra can be fit using a linear combination of polylysine basis spectra to evaluate the content of each secondary structures (**Figure 2-6**).[172, 235] The analysis suggested that β-sheets are the major constituent of Helix1-C16 and C16-Helix2 conjugates, while double-chain alkylated peptides present higher contents of α-helix secondary structures.

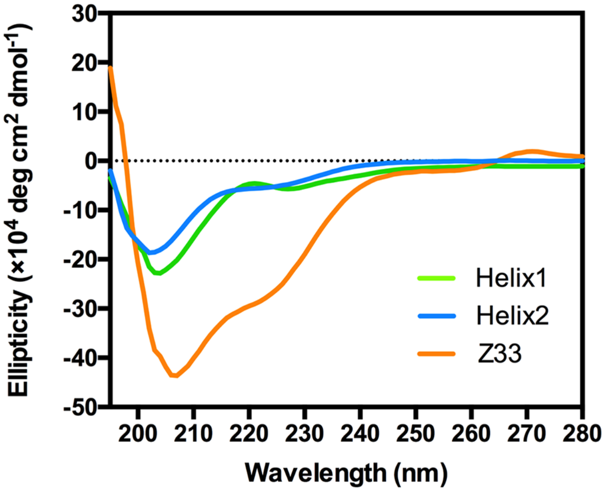

Figure 2-5. Normalized CD Spectra of Helix1, Helix2, and Z33 at 100 µM in water, pH 7.4.

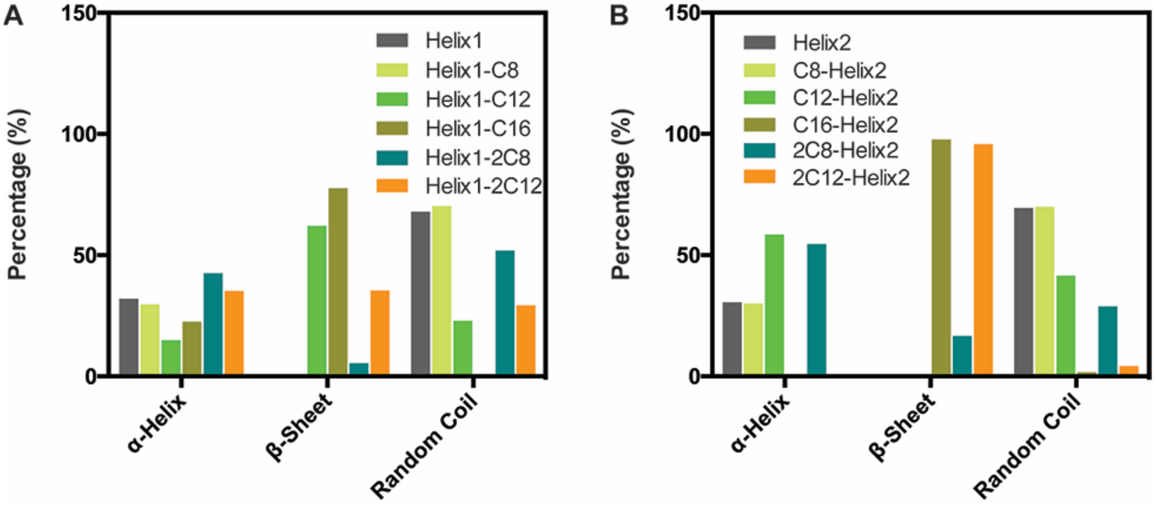

Figure 2-6. Analysis of CD spectra for Helix1- and Helix2-based IAs. The content of three main secondary structures in (**A**) Helix1-based and (**B**) Helix2-based molecules. The CD data were fit from 200 nm to 240 nm using a linear combination of polylysine basis spectra to determine approximate *α*-helix, *β*-sheet, and random coil peptide secondary structure.

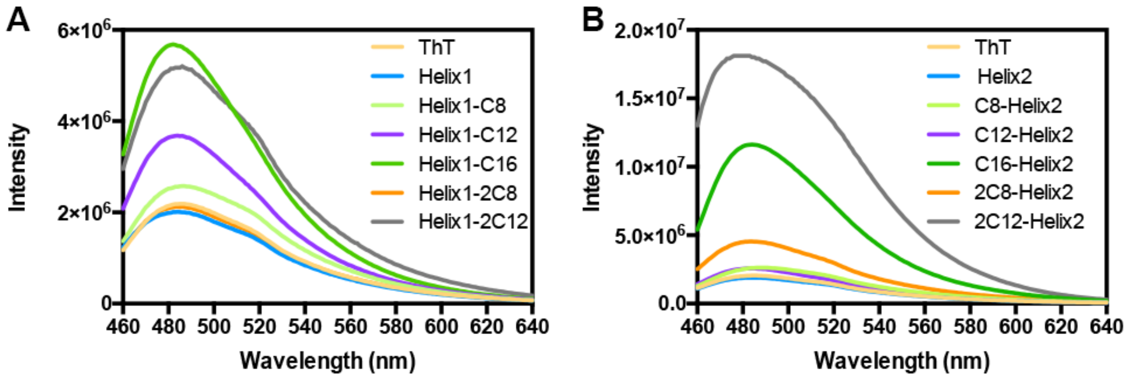

Figure 2-7. Fluorescence of ThT dye with (**A**) Helix1 and Helix1-based and (**B**) Helix2 and Helix2-based immuno-amphiphiles at 100 µM in deionized water, pH 7.4.

To further confirm the component of secondary structures in the self-assembled conjugates, I performed Thioflavin-T (ThT) assays to examine the existence of *β*-sheet secondary structures in both Helix1-based and Helix2-based conjugates. ThT is a fluorescent dye with large enhancement of its fluorescence upon binding to *β*-sheets.[236-237] As shown in **Figure 2-7 A**, ThT emissions of pre-incubated Helix1 and Helix1-2C8 at 482 nm maintain a similar or slightly higher level compared with that of the pure ThT solution, implying the lack of *β*-sheets in those solutions. In stark contrast, a dramatic increase in fluorescence was observed in the pre-incubated Helix1-C16 solution, further confirming the presence of *β*-sheet assemblies for this conjugate which is in consistency with the CD results. In **Figure 2-7 B**, the pre-incubated C16-Helix2 can largely increase the fluorescence of ThT. A minor increase was also observed in the 2C8-Helix2 solution, indicating that *β*-sheet conformation truly exist in the 2C8-Helix2. Combined with the CD spectrum in **Figure 2-4 B** and CD analysis result **Figure 2-6 B**, I would deduce that the conformation of 2C8-Helix2 is a mixture of α-helix and β-sheet.

One may argue that the observed CD signals may come from the unassembled monomers in solution, not from those within the assembled filaments. To exclude this possibility, CD spectra were collected from a series of diluted solutions of α-helix IA (represented by Helix1-2C8) (**Figure 2-8 A**) and β-sheet IA (represented by Helix1-C16) (**Figure 2-8 B)**. The helical content increases as the increase of Helix1-2C8 concentration (**Figure 2-8 A)**. Although at the lower concentrations under CMC there are slight helical signals, their contributions to the overall secondary structures at higher concentrations are very limited. Because the concentration for unassembled, monomeric Helix1-2C8 is constant and will not change above the CMC. This observation clearly suggests that it is the assembled structures not the unassembled monomers that dominate the CD absorption associated with the helical contents. In a similar way, the β-sheet CD signals for Helix1-C16 solutions (**Figure 2-8 B**) became prominent and stable only when the IA concentration surpassed the CMC value, again revealing that peptide conjugates within the filamentous structures is the major contributor to the observed CD absorption.

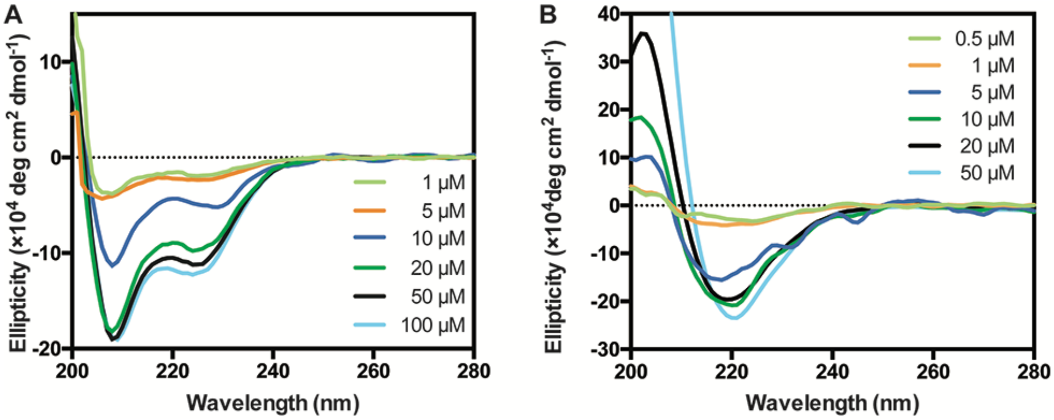

Figure 2-8. Normalized CD Spectra of (**A**) Helix1-2C8 and (**B**) Helix1-C16 at various concentrations in water, pH 7.4. These studies suggest that peptide conjugates within their supramolecular assemblies primarily contribute to the observed CD absorption. Both conjugates appear to be unstructured random coils when concentrations are dropped below their respective CMCs.

Considering the difference in contour length between *β*-sheets (3.4 Å per residue) and *α*-helices (1.5Å advancement per residue), I would expect dramatic diameter differences for the assembled filaments if these conjugates all assembled into the classic core-shell peptide amphiphile nanofibers. The TEM imaging studies revealed that the filaments formed by self-assembly of Helix1-2C8 and 2C8-Helix2 measure the diameters of ~11.0 nm and ~9.7 nm, respectively, matching well with the core-shell model of *α*-helical conformation. It should be noted that filaments of larger diameters can be frequently observed, and can be attributed to further bundling and intertwining of the core-shell filaments. It is interesting, however, filaments of hydrogen-bonded *β*-sheets did not appear to be much larger, but rather their diameters fell into a similar range, with ~9.6 nm for Helix1-C16 and ~12.4 nm for C16-Helix2. I therefore speculate that these *β*-sheet rich filaments bear more resemblance to amyloid fibrils rather than the typical core-shell cylindrical micelles. The diameter of the filaments depends not only on the conformation of the peptide but also the degree of stretching of the alkyl tails. There is a delicate correlation and balance among the shorter alkyl tail, steric hindrance, and represented conformation for assembly of 2C8 conjugated IAs. In this regard, it's rather difficult to project the diameters of their filamentous assemblies. Bundles and twisted structures such as ribbon-like assemblies (**Figure 2-2**) can be observed in these assembly systems, likely due to the longer peptide sequences of Helix1 and Helix2 that dominates the assembly process.

These results led to the conclusion that the molecular packing within the hydrophobic domains contributes significantly to the peptide conformation within the filament corona. Considering the packing geometry of α-helix and β-sheet, the center-to-center distance among helices is typically around 12 Å depending on the side chain lengths,[238-239] while β-strands are spaced by a hydrogen bond distance within the β-sheet, ~4.7 Å.[240-241] This difference in packing requirements eludes that a looser packing among the molecular units is important for the formation of α-helix over β-sheets. For conjugation with two shorter C8 tails, not only did the double chain afford more volume to relieve the crowdedness of packing, but also that the two C8 chains were not symmetrically conjugated onto the two helical peptides due to the use of lysine residue as the anchoring point (**Figure 2-13** and **Figure 2-14**). In this way, the two C8 alkyl chains are placed asymmetrically at one terminus of the peptide and would likely introduce some steric hindrance for molecular arrangement, resulting in relatively larger CMC and looser packing that favor the presentation of helical conformation.

2.4.4 Effect of Alkyl Chain Length

It is known that long alkyl chains can be packed in a highly ordered fashion within their supramolecular assemblies,[242-243] thus likely forcing the peptide segments into closer proximity. As such, increasing the length of the two alkyl tails to C12 (lauric acid) may offset the effect of looser packing induced by the double chain alkylation. To validate this assumption, Helix1-2C12 and 2C12-Helix2 were synthesized and characterized (**Figure 2-15, 2-16, 2-25**). They both exhibit lower CMCs and form immunofibers with wider diameters than 2C8 conjugates in aqueous solutions at neutral pH. It was found that Helix1-2C12 retains the α-helix conformation, while 2C12-Helix2 shows β-sheet structures. This conformational difference could result from the sequence difference between Helix1 and Helix2. The recurrence of the β-sheet in the double chain alkylation suggests that the increase of the hydrophobicity in the double chain alkylated conjugates can potentially promote the formation of β-sheets, leading to the conclusion that the packing of the peptides is determined not only by the way of alkylation but also the overall hydrophobicity of the conjugated alkyl tails. When comparing 2C8 with C16 conjugates, the interfacial area per peptide chain in 2C8 conjugates is expected to be greater as a result of the increased steric hindrance, thus providing more room and flexibility for the formation of α-helix. However, by changing 2C8 tails to 2C12 tails, a tighter packing can be resulted due to the potential of crystallization by longer alkyl chains, which may promote *β*-sheet conformation.

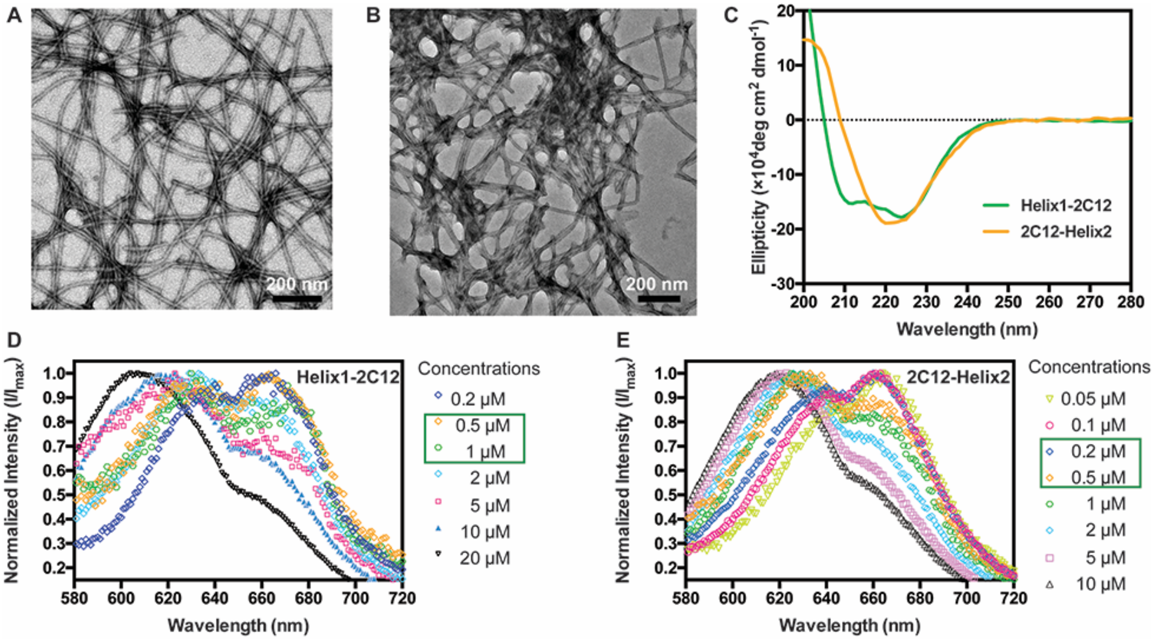

Figure 2-9. Characterization of Helix1-2C12 and 2C12-Helix2. TEM images of (**A**) Helix1-2C12 and (**B**) 2C12-Helix2 display nanofibers morphology with diameters of 15.7 ± 1.4 nm, and 13.4 ± 0.9 nm, respectively. The samples were prepared in deionized water at pH 7.4. (**C**) Normalized CD Spectra of 100 µM Helix1-2C12 and 2C12-Helix2 in water, pH 7.4. Emission spectra of the reporter dye Nile Red when incubated with (**D**) Helix1-2C12 and (**E**) 2C12-Helix2 for determining the CMC values.

Given that the looser packing of double-chain alkylated peptides may account for stabilization of *α*-helix assemblies, I presume that shortening the length of single alkylated chains (low potential for crystallization) may likely reduce the packing order within the hydrophobic domains. In order to confirm this assumption, I chose two shorter alkyl chains (lauric acid, C12; octanoic acid, C8) to conjugate with the Helix1 and Helix2, respectively.

Again, their assembly behavior was characterized using TEM, Nile Red assays, and CD. No well-defined nanostructures and emission maximum transitions were observed for either Helix1-C8 or C8-Helix2 at the concentration of 100 µM (**Figure 2-10**), indicating that these two conjugates did not self-assemble at and below this concentration. Helix1-C12 and C12-Helix2 (**Figure 2-11 A** and **B**) were observed to associate into filaments of 12.2 ± 1.4 nm and 9.1 ± 1.6 nm in diameter, respectively. Strong lateral adhesion among C12-Helix2 filaments was observed, likely due to the electrostatic attractions among lysine/arginine residues and glutamic/aspartic acid residues (**Figure 2-11 B**). CMC measurements suggested both C12 conjugates started to assemble within the micromolar concentration range, with the Helix1-C12 showing a slightly higher CMC value (**Figure 2-11 C** and **D**). In the CD studies (**Figure 2-11 E** and **F**), both Helix1-C8 and C8-Helix2 showed similar absorption phenomena to those of the unconjugated, free peptides, for they do not possess the ability to aggregate under the studied conditions.[242]

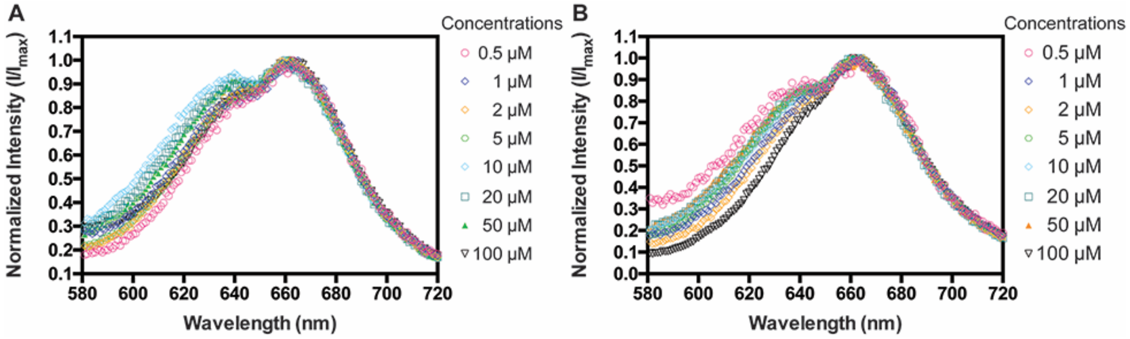

Figure 2-10. Emission spectra of the reporter dye Nile Red when incubated with (**A**) Helix1-C8, (**B**) C8-Helix2 for determining the critical micelle concentration (CMC) values. All spectra shown here are normalized by the emission maximum. There was no detectable peak shift observed even the conjugate concentrations reached 100 µM.

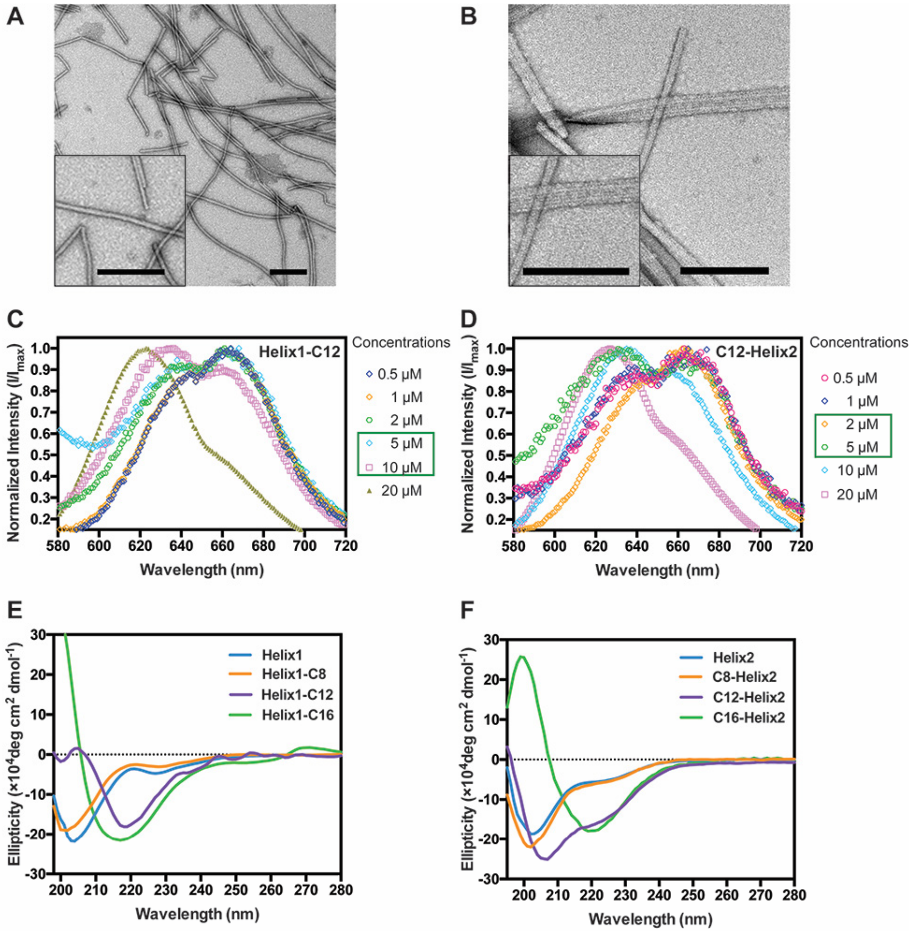

Figure 2-11. Characterization of different Peptide conjugates. TEM images of (**A**) Helix1-C12 and (**B**) C12-Helix2 display nanofibers morphology with diameters of 12.9 ± 0.9 nm, and 13.9 ± 1.5 nm, respectively. All scale bars: 200 nm. Emission spectra of the reporter dye Nile Red when incubated with (**C**) Helix1-C12 and (**D**) C12-Helix2 for determining the CMC values. Normalized CD spectra of 100 μM (**E**) Helix1, Helix1-C8, Helix1-C12, and Helix1-C16 and (**F**) Helix2, C8-Helix2, C12-Helix2, and C16-Helix2 in water, pH 7.4.

Interestingly, β-sheet absorption features appeared in the CD spectrum of Helix1-C12, whereas α-helix secondary structure was observed in the C12-Helix2 system. Helix2 peptide may have a relatively higher propensity to assume the helical conformation, which might be rooted in their difference in peptide sequence. This observation also suggests that it is possible to preserve the α-helical conformation within their filamentous assemblies using the single-chain conjugation strategy. Considering the random coil conformation for C8-Helix2 and the free Helix2 peptide, the preservation of α-helical conformation within their filamentous assemblies again suggests that this the α-helical stability is not just linked to conjugation chemistry, but rooted in the supramolecular assembly process.

The peptide sequences, CMCs, and secondary structures of all the studied molecules in this work are summarized in **Table 2-1**. Details of molecular structures and characterization are shown in **Figure 2-12** to **Figure 2-27**. As we can see, both long single-chain and double-chain alkylation can effectively promote the formation of supramolecular filaments, but the resultant assemblies differ in morphology, CMCs, and secondary structures. The length and number of alkyl chains are known to promote the aqueous self-assembly of the resultant conjugates.[244] Jan van Hest and coworkers found that the GANPNAAG peptide conjugated with C12 or shorter alkyl chains showed no aggregates under their studied conditions, but in the C14 conjugates and C16 or longer conjugates fibrous aggregates and tubular structures can be found.[197] The studies on self-assembly of immuno amphiphiles bearing C8, C12, and C16 conjugated chains corroborate van Hest's findings. The CMCs of the single-chain alkylated amphiphiles decreases as the length of alkyl chain increases,[198, 245] due to the enhanced hydrophobicity that promotes the aggregation potential. Alkyl chain conjugation was previously demonstrated to enhance the stability of α-helix secondary structures and bioactivities.[187, 189, 198, 246] Mihara and co-workers found that longer *N*-terminal alkylated 2α-helix peptide underwent a higher rate of α-to-β transitions, indicating the formation of β-sheets promoted by long alkyl chains.[196] My results showed the recurrence of α-helix conformation in the alkylated Helix1 and Helix2 peptides. I also showed that a relatively long alkyl chains could induce the formation of β-sheets. To the best of my knowledge, the α-to-β transitions regulated by single- and double-alkylation are unprecedented.

Table 2-1. All the studied IA molecules, their CMC values, and peptide conformation measured at 100 μM.

Abbreviation	Peptide conjugates	Conformation (100 μM)	CMC (μM)
Helix1-C8	FNMQQQRRFYEALHDK-$C_8H_{15}O$	Random coil	>100
Helix1-C12	FNMQQQRRFYEALHDK-$C_{12}H_{23}O$	β-sheet	5-10
Helix1-C16	FNMQQQRRFYEALHDK-$C_{16}H_{31}O$	β-sheet	0.5-1
Helix1-2C8	FNMQQQRRFYEALHDKK-$(C_8H_{15}O)_2$	α-helix	10-20
Helix1-2C12	FNMQQQRRFYEALHDKK-$(C_{12}H_{23}O)_2$	α-helix	0.5-1
C8-Helix2	$C_8H_{15}O$-PNLNEEQRNAKIKSIRDD	Random coil	>100
C12-Helix2	$C_{12}H_{23}O$-PNLNEEQRNAKIKSIRDD	α-helix	2-5
C16-Helix2	$C_{16}H_{31}O$-PNLNEEQRNAKIKSIRDD	β-sheet	0.5-1
2C8-Helix2	$(C_8H_{15}O)_2$-KPNLNEEQRNAKIKSIRDD	α-helix	5-10
2C12-Helix2	$(C_{12}H_{23}O)_2$-KPNLNEEQRNAKIKSIRDD	β-sheet	0.2-0.5

Helix1: FNMQQQRRFYEALHD-NH$_2$

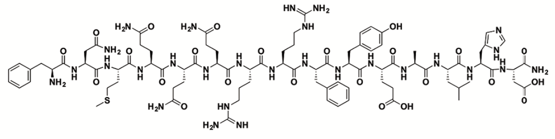

Helix2: Ac-PNLNEEQRNAKIKSIRDD

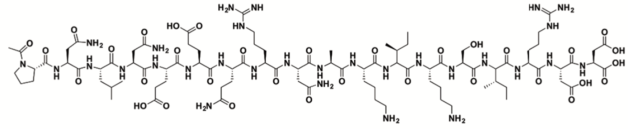

Z33: FNMQQQRRFYEALHDPNLNEEQRNAKIKSIRDD

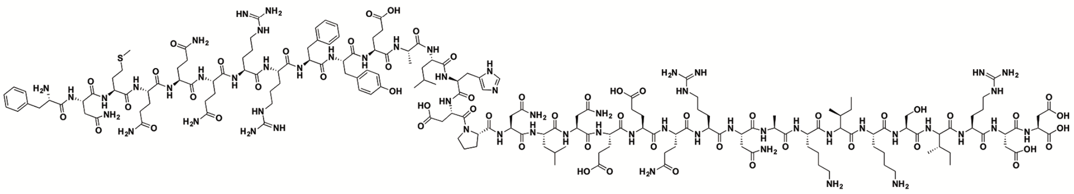

Figure 2-12. Peptide sequences and chemical structures of Helix1, Helix2, and Z33.

FNMQQQRRFYEALHDK-C8 (Helix1-C8)

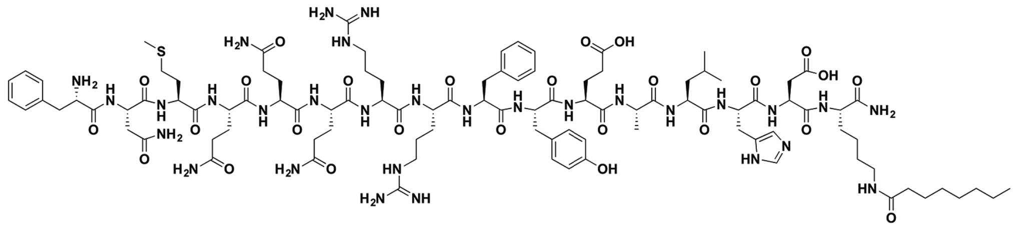

FNMQQQRRFYEALHDK-C12 (Helix1-C12)

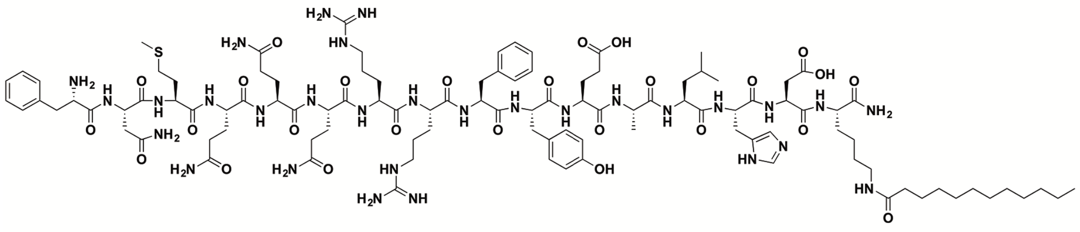

FNMQQQRRFYEALHDK-C16 (Helix1-C16)

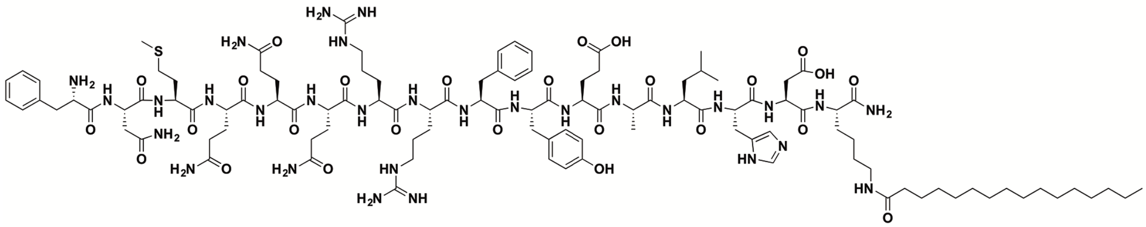

FNMQQQRRFYEALHDKK-2C8 (Helix1-2C8)

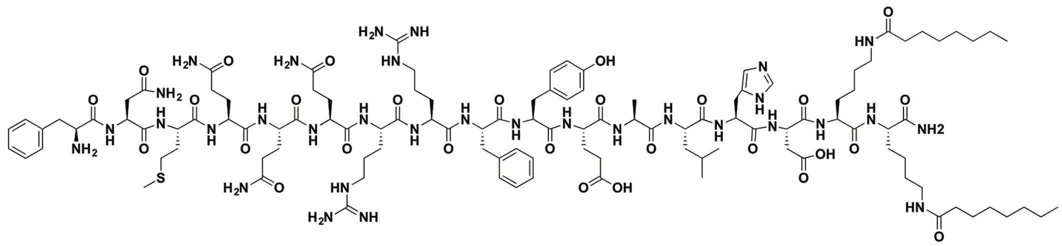

FNMQQQRRFYEALHDKK-2C12 (Helix1-2C12)

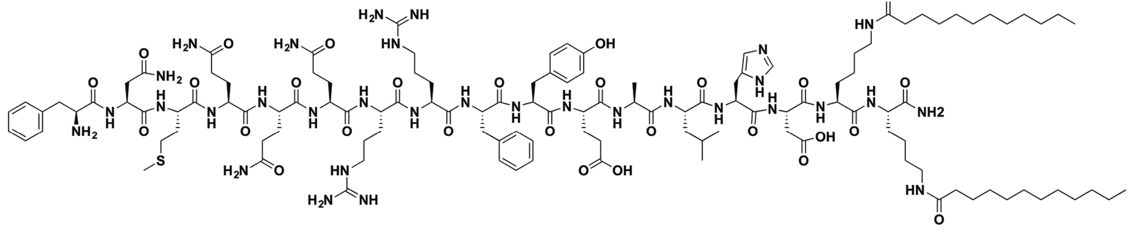

Figure 2-13. Chemical structures of Helix1-C8, Helix1-C12, Helix1-C16, Helix1-2C8, and Helix1-2C12.

C8-PNLNEEQRNAKIKSIRDD (C8-Helix2)

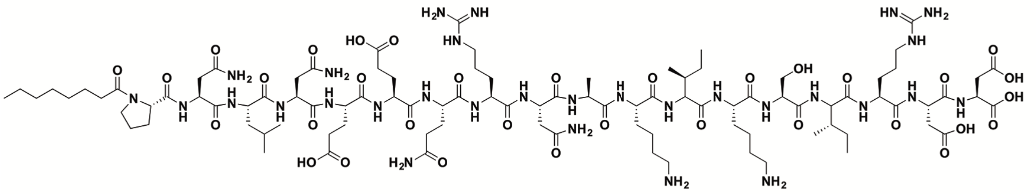

C12-PNLNEEQRNAKIKSIRDD (C12-Helix2)

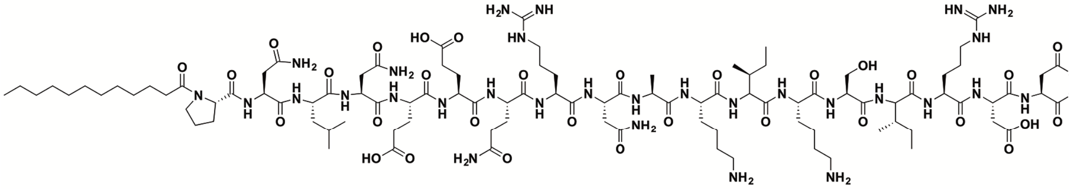

C16-PNLNEEQRNAKIKSIRDD (C16-Helix2)

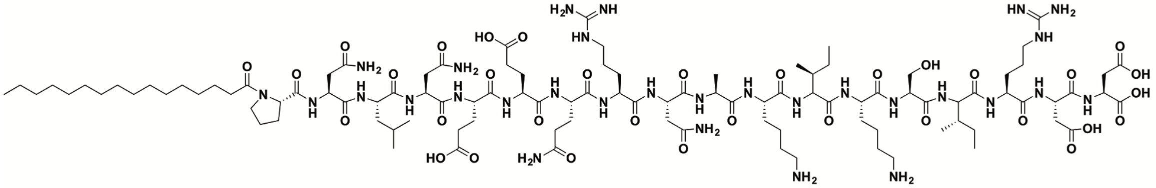

2C8-KPNLNEEQRNAKIKSIRDD (2C8-Helix2)

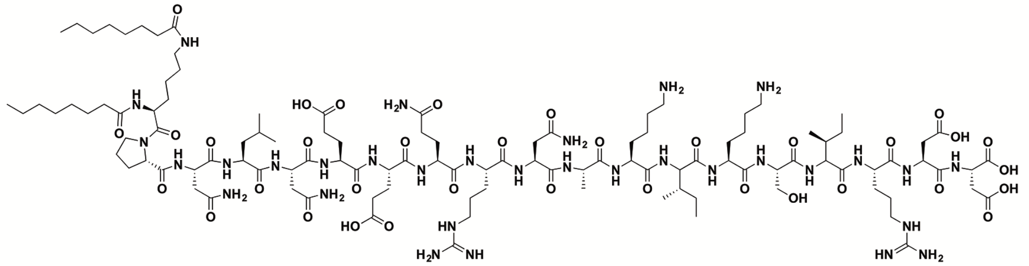

2C12-KPNLNEEQRNAKIKSIRDD (2C12-Helix2)

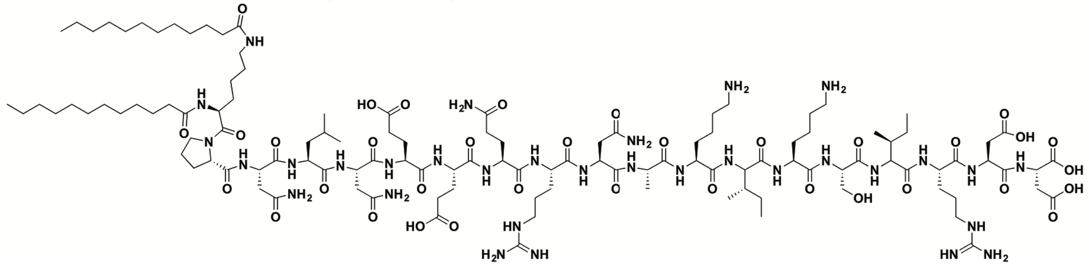

Figure 2-14. Chemical structures of C8-Helix2, C12-Helix2, C16-Helix2, 2C8-Helix2, and 2C12-Helix2.

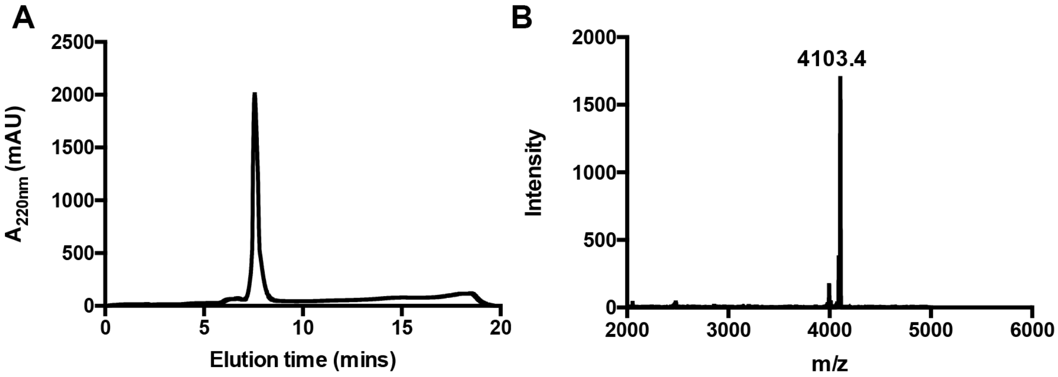

Figure 2-15. RP-HPLC (**A**) and MALDI-TOF MS (**B**) characterization of Z33. The RP-HPLC spectrum confirms the purity of the product (>99%). The expected mass is 4102.0. The peak at 4103.4 corresponds to $[M+H]^+$.

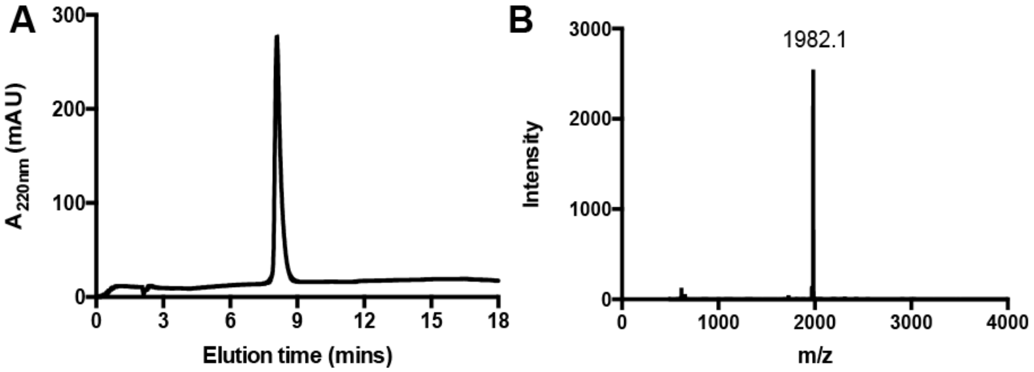

Figure 2-16. RP-HPLC (**A**) and MALDI-TOF MS (**B**) characterization of Helix 1. The RP-HPLC spectrum confirms the purity of the product (>99%). The expected mass is 1980.9. The peak at 1982.1 corresponds to $[M+H]^+$.

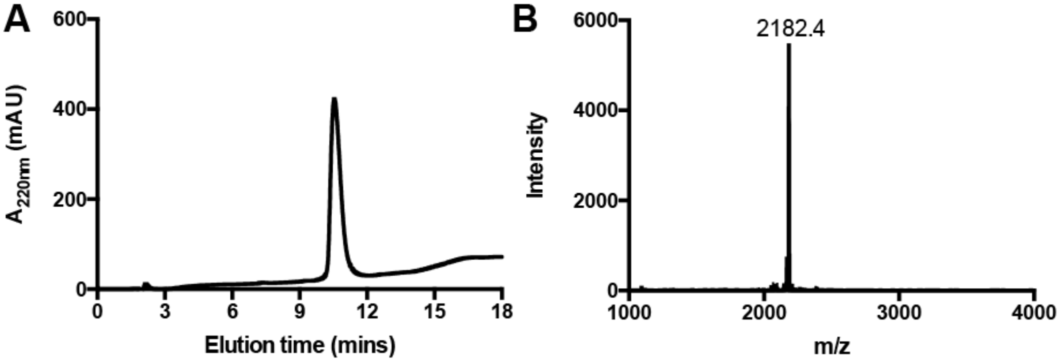

Figure 2-17. RP-HPLC (**A**) and MALDI-TOF MS (**B**) characterization of Helix 2. The RP-HPLC spectrum confirms the purity of the product (>99%). The expected mass is 2181.3. The peak at 2182.4 corresponds to $[M+H]^+$.

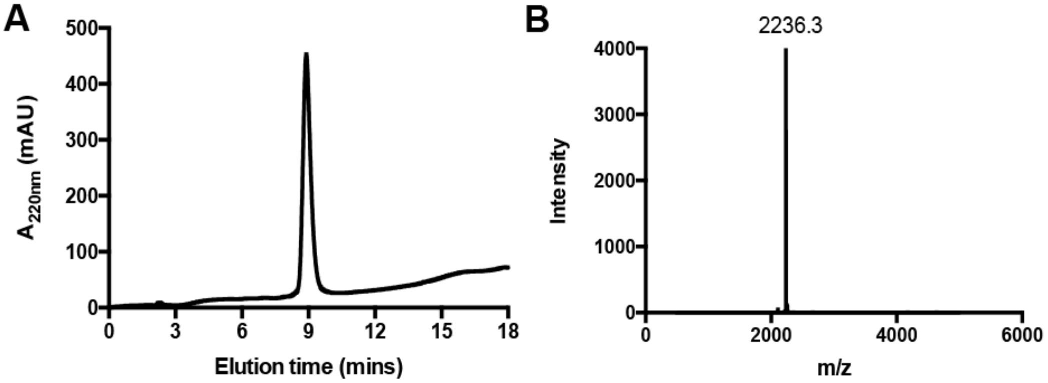

Figure 2-18. RP-HPLC (**A**) and MALDI-TOF MS (**B**) characterization of Helix1-C8. The RP-HPLC spectrum confirms the purity of the product (>99%). The expected mass is 2235.1. The peak at 2236.3 corresponds to $[M+H]^+$.

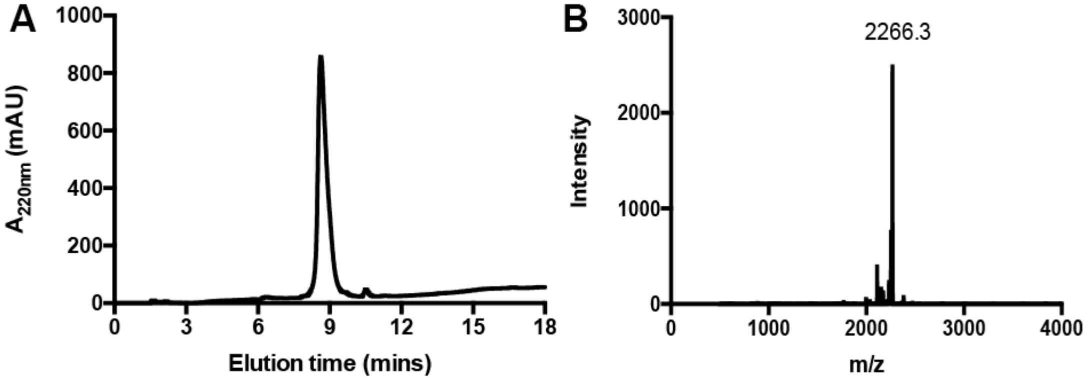

Figure 2-19. RP-HPLC (**A**) and MALDI-TOF MS (**B**) characterization of C8-Helix2. The RP-HPLC spectrum confirms the purity of the product (>99%). The expected mass is 2265.2. The peak at 2266.3 corresponds to $[M+H]^+$.

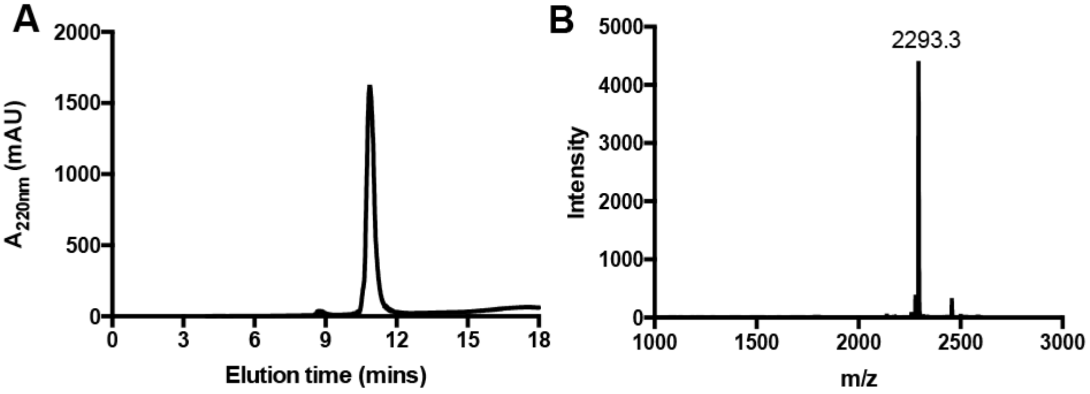

Figure 2-20. RP-HPLC (**A**) and MALDI-TOF MS (**B**) characterization of Helix1-C12. The RP-HPLC spectrum confirms the purity of the product (>99%). The expected mass is 2292.2. The peak at 2293.3 corresponds to $[M+H]^+$.

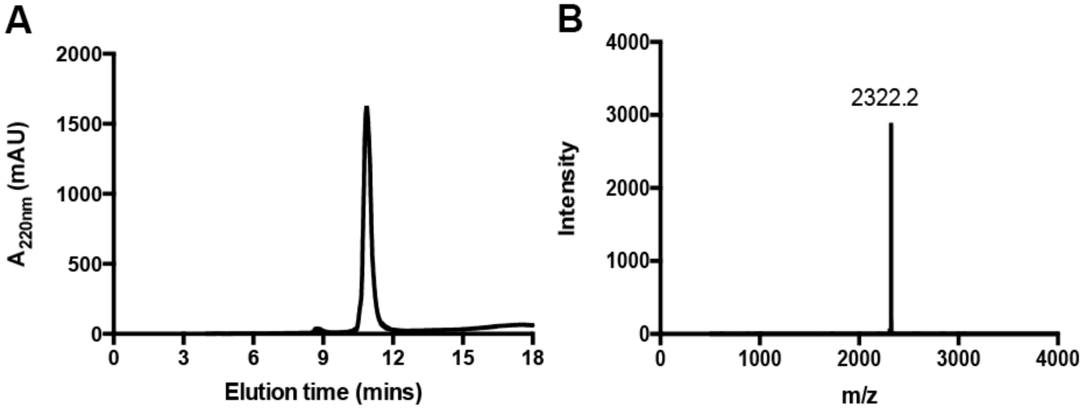

Figure 2-21. RP-HPLC (**A**) and MALDI-TOF MS (**B**) characterization of C12-Helix2. The RP-HPLC spectrum confirms the purity of the product (>99%). The expected mass is 2321.2. The peak at 2322.2 corresponds to $[M+H]^+$.

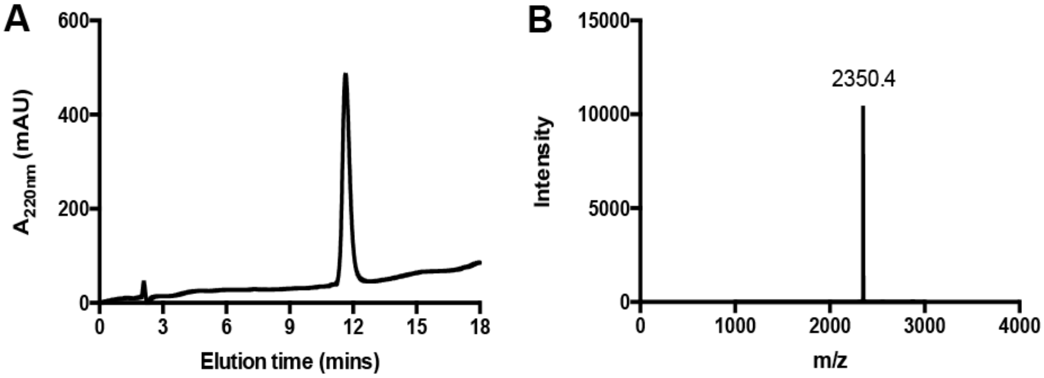

Figure 2-22. RP-HPLC (**A**) and MALDI-TOF MS (**B**) characterization of Helix1-C16. The RP-HPLC spectrum confirms the purity of the product (>99%). The expected mass is 2248.8. The peak at 2350.4 corresponds to $[M+H]^+$.

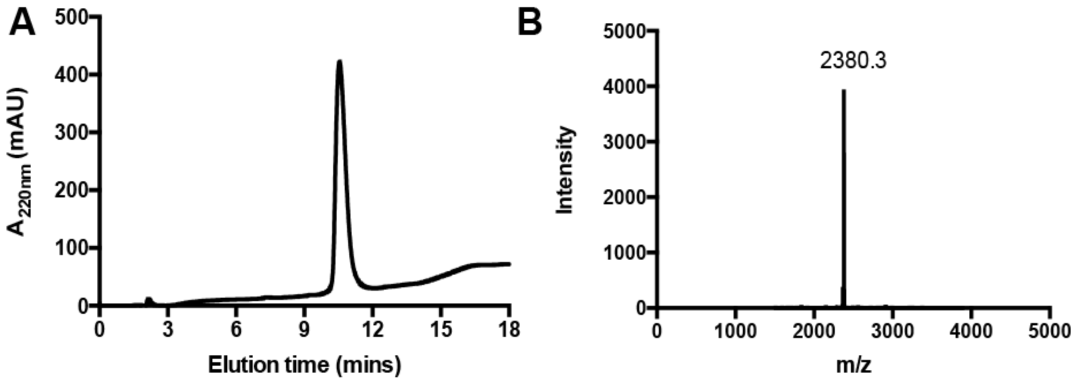

Figure 2-23. RP-HPLC (**A**) and MALDI-TOF MS (**B**) characterization of C16-Helix2. The RP-HPLC spectrum confirms the purity of the product (>99%). The expected mass is 2378.7. The peak at 2380.3 corresponds to $[M+H]^+$.

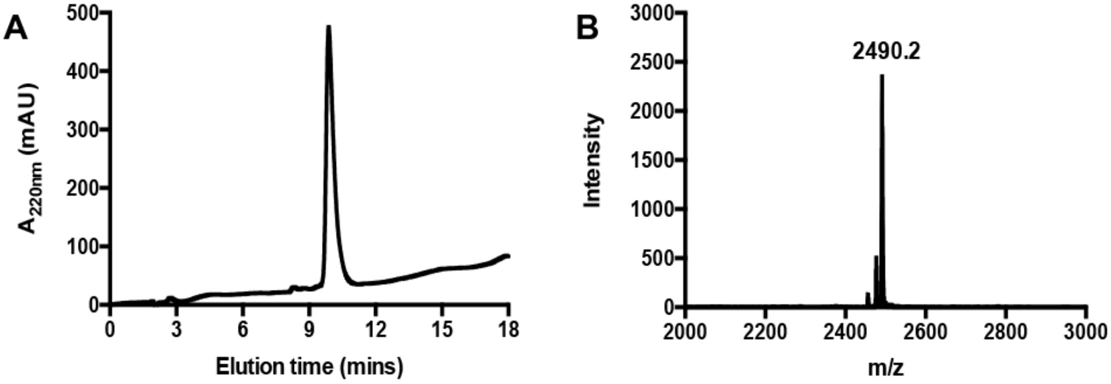

Figure 2-24. RP-HPLC (**A**) and MALDI-TOF MS (**B**) characterization of Helix1-2C8. The RP-HPLC spectrum confirms the purity of the product (>99%). The expected mass is 2489.3. The peak at 2490.2 corresponds to $[M+H]^+$.

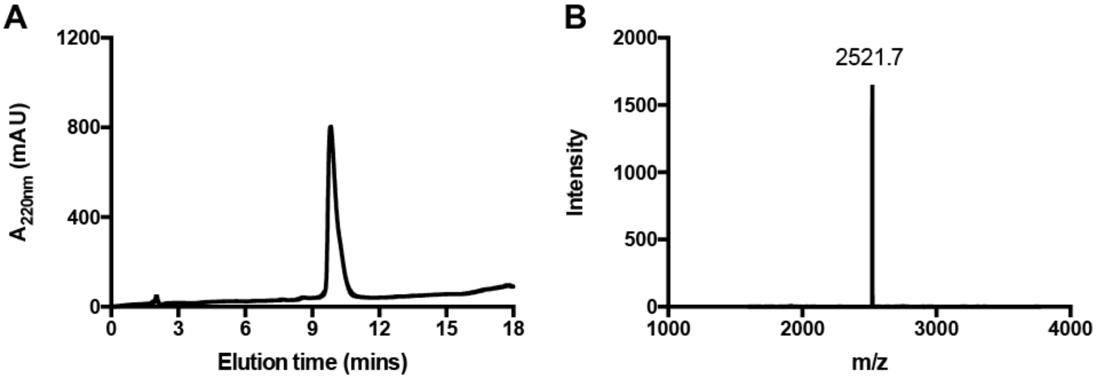

Figure 2-25. RP-HPLC (**A**) and MALDI-TOF MS (**B**) characterization of 2C8-Helix2. The RP-HPLC spectrum confirms the purity of the product (>99%). The expected mass is 2520.9. The peak at 2521.7 corresponds to $[M+H]^+$.

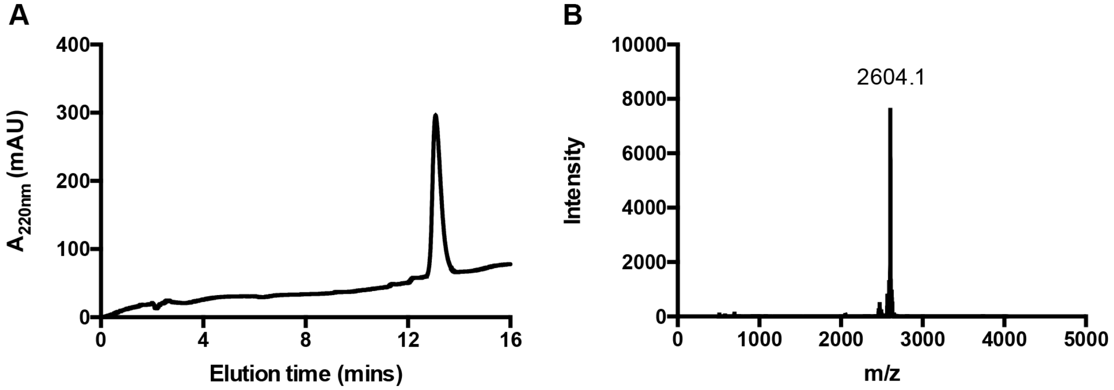

Figure 2-26. RP-HPLC (**A**) and MALDI-TOF MS (**B**) characterization of Helix1-2C12. The RP-HPLC spectrum confirms the purity of the product (>99%). The expected mass is 2603.2. The peak at 2604.1 corresponds to $[M+H]^+$.

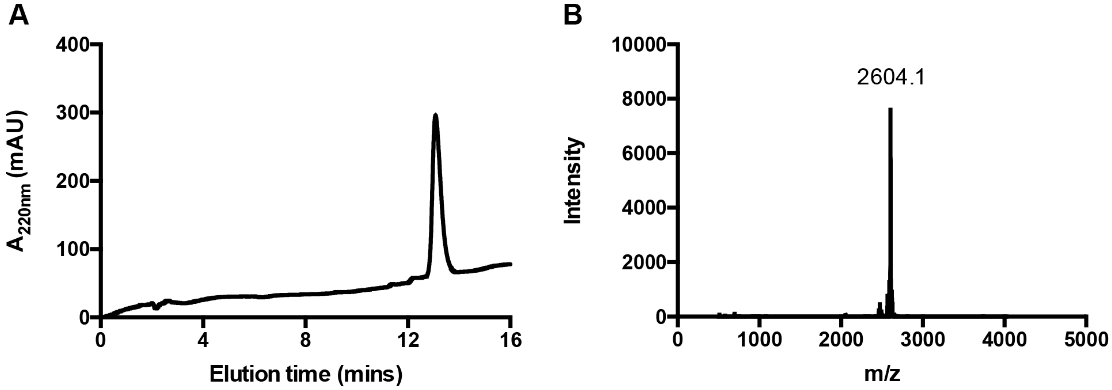

Figure 2-27. RP-HPLC (**A**) and MALDI-TOF MS (**B**) characterization of Helix1-2C12. The RP-HPLC spectrum confirms the purity of the product (>99%). The expected mass is 2603.2. The peak at 2604.1 corresponds to $[M+H]^+$.

2.5 Conclusion

In summary, two series of Z33-based immuno-amphiphiles were successfully designed and synthesized. I found that the way of peptide alkylation can have a significant impact on the self-assembly behavior of the resultant conjugates, leading to variations in CMCs, assembled morphology, and most notably the peptide conformation. These results clearly demonstrate that although both single-chain and double-chain alkylation can promote the formation of supramolecular filaments. For single-chain alkylation, self-assembled IAs with longer alkyl chains likely induce a tighter packing between adjacent molecules, thus promoting the formation of β-sheet assemblies. Importantly, I found short double-chain alkylation could effectively preserve the α-helical conformation, although increasing the length of double chains may lead to the recurrence of β-sheets. Compared to the single-chain alkylation, the double-chain alkylation could likely introduce more steric hindrance and provide more volume for loose packing that favor the presentation of helical conformation. Clearly, there are many variation factors related to the exact sequences of each conjugated peptides, my studies show important guiding principles in the design of supramolecular filaments containing α-helical peptides. Longer single alkyl chains favor the formation of β-sheets, while short double-chain alkylation promotes the preservation of α-helical secondary structures. I believe that this strategy of tuning the length and number of alkyl chains can be further developed and applied in various peptide-based self-assembling systems to obtain the desired conformation in a simple yet effective way. It has been well-known that many systems based on helices can be used as responsive biomaterials triggered by various stimuli to act in biomedical, gelation, and bio-sensing applications.[51] Although the peptide sequences I chose to study here are not directly related to drug delivery or tissue engineering, the conclusion derived from my studies, in my opinion, can be extended to peptides implicated in tumor targeting and stem cell stimulations. This strategy can also be applied in the incorporation of collagen-like triple helices into filamentous assemblies for cellular applications and tissue engineering.[247-248] Another perspective practice may rely on the presentation of helical antimicrobial peptides as anti-infective agent in filamentous networks for cell culture, biomedical, and immune applications.[249]

3 Bioinspired Supramolecular Engineering of Self-Assembling Immunofibers for High Affinity Binding of Immunoglobulin G[d]

3.1 Overview

Many one-dimensional (1D) nanostructures are constructed by self-assembly of peptides or peptide conjugates containing a short β-sheet sequence as the core building motif essential for the intermolecular hydrogen bonding that promotes directional, anisotropic growth of the resultant assemblies. While this molecular engineering strategy has led to the successful production of a plethora of bioactive filamentous β-sheet assemblies for interfacing with biomolecules and cells, concerns associated with effective presentation of α-helical epitopes and their function preservation have yet to be resolved. In this context, I report on the direct conjugation of the protein A mimicking peptide Z33, a motif containing two α-helices, to linear hydrocarbons to create self-assembling immuno-amphiphiles (IAs). The results suggest that the resulting amphiphilic peptides can, despite lacking the essential β-sheet segment, effectively associate under physiological conditions into supramolecular immunofibers (IFs) while preserving their native α-helical

---

[d] Reprinted with permission from Li, Y.; Lock, L. L.; Wang, Y.; Ou, B.; Stern, D.; Schön, A.; Freire, E.; Xu, X.; Li, Z. J.; Ghose, S.; Cui, H. Bioinspired Supramolecular Engineering of Self-Assembling Immunofibers for High Affinity Binding of Immunoglobulin G, ***Biomaterials***, **2018**, 178, 448-457. Copyright © 2018 Elsevier Ltd.

conformation. Isothermal titration calorimetry (ITC) measurements confirmed that these self-assembling immunofibers can bind to the human immunoglobulin G class 1 (IgG1) with high specificity at pH 7.4, but with significantly weakened binding at pH 2.8. I further demonstrated the accessibility of Z33 ligand in the immunofibers using transmission electron microscopy (TEM) and confocal imaging. I believe these results shed important light into the supramolecular engineering of α-helical peptides into filamentous assemblies that may possess an important potential for antibody isolation.

3.2 Introduction

Supramolecular 1D nanostructures can be formed either by self-assembly of low molecular weight surfactants[250] or amphiphilic block copolymers[251-252] as a result of minimizing system free energy to assume a spontaneous interfacial curvature, or by self-assembly of synthetic or naturally occurring peptides and their derivatives via directional, intermolecular hydrogen bonding.[44, 220, 253-257] Given the inherent biodegradability and the potential bioactive feature, peptide-based 1D assemblies have been widely explored over the past three decades for their potential biomedical applications in regenerative medicine,[22, 41, 44, 258-259] drug delivery,[220, 260-267] immunotherapy,[26, 174, 268] and disease diagnostics.[180, 269-271] In order to effectively modulate the assembly behavior and to enhance the bioactive features, a hydrophobic auxiliary segment has been often placed on either the *N*- or *C*- terminus of the intended peptide sequence. The conjugation strategy has been pioneered and developed by a number of research laboratories.[31, 186, 220, 254, 272-276] For instance, the Stupp laboratory has molecularly crafted a class of peptide amphiphiles (PAs) by conjugating linear hydrocarbons onto a *β*-sheet-forming sequence that could self-assemble into supramolecular nanofibers under the physiological conditions.[31, 41, 44, 182-185] To impart the PA assemblies with the desired bioactivities to interface with biology, a variety of bioactive epitopes, such as cell adhesion motif RGD, have been incorporated into the molecular design.[31, 41, 182-183, 186] In one example, Webber *et al.* investigated bioactive PA nanofibers displaying the RGDS epitope on the surface for therapeutic delivery of bone-marrow mononuclear cells (BMNCs), implying an enhanced biological adhesion.[41] In an effort to modulate immunogenicity of peptide assemblies, Collier and coworkers covalently linked the self-assembling peptide Q11 to an antigen OVA peptide and found that the resultant supramolecular OVA-Q11 nanofibers possess enhanced immunogenicity.[174] This direct placement of bioactive peptide on either *C*- or *N*- terminus of a self-assembling peptide motif has become a popular strategy to create bioactive materials for a specific biomedical application. In the cases where the epitope has to retain an *α*-helical conformation to be bioactive, adjusting hydrophobic segments[277-278] and tuning solvent property[193] are often adopted to solve the potential spacing incompatibility issue of presenting an *α*-helical motif on *β*-sheet assemblies.

High affinity antibody-binding particles and materials are receiving rapidly growing interest in the pharmaceutical industry, as driven by the increasing demand of monoclonal antibodies for biological therapeutics.[1, 279-280] Protein A, a well-known antibody-binding ligand, has the capacity of specific binding to the Fc-portion of IgG from most mammalian species, including human.[212-213] However, the large size of protein A limits its industrial application, and as such a number of synthetic and minimized domains of protein A have been designed and studied.[214-216] The Z-domain of protein A is the first and most famous synthetic domain with 59 amino acid residues and a dissociation constant (K_d) of ~10 nM when bound to human IgG1.[217-219] To further minimize the Z-domain of protein A, a two-helix derivative Z33 was designed without significantly changing the binding affinity (K_d = 43 nM).[214] While various high affinity ligands have been identified, the way to present ligands on a desired substrate is equally essential for ligand-protein interactions. In this context, I report on the direct conjugation of the protein A mimicking peptide Z33, a motif containing two α-helices, to linear hydrocarbons to create self-assembling IAs and demonstrate for the first time that the resultant supramolecular immunofibers possess high binding affinity to human IgG1. Similar to protein A, the chosen Z33 sequence is capable of recognizing various members of the human immunoglobulin family. But given that the modern bioprocessing technology has enabled the production of one particular type of immunoglobulins, I focus my studies only on the specific interactions between Z33 conjugates and human IgG1. A variety of techniques were utilized to characterize the self-assembly and binding properties of the self-assembled IFs to human IgG1, and I envision the promising prospects of these biomaterials would enable their potential use for affinity precipitation and purification of monoclonal antibodies.

3.3 Experimental Procedures

3.3.1 Materials and Molecular Synthesis

All Fmoc amino acids and resins were obtained from Advanced Automated Peptide Protein Technologies (Louisville, KY). Fmoc-Lys(Fmoc) were purchased from Novabiochem (San Diego, CA). The therapeutic human IgG1 was obtained from Bristol-Myers Squibb (Devens, MA), and IgG elution buffer was sourced from Thermo Fisher Scientific (Rockford, IL). FITC-IgG was purchased from Sigma-Aldrich (St. Louis, MO) and human IgG-coated gold nanoparticles were purchased from Nanocs Inc. (New York, NY). All other reagents were obtained from VWR (Radnor, PA) and used as received without further purification.

All immuno-amphiphiles were synthesized via direct conjugation of alkyl chains to the *N*-terminus of a peptide sequence. In brief, Z33 peptide was first synthesized on the Focus XC automatic peptide synthesizer (AAPPTEC, Louisville, KY) using standard 9-fluorenylmethoxycarbonyl (Fmoc) solid phase synthesis protocols. Fmoc deprotections were performed using a 20% 4-methylpiperidine in DMF solution for 10 minutes, repeated once. For the synthesis of 2C8-Z33, a bis Fmoc protected lysine was added to the *N*-terminus of Z33. For the synthesis of RB-C12-Z33, Fmoc-Lys-methylthiotetrazole (Kmtt) was added to the *N*-terminus of Z33 for selective deprotection. Rhodamine B was conjugated to the side chain of Kmtt after deprotection of the mtt group (TFA/TIS/DCM in a ratio of 3:5:92). C12 (or 2C8) alkyl chain was then manually coupled at the *N*-terminus (after Fmoc removal) of Z33 peptide with lauric acid (or octanoic acid)/HBTU/DIEA at a ratio of 4 (or 8): 4: 6 relative to the Z33 peptide, and shook overnight at room temperature. In all cases, reactions were tested using the ninhydrin test (Anaspec Inc., Fremont, CA) for free amines. Completed IAs were cleaved from the solid support using a mixture of TFA/TIS/H2O in a ratio of 92.5:5:2.5 for 2.5 hours. Excess TFA was removed by evaporation and ice-cold diethyl ether was added to precipitate the crude product. The precipitated IAs were collected by centrifugation and then washed 2 more times with diethyl ether and centrifuged to remove the remaining solvent.

The IAs were purified by preparative RP-HPLC using a Varian Polymeric Column (PLRP-S, 100 Å, 10 μm, 150 × 25 mm) at 25 °C on a Varian ProStar Model 325 preparative HPLC (Agilent Technologies, Santa Clara, CA) monitored at 220 nm for the absorbance of peptide segments. Collected fractions were analyzed by MALDI-ToF (BrukerAutoflex III MALDI-ToF instrument, Billerica, MA) and product-containing fractions were then lyophilized (FreeZone -105 °C 4.5 L freeze dryer, Labconco, Kansas City, MO) and stored at -30°C.

3.3.2 Self-Assembly of IAs and TEM Imaging

IAs were pretreated with hexafluoroisopropanol (HFIP) to remove the preformed nanostructures during the purification process. After the removal of HFIP via evaporation by air, IAs were dissolved in phosphate-buffered saline (PBS) at 1 mM and aged overnight at room temperature; 10 μL of 10 fold diluted sample was spotted on a copper grid covered with carbon film (Electron Microscopy Sciences, Hatfield, PA), and negatively stained using 2% uranyl acetate for 30 seconds. All samples were dried for at least 3 hours before TEM imaging on an FEI Tecnai 12 TWIN electron microscope.

3.3.3 Circular Dichroism (CD) Spectroscopy

IAs and Z33 peptide samples were instantly diluted from the 1 mM stock solution to 100 μM in PBS prior to the CD experiment conducted on a Jasco J-710 spectropolarimeter (JASCO, Easton, MD) at 25°C. The samples were loaded into a 1 mm path length quartz UV-Vis absorption cell (ThermoFisher Scientific, Pittsburgh, PA) and the spectra were collected from 190 nm to 280 nm as the average of three scans. A background spectrum of the solvent was acquired and subtracted from the sample spectrum and the signal was converted from ellipticity (mdeg) to mean molar ellipticity ($\mathrm{deg \cdot cm^2 \cdot dmol^{-1}}$).

3.3.4 ITC Experiment

ITC experiments were performed using a high precision VP-ITC titration calorimetric system (Microcal Inc.). The human IgG1 solution was titrated with immuno-amphiphiles in PBS (pH 7.4) or IgG elution buffer (pH 2.8) at 15°C. The IgG1 concentration was calculated using the mass extinction coefficient of 1.4 at 280 nm for a 0.1% (1 mg/mL) IgG solution. The concentration of immuno-amphiphles was determined by total nitrogen assay.[281] The heat evolved after each injection was obtained from the integral of the calorimetric signal. The heat associated with the binding of immuno-amphiphiles to IgG1 was obtained by subtracting the heat of dilution. Analysis of the data was performed using MicroCal Origin package.

3.3.5 Confocal Imaging

The fluorescence of Rhodamine B labelled C12-Z33 (RB-C12-Z33) and FITC-IgG was imaged using a confocal laser scanning microscope (CLSM, LSM 510, Zeiss). 1 mM RB-C12-Z33 stock solution was prepared in PBS and aged overnight. 100 μM RB-C12-Z33 and 2 μM FITC-IgG were premixed in PBS and spotted on a microscope slide and covered by a coverslip. Red channel and green channel were used to record the fluorescence from RB-C12-Z33 and FITC-IgG, respectively. All fluorescence images were taken under identical conditions.

3.4 Results and Discussions

3.4.1 Molecular Design

The IgG binding IAs studied here are designed to include the overall hydrophilic Z33 peptide sequence (FNMQQQRRFYEALHDPNLNEEQRNAKIKSIRDD) and one or two hydrophobic alkyl chains. The Z33 peptide is a two-helix derivative from protein A (**Figure 3-1 A**) that specifically binds to the Fc-portion of human IgG1 with a high binding affinity (K_d=43 nM).[215, 282-283] Two IAs, C12-Z33 and 2C8-Z33 (**Figure 3-1 B**), were synthesized via direct conjugation of lauric acid (C12) or two octanoic acids (2C8) onto the *N*-terminus of Z33 peptide. The Region 2 (*β*-sheet forming segment) in typical PA structures was not included in the molecular design due to the intention of preserving the *α*-helical conformation of Z33 peptide. Benefited by the high water solubility of Z33 peptide, Region 3 (charged group) was not included either. As shown in **Figure 3-1 C**, these designed IAs were expected to self-assemble in aqueous solutions into supramolecular IFs of high binding affinity to IgGs. I also synthesized the free Z33 peptide as the positive control molecule for comparison with the Z33 containing IFs. Another negative control molecule, C12-SZ33, was designed by conjugating C12 onto the *N*-terminus of Z33 with a scrambled Z33 sequence. All the molecules were synthesized and purified using automated solid-phase peptide synthesis (SPPS) methods and RP-HPLC. The purity and expected molecular masses of the synthesized compounds were confirmed using analytical HPLC and mass spectrometry, respectively. Details for chemical structures and molecular characterization are shown in **Figure 3-2** to **Figure 3-6**.

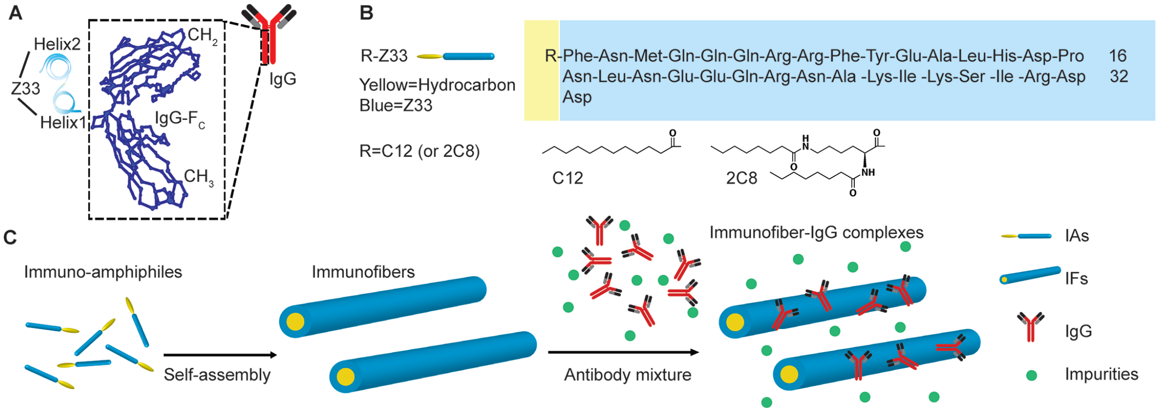

Figure 3-1. (**A**) Schematic illustration of the Z33 peptide binding to Fc-portion of human IgG1. (**B**) The sequences of C12-Z33 and 2C8-Z33. Alkyl groups and Z33 are indicated with the yellow and blue shaded areas, respectively. (**C**) Schematic illustration of the self-assembly of IAs and the binding between IFs and IgG.

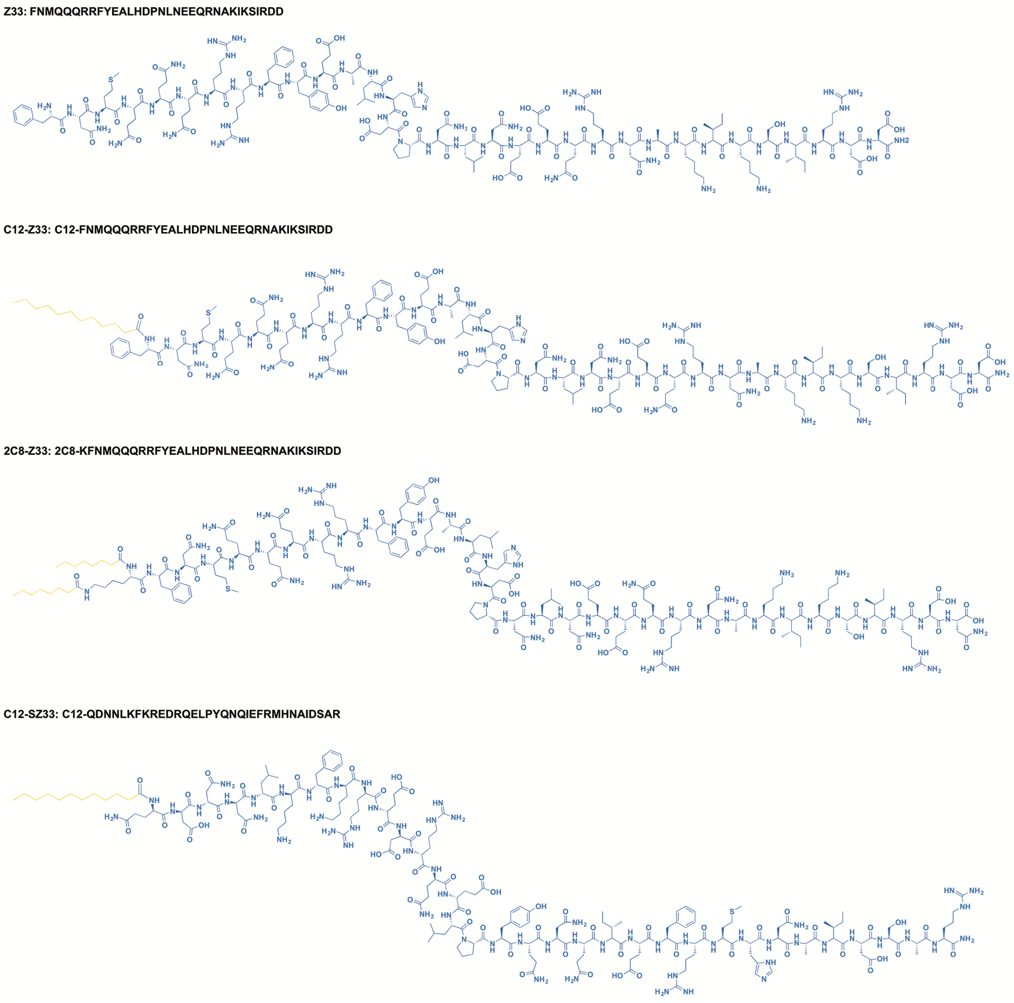

Z33: FNMQQQRRFYEALHDPNLNEEQRNAKIKSIRDD

C12-Z33: C12-FNMQQQRRFYEALHDPNLNEEQRNAKIKSIRDD

2C8-Z33: 2C8-KFNMQQQRRFYEALHDPNLNEEQRNAKIKSIRDD

C12-SZ33: C12-QDNNLKFKREDRQELPYQNQIEFRMHNAIDSAR

Figure 3-2. Chemical structures of Z33, C12-Z33, 2C8-Z33, and C12-SZ33. The peptide and alkyl chain are shown in blue and yellow, respectively.

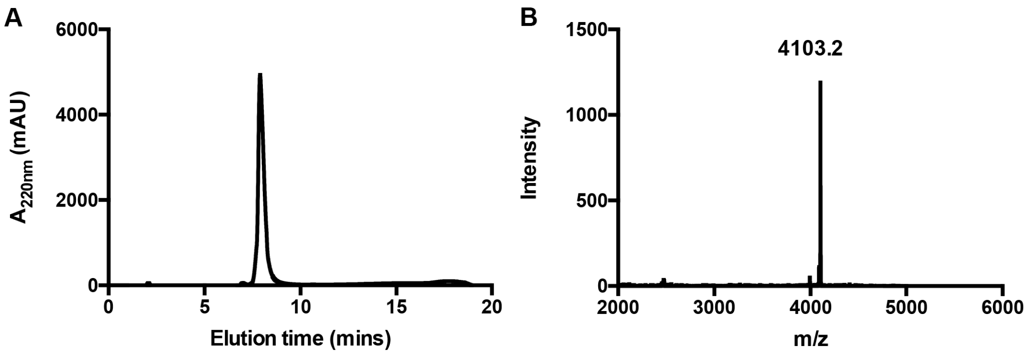

Figure 3-3. RP-HPLC (**A**) and MALDI-TOF MS (**B**) characterization of Z33. The RP-HPLC spectrum confirms the purity of the product (>99%). The expected mass is 4102.0. The peak at 4103.2 corresponds to $[M+H]^+$.

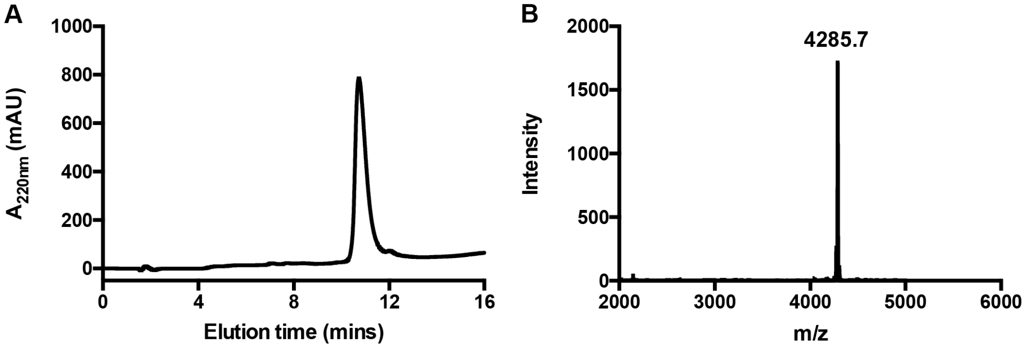

Figure 3-4. RP-HPLC (**A**) and MALDI-TOF MS (**B**) characterization of C12-Z33. The RP-HPLC spectrum confirms the purity of the product (>99%). The expected mass is 4284.2. The peak at 4285.7 corresponds to $[M+H]^+$.

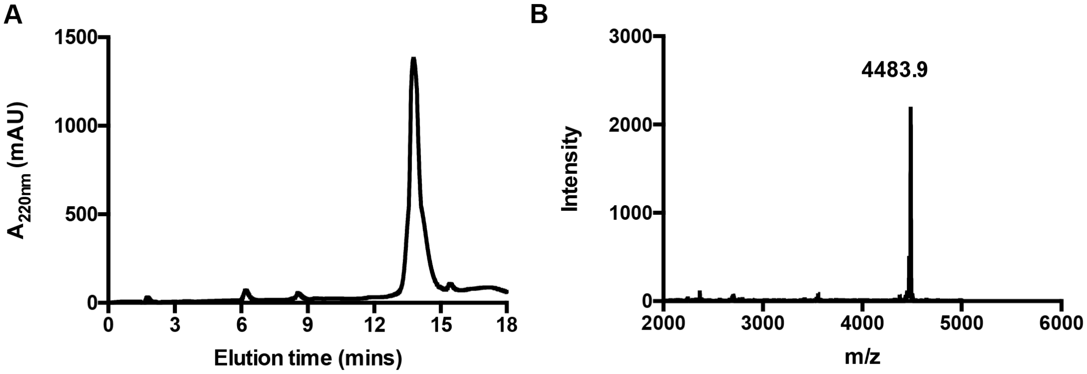

Figure 3-5. RP-HPLC (**A**) and MALDI-TOF MS (**B**) characterization of 2C8-Z33. The RP-HPLC spectrum confirms the purity of the product (>99%). The expected mass is 4482.3. The peak at 4483.9 corresponds to $[M+H]^+$.

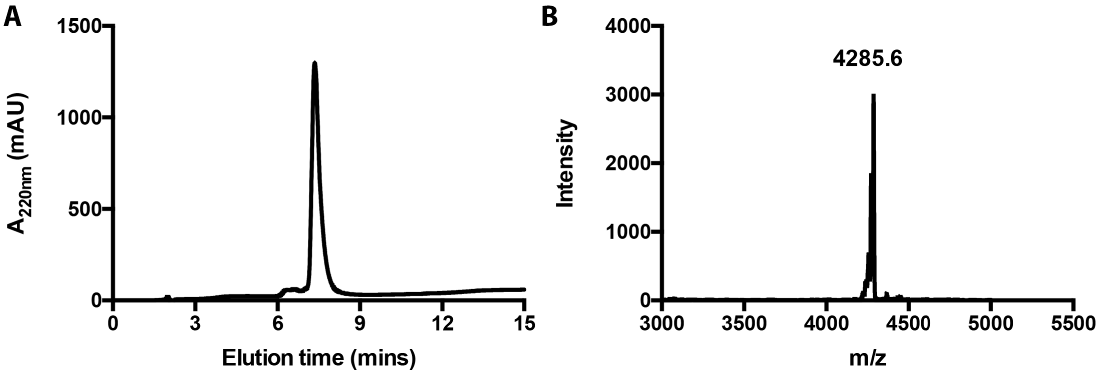

Figure 3-6. RP-HPLC (**A**) and MALDI-TOF MS (**B**) characterization of C12-SZ33. The RP-HPLC spectrum confirms the purity of the product (>99%). The expected mass is 4284.2. The peak at 4285.6 corresponds to $[M+H]^+$.

3.4.2 Molecular Assembly and Characterization

The self-assembly of the designed IAs was conducted in a two-step procedure. The IAs were first pretreated with HFIP to eliminate any pre-existing nanostructures that may affect its solubility and complicate the self-assembly processes. After HFIP removal, PBS was added to reach a final concentration of 1 mM. Given the amphiphilic nature of the molecular design, it is expected that the alkyl segments are embedded within the core of the IFs while the bioactive Z33 sequences are displayed on the surface. After aging overnight at room temperature, TEM and CD were utilized to characterize the morphology of the resultant supramolecular nanostructures.

Given the vital role of solution pH in the current IgG purification method, I evaluated the self-assembly behavior of C12-Z33 at both binding and elution conditions. Physiological pH (~7.4) is normally used as the binding condition, while acidic pH (~2.8) is to elute antibodies from the protein A affinity column.[284-285] As such, PBS (pH 7.4) and

IgG elution buffer (pH 2.8) were chosen as the aqueous environment to promote the self-assembly of C12-Z33. The morphologies of C12-Z33 IFs at different pH were studied by regular TEM (**Figure 3-7 A-D**). It was found that the C12-Z33 molecule could self-assemble into filaments under both conditions. Representative TEM images from a solution of 100 μM C12-Z33 revealed that C12-Z33 self-assembled into filamentous structures with a diameter of 16.0 ± 1.7 nm, a value that is significantly smaller than the fully extended molecular length (~22 nm in the case of β-sheets) but larger than the molecular length if all of the amino acids are forming in helical structures (~12 nm). The observed nanofibers are several micrometers in length.

To further understand the molecular packing within the IFs, CD was used to study the peptide secondary structure (**Figure 3-7 E**). Strong negative signals at ~222 nm (n-π*) and 208 nm (π-π*) are indicative of α-helical secondary structure of Z33 segment in the self-assembled state, as shown in the free Z33 peptide. On the basis of the CD spectra and the measured diameter of IFs, it is reasonable to assume that the peptides maintained their α-helix secondary structure when forming IFs at both pH 7.4 and pH 2.8. The difference in mean molar ellipticity between C12-Z33 and the free Z33 peptide may be a combinative result of peptide alkylation and subsequent molecular assembly into IFs. Tirrell and others have suggested that lipidation of small molecule peptides could enhance the stability of α-helix secondary structures of the conjugated peptides.[225, 254, 273, 286-287]

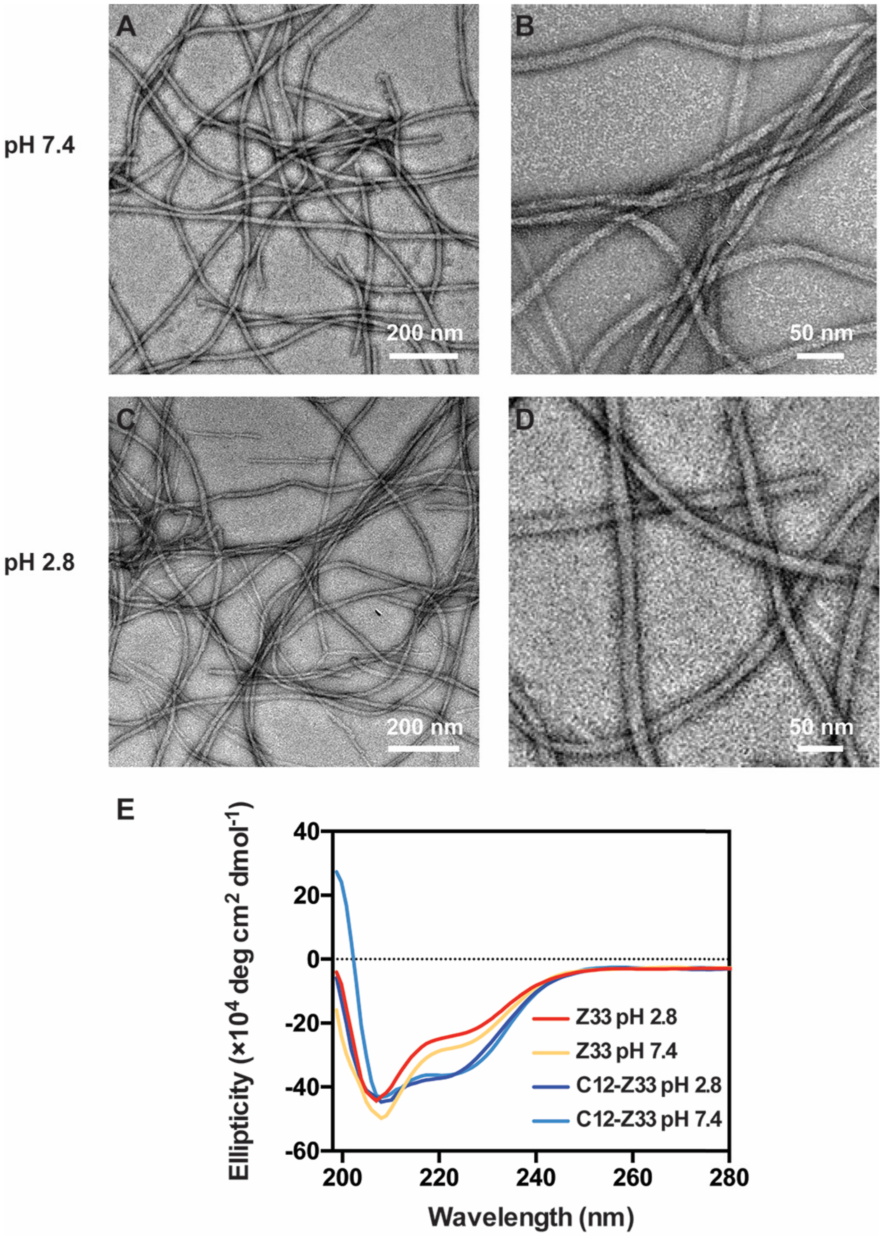

Figure 3-7. Molecular assembly and nanostructure characterization of IAs. TEM characterization of C12-Z33 at pH 7.4 (**A**, **B**) and 2.8 (**C**, **D**). The TEM samples were prepared at concentration of 100 μM in PBS (pH 7.4) and IgG elution buffer (pH 2.8), respectively. The TEM samples were negatively stained with 2 wt% uranyl acetate aqueous solution. (**E**) Normalized CD spectra of Z33 peptide and C12-Z33 at pH 7.4 and 2.8, respectively.

3.4.3 Binding Affinity Measurements

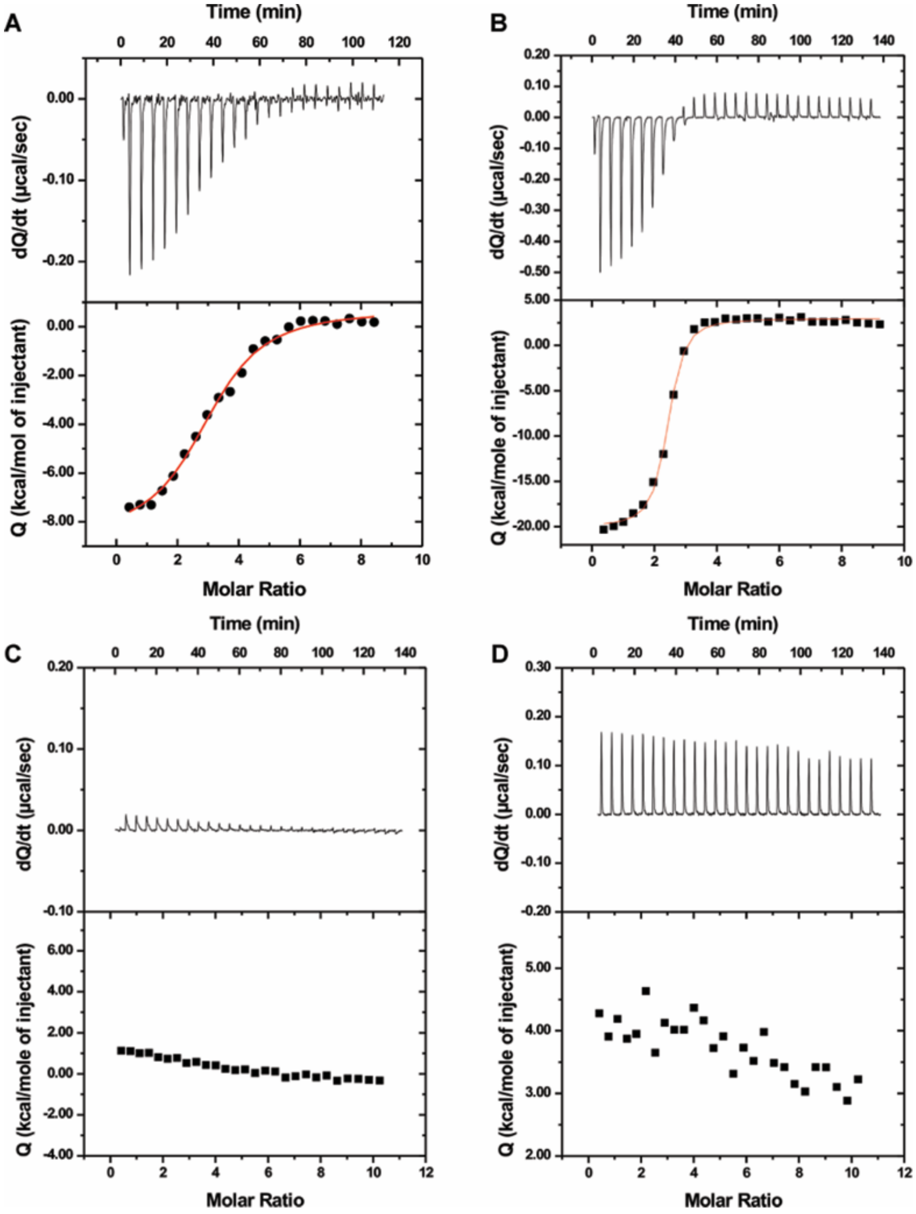

Figure 3-8. ITC profiles and binding curves for the stepwise injection of 100 μM C12-Z33 into a solution of 2 μM IgG1 at 15 °C in (**A**) PBS buffer, pH 7.4, and (**C**) IgG elution buffer, pH 2.8. ITC profiles and binding curves for the stepwise injection of 100 μM (**B**) Z33 and (**D**) C12-SZ33 into 2 μM IgG1 in PBS at 15 °C, pH 7.4.

Table 3-1. Thermodynamic parameters for binding of Z33-based ligands to IgG1 at 15 °C in PBS at pH 7.4. Data are reported per ligand/Z33.

Ligands	$K_{d,Z33}$ (nM)	$\Delta H°$ (kcal·mol^{-1})	N (Ligands/IgG)
Z33	60	-23.1	2.3
C12-Z33	650	-9.3	3.1
2C8-Z33	1115	-2.8	9.1

Table 3-2. Recalculation of the thermodynamic parameters (per IgG1) for binding of Z33-based ligands to IgG1 at 15 °C in PBS at pH 7.4. Please note K_d, the binding affinity constant, differs when the data are normalized according to IgG1.

Ligands	$K_{d,IgG1}$ (nM)	$\Delta G°$ (kcal·mol^{-1})	$\Delta H°$ (kcal·mol^{-1})	$-T\Delta S°$ (kcal·mol^{-1})
Z33	26	-10.0	-53.4	43.4
C12-Z33	209	-8.8	-28.9	20.1
2C8-Z33	122	-9.1	-25.9	16.8

Isothermal titration calorimetry measurement is an effective way to assess the binding affinity between proteins and ligands.[161, 288-291] Given the preservation of the *α*-helical conformation within supramolecular IFs, I expect a high IgG binding ability by C12-Z33 IFs. ITC was then used to investigate thermodynamic properties of their binding to human IgG1. The heat associated with the binding reaction is recorded during the stepwise titrations. The binding thermodynamic parameters including dissociation constant (K_d), molar enthalpy change ($\Delta H°$), and stoichiometry (N), are obtained via data fitting or direct calculations.[288]

In a typical ITC experiment, a solution of 100 μM C12-Z33 in PBS buffer was aged overnight and then titrated into a PBS buffer solution of 2 μM IgG1 at 15 °C, pH 7.4. Representative thermograms and binding isotherms were shown in **Figure 3-8 A** and the thermodynamic parameters reported per ligand are summarized in **Table 3-1**. The ITC results for the binding of C12-Z33 to IgG1 revealed an enthalpy driven binding event characterized by a K_d of 650 nM. To further compare the binding efficiency of C12-Z33, I synthesized the Z33 peptide which was shown to bind tightly to IgG1 with a K_d of 43 nM measured by surface plasmon resonance.[216] The representative thermograms and binding isotherms of the free Z33 peptide to IgG1 were shown in **Figure 3-8 B**. In addition to an approximately 100-fold better affinity, the stoichiometry for Z33 was 2.3, whereas the apparent stoichiometry for C12-Z33 was 3.1 (**Table 3-1**), indicating that not all of the C12-Z33 in IFs were available for binding to the IgG1 molecule.

While normalization per ligand allows for the determination of the apparent stoichiometry of binding, comparison of the thermodynamic parameters should be done after normalization per mole of IgG1, as shown in **Table 3-2**. The binding of Z33 to IgG1 was characterized by a large favorable enthalpy opposed by a large unfavorable entropy change. The thermodynamic signature for the binding of C12-Z33 was similar, although the magnitudes of the enthalpy and entropy changes were smaller. C12-Z33 binds with less unfavorable entropy than Z33; however, the loss in favorable enthalpy is even larger, which results in an overall lower binding affinity. An overall loss in the favorable binding enthalpy could be possibly rooted in the disassembly/disruption of the IFs. There is also a possibility that favorable interactions with IgG1 are limited due to steric restrictions on the closely packed IFs. Stepwise injection of IgG1 with C12-Z33 was also performed in IgG elution buffer (pH 2.8) at 15 °C (**Figure 3-8 C**), revealing a significantly reduced binding affinity suitable for elution from the IFs.

To exclude the non-specific binding between IFs and IgG1, C12-SZ33 with scrambled Z33 peptide sequence was used as negative control. This C12-SZ33 IA shows similar self-assembly properties with β-sheet secondary structures characterized with TEM and CD (**Figure 3-9 A and B**). ITC experiment was carried out by injecting 100 μM C12-SZ33 IAs into 2 μM IgG1 solution at 15 °C in PBS at pH 7.4 to measure their binding ability. The thermograms and binding isotherms in **Figure 3-8 D** show that the scrambled C12-SZ33 lacks the ability to bind with IgG1, suggesting that the binding between C12-Z33 IFs and IgG1 relies on the specific sequence of Z33 peptide.

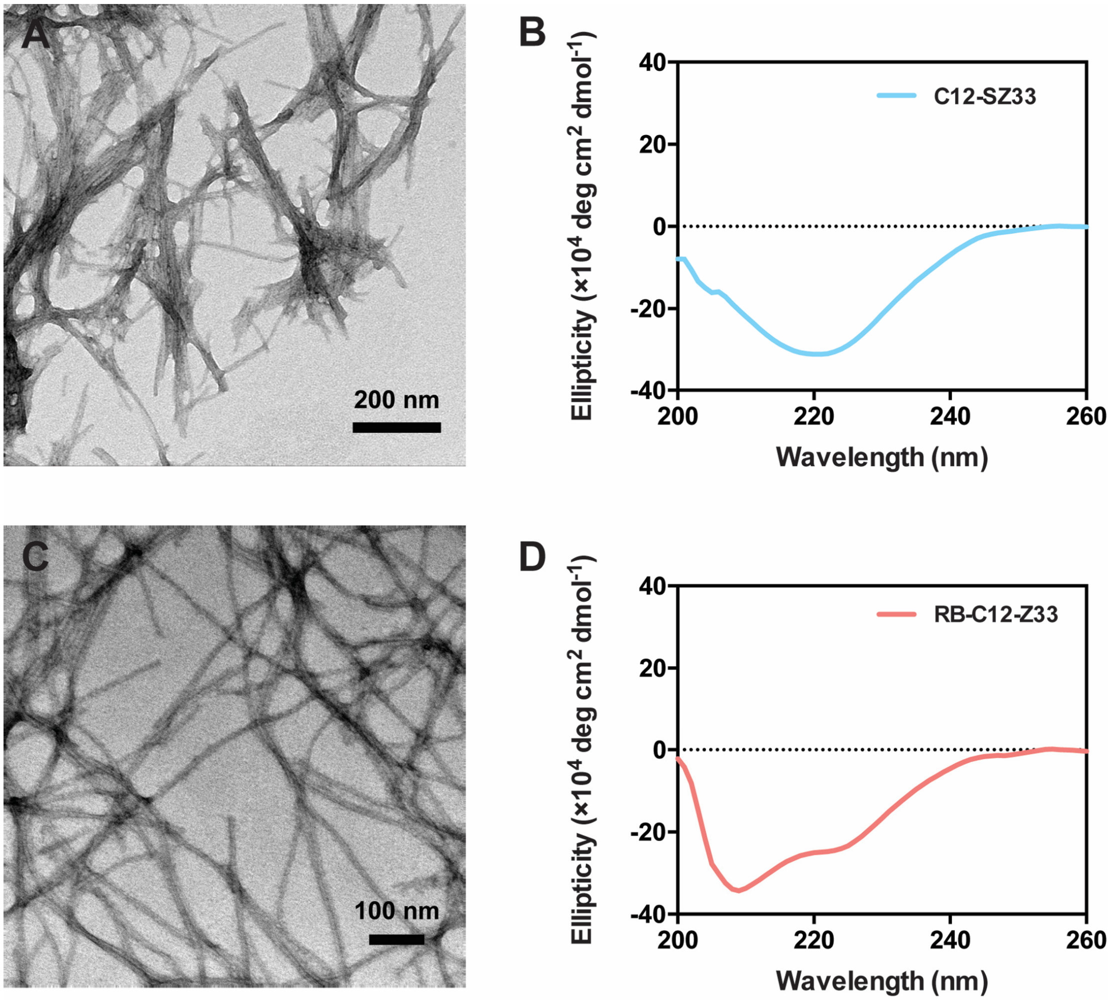

Figure 3-9. TEM images of 100 µM (**A**) C12-SZ33 and (**C**) RB-C12-Z33 in PBS, pH 7.4. Both molecules self-assembled into nanofibers with diameters of 11.5 ± 1.5 nm and 13.8 ± 1.8 nm respectively. Normalized CD spectra of 100 µM (**B**) C12-SZ33 and (**D**) RB-C12-Z33 nanofibers in PBS at pH 7.4 showed *β*-sheet and *α*-helix conformation, respectively.

3.4.4 The Universality of the Functional Design of Supramolecular IFs

To further evaluate the universality of the functional design of supramolecular IFs, I synthesized a double chain alkylated IA 2C8-Z33 (**Figure 3-10 A-E**). Supramolecular IFs of a uniform diameter were also observed in TEM imaging (**Figure 3-10 A and B**), with their *α*-helix secondary structure confirmed by CD (**Figure 3-10 C**). According to the

ITC studies (**Figure 3-10 D and E**, **Table 3-1**), binding between 2C8-Z33 and IgG1 occurred at 15 °C in PBS, pH 7.4, whereas no detectable binding occurred in elution buffer, pH 2.8. The apparent stoichiometry for the binding of 2C8-Z33 at pH 7.4 was 9.1, indicating a further compromised efficiency of binding. Although 2C8-Z33 binds with a less favorable enthalpy of binding than C12-Z33, the contribution from the entropy is less unfavorable, which results in slightly improved binding affinity (**Table 3-2**). These results led to the conclusion that these self-assembled IFs maintain favorable binding ability to IgG1. There is nevertheless a loss in overall binding affinity observed for the IFs, which is of enthalpic origin. The loss in favorable enthalpy can be explained by the loss of interactions due to steric restrictions in the IFs and an unfavorable enthalpy contribution associated with the disassembly process of supramolecular nanostructures.

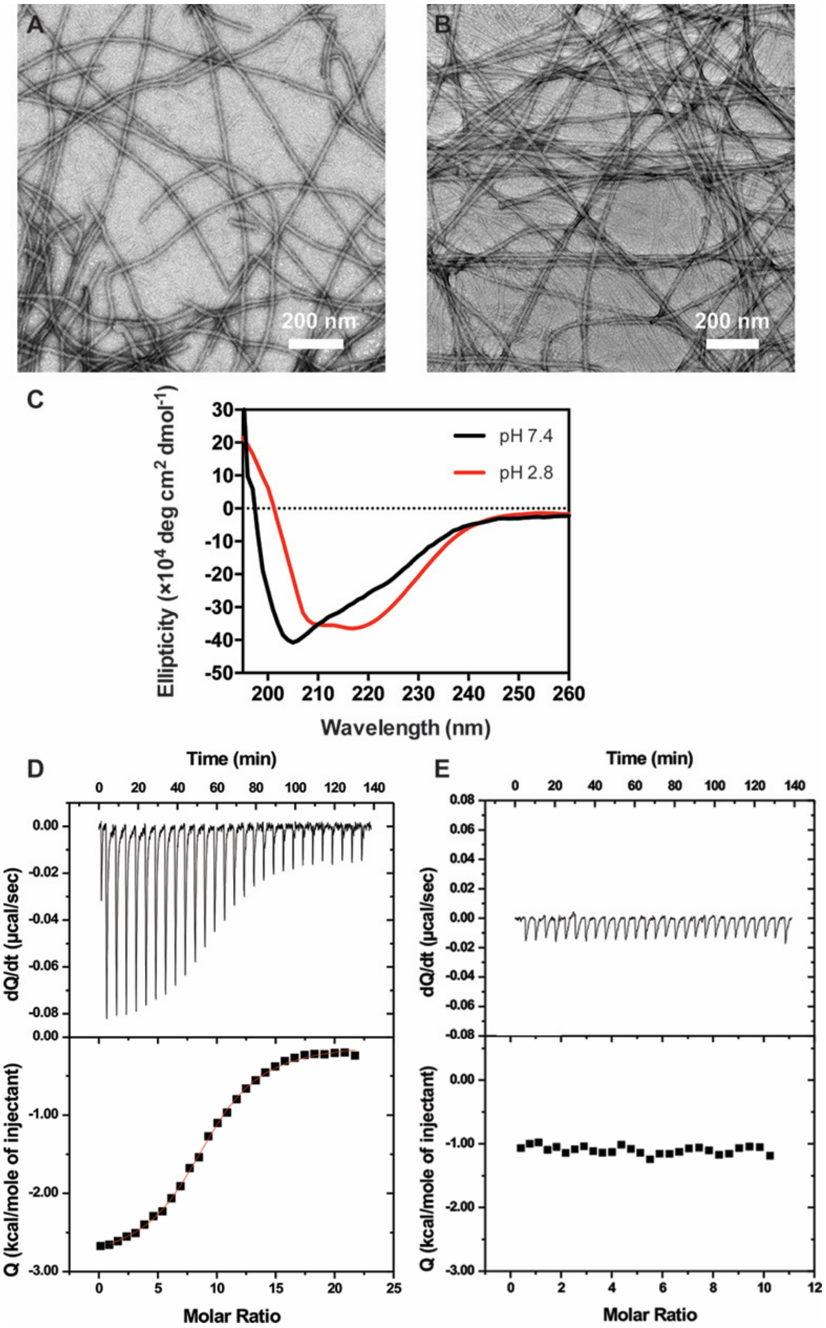

Figure 3-10. TEM characterization of 2C8-Z33 in (**A**) PBS at pH 7.4 with a diameter of 16.8 ± 1.5 nm and (**B**) IgG elution buffer at pH 2.8 with a diameter of 17.3 ± 1.9 nm. The preparation of TEM sample was similar with that of C12-Z33. (**C**) Normalized CD spectra of 100 μM 2C8-Z33 in PBS at pH 7.4 showed α-helix secondary structures. ITC profiles for the stepwise injection of 100 μM 2C8-Z33 into a solution of 2 μM IgG1 in (**D**) PBS buffer, pH 7.4 and (**E**) IgG elution buffer, pH 2.8.

3.4.5 The Direct Visualization of IgG Bound to the Surface of IFs

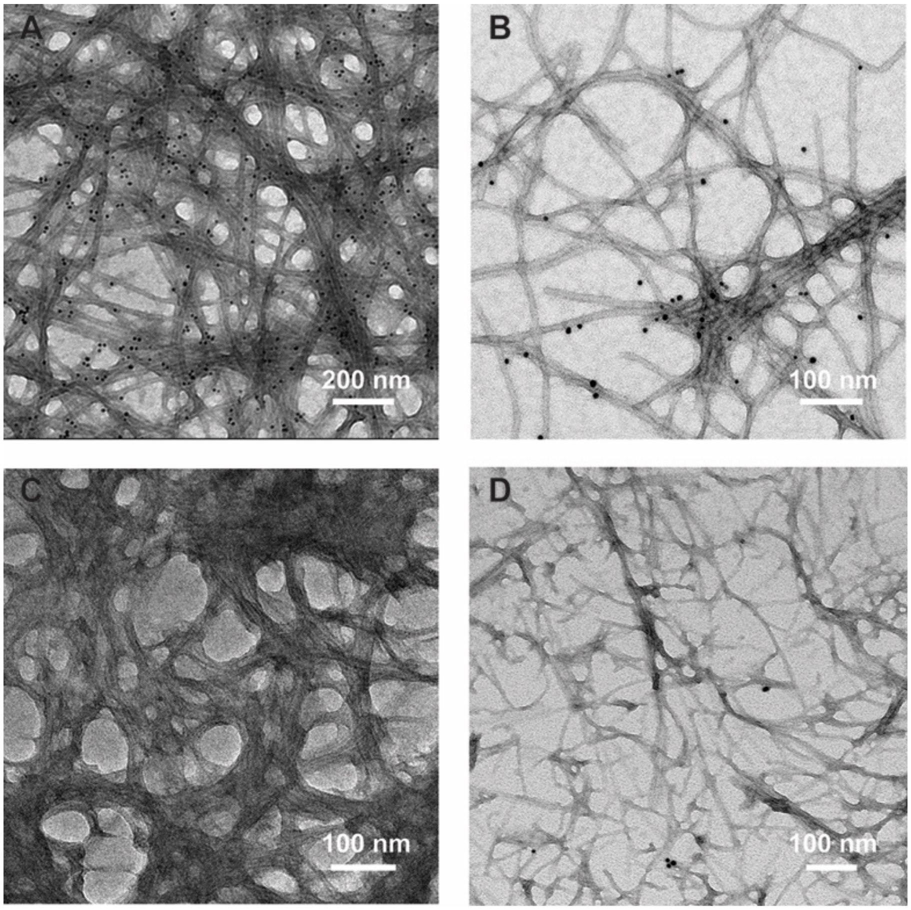

Figure 3-11. TEM images of (**A**, **B**) 100 μM C12-Z33 and (**C**, **D**) 100 μM C12-SZ33 after incubation with IgG-coated Au nanoparticles in PBS, pH 7.4. IgG concentration: 0.33-0.66 μM.

The difficulty in identifying the IgG structure in TEM limits the visualization of the binding events between immunofibers and IgG directly. To confirm that the IgG is present on the surface of the immunofibers, the preformed C12-Z33 and C12-SZ33 immunofibers were incubated with 10 nm human IgG-coated Au nanoparticles for 2 h separately. After a drop of each solution was placed onto a TEM grid, the grid was blotted with a filter paper and left to dry naturally. Then, the grid was washed carefully 3 times with PBS buffer, in an effort to remove the unbounded Au nanoparticles before staining the sample with uranyl acetate. TEM images of C12-Z33 incubated with IgG-coated Au nanoparticles in both dense and sparse (**Figure 3-11 A** and **B**) areas confirmed the binding of IgG to the surfaces of Z33-presenting nanofibers. In sharp contrast, very few Au nanoparticles were observed to attach onto the control nanofibers bearing the scrambled Z33 sequence (**Figure 3-11 C** and **D**). This study suggests that the co-localization of C12-Z33 immunofibers and IgG-coated Au nanoparticles is indeed a result of specific binding. It should be noted that the density of Au nanoparticles was relatively low on the long immunofibers, likely due to the limited accessibility of the tight packing of Z33 immuno-amphiphiles after their self-assembly into nanofibers. Another possibility is that the IgG-coated Au nanoparticles could be bound to the C12-Z33 in the monomer state and then taken away in the washing steps. The IgG concentration (0.33-0.66 μM) in the IgG-coated Au nanoparticles was actually lower than the critical micelle concentration value for C12-Z33, which is 2-5 μM (**Figure 3-12**).

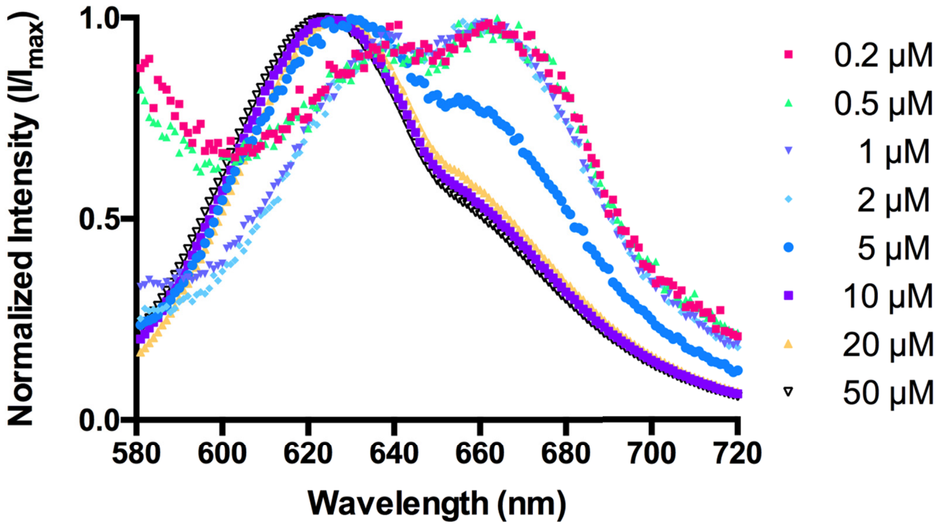

Figure 3-12. CMC measurement of C12-Z33. Emission spectra of the reporter dye Nile Red monitored by a Fluorolog fluorometer (Jobin Yvon, Edison, NJ) after incubated with a series of concentrations of C12-Z33. Excitation wavelength was fixed at 560 nm; emission spectra were monitored 580−720 nm. The CMC of C12-Z33 is determined by a blue-shift of the emission maximum, where the transition indicates the dye partitioning into the hydrophobic compartment of assembled nanostructures. All spectra shown here are normalized by the emission maximum. The CMC range for C12-Z33: 2-5 μM.

To better visualize the interactions between C12-Z33 immunofibers and IgG, labelling the C12-Z33 with the fluorescent dye (Rhodamine B) allows for direct imaging of fluorescent immunofibers and FITC-IgG under a confocal laser scanning microscope. Rhodamine B has been extensively used for staining biomaterials. Rhodamine B labelled C12-Z33 (RB-C12-Z33) was synthesized by adding an extra Kmtt residue at the *N*-terminus of Z33. Rhodamine B and C12 were conjugated to the amine group on the side chain and backbone of the newly added lysine separately. The chemical structure and molecular characterization of RB-C12-Z33 are shown in **Figure 3-13** and **Figure 3-14**. I assume that the fluorescent labelling will not interfere with the binding ability of C12-Z33 because the dye is located remotely from the binding sequence Z33 and would be embedded in the hydrophobic core after self-assembling into the immunofibers. The self-assembled fibrous morphology in PBS was confirmed using TEM (**Figure 3-9 C**). 100 μM RB-C12-Z33 diluted from a 1 mM stock solution and 2 μM FITC-IgG were premixed in PBS. 30 μL solution was spotted on a clean microscope slide right before imaging and covered by a coverslip to obtain a thin layer of liquid. Fluorescence images (**Figure 3-15 A-C**) were then taken by a confocal laser scanning microscope and showed co-localization of fluorescence signals from both RB-C12-Z33 (red) and FITC-IgG (green). It was found that FITC-IgG formed large bright assemblies that were never observed in the pure FITC-IgG solution and the solution incubated with scrambled Z33 (C12-SZ33) under the same conditions (**Figure 3-16**). These findings suggest the binding of FITC-IgG to RB-C12-Z33 or C12-Z33 was specific and triggered the formation of large aggregates, and that the observed assemblies are not a result of electrostatic or other types of interactions because FITC-IgG was well dispersed in the presence of C12-SZ33.

RB-C12-Z33

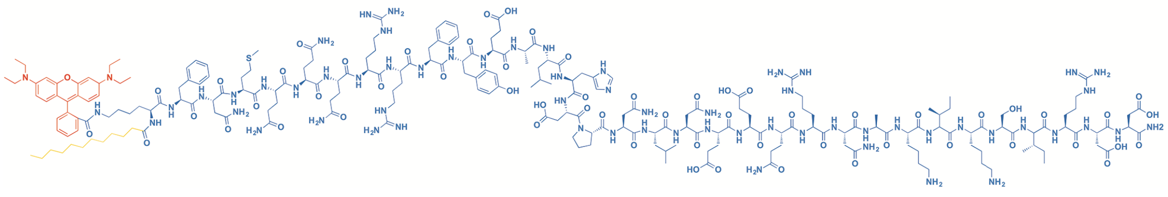

Figure 3-13. Chemical structures of RB-C12-Z33. The peptide, alkyl chain, and Rhodamine B are shown in blue, yellow, and red, respectively.

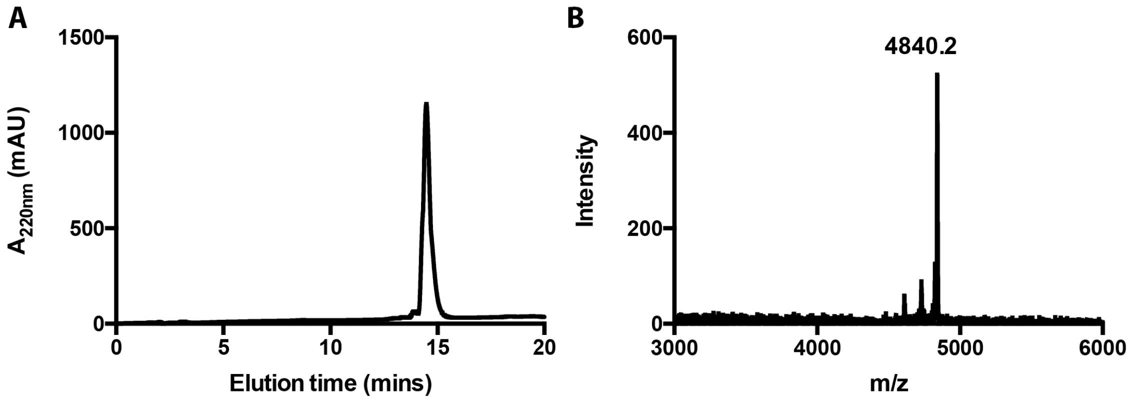

Figure 3-14. RP-HPLC (**A**) and MALDI-TOF MS (**B**) characterization of RB-C12-Z33. The RP-HPLC spectrum confirms the purity of the product (>99%). The expected mass is 4838.5. The peak at 4840.2 corresponds to $[M+H]^+$.

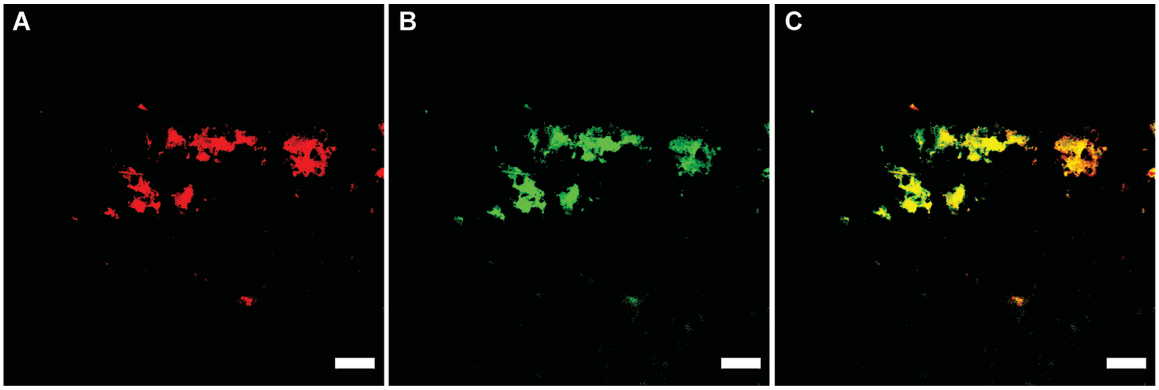

Figure 3-15. Confocal fluorescence images of 100 μM RB-C12-Z33 incubated with 2 μM FITC-IgG in PBS (pH 7.4) show co-localization of the fluorescence signal of Rhodamine B with that of the FITC. (**A**) Image of Rhodamine B fluorescence. (**B**) Image of FITC fluorescence. (**C**) Merged image of (**A**) and (**B**). Scale bar: 20 μm.

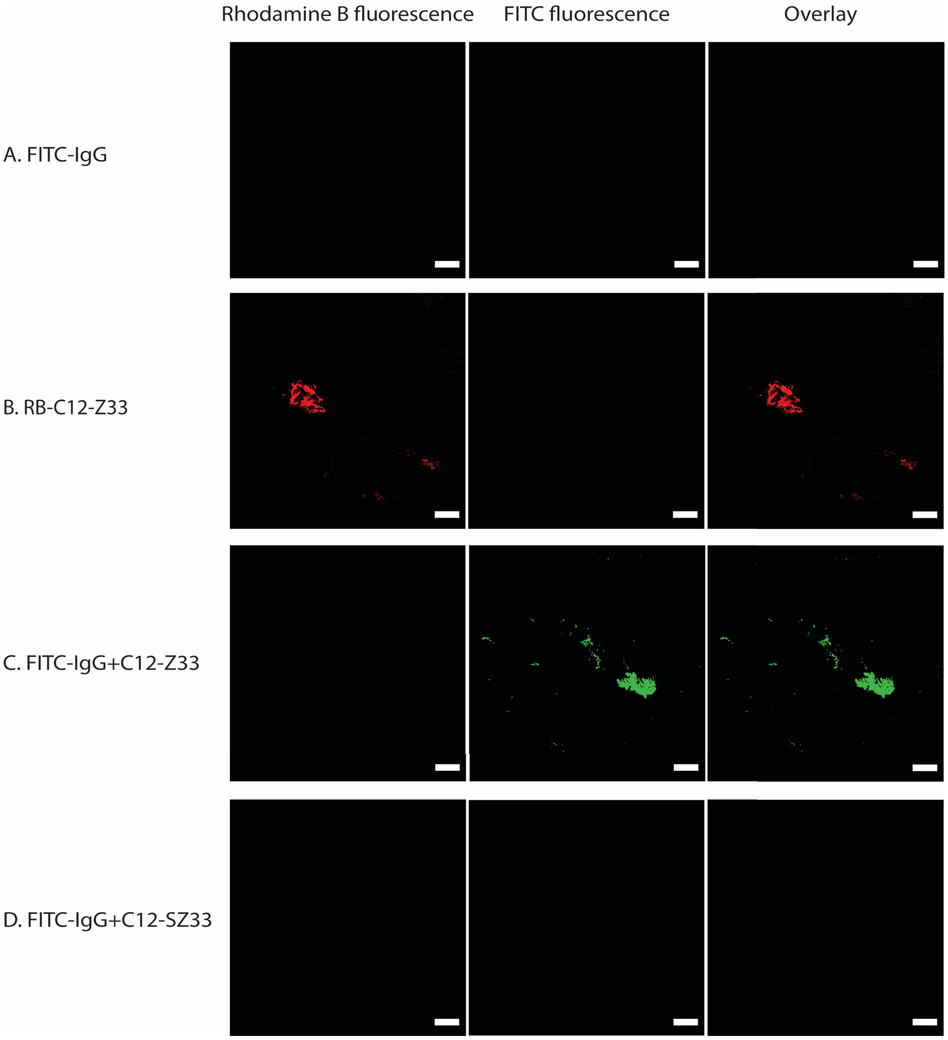

Figure 3-16. Confocal fluorescence images of (**A**) 2 μM FITC-IgG, (**B**) 100 μM RB-C12-Z33, (**C**) 2 μM FITC-IgG incubated with 100 μM C12-Z33, and (**D**) 2 μM FITC-IgG incubated with 100 μM C12-SZ33 in PBS, pH 7.4. All fluorescence images were taken under identical conditions. Compared to the bright fluorescence of FITC-IgG when incubated with RB-C12-Z33, no fluorescent signals were detected or after incubated with C12-SZ33, while comparable fluorescence was observed when incubated with C12-Z33. This showed that FITC-IgG was dispersed well in the PBS buffer or in the presence of C12-SZ33, while the binding to RB-C12-Z33 or C12-Z33 induced the aggregation of FITC-IgG and thus the strong fluorescence. Scale bar: 20 μm.

3.5 Conclusion

In conclusion, I demonstrated that incorporating the protein A mimicking peptide immuno-amphiphile design via direct alkylation at the *N*-terminus of the Z33 peptide could lead to the formation of supramolecular nanostructures with high binding affinity to target antibodies. These Z33 IAs can self-assemble into uniform immunofibers at both physiological pH (7.4) and low pH (2.8), displaying an α-helix secondary structure in the self-assembled state. The results clearly showed that the immunofibers can bind to human IgG1 at physiological pH with a nanomolar K_d and reduce binding ability at low pH, the elution condition, as expected. The binding event can be visualized by TEM images and fluorescence imaging. Antibody-related products have become the most rapidly growing field for therapeutic applications. In the pharmaceutical industry, antibody purification mainly relies on affinity chromatography based on immobilization of antibody-binding ligands with high selectivity but suffering from the high chromatography media cost and limited capture productivity.[284-285, 292] Although the binding affinity of IFs to human IgG1 is slightly compromised relative to that of the unincorporated Z33 peptide, these IFs may present a promising system for IgG capturing. However, there are still many challenges ahead for the development of an IFs-based binding system. One potential challenge is that the capture rate and selectivity must be optimized for use in more complicated conditions such as lysed cells. Another challenge is that the separation of the IF-IgG complex from other components and the recovery process of IgG from IF-IgG complex needs to be further explored. Despite these challenges, I believe that the Z33 containing immunofibers can serve as an effective IgG capturing and possible affinity purification agent for applications in the pharmaceutical industry.

4 Supramolecular Copolymers as Reversible Affinity Precipitants for Selective Capture and Recovery of Monoclonal Antibodies[d]

4.1 Overview

The separation and purification of therapeutic proteins from their biological resources poses a great limitation for industrial manufacturing of biologics in a cost-effective manner. I report here a supramolecular copolymeric system that can undergo multiple levels of reversible assembly processes for efficient capture, one-step precipitation and facile recovery of monoclonal antibodies (mAbs). These supramolecular copolymers, namely immunofibers (IFs), are formed by co-assembly of a protein A-mimicking ligand amphiphile with a rationally designed filler molecule. I found that the composition of IFs and the molar ratio of ligand to proteins contribute significantly to the mAb capture efficiency. Under the optimized conditions, IFs can specifically capture mAbs with a precipitation yield greater than 99%, leading to an overall mAb recovery yield of >94%. I also demonstrated the feasibility of capturing and recovering two mAbs from clarified cell culture harvest. Importantly, the added IFs can be easily removed via membrane separation after mAb elution, without introducing new contaminants in the process. These results showcase the highly promising potential of supramolecular copolymers as affinity precipitants for mAb purification.

4.2 Introduction

Supramolecular polymers formed by self-assembly of peptides and peptide derivatives have been widely explored for use in regenerative medicine,[31-32, 34-35, 46, 293] drug delivery,[22, 26-27, 181, 294-301] and disease diagnostics.[36-37, 302] As molecular building units, peptides are particularly attractive for creating supramolecular materials for biomedical applications due to their inherent biodegradability and biocompatibility, and most importantly, their ability to incorporate a variety of bioactive epitopes for specific biological interfacing.[39-43] In a typical supramolecular polymeric system, reversible transitions can occur at multiple length scales,[46] including the intramolecular chain adjustment to adopt various conformations,[47] the intermolecular interactions to assemble into discrete polymeric nanostructures,[40, 48-49] and the inter-particle interactions to percolate into a 3D network (gelation) or to cause macroscopic phase separation (coacervation or precipitation).[50-52] The transitions among different assembly states can be induced by changes in temperature,[303] pH,[304] ionic strength,[305] concentration,[40] or molecular interactions.[40, 51] While there have been some reports in the literature to exploit the soluble-insoluble transition of elastin-like polypeptides (ELP) based on their unique thermo-responsive property,[51, 151, 306-308] macroscopic phase separation is generally considered as a failure in supramolecular design of a peptide-based system. In this context, I purposely took advantage of the inherent reversible transitions in supramolecular systems to develop peptide-based supramolecular polymers as effective affinity precipitants for selective capture of monoclonal antibodies.

Monoclonal antibodies (mAbs) have received considerable attention over the past three decades for the treatment of human diseases in oncology, hematology, dermatology, rheumatology, etc.[1-2] Affinity precipitation has been increasingly explored as a promising alternative to purify mAbs and other therapeutic proteins,[11, 309] as the conventional protein A affinity chromatography method suffers from limited production capacities and high media cost.[6, 9] A typical protein precipitant features high mAb capture affinity as well as reversible soluble-insoluble transitions.[13, 162] The precipitation can be triggered either by the ligand-mAb interactions or applying external stimuli.[15] Although affinity precipitation can potentially overcome the chromatography limitations associated with column size and ligand immobilization,[16] it demands high mAb capture selectivity and also the effective clearance of precipitants from the product pool. Despite recent efforts in the development of new affinity precipitants,[17-21] the challenges in achieving a high capture efficiency and effective removal of the added precipitants have yet to be resolved, limiting their potential for industrial bioprocessing applications.

In fact, the facile incorporation of affinity ligands into supramolecular polymers and the reversible soluble-insoluble phase transition enable their promising potential for the affinity capture, one-step precipitation and recovery of mAbs. The transition between monomeric units and their assembled nanostructures provides an effective means for their effective removal from the protein product pool through dissociation (not chemical degradation). In light of this, I have designed and synthesized self-assembling immuno-amphiphiles by incorporating Z33, a protein A mimicking peptide that binds to the Fc-portion of IgG in a pH sensitive manner.[214, 310] However, although a high binding affinity was probed between the immuno-amphiphile and mAbs, the capture/precipitation efficiency of mAbs by its supramolecular form was found to be very modest. I attributed this low capture efficiency to the possible steric hindrance among tightly packed ligands that prevents their effective binding to target proteins.

Co-assembly of two or more peptide building blocks represents an effective strategy to craft supramolecular nanostructures with different structural and functional properties.[311-314] For example, it has been shown that mixing of catanionic drug amphiphiles provides a means of forming tubular morphologie.[173] To modulate the epitope density and achieve enhanced bioactivities, co-assembly of bioactive peptide amphiphiles (PAs) with an inert molecule has been developed by the Stupp lab and others.[315-318] For example, in an effort to modulate cell adhesion to supramolecular artificial extracellular matrices, 10 wt.% RGDS-presenting PA co-assembled with a diluent PA showed maximum adhesion.[315] Inspired by this strategy, I report here the co-assembly of mAb binding immuno-amphiphiles with a filler molecule into one class of supramolecular copolymers, which is termed immunofibers (IFs), for efficient mAb capture, precipitation, and recovery. I believe these results shed important light on the use of supramolecular systems for non-chromatographic purification of mAbs and other protein therapeutics.

4.3 Experimental Procedures

4.3.1 Materials and Molecular Synthesis

All Fmoc amino acids and resins were obtained from Advanced Automated Peptide Protein Technologies (AAPPTEC, Louisville, KY). The pure mAb1, pure Fc-fusion protein, and mAb1 and mAb2 in clarified Chinese hamster ovary (CHO) cell culture harvest were obtained from Bristol-Myers Squibb (Devens, MA). The cell culture was clarified using depth filtration. IgG (FITC) from human serum was purchased from Sigma-Aldrich (St. Louis, MO) and was further purified by ProA-HPLC. Unless otherwise specified, all other reagents were obtained from VWR (Radnor, PA) and used as received without further purification.

Filler and ligand molecules were synthesized via direct conjugation of lauric acid (C12) to the *N*-terminus of corresponding peptide sequences. VVEE and VVKKGGZ33 were synthesized on the Focus XC automatic peptide synthesizer (AAPPTEC, Louisville, KY) using standard 9-fluorenyl-methoxycarbonyl (Fmoc) solid phase synthesis protocols. Fmoc deprotections were performed using a 20% 4-methylpiperidine in DMF solution for 15 min, repeating once. C12 alkyl chain was then manually coupled at the *N*-terminus of two peptides after Fmoc deprotection. In all cases, reactions were tested using the ninhydrin test (Anaspec Inc., Fremont, CA) for free amines. The crude products were cleaved from the solid support using a mixture of trifluoroacetic acid (TFA)/triisopropylsilane (TIS)/H2O in a ratio of 92.5:5:2.5 for 2.5 h. Excess TFA was removed by evaporation and ice-cold diethyl ether was added to precipitate the crude products, followed by centrifugation. The precipitates were then washed two more times with diethyl ether and centrifuged to remove the remaining solvent.

The crude products were purified by preparative RP-HPLC using a Varian Polymeric Column (PLRP-S, 100 Å, 10 μm, 150×25 mm) at 25 °C on a Varian ProStar Model 325 preparative HPLC (Agilent Technologies, Santa Clara, CA) monitored at 220 nm for the absorbance of peptide segments. Collected fractions were analyzed by MALDI-TOF (BrukerAutoflex III MALDI-TOF instrument, Billerica, MA) and product-containing fractions were then lyophilized (LabconcoTM FreeZone −105 °C, 4.5 L freeze dryer, Kansas City, MO) and stored at −30 °C.

4.3.2 CMC Measurement

The CMCs of the filler and ligand molecules in PBS were determined using Nile Red, a lipophilic dye that fluoresces depending on solvent polarity and local environment. Nile Red prefers to partition into the hydrophobic domains if there exist any supramolecular assemblies. The CMC is determined by a blue-shift of the emission maximum, whereas this transition occurs as the incubated molecules exceed their CMC values. Nile Red was initially dissolved in acetone (20 μM) and Nile Red solution (10 μL) was loaded into several centrifuge tubes. After the solvent evaporated under room temperature, filler or ligand solutions (500 μL) in PBS at various concentrations were added into the centrifuge tubes containing dry Nile Red and aged overnight. Fluorescent spectra of Nile Red were then monitored by a Fluorolog fluorometer (Jobin Yvon, Edison, NJ) with fixed excitation wavelength at 560 nm; emission spectra were monitored at 580-720 nm.

4.3.3 Self-Assembly, Co-Assembly, and TEM Imaging

Mixtures of filler and ligand molecules in powder form at molar ratios of 0:1, 5:1, 25:1, 50:1, and 50:0 were pretreated with hexafluoroisopropanol (HFIP), a good solvent for the peptide amphiphiles, to eliminate any pre-existing nanostructures that could be possibly formed during the synthesis and purification process. HFIP was then removed by evaporation, followed by addition of PBS (20 mM sodium phosphate, 150 mM sodium chloride, pH 7.4) to prepare IF stock solutions at a final ligand concentration of 50 μM. The stock solutions were aged overnight at room temperature before use. Stock solutions (10 μL) were spotted on carbon film coated copper grids with 400 square mesh (Electron Microscopy Sciences, Hatfield, PA) and the excess was removed with filter paper to leave a thin film of sample on the grid. After letting the sample dry for 5 min, 2% uranyl acetate (10 µL) was added to the sample grid, and the excess was removed after 30 s. All samples were dried for at least 3 h before imaging. Bright-field TEM imaging was performed on a FEI Tecnai 12 TWIN Transmission Electron Microscope and all TEM images were required by a SIS Megaview III wide-angle CCD camera.

4.3.4 Cryo TEM

50:1 IFs were prepared in PBS one day before the imaging. Prior to sample preparation, lacey carbon film coated copper grids with 300 square mesh (Electron Microscopy Sciences, Hatfield, PA) were treated with plasma air to make the carbon film hydrophilic. 6 µL sample solution for 50:1 IFs, 50:1 IFs incubated with 5 µM mAb1 for 30 minutes, and 5 µM mAb1 were dropping onto the grids, separately. A thin film of the sample solution was generated using the Vitrobot with a controlled humidity chamber and the grid was blotted and plunged into liquid ethane pre-cooled by liquid nitrogen. All vitrified samples were transferred to a cryo-holder filled with liquid nitrogen to prevent sublimation of vitreous water. Cryo-TEM imaging was performed on the FEI Tecnai 12 TWIN Transmission Electron Microscope, operating at 80 kV. The images were recorded by a 16 bit 2K × 2K FEI Eagle bottom mount camera.

4.3.5 CD Spectroscopy

The CD spectra of assembled IFs at filler:ligand molar ratios of 0:1, 5:1, 25:1, 50:1 were collected on a Jasco J-710 spectropolarimeter (JASCO, Easton, MD) using a 1 mm path length quartz UV-vis absorption cell (ThermoFisher Scientific, Pittsburgh, PA) at 25 °C. A background spectrum of the solvent was acquired and subtracted from the sample spectrum. The collected data was averaged from three scans and normalized with respect to the ligand concentration.

4.3.6 ITC Experiment

ITC experiments were performed using a high precision VP-ITC titration calorimetric system (Microcal Inc.). The 40 μM IF solution was titrated with 100 μM mAb1 in PBS (pH 7.4) at 25 °C. The heat evolved after each injection was obtained from the integral of the calorimetric signal. The heat associated with the binding of IFs to mAb1 was obtained by subtracting the heat of dilution. Analysis of the data was performed using MicroCal Origin package.

4.3.7 Precipitation of Pure mAb1 and Pure Fc-fusion Protein

IF stock solutions at desired filler:ligand molar ratios were prepared one day before the precipitation experiment. In experimental groups, pure mAb1 and pure Fc-fusion protein at certain concentrations were well-mixed and incubated with IF solution (100 μL) for 30 minutes. Protein control groups were prepared with pure mAb1 and pure Fc-fusion protein at same concentrations in PBS. Peptide control groups were prepared with IF solution (100 μL) at desired filler:ligand molar ratios. Ammonium sulfate (abbreviated as salt below) in PBS was then added to all experimental groups and control groups to reach desired final salt concentrations and precipitate proteins and IFs. After 30 minutes, the solution was centrifuged at 15000 rpm for 15 minutes. The supernatant was taken out and analyzed by ProA-HPLC (POROS™ A 20 μm Column, Stainless Steel, 2.1 x 30 mm, 0.1 mL) to determine the protein concentrations and by RP-UPLC (ACQUITY UPLC Peptide BEH C18 Column, 300 Å, 1.7 μm, 2.1 x 150 mm) to determine filler and ligand concentrations. The precipitated amount of each species was calculated by subtracting the amount in the supernatant from the amount added. The precipitation yield was calculated by dividing the precipitated amount by the amount added.

4.3.8 Precipitation of IgG (FITC) and mCherry

IgG (FITC) (5 μM), mCherry (5 μM), and the mixture of two proteins were well-mixed and incubated with 50:1 IFs (100 μL) for 30 minutes. Three protein control groups with IgG (FITC) (5 μM), mCherry (5 μM), and the mixture of two proteins were prepared in PBS (100 μL). Salt solution in PBS was then added to all experimental groups and control groups to reach a final concentration of 0.75 M. After 30 minutes, the solution was centrifuged at 15000 rpm for 15 minutes. All samples were imaged by the ChemiDoc MP imaging system (Bio-Rad, Hercules, CA). The supernatant was taken out and analyzed by a fluorescence plate reader. Green channel was excited at 480 nm and collected at 498-605 nm. Red channel was excited at 550 nm and collected at 580-720 nm.

4.3.9 Resuspension of Pure mAb1

5 μM pure mAb1 were well-mixed and incubated with 50:1 IFs (100 μL) for 30 minutes. The same procedures were performed to precipitate both mAbs and IFs. Three buffers (40 mM sodium acetate at pH 3.7, 40 mM sodium phosphate at pH 7.4, and sodium carbonate at pH 10.1) were tested to resuspend the precipitates. Resuspension buffer (1 mL) was added to the precipitates followed by pipetting up and down. After the solution was centrifuged at 15000 rpm for 15 minutes, the supernatant was taken out and analyzed by ProA-HPLC and RP-UPLC to determine the protein, filler, and ligand concentrations.

4.3.10 Capture and Recovery of Pure mAbs and mAbs in Clarified Bulk

Pure mAb1 (5 μM) or mAbs at clarified bulk state (5 μM) were well-mixed and incubated with 50:1 IFs (100 μL) for 30 minutes. Same procedures were performed to precipitate both mAbs and IFs. The precipitates were resuspended in PBS (1 mL, 40 mM sodium phosphate, pH 7.4) and transferred to a dialysis tube (Pur-A-Lyzer Maxi, 50 kDa cut-off molecular weight, Sigma-Aldrich, St. Louis, MO). The resuspended solution was then dialyzed against 40 mM sodium phosphate (1 L) at pH 7.4 for 24 h and 40 mM sodium acetate (1 L) at pH 3.7 for 24 h successively. The dialysis buffers were replaced three times per 24 h. The protein, filler, and ligand concentrations were determined by ProA-HPLC and RP-UPLC.

4.3.11 Size Elusion Chromatography (SEC)

The SEC was performed on an Agilent AdvanceBio SEC column (300 Å, 2.7 μm, 4.6x150 mm) using PBS (pH 7.4) as mobile phase at room temperature. Absorbance at 280 nm was used to monitor the elution of different components in CB.

4.4 Results and Discussions

4.4.1 Design Principles and Molecular Characterization

The overall purification process is illustrated in **Figure 4-1 A**. The building units of the supramolecular polymers containing mAb-binding peptides are expected to spontaneously co-assemble into IFs under physiological conditions and then capture and precipitate mAbs in a specific manner. After phase separation and resuspension, mAbs can be recovered under elution conditions, while IFs are continuously dissociated into monomers and removed via membrane separation. As shown in **Figure 4-1 B**, the supramolecular system contains two self-assembling constituents: a filler molecule and a ligand molecule. The filler molecule, C12-VVEE, serves as a diluting agent used to modulate the distribution density of the ligand molecule (**Figure 4-1 B**). The alkyl chain, C12, was conjugated to the *N*-terminus of the respective ligand and filler molecules to provide the necessary driving force (hydrophobic interactions) for assembly under aqueous conditions. The ligand molecule, C12-VVKKGGZ33, is the active component specifically designed for mAb binding (**Figure 4-1 B**). Specifically, a monoclonal human IgG1 antibody (abbreviated as "mAb1") was continuously used in this work. The sequence VVKK was molecularly crafted to match with the hydrophobic segment (VV) of VVEE to facilitate the formation of the hydrogen network throughout the resultant IFs, while providing cohesive interactions through electrostatic complexation to promote the co-assembly of the two components and also to avoid possible self-sorting (demixing) that has been observed in other co-assembly systems.[318-320] A double glycine (GG) segment was inserted as a spacer between C12 and Z33 to extend the Z33 ligand further out of the IFs surface for better accessibility. The filler and ligand molecules were synthesized using automated solid-phase peptide synthesis (SPPS) methods. Chemical structures of filler and ligand molecules and their RP-HPLC and MALDI-TOF MS characterization are shown in **Figures 4-2, 4-3,** and **4-4**.

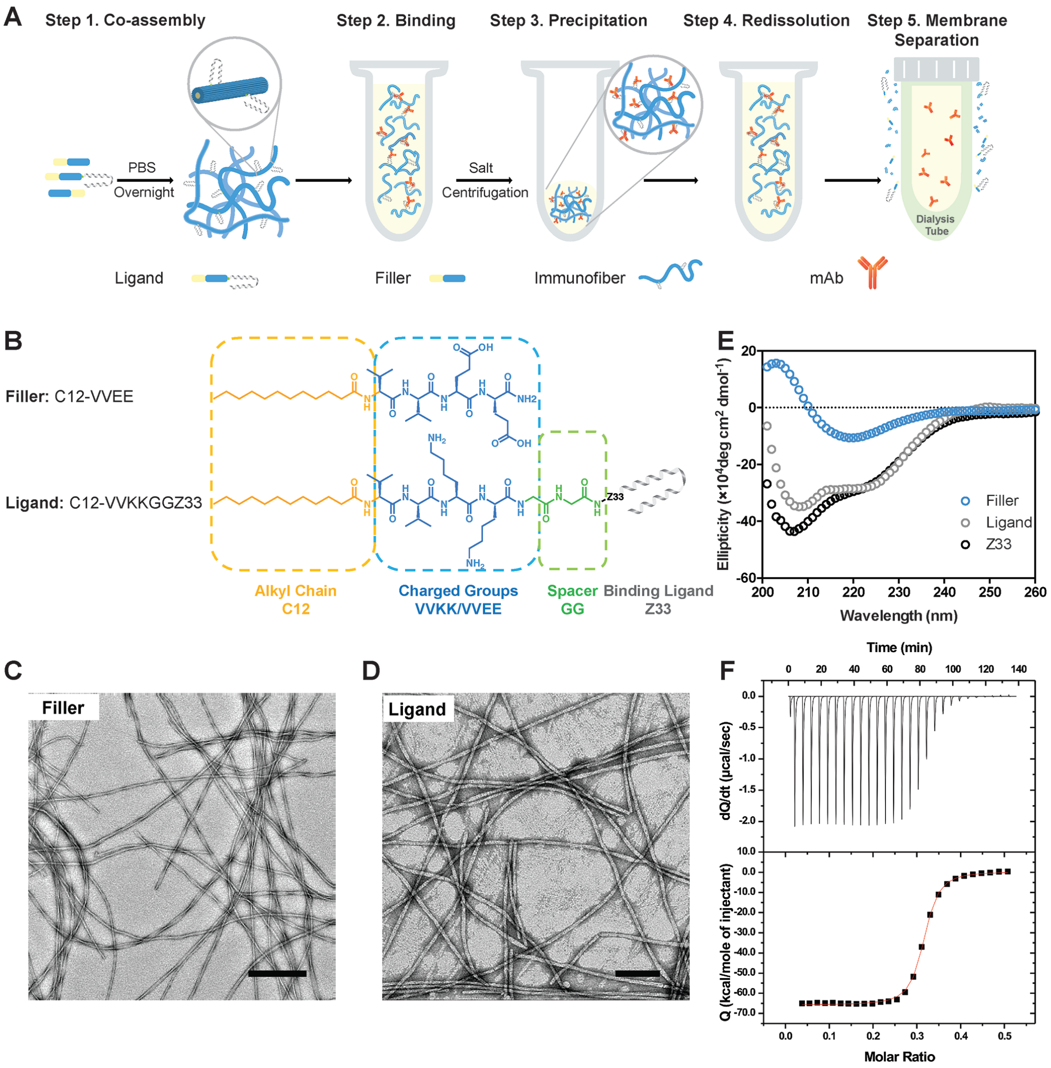

Figure 4-1. The overview of the purification process, design of filler and ligand, and molecular characterization. (**A**) Schematic illustration of the overall mAb purification process using co-assembled IFs. (**B**) Chemical structures and key design components of the filler and ligand molecules. Representative transmission electron microscopy (TEM) images of self-assembled filamentous structures formed by (**C**) filler and (**D**) ligand with a diameter of 7.4 ± 0.6 nm and 14.9 ± 1.5 nm, respectively. Filament diameters are represented as mean ± SD (n = 30). TEM sample was stained with 2 wt % uranyl acetate aqueous solution to improve imaging quality. Scale bars in (**C**-**D**) are 100 nm. (**E**) Normalized CD spectra of self-assembled filler, self-assembled ligand, and free Z33 peptide. (**F**) ITC profiles and binding curves for the stepwise injection of 100 µM mAb1 into a solution of 40 µM ligand molecule at 25 °C in PBS, pH 7.4.

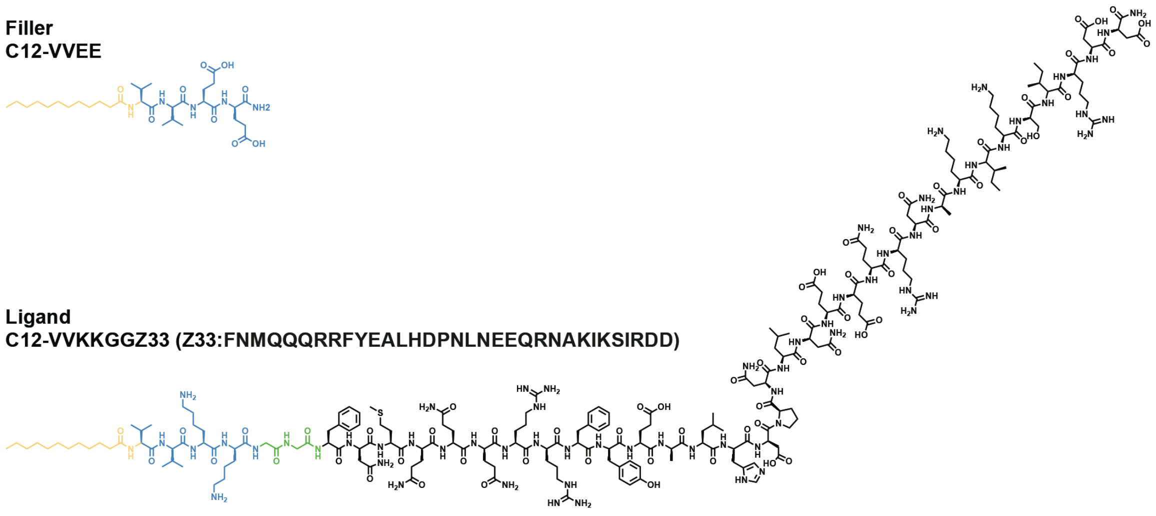

Figure 4-2. Chemical structures of filler (C12-VVEE) and ligand (C12-VVKKGGZ33) molecule. The alkyl chain (C12), VVKK/EE, GG, and Z33 are shown in yellow, blue, green, and black, respectively.

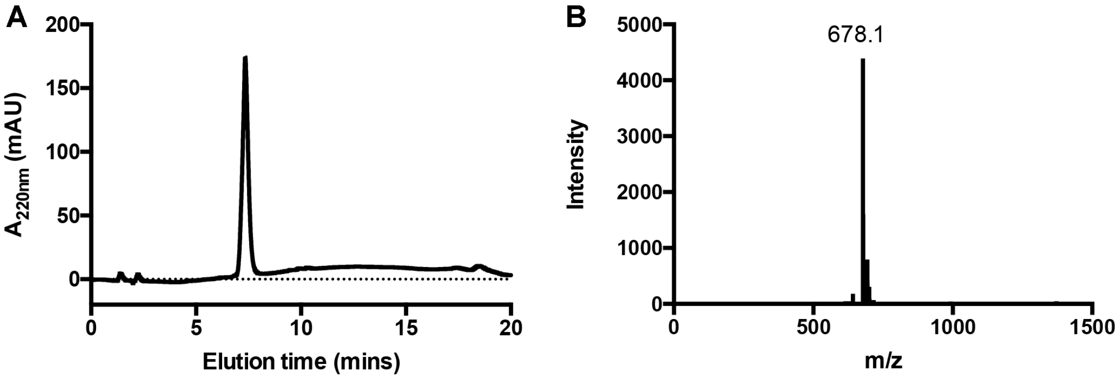

Figure 4-3. RP-HPLC (**A**) and MALDI-TOF MS (**B**) characterization of C12-VVEE. The RP-HPLC spectrum confirms the purity of the product (>99%). The expected mass is 655.4. The peak at 678.1 corresponds to $[M+Na]^+$.

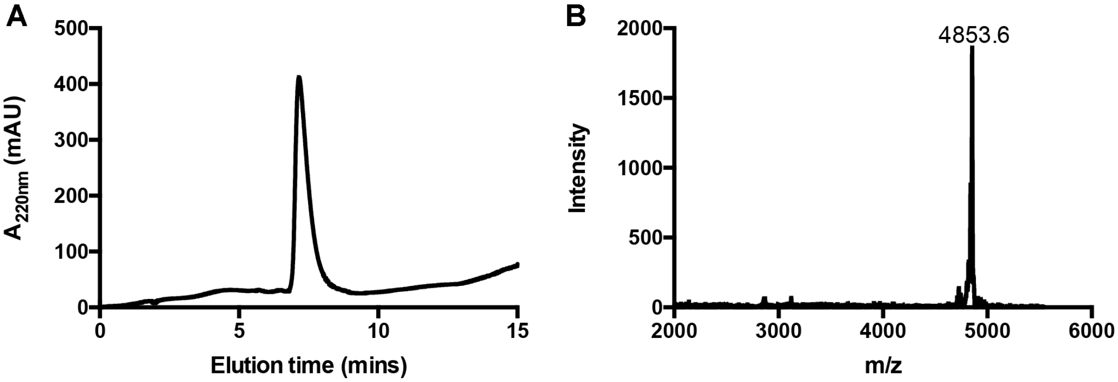

Figure 4-4. RP-HPLC (**A**) and MALDI-TOF MS (**B**) characterization of C12-VVKKGGZ33. The RP-HPLC spectrum confirms the purity of the product (>99%). The expected mass is 4852.6. The peak at 4853.6 corresponds to $[M+H]^+$.

The filler and ligand molecules can each self-assemble into filamentous structures (**Figure 4-1 C-D**) with diameters of 7.4 ± 0.6 nm and 14.9 ± 1.5 nm, respectively. Unlike the self-assembled ligand nanostructures that mainly consist single fibers, twisted or helical ribbons were predominantly observed in the filler morphology due to the merging of single filler fibers. Circular dichroism (CD) spectra revealed the formation of β-sheet secondary structures in the self-assembled fillers, while ligand molecules effectively preserved the α-helix conformation as evidenced by the two negative peaks at around 208 nm and 222 nm that were observed in the original Z33 peptide (**Figure 4-1 E**).[310] Isothermal titration calorimetry (ITC) measurement showed the ligand molecule binds to mAb1 with a K_d of 36.0 ± 2.1 nM for ligand molecules at 25 ℃ (**Figure 4-1 F**), similar to the reported value (26 nM) for free Z33 peptide.[214, 310] However, the self-assembled ligand molecules alone were unable to precipitate mAbs likely due to the overcrowding of Z33 (**Figure 4-5**). The binding signal obtained using the ITC may have mostly come from the binding between mAbs and the monomeric ligand molecules, which could probably shift the self-assembly equilibrium to the monomer side. As such, I anticipated that the co-assembly strategy could modulate Z33 ligand density and optimize the protein binding property for mAb purification.

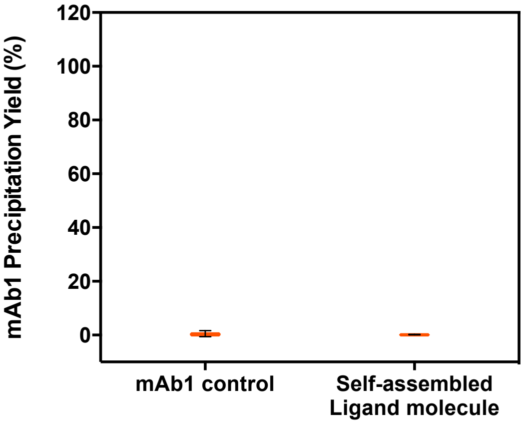

Figure 4-5. mAb1 precipitation after incubation with self-assembled ligand molecule. 20 µM mAb1 was incubated with 50 µM self-assembled ligand molecule and 1 M ammonium sulfate. In the control group, 20 µM mAb1 was incubated with 1 M ammonium sulfate. Both mAb1 control group and self-assembled ligand group showed negligible mAb precipitation. All experiments were performed in triplicate and the data is shown as mean ± standard deviation.

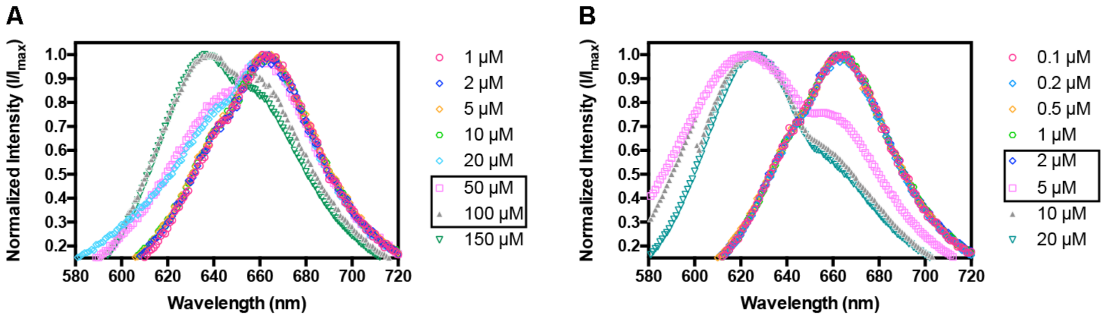

Figure 4-6. CMC measurement of (**A**) filler and (**B**) ligand. The CMC ranges are 50-100 µM and 2-5 µM, respectively. Emission spectra of the reporter dye Nile Red monitored by a Fluorolog fluorometer (Jobin Yvon, Edison, NJ) after incubation with a series of concentrations of filler or ligand. Excitation wavelength was fixed at 560 nm; emission spectra were monitored 580-720 nm. The CMC value was determined by a blue-shift of

the emission maximum, where the transition indicates the dye partitioning into the hydrophobic compartment of assembled nanostructures. All spectra shown here are normalized by the emission maximum.

For a co-assembled IF system, the filler:ligand ratio was expected to have a great impact on the mAb binding, since it determines the Z33 density on IF surfaces. Considering the dynamic equilibrium between IFs and monomers, the ligand molecule was determined to possess a critical micelle concentration (CMC) in the range of 2-5 μM (**Figure 4-6**). Therefore, a concentration of 50 μM was set for ligand molecules to ensure its majority in the assembled state. Three filler:ligand ratios, 5:1, 25:1, and 50:1, were then randomly selected and the corresponding IFs were constructed by mixing 50 μM ligands and different amount of fillers accordingly. Ratios higher than 50:1 were not tested due to the solubility limitation of filler molecules at neutral pH. Filamentous nanostructures were observed formed by co-assembled filler and ligand molecules at 5:1, 25:1, and 50:1 molar ratios (**Figure 4-7 A-C**) with a diameter of 14.1 ± 0.8 nm, 8.4 ± 0.9 nm, and 7.5 ± 0.9 nm, respectively. At 25:1 and 50:1 molar ratios, a great portion of single fibers were found to merge into twisted or helical ribbons due to the increased concentration of the filler molecule (**Figure 4-1 C**). For co-assembled IFs at the three selected filler:ligand ratios, the apparent conformation, according to CD measurements, shifted from α-helix to β-sheet with increasing filler:ligand molar ratio as a result of increased dominance by the filler assemblies (**Figure 4-7 D**). To prove mAb binding on the IF surface, the TEM image of a mixture of 5 μM mAb1 and 50:1 IFs ratios was taken (**Figure 4-7 E**). Although it is hard to differentiate the mAb1 structures from the background, I observed that IFs exhibit more blurring borders possibly due to mAb binding. To avoid the noise from staining and drying effect and to better visualize the mAb-IF interactions, the mixture of 50:1 IFs and mAb1 was then imaged using cryogenic(cryo)-TEM. As shown in **Figure 4-7 F**, it's clear to see the IFs were spotted with high-density of black dots. In contrast, 50:1 IFs without addition of mAb1 showed sharper edges and smoother surfaces (**Figure 4-7 G**). The black dots were identified as the mAb structures as shown in **Figure 4-7 H**, confirming the binding of mAb1 onto IF surfaces.

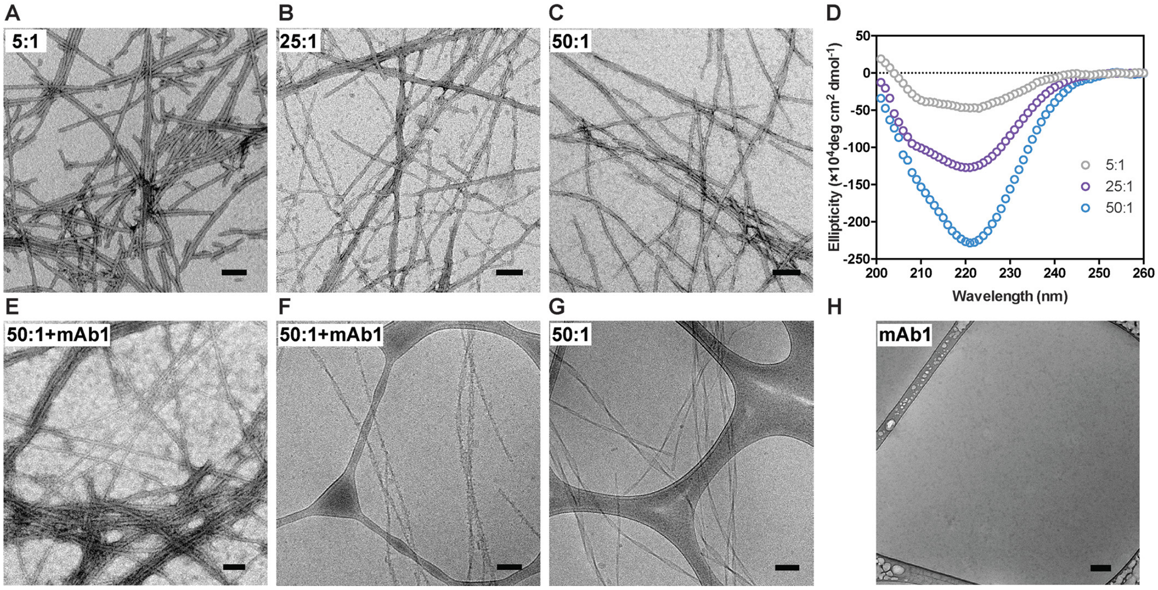

Figure 4-7. Representative TEM images of supramolecular copolymers formed by filler and ligand molecules at (**A**) 5:1, (**B**) 25:1, and (**C**) 50:1 molar ratios with a diameter of 14.1 ± 0.8 nm, 8.4 ± 0.9 nm, and 7.5 ± 0.9 nm, respectively. Filament diameters are represented as mean ± SD (n = 30). (**D**) CD spectra of co-assembled IFs at different spacer:ligand molar ratios. The spectra were normalized by the concentration of the ligand molecules, showing a transition of the apparent conformation from α-helix to β-sheet with the increase of the spacer:ligand molar ratio. (**E**) Representative TEM image of 50:1 IFs+mAb1. Representative cryo-TEM images of (**F**) 50:1 IFs+mAb1, (**G**) 50:1 IFs, and (**H**) mAb1 in PBS showed the binding between mAb1 and IFs. All TEM sample was stained with 2 wt % uranyl acetate aqueous solution to improve imaging quality. Scale bars are 100 nm.

4.4.2 Mechanism Studies of Protein Precipitation and Yield Optimization

To understand the basic principles behind the IF-protein interactions, I carried out a series of protein capture experiments by controlling one variable at a time. In addition to mAb1 (144 kDa, pI: 8.4), an Fc-fusion protein (78 kDa, pI: 6.5) that has the same Fc fragment as mAb1, were used in the following studies. I first investigated the effect of the filler:ligand ratio on the protein precipitation efficiency. As described above, 5:1, 25:1, and 50:1 IFs were constructed and two proteins from 448 μM stock were added into each IF solution (100 μL), respectively, to reach a final concentration of 20 μM. 1 M ammonium sulfate (abbreviated as "salt" below) was used to promote the soluble-insoluble transition of this supramolecular system. After centrifugation, the supernatant was analyzed by ProA-HPLC to determine the protein concentration and the protein precipitation yield was then calculated. In the control group without any IFs (0:0), adding salt was not able to precipitate any proteins (**Figure 4-8 A**). In the other control group with filler only (50:0), very little mAb1 and less than 15% of Fc-fusion proteins were precipitated (**Figure 4-8 A**), suggesting there existed little to no non-specific binding between proteins and filler molecules as a result of the overall charge of IFs. Importantly, the precipitation yield for both mAb1 and Fc-fusion protein increases with increasing filler:ligand ratios (**Figure 4-8 A**), which could be interpreted by the enlarged spacing between ligands that facilitates effective protein binding (**Figure 4-8 B**). Moreover, the two proteins are oppositely charged at the tested pH (7.4) according to their pIs but both of them can be captured and precipitated by the negatively charged IFs. This suggests that it was the specific binding of protein to ligand molecules that played the dominant role in the protein precipitation instead of the electrostatic-mediated protein enrichment. It is important to note that for all co-assembled groups, over 95% filler and ligand molecules were precipitated concomitantly with the target proteins (**Figure 4-8 C** and **D**), suggesting that it is the binding step, not the precipitation step that determines the overall protein precipitation yield. The precipitation of Fc-fusion proteins suggests that this supramolecular system with Z33 ligand can be used to capture any proteins of interest with an Fc domain, not limited only to mAbs.

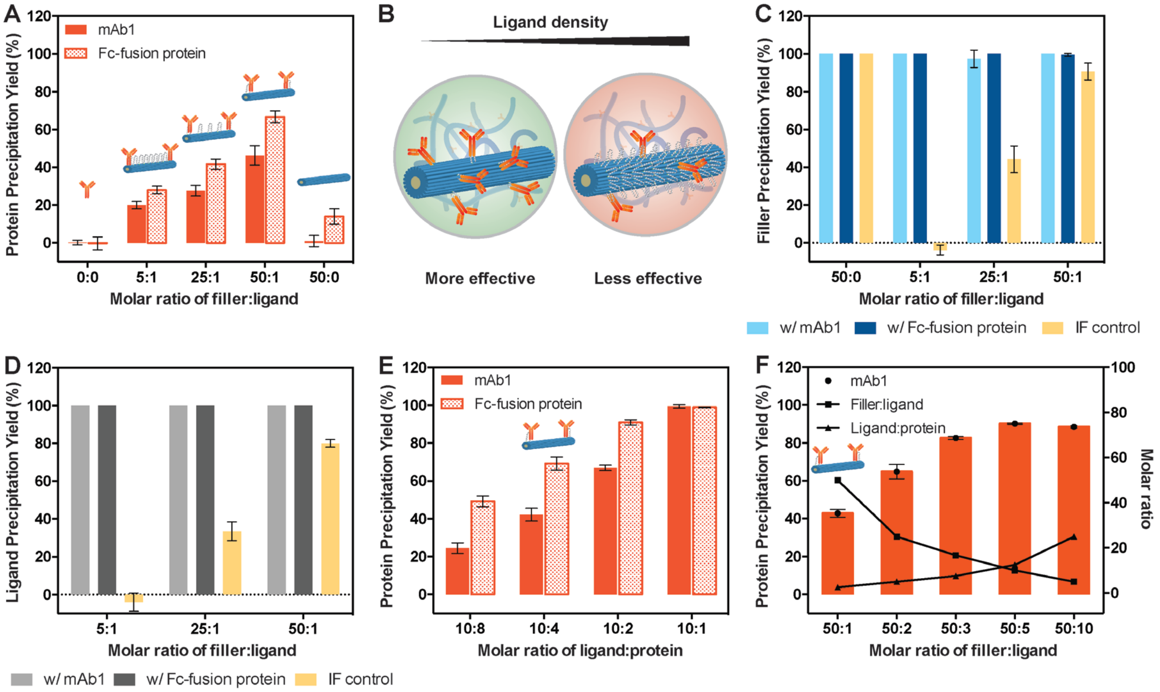

Figure 4-8. Key experimental parameters in the selective capture of mAbs and Fc-fusion proteins. (**A**) Precipitation yields of mAb1 and Fc-fusion protein at different molar ratios of filler:ligand with fixed ligand concentration. (**B**) Schematic illustration of the effect of ligand density in IFs when the ligand concentration is fixed. Precipitation yields of (**C**) filler and (**D**) ligand molecule in co-assembled IFs at different molar ratios of filler:ligand with fixed ligand concentration. Precipitation yields of mAb1 and Fc-fusion protein at different (**E**) molar ratios of ligand:protein with fixed ligand concentration and (**F**) molar ratios of filler:ligand with fixed filler concentration. As a proof of concept, purified mAb1

and Fc-fusion protein were used in (**A**, **C-F**). All experiments were performed in triplicate and the data is shown as mean ± standard deviation.

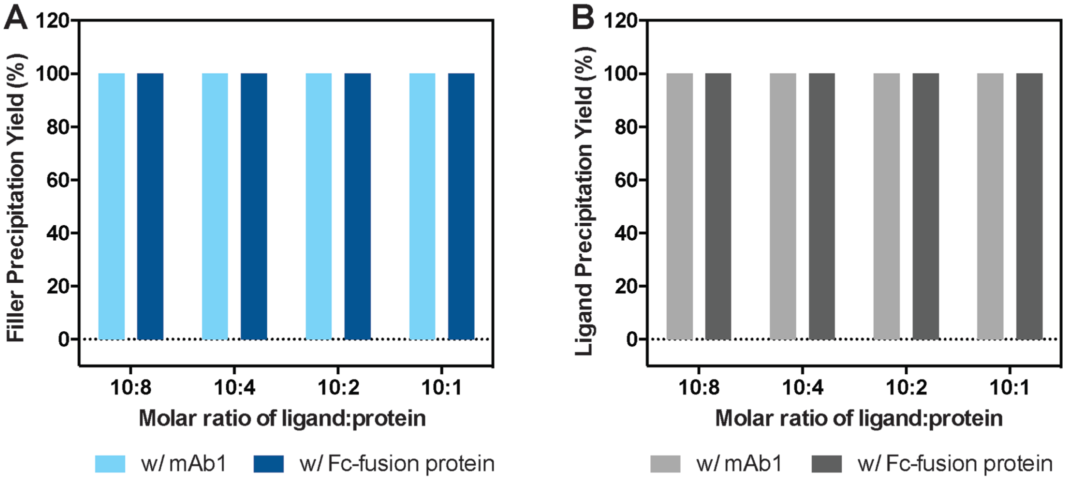

Figure 4-9. Precipitation yields of (**A**) filler and (**B**) ligand molecule for 50:1 IFs at various ligand:protein ratios and 1 M ammonium sulfate conditions. The IFs were incubated with mAb1or Fc-fusion protein. All experiments were performed in triplicate and the data is shown as mean ± standard deviation.

To further improve the precipitation yields, I considered whether the ligand:protein molar ratio significantly contributes to the precipitation efficiency, as it is the key factor that affects the binding equilibrium. At a fixed 50:1 filler:ligand ratio, ligand:protein ratios were varied from 10:1 to 10:8 by increasing protein concentration from 5 µM to 40 µM. Ligand:protein molar ratios higher than 10:1 were not investigated due to the detection limit of the ProA column at low mAb concentrations. As expected, higher precipitation yields were obtained at lower protein concentrations (**Figure 4-8 E**). At the ligand:protein ratio of 10:1, both proteins can be precipitated at a yield greater than 99%. This optimized 10:1 ratio was much higher than the theoretical mAb (or Fc-fusion protein):Z33 ratio (2:1), probably resulting from the limited ligand accessibility on IFs due to steric hindrance or compromised surface area due to the merging of IFs. A more efficient ligand:protein ratio could be potentially achieved by improving the ligand flexibility on IF surface and minimizing IF merging. Again, in these experiments, it was observed that over 95% filler and ligand molecules were co-precipitated with the target proteins (**Figure 4-9**), confirming that the protein precipitation yield was limited by the saturation of accessible ligands.

To investigate which of the two ratios is more dominant and to obtain a higher yield at higher protein concentrations, I then conducted another series of experiments for 20 μM mAb1. Unlike the IF settings in **Figure 4-8 A**, I fixed the filler concentration at 2.5 mM while increasing the ligand concentration up to 500 μM (solubility limit). In this case, a decrease in filler:ligand ratio means an increase in ligand:protein ratio. As shown in **Figure 4-8 F**, when more ligands were added, the precipitation yield increased but plateaued at around 90%. These results suggest that the ligand:protein ratio is critical and outweighs the filler:ligand ratio in protein capture. Importantly, the high precipitation yield for the 20 μM mAb1 concentration is a very promising result, as this value approaches to the industrial titer level.[5] Furthermore, the fact that the precipitation yield leveled out after the 250 μM ligand concentration suggests that there exists an optimal ligand density, above which steric hindrance may come to play.

To understand the mechanism of the soluble-insoluble transition of the IF-protein complexes, the IFs under optimized conditions were further investigated ligand for 50:1 IFs with 10:1 ligand:protein molar ratio at different salt concentrations. Salt concentration higher than 1 M was not tested due to the instability of proteins (**Figure 4-10 A**). Results showed that 30-40% proteins were precipitated under no salt conditions (**Figure 4-11 A**). There is a possibility that these proteins with two binding sites could crosslink ligands from different IFs, promoting the formation of large filament networks that tend to precipitate. As more salt was added, the protein precipitation yield increased significantly (**Figure 4-11 A**), which could be attributed to the fact that the addition of salt has a more pronounced effect on the soluble-insoluble transition of IFs. For all salt groups, over 95% filler and ligand molecules were precipitated concomitantly with the target proteins (**Figure 4-11 B** and **C**). Similar result was seen for the IF control. It is reasonable to assume that salt promotes the agglomeration of IFs, leading to more efficient precipitation of proteins that are already bound to IFs. However, high salt concentration is known to increase the risks of protein instability and the formation of high molecular weight aggregates.[321] Moreover, the probability of non-specific precipitation of impurities will increase as well. Precipitation at an even lower salt concentration or without salt altogether can be potentially achieved by further improving the design of IFs to obtain more flexible ligands on IFs and improve the IF-protein interactions.

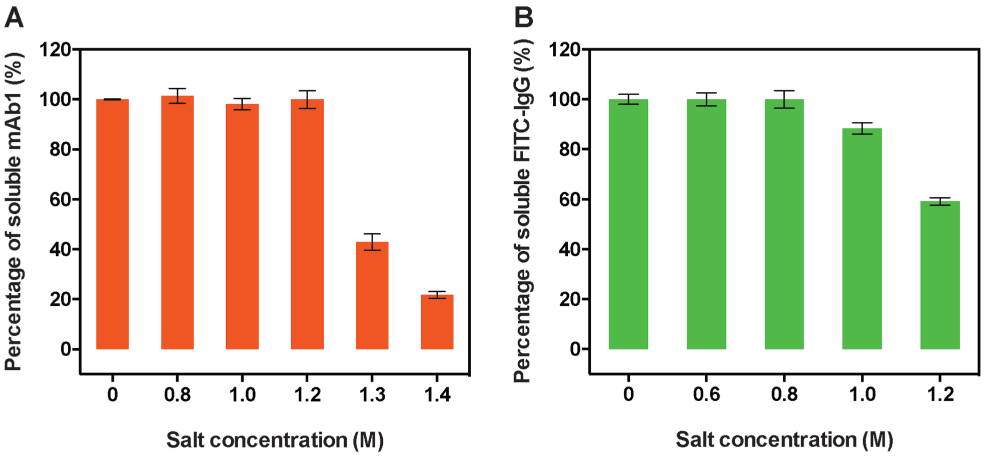

Figure 4-10. Stability of mAb1 (**A**) and IgG (FITC) (**B**) at various salt concentrations. Proteins were incubated with salt for 30 minutes and centrifuged at 15000 rpm for 15 minutes. All experiments were performed in duplicate and the data is shown as mean ± standard deviation.

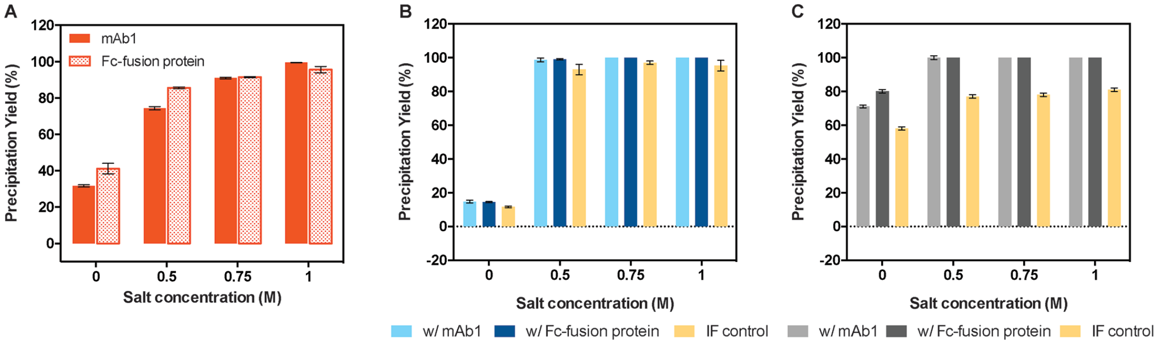

Figure 4-11. Precipitation yields of (**A**) mAb1 and Fc-fusion protein, (**B**) filler, and (**C**) ligand for 50:1 IFs with 10:1 ligand:protein molar ratio at different salt conditions. All experiments were performed in triplicate and the data is shown as mean ± standard deviation.

4.4.3 Selectivity of Co-Assembled IFs

High selectivity is one of the most important characteristics of a precipitant that specifically target proteins while avoiding impurities.[146] To investigate the selectivity of IFs and also to visualize the protein precipitation process, a green fluorescent antibody, IgG (FITC), and a non-specific red fluorescent protein, mCherry (28.8 kDa, pI:6.2), were used for the protein precipitation experiment. IgG (FITC), mCherry, and the mixture of two proteins were incubated with 50:1 IFs at a 10:1 ligand:protein ratio. Individual proteins and protein mixtures were also prepared in PBS as control groups. To trigger the precipitation, 0.75 M was added because the IgG (FITC) was unstable in the 1 M salt solution (**Figure 4-10 B**). As shown in **Figure 4-12 A**, **B**, and **Figure 4-13**, after centrifugation, no precipitates were observed in the control groups (i-iv), while IgG (FITC) was precipitated in the presence of IFs (v). However, red precipitates were barely seen for mCherry (vi), revealing that non-specific protein was not precipitated by IFs. In particular, color separation appeared at the solid-liquid interface in the (vii) group with the mixture of two proteins, allowing for the direct visualization of the favorable selectivity of IFs towards

IgG (FITC). The selectivity was further confirmed by the fluorescence spectra of the supernatants of all groups (**Figure 4-12 C** and **D**). Fluorescence of IgG (FITC) dropped in (v) and (vii) compared to the control groups in (ii) and (iv) after incubation with 50:1 IFs, while fluorescence of mCherry in (vi) and (vii) remained similar to those of control groups (iii) and (iv), further supporting the selective precipitation of IgG (FITC).

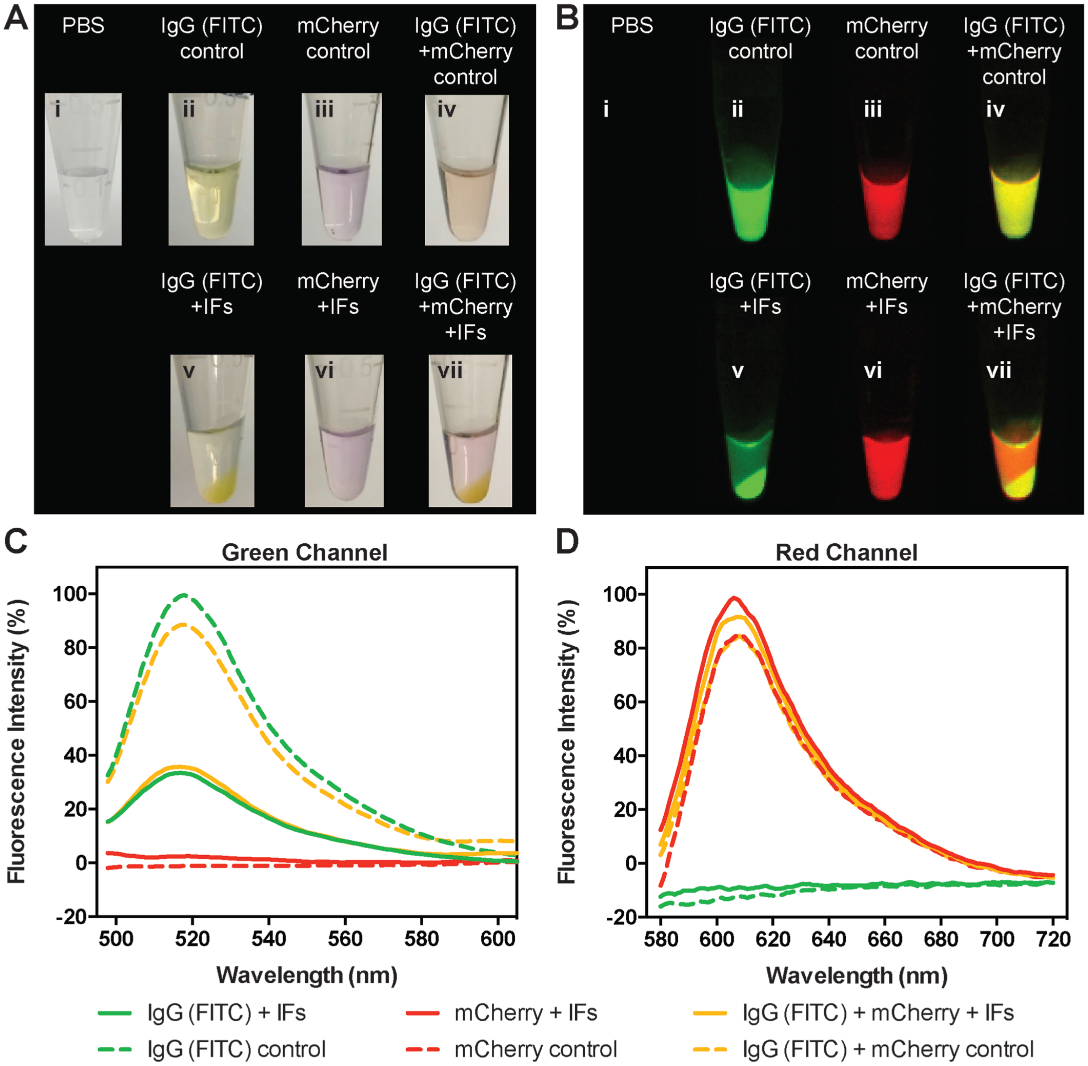

Figure 4-12. Selectivity of co-assembled IFs in precipitating immunoglobulin G (IgG). (**A**) Photographs and (**B**) fluorescence images of i) PBS, ii) IgG (FITC), iii) mCherry, iv) IgG (FITC)+mCherry, v) IgG (FITC)+IFs, vi) mCherry+IFs, and vii) IgG (FITC)+mCherry+IFs. IgG (FITC) and mCherry were incubated with 50:1 IFs and 0.75 M

ammonium sulfate was used to trigger precipitation. Green precipitates were observed in v) and vii), indicating the precipitation of IgG (FITC). However, the precipitation of mCherry was not observed in vi) and vii), showing high specificity of mAb precipitation by IFs. Fluorescence measurements of supernatant in sample i)-vii) on the (**C**) green and (**D**) red channels. Fluorescence of IgG (FITC) dropped in v) and vii) after incubated with 50:1 IFs, while fluorescence of mCherry remained similar with control groups.

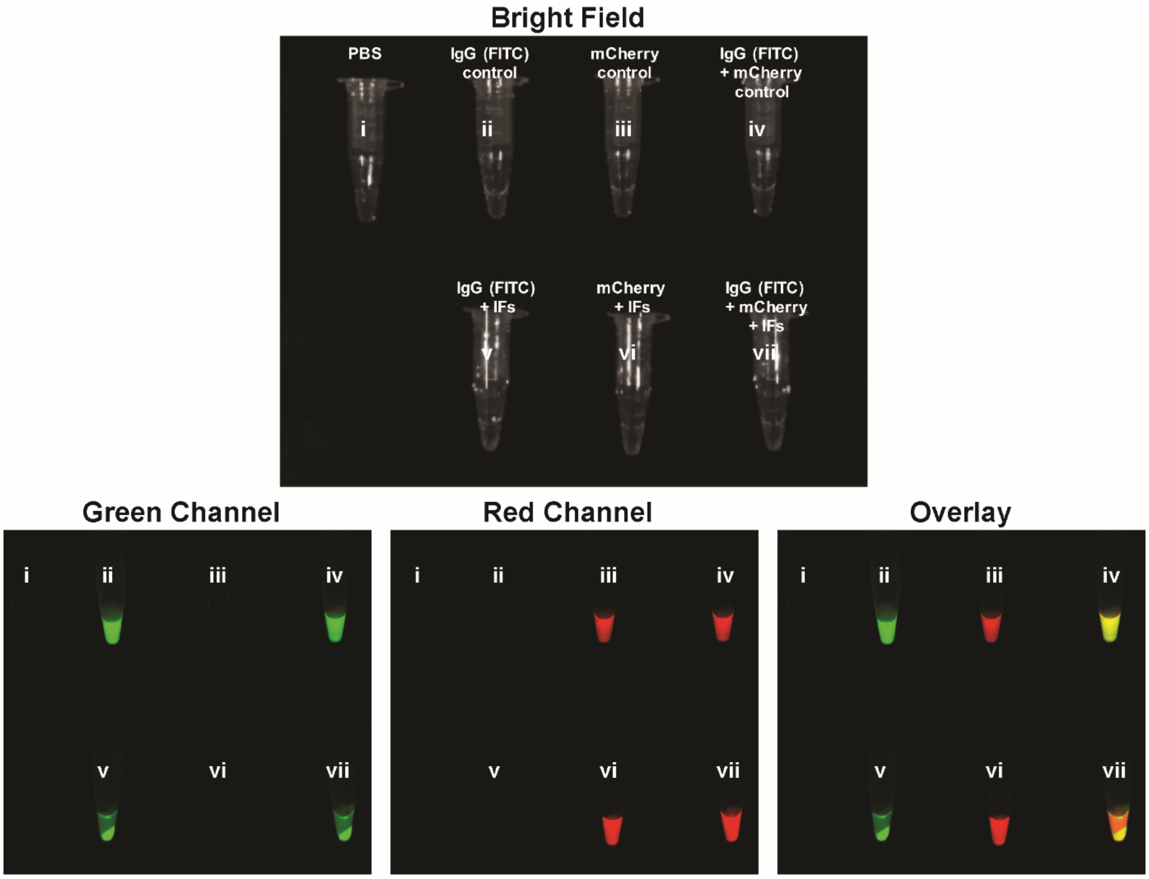

Figure 4-13. Supplementary bright field and fluorescence images for **Figure 4-12**: i) PBS; ii) IgG (FITC) control; iii) mCherry control; iv) IgG (FITC)+mCherry control; v) IgG (FITC) +IFs; vi) mCherry+IFs; vii) IgG (FITC)+mCherry+IFs.

4.4.4 Protein Recovery

Given the reversibility of the soluble-insoluble transition and the mAb binding process, I proceeded to investigate whether the mAb could be recovered from the precipitates. Similar to protein A, the Z33 ligands release the bound target molecules in low pH.[214, 322] After precipitation, most salts were removed along with the supernatant. To redissolve the precipitates, three buffers at pH 3.7, 7.4, and 10.1 were added to the precipitates, respectively. I found that both mAb1 and IFs were insoluble at pH 3.7 (**Figure 4-14 A-C**), while around 80% and 100% mAb1 resuspension yield were obtained for pH 7.4 and pH 10.1 buffer, respectively (**Figure 4-14 A**). Similar resuspension yields were obtained for the filler molecules in pH 7.4 and pH 10.1 buffers (**Figure 4-14 B**). This trend in resuspension yield can be attributed to the pH-dependent solubility of filler molecules. The glutamic acid residues (pKa 4.15) in the filler molecule are barely ionized in pH 3.7, but are negatively charged at neutral or basic pH, leading to a much higher solubility. To maintain the stability of mAbs, I decided to use PBS buffer at pH 7.4 instead of pH 10.1 to resuspend the precipitates, and then transferred the solution to a dialyzer with a 50 kDa cut-off membrane to separate the mAbs (~150 kDa) and IFs (monomeric size <5 kDa). The membrane separation was first conducted in PBS at pH 7.4 for 24 h to remove the filler molecules, and then conducted in elution buffer at pH 3.7 for 24h to remove the unbound ligand molecules. Under the optimized conditions, 100 μL pure mAb1 at 5 μM can be precipitated by the 50:1 IFs with a yield of more than 99% and recovered with a final mAb recovery yield greater than 94% (**Figure 4-14 D**). Meanwhile, more than 99% filler and ligand molecules were eventually removed by the membrane separation process (**Figure 4-14 D**).

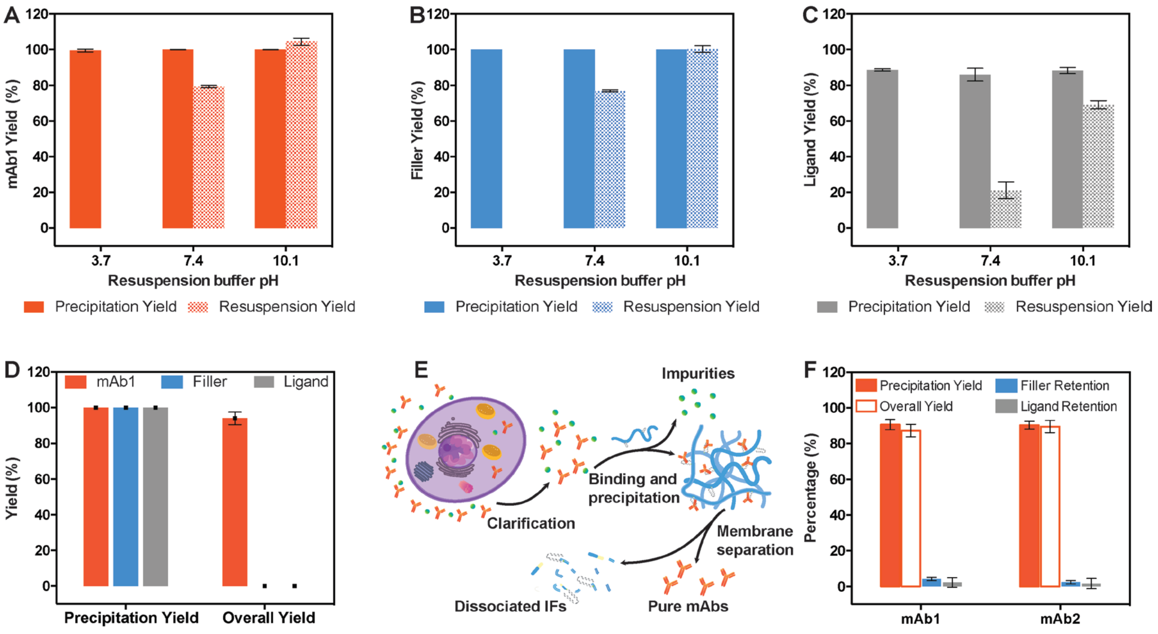

Figure 4-14. mAb recovery and purification. Resuspension yields of (**A**) mAb1, (**B**) filler, and (**C**) ligand molecules in three resuspension buffers at pH 3.7, pH 7.4, and pH 10.1, respectively. The precipitated samples were 50:1 IFs and mAb1 at 10:1 ligand:protein molar ratio with 1 M ammonium sulfate. (**D**) Precipitation and overall yields of mAb1, filler, and ligand molecules after the incubation of pure mAb1 with 50:1 IFs and 1 M ammonium sulfate. (**E**) Schematic illustration of the process of purifying mAbs from CB using IFs. (**F**) mAb precipitation yields, overall yields, and percentage retention of filler and ligand molecules after the whole purification process for mAb1 CB and mAb2 CB. All experiments were performed in triplicate and the data is shown as mean ± standard deviation.

4.4.5 Capture and Recovery of mAbs from Cell Culture Harvest

To demonstrate the feasibility for potential industrial applications, I explored the capture and recovery of 5.8 mg/mL mAb1 and mAb2 (human IgG4, 144 kDa, pI:7.7, a commercialized antibody for cancer treatment) from clarified bulk (CB) of cell culture harvest using optimized IF system (**Figure 4-14 E** and **F**). mAbs were precipitated with a yield about 90%. After the entire process, 87% and 89% of mAb1 and mAb2 were fully recovered (**Figure 4-14 F**), respectively. Meanwhile most filler and ligand molecules were removed (**Figure 4-14 F**) after membrane separation, showing that these materials would introduce little to no additional contaminants. Compared to pure mAb1, the lower precipitation yields may be attributable to the macromolecular crowding in the CB environment.[323] The presence of high concentration macromolecular impurities such as host cell proteins and DNAs may alter the molecular motions, accessibility, and intermolecular interactions for both IFs and the target mAbs, leading to compromised mAb binding efficiency.[324] To further prove the selectivity of IFs in CB conditions and to confirm the purity of the mAb product, the purity level of the mAbs during the purification process was tracked with size exclusion chromatography (SEC). The result shows most impurities were left in the supernatant, suggesting a promising selectivity of the IFs for isolating the target mAbs from impurities (**Figure 4-15**). A single peak was observed for both purified mAb1 and mAb2 with decent peak shape and the elution time remained the same, suggesting the high purity and good quality of these mAbs after purification.

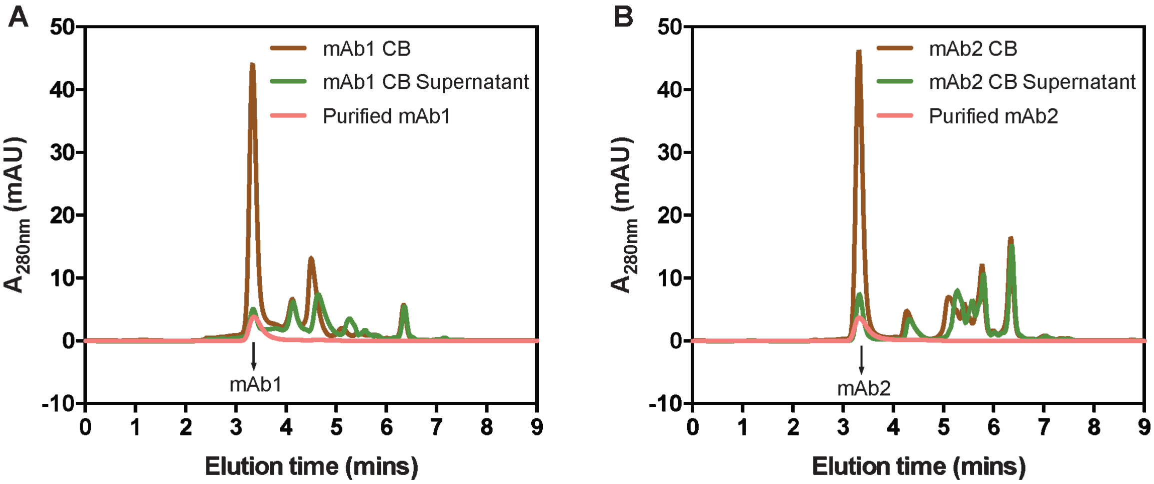

Figure 4-15. SEC spectra of the sample solutions for CB, CB supernatant, and product pool after membrane separation for (**A**) mAb1 and (**B**) mAb2.

4.5 Conclusion

In conclusion, I demonstrated the design and construction of a supramolecular copolymer system with multiple reversible transitions for successful capture, precipitation, and recovery of mAbs. Z33 affinity ligands were incorporated into the IF design to achieve reversible mAb binding. The reversible soluble-insoluble transition of co-assembled IFs enables the precipitation and redissolution of mAbs. The reversible assembly of IFs favors convenient removal of IFs from the mAb product pool. I found that multiple experimental parameters, in particular the filler:ligand molar ratio, ligand:protein molar ratio, and salt concentration could all affect the mAb precipitation and recovery yields. Under optimized conditions, more than 99% pure mAb1 was precipitated and more than 94% of pure mAb1 was recovered after resuspension and membrane separation. Meanwhile, little to no IFs were found to remain in the mAb product pool. I confirmed that the IF system shows great selectivity towards IgG over a control protein, mCherry. Furthermore, I demonstrated the capture and recovery of mAbs from cell harvest with promising overall yields and IF clearance performance.

While highly promising, the reported system can benefit from further optimization in molecular design to achieve better purification efficiency under low salt concentrations. Membrane separation is another unit operation in this work that contributes to the overhead of the purification process. However, membrane separation could also be used in the precipitation step to separate the precipitates and supernatant, thus combining the two unit operations into one. Future work will seek to evaluate process scalability and robustness and analyze the overall process cost, time, efficiency, and product quality. After further development, I envision that the co-assembled IFs can eventually serve as an economical alternative to the traditional chromatography methods for highly efficient purification of mAbs and other proteins of interest. Additionally, the reported system shows a great potential for new applications involved with molecular recognition and targeting and may be particularly useful for the purification and concentration of therapeutic antibodies in convalescent plasma for COVID-19 treatment.

5 Manipulation of Epitope Radial Topography in High-Affinity Supramolecular Polymers for Binding-Triggered Antibody Precipitation

5.1 Overview

Supramolecular polymers, formed by self-assembly of monomeric units, represent attractive materials for various biomedical applications including drug delivery, regenerative medicine, and biosensing. Challenges still remain in the strategy for epitope presentation on supramolecular polymers to obtain their optimal bioactivity. Here I report on the manipulation of epitope radial topography in supramolecular immunofibers (IFs) for the binding-triggered precipitation of monoclonal antibodies. A series of IF building blocks are rationally designed by incorporating various oligo ethylene glycol (OEG) or polyethylene glycol (PEG) linkers for more efficient presentation of the mAb-binding peptide on the IF surface. The results suggest that the mAb-IF interactions could be significantly improved via increasing the linker length; however, too long a linker has an adverse impact on the function of the resultant supramolecular polymers. Through the optimization of several key parameters that impact the mAb precipitation, I demonstrate that the desired IF system is able to precipitate mAbs without the use of additional salt and promising mAb precipitation and elution yields were obtained, especially when using a sequential precipitation strategy. I believe these results shed important light on designing supramolecular nanostructures for specific molecular recognition and the IF system could be potentially used for purification of mAbs and other proteins of interest.

5.2 Introduction

Supramolecular assembly is a fascinating bottom-up approach to construct hierarchical and functional nanostructures.[42, 325-329] Among the recently developed supramolecular polymers, peptide-based materials are notably appealing because of their biocompatibility, biodegradability, and low toxicity.[40, 330-336] The presentation of bioactive epitopes on a supramolecular substrate enables the active-targeting of the nanostructures for efficient molecular/cellular recognition and signaling, as well as the precise delivery and accumulation of therapeutics at desired sites.[315, 337-338] In light of the steric hindrance introduced by anchoring these epitopes on supramolecular polymer surfaces, the epitope spatial arrangement plays an important role in regulating their functionality.[257, 316, 339] Co-assembly of bioactive building units with an inert molecule has been shown to effectively modulate the epitope density and achieve enhanced bioactivities.[316-317] Meanwhile, the use of flexible linkers for spacing out the epitope in the radial direction of the resultant nanostructures is equally essential to improve the epitope accessibility and their interactions with the target biomolecules.[45, 339-340]

Affinity precipitation has been increasingly explored as a promising alternative to protein A chromatography for the purification of monoclonal antibodies (mAbs) and other therapeutic proteins.[6, 9, 341] The use of salt to trigger or aid the precipitation of antibodies is prevalent during the purification process.[342-343] However, high salt concentration is known to increase the risks of protein instability and the non-specific precipitation of impurities present in the solution.[344-345] Effort has been devoted to minimizing the usage of additional salt (besides that present in the cell culture media for protein stabilization) by developing more advanced protein precipitating systems.[346] In the previous effort to construct supramolecular immunofibers (IFs) for the affinity precipitation of mAbs, the functional building unit containing Z33, a protein A mimicking peptide that binds to the Fc-portion of immunoglobulin G (IgG) from most mammalian species in a pH-specific manner, was co-assembled with an inert component to effectively modulate the distribution of Z33 on the IF surface.[214, 310] However, this system was limited by the high ammonium sulfate (abbreviated as "salt" below) concentration necessary to achieve decent mAb precipitation yields.

To overcome the shortcomings of the IF system, I hypothesized that in addition to modulating the Z33 distribution by co-assembly, increasing the linker length for Z33 conjugation would further improve mAb-IF interactions due to the increased Z33 flexibility and accessibility. Given the dual Fc-binding sites on mAbs, specifically IgG, and the multivalence of IFs, the enhanced multivalent mAb-IF binding could potentially result in IF crosslinking into large complexes and consequently facilitate mAb precipitation under low salt conditions. OEG (or PEG) linkers have been widely used in bioconjugation, benefiting from their water solubility, chain flexibility, and lack of toxicity.[347-349] To prove this hypothesis, a series of IF systems with various OEG (or PEG) linkers for Z33 presentation are designed and constructed in the present work. By comparing the mAb precipitation performances of different IF systems, I demonstrated the importance of linker length for the mAb-IF interaction and precipitation under low salt conditions. Moreover, the key parameters that impact the mAb precipitation yield are identified and discussed. I also demonstrated the promising mAb precipitation and elution yield using the sequential precipitation strategy.

5.3 Experimental Procedures

5.3.1 Materials and Molecular Synthesis

All Fmoc amino acids and resins were obtained from Advanced Automated Peptide Protein Technologies (Louisville, KY). The pure mAb1, and mAb1 and mAb2 in clarified Chinese hamster ovary (CHO) cell culture harvest were obtained from Bristol-Myers Squibb (Devens, MA). The cell culture was clarified using depth filtration. The Fmoc-N-amido-O(P)EGn-acids were purchased from PurePEG (San Diego, CA) and BroadPharm (San Diego, CA). Lauric acid (C12) was obtained from MilliporeSigma (St. Louis, MO). Unless otherwise specified, all other reagents were obtained from VWR (Radnor, PA) and used as received without further purification.

Filler and ligand molecules were synthesized using the method described previously. In brief, C12-VVEE and C12-VVKK$[O(P)EG]_n$GGZ33 (n=4, 8, 12, 16, 36, 45) were synthesized on the Liberty Blue automatic microwave peptide synthesizer (CEM Corporation, Matthews, NC) using standard 9-fluorenyl-methoxycarbonyl (Fmoc) solid phase synthesis protocols. Crude products were cleaved from the solid support using a mixture of trifluoroacetic acid (TFA)/ triisopropylsilane (TIS)/H_2O in a ratio of 92.5:5:2.5 for 2.5 h. Excess TFA was removed by evaporation and ice-cold diethyl ether was added to precipitate the crude products, followed by centrifugation. The crude products were purified by preparative RP-HPLC using a Varian Polymeric Column (PLRP-S, 100 Å, 10 μm, 150×25 mm) at 25 °C on a Varian ProStar Model 325 preparative HPLC (Agilent Technologies, Santa Clara, CA) monitored at 220 nm for the absorbance of peptide segments. Collected fractions were analyzed by MALDI-TOF (BrukerAutoflex III MALDI-TOF instrument, Billerica, MA) and product-containing fractions were then lyophilized (Labconco^{TM} FreeZone −105 °C, 4.5 L freeze dryer, Kansas City, MO) and stored at −30 °C.

5.3.2 CMC Measurement

The CMCs of the ligand molecules in PBS were determined using Nile Red, a hydrophobic dye that undergoes changes in both fluorescence intensity and emission wavelength (a blue-shift) upon partition into the hydrophobic domains of supramolecular assemblies. Nile Red was initially dissolved in acetone at 20 μM and 10 μL aliquots were loaded into several centrifuge tubes. After the acetone evaporated under room temperature, 500 μL fresh ligand solutions in PBS at various concentrations were added into the centrifuge tubes containing dry Nile Red and aged overnight for assembly. Fluorescent spectra of Nile Red were then monitored by a Fluorolog fluorometer (Jobin Yvon, Edison, NJ) with fixed excitation wavelength at 560 nm; emission spectra were monitored at 580-720 nm. The ratio of the emission intensity at 635 nm (emission maximum of Nile red in a hydrophobic environment) to that at 660 nm (emission maximum of Nile red in an aqueous environment) was then plotted against the tested concentrations to obtain a transition curve and the CMC value was determined by the intersection of the two fitting lines.

5.3.3 Self-Assembly, Co-Assembly, and TEM Imaging

For self-assembly, filler or ligand molecules were dissolved in PBS (20 mM sodium phosphate, 150 mM sodium chloride, pH 7.4) to reach a final concentration of 2.5 mM or 400 μM, respectively, and aged for 24 h at room temperature. To construct co-assembled IFs, filler and ligand molecules were pretreated with hexafluoroisopropanol (HFIP) to eliminate any pre-existing nanostructures that could be possibly formed during the synthesis and purification process. After HFIP evaporation, filler and ligand molecules were dissolved in PBS (20 mM sodium phosphate, 150 mM sodium chloride, pH 7.4) to reach desired concentrations and aged for 24 h at room temperature. 10 μL stock of each sample solution were then spotted on carbon film coated copper grids with 400 square mesh (Electron Microscopy Sciences, Hatfield, PA) and the excess was removed with filter paper to leave a thin film of sample on the grid. After letting the sample dry for 5 min, 10 μL 2% uranyl acetate was added to the sample grid, and the excess was removed after 30 s. All samples were dried for at least 3 h before imaging. Bright-field TEM imaging was performed on a FEI Tecnai 12 TWIN Transmission Electron Microscope and all TEM images were required by a SIS Megaview III wide-angle CCD camera.

5.3.4 CD Spectroscopy

The CD spectra of self-assembled ligand molecules were collected on a Jasco J-710 spectropolarimeter (JASCO, Easton, MD) using a 1 mm path length quartz UV-vis absorption cell (ThermoFisher Scientific, Pittsburgh, PA) at 25 °C. A background spectrum of the solvent was acquired and subtracted from the sample spectrum. The collected data was averaged from three scans and normalized with respect to the ligand concentration.

5.3.5 ITC Experiment

ITC experiments were performed using a high precision VP-ITC titration calorimetric system (Microcal Inc.). 40 μM ligand solution was titrated with 100 μM mAb1 in PBS (pH 7.4) at 25 °C. The heat evolved after each injection was obtained from the integral of the calorimetric signal. The heat associated with the binding between ligand molecule and mAb1 was obtained by subtracting the heat of dilution. Analysis of the data was performed using MicroCal Origin package.

5.3.6 mAb Precipitation Experiment

IF stock solutions at desired filler and ligand concentrations were prepared one day before the precipitation experiment. Pure mAb1 from a concentrated solution (448 µM, 64.5 g/L) was then added into 100 µL IF solutions to reach a desired final concentration and incubated for 30 min at room temperature. The solution was then centrifuged at 15000 rpm for 15 minutes. For 1 M salt group, ammonium sulfate was added to the mAb-IF mixtures to reach final concentration of 1 M and incubated for another 30 min before centrifugation. The supernatant was taken out and analyzed by ProA-HPLC (POROS™ A 20 µm Column, Stainless Steel, 2.1 x 30 mm, 0.1 mL) to determine mAb concentration. The precipitated amount of each species was calculated by subtracting the amount in the supernatant from the amount added. The precipitation yield was calculated by dividing the precipitated amount by the amount added.

5.3.7 Sequential Precipitation and mAb Elution

Three IF stock solutions, IF1(2.5 mM filler, 250 µM O16), IF2 (2.5 mM filler, 750 µM O16), and IF3 (2.5 mM filler, 200 µM O16), were prepared one day before the precipitation experiment. Pure mAb1 from a concentrated solution (448 µM, 64.5 g/L) was added into 100 µL IF1 and 100 µL IF2 to reach a desired final concentration of 40 µM and 80 µM, respectively. After a 4-hour incubation, the samples were then centrifuged at 15000 rpm for 15 minutes and the supernatant was transferred to 100 µL IF3 for another 4-hour incubation and subsequent centrifugation. 200 µL PBS and 400 µL elution buffer (40 mM sodium acetate, pH 3.7) were then used to wash and resuspend the precipitates from two precipitation steps. The supernatant from each precipitation step, wash step, and elution step were analyzed by ProA-HPLC (POROS™ A 20 µm Column, Stainless Steel, 2.1 x 30 mm, 0.1 mL) to determine mAb concentration.

5.4 Results and Discussions

5.4.1 Molecular Design and Characterization

As described in Chapter 4, the co-assembled IF system is formed by filler and ligand molecules. The filler molecule, C12-VVEE, is designed to modulate the distribution of the ligand molecule in the co-assembled IFs (**Figure 5-1 A** and **Figure 5-2**). The Z33 peptide, which possesses a two-helix motif, is conjugated on the *C*-terminus of the ligand molecule, C12-VVKK[Linker]Z33, for specific mAb capture (**Figure 5-1 A** and **Figure 5-2**). In the previous ligand design (G2), a double glycine (GG) segment was inserted as a linker between the IF surface and Z33. To further increase the Z33 flexibility and accessibility, a series of ligand molecules, O4, O8, O12, O16, O36, and P2000, with various OEG (or PEG) linkers (n=4, 8, 12, 16, 36, 45) were designed and summarized in **Table 5-1**. The calculated length of fully extended linkers and molecular weight of each ligand molecule are also listed in **Table 5-1**. As shown in **Figure 5-1 B**, with increasing OEG (or PEG) length, the Z33 is expected to be extended further away from the IF surface. I hypothesized that the incorporation of OEG (or PEG) linkers would further reduce the steric hindrance in the radial direction of the IFs and improve mAb-IF interactions for both Fc binding sites. The filler and ligand molecules were synthesized using automated solid-phase peptide synthesis (SPPS) methods. Details of the chemical structures and molecular characterization are shown in **Figure 5-2** to **Figure 5-4**.

Table 5-1. Summary of ligand molecule design with various linkers.

Ligand Molecule C12-VVKK[Linker]Z33	Linker	Calculated Length of Fully Extended Linker (nm)	Molecular Weight (kDa)	CMC (μM)
G2	GG	0.7	4.9	2.0
O4	OEG4	1.9	5.0	5.1
O8	OEG8	3.5	5.2	6.0
O12	OEG12	5.1	5.3	8.5
O16	OEG16	6.7	5.5	10.5
O36	OEG36	14.6	6.4	9.1
P2000	PEG2000	18.2	6.8	8.1

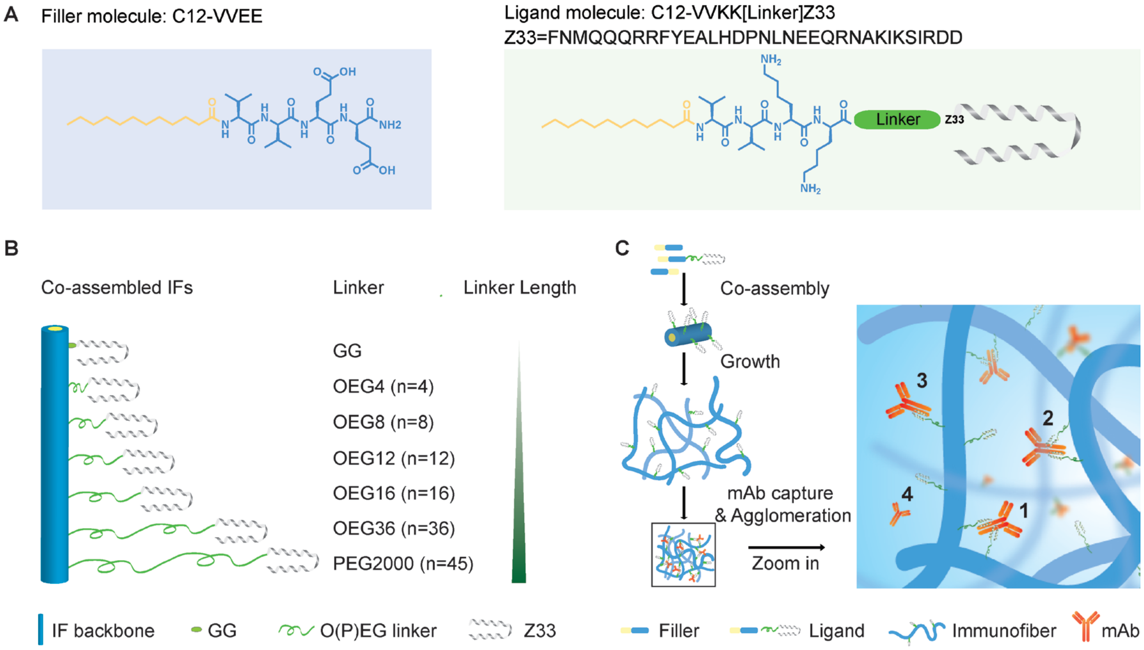

Figure 5-1. Molecular design of the IF building units with OEG (or PEG) linkers and the formation of IFs for mAb capture. (**A**) Chemical structures of the filler molecule, C12-

VVEE, and the ligand molecules, C12-VVKK[Linker]Z33. (**B**) Schematic illustration of the ligand molecule design with various linkers and the effect of linker length on the presentation of Z33 peptide on co-assembled IFs. **(C)** Co-assembly of filler and ligand molecules into supramolecular IFs and four possible states of mAbs in an IF solution: **1**) Two Fc-portions of a mAb bound to two ligands from two different IFs. **2**) Two Fc-portions of a mAb bound to two adjacent ligands from the same IF. **3**) Only one Fc-portion of a mAb bound to one ligand on an IF. **4**) Free mAbs in the solution bound to zero, one, or two monomer ligands that are not assembled in IFs.

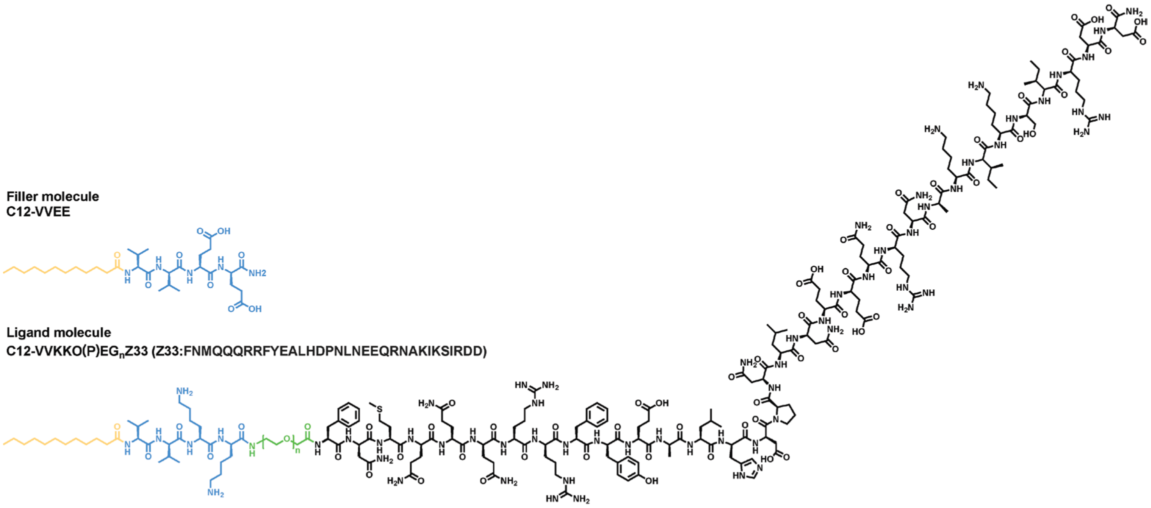

Figure 5-2. Chemical structures of filler and ligand molecule. The alkyl chain (C12), VVKK/EE, OEG$_n$, and Z33 are shown in yellow, blue, green, and black, respectively.

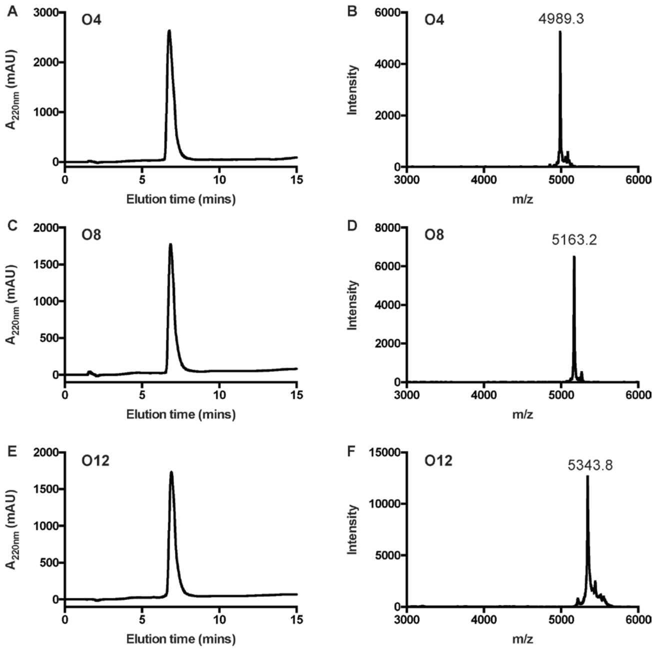

Figure 5-3. RP-HPLC and MALDI-TOF MS characterization of O4 (**A-B**), O8 (**C-D**), and O12 (**E-F**).

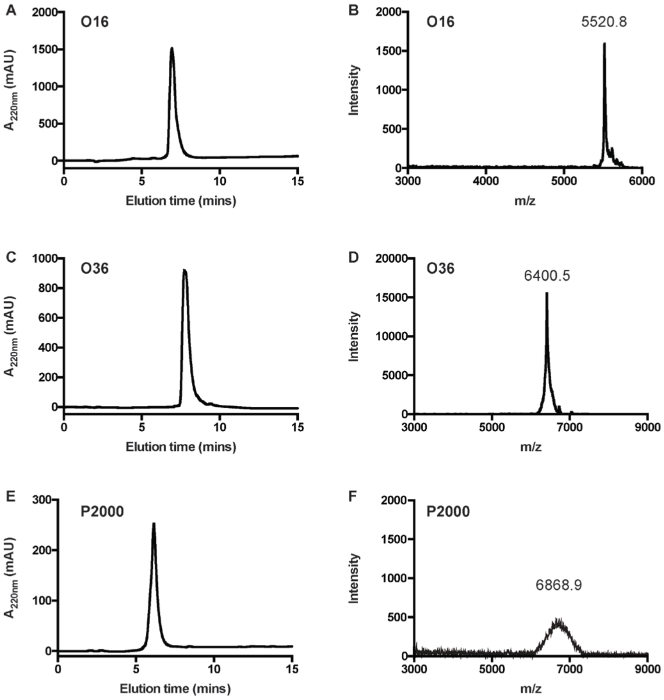

Figure 5-4. RP-HPLC and MALDI-TOF MS characterization of O16 (**A-B**), O36 (**C-D**), and P2000 (**E-F**).

Figure 5-1 C illustrates the spontaneous co-assembly process of filler and ligand molecules in aqueous solution, forming filamentous IFs with Z33 displayed on the IF surface. Upon the addition of mAbs, there are four possible states of mAbs in the IF solution. **States 1** and **2** represent two Fc-portions of a mAb bound to two ligands from two different IFs or the same IF, respectively. In **State 3**, only one Fc-portion of a mAb is bound to one ligand on an IF. Given the equilibrium between ligand monomers and co-assembled structures, it's also possible that in **State 4** mAbs are bound to zero, one, or two monomer ligands in the solution instead of those assembled in IFs. mAb binding and precipitation represent two separate process. The previous results showed that 1 M salt was not able to precipitate mAb1 directly, but it served as a strong charge screening agent to precipitate almost all IFs and thus precipitate mAbs that are bound to IFs (**State 1-3**). Under no salt conditions, however, binding to IFs may not be sufficient for mAbs to be precipitated. I speculate that the key to the precipitation of mAbs under no salt conditions lies in the formation of the cross-linked mAb-IF complexes, which is mainly triggered by mAbs in **State 1**. In this regard, increasing the linker length could probably promote the mAb binding to the Z33 peptides on different IFs and thus increase the **State 1** probability.

5.4.2 Molecular Assembly and Characterization

To estimate the behavior of the filler and ligand molecules in the co-assembled IFs, I first investigated their self-assembly properties in PBS, pH 7.4. With OEG (or PEG) linkers, the critical micelle concentrations (CMCs) of ligand molecules are relatively higher than the previous G2 ligand, ranging from 5.1 to 10.5 μM (**Table 5-1** and **Figure 5-5**). The CMC decrease seen in O36 and P2000 may relate to the entanglement of long PEG chains. As shown in Chapter 4, the filler molecule is able to self-assemble into filamentous structures with a diameter of 7.4 ± 0.6 nm (**Figure 5-6 A**), showing *β*-sheet characteristic hydrogen bonding. Representative transmission electron microscopy (TEM) images reveal that each of the ligand molecules can self-assemble into filamentous structures with diameters of 11.1 ± 0.9 nm (O4), 12.6 ± 1.2 nm (O8), 13.6 ± 1.2 nm (O12), 14.9 ± 1.3 nm (O16), 18.5 ± 1.8 nm (O36), 19.3 ± 2.0 nm (P2000), respectively (**Figure 5-6 B-G)**. As expected, the IF diameter increased with the increase of the linker length. To gain insight into the molecular packing within the self-assembled ligand molecules, the circular dichroism (CD) spectra were collected for each of the newly designed ligand molecules. The negative peaks around 208 nm and 222 nm suggest the preservation of *α*-helix secondary structures in all the self-assembled ligand molecules (**Figure 5-6 H**), as shown in the original Z33 peptide.[310] Isothermal titration calorimetry (ITC) were used to determine the binding affinity between a monoclonal human IgG1 (144 kDa, abbreviated as "mAb1" below) and ligand molecules O4-O16. The dissociation constant K_d ranges between 50 nM and 70 nM, similar to the reported value (26 nM) for free Z33 peptide, showing that the conjugation of OEG linkers within ligand molecules would not significantly impair their mAb binding affinity (**Figure 5-7**).[214, 310]

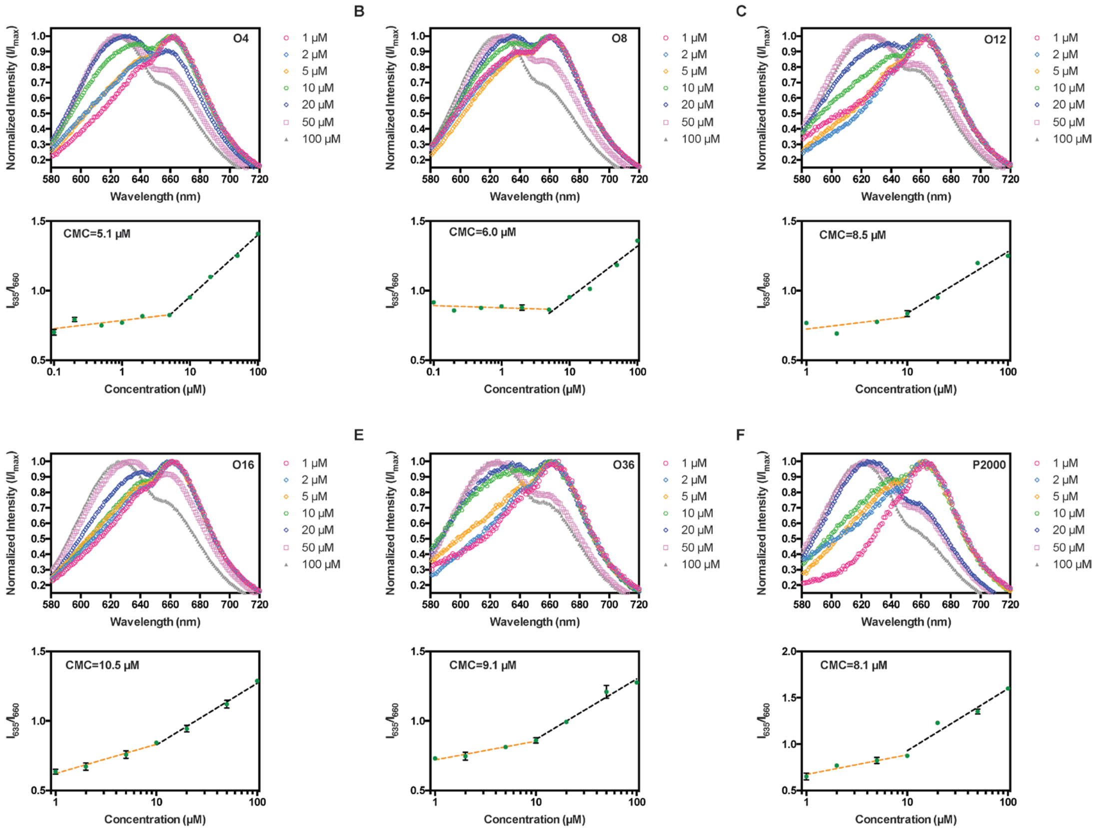

Figure 5-5. CMC measurement of O4-P2000. Normalized emission spectra of the reporter dye Nile Red monitored by a Fluorolog fluorometer (Jobin Yvon, Edison, NJ) after incubation with a series of concentrations of ligand molecules. Plotting the ratio of intensity at 635 nm (emission maximum of Nile red in a hydrophobic environment) to that at 660 nm (emission maximum of Nile red in an aqueous environment) against the tested concentration indicates the transition that occurs when the concentration exceeds the CMC. The CMC value for each ligand molecule was then determined by the intersection of the two fitting lines.

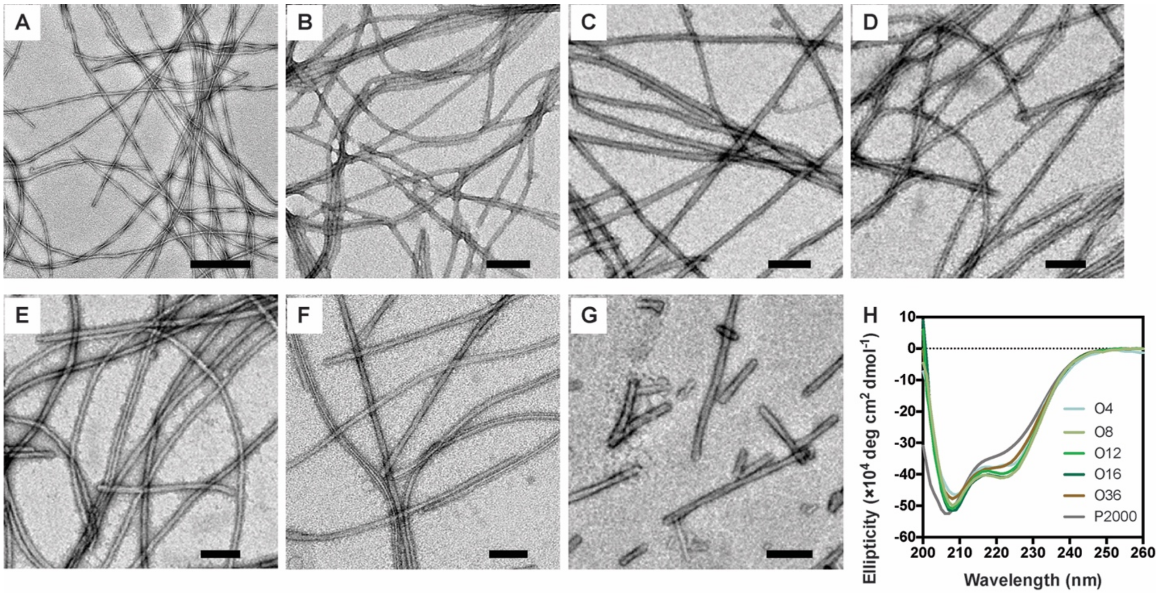

Figure 5-6. Characterization of filler and ligand molecules. Representative TEM images of self-assembled filler and ligand molecules (**A**:C12-VVEE, **B**:O4; **C**:O8; **D**:O12; **E**:O16; **F**:O36; **G**:P2000) in PBS with a diameter of 7.4 ± 0.6 nm, 11.1 ± 0.9 nm, 12.6 ± 1.2 nm, 13.6 ± 1.2 nm, 14.9 ± 1.3 nm, 18.5 ± 1.8 nm, 19.3 ± 2.0 nm, respectively. Diameters are given as mean ± SD (n = 30). Scale bars: 100 nm. (**H**) Normalized CD spectra of self-assembled ligand molecules with different OEG (or PEG) linkers suggest the formation and retention of *α*-helix secondary structures.

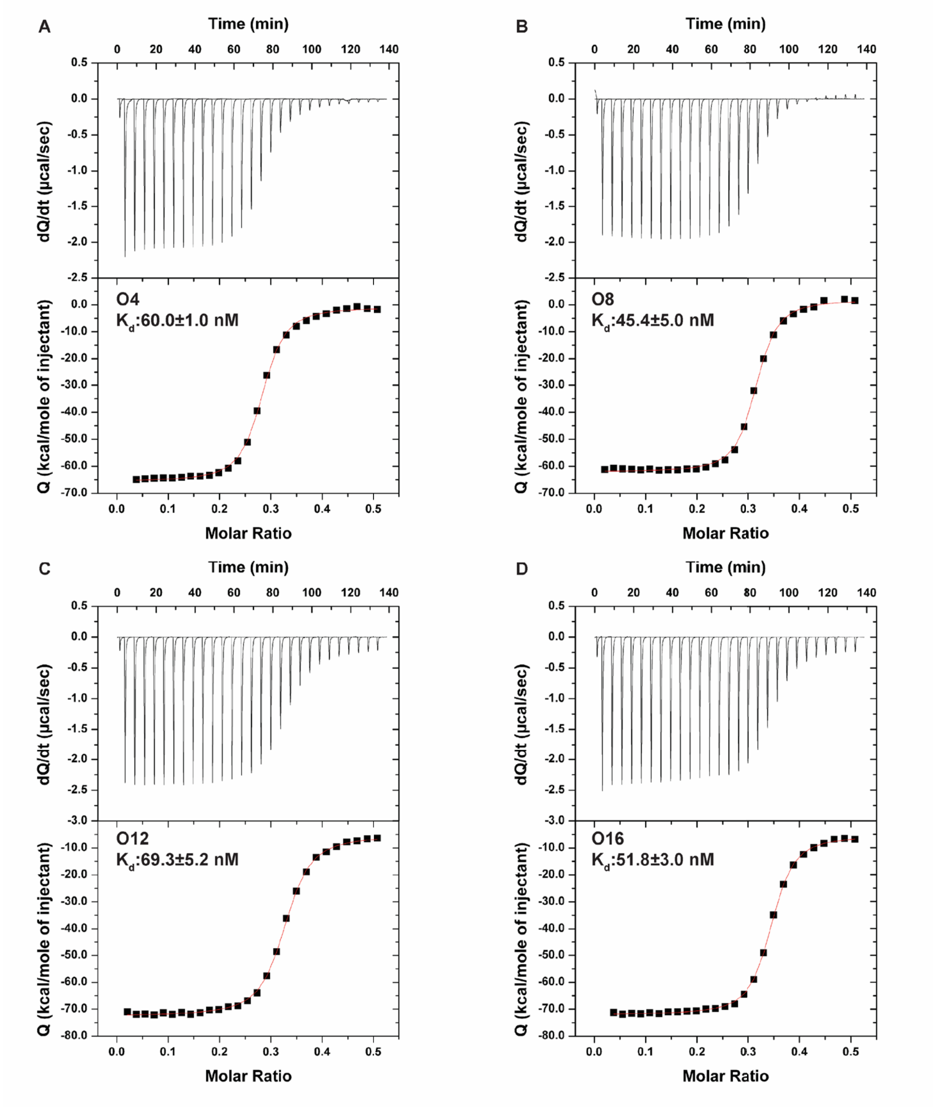

Figure 5-7. ITC profiles and binding curves for the stepwise injection of 100 µM mAb1 into 40 µM (**A**) O4, (**B**) O8, (**C**) O12, (**D**) O16 at 25 °C in PBS, pH 7.4.

5.4.3 Impact of Linker Length and Ligand Selection

To compare the ligand performance, 100 µM ligand molecules were individually co-assembled with 2.5 mM filler molecules in 100 µL PBS (pH 7.4). The filler molecule at 2.5 mM (solubility limit) was found to give the best mAb precipitation results and was consistently used in this work. Pure mAb1 from a stock solution was then added into different IF solutions to reach a final concentration of 20 μM and incubated for 30 min at room temperature. To investigate salt effects on the mAb precipitation yield, two parallel experiments were performed for each co-assembled IF system: one with 1 M salt and one without salt (**Figure 5-8 A**). After centrifugation, the supernatant was analyzed by ProA-HPLC to determine the remaining mAb concentration and calculate the mAb precipitation yield. With 1 M salt, the mAb precipitation yield showed significant improvement from 65% to higher than 88% when replacing the GG linker with O(P)EG linkers in the ligand design. In particular, greater than 95% mAb precipitation yields were obtained for O4-O36. Since there's no bias against the IF precipitation efficiency under 1 M salt conditions, this mAb precipitation yield increase from G2 to the new ligand molecules with OEG (or PEG) linkers specifically reflects the significant improvement in the mAb binding efficiency as a result of the increased linker length and flexibility. A slight drop in the mAb precipitation yield was seen for P2000, likely due to the entanglement of long PEG chains that undermines the accessibility of the Z33 peptide for mAb capture.

Under no salt conditions, the mAb precipitation yields were generally lower than salt groups, while an upward trend was observed with an increase of the OEG linker length. Unlike the salt group, the mAb precipitation yield under no salt conditions was determined by a combination of mAb binding efficiency and the precipitation efficiency of the mAb-IF complexes. From O4 to O36, there are no obvious differences in the mAb binding efficiency as indicated by the salt group data set. The increase in the mAb precipitation yield under no salt conditions represents an enhancement in the mAb precipitation efficiency, possibly caused by the improved crosslinking between IFs. More importantly, the yield difference between 1 M salt and no salt groups was gradually diminished with increasing the linker length, leading to a less than 10% yield discrepancy for O36. This was considered very promising for mAb precipitation, in that the improved mAb-IF interactions achieved by using OEG or (PEG) linkers could potentially substitute for the salt contribution to mAb precipitation.

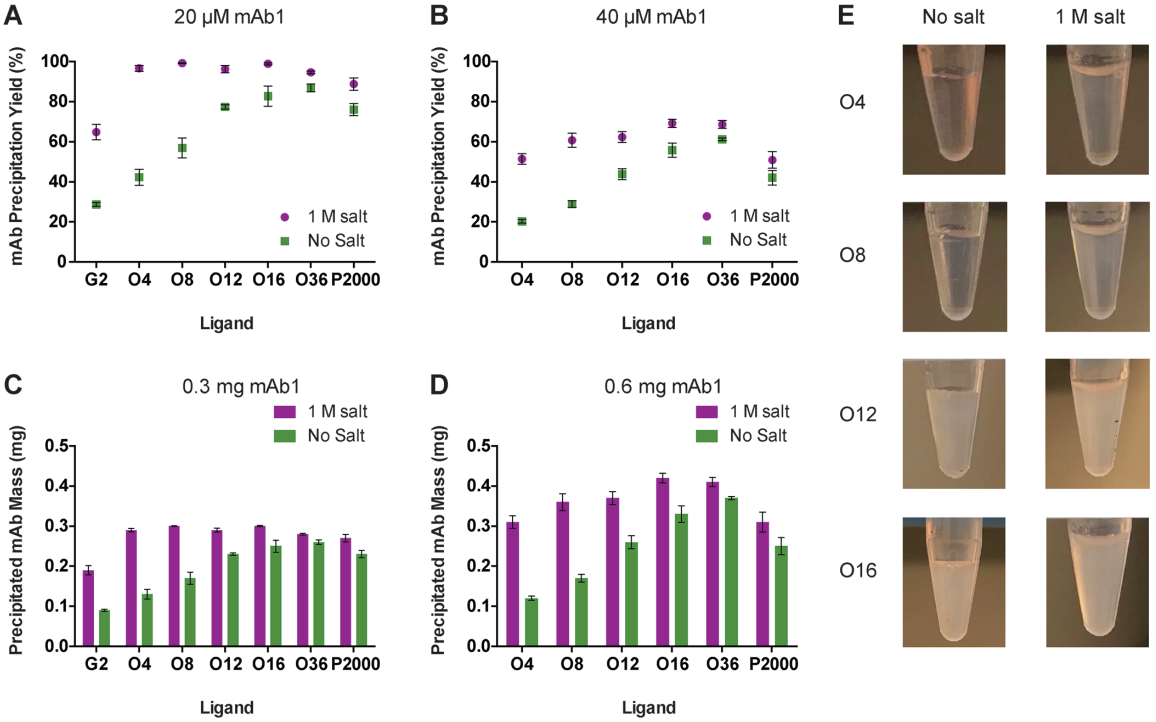

Figure 5-8. Comparison of mAb precipitation performance of IFs with different ligand molecules. mAb precipitation yields for (**A**) 20 µM and (**B**) 40 µM mAb1 incubated with various co-assembled IFs (2.5 mM filler, 100 µM ligand) under 1 M salt or no salt conditions. Precipitated mAb mass from 100 µL samples of (**C**) 20 µM (0.3 mg) and (**D**) 40 µM (0.6 mg) mAb1 incubated with various 100 IFs (2.5 mM filler, 100 µM ligand) under 1 M salt or no salt conditions. (**E**) Photographs of co-assembled IFs (2.5 mM filler, 100 µM ligand) after mixed with 40 µM mAb for 5 min under 1 M salt or no salt conditions. All experiments were performed in triplicate and the data is shown as mean ± standard deviation.

To confirm the above observation and have a preliminary understanding of the mAb binding capacity for this IF system, the experiments were repeated with a higher mAb1 concentration (40 μM). Similar yield trends were observed in **Figure 5-8 B**, except for a slightly upward trend in the 1 M salt group for O4-O36, indicating an improvement in mAb binding efficiency with increasing the OEG linker length. Despite the consistent drop in the mAb precipitation yield from 20 to 40 μM mAbs, the precipitated mAb mass for a 100 μL sample (20 μM:0.3 mg; 40 μM:0.6 mg) were actually similar or higher for 40 μM mAbs (**Figure 5-8 C-D)**, showing that the Z33 peptide displayed on the IF surfaces were not fully saturated by 20 μM mAb1 and could potentially be further utilized if more mAbs were added.

The difference in mAb precipitation yield can also be revealed by the cloudiness of the IF solution. IF solutions of O12, O16, O36, and P2000 became cloudy within 5 minutes after the mAb addition, which was not seen in the first three IF systems. **Figure 5-8 E** shows the sample vials of O4-O16 IFs after being mixed with 40 μM mAb1 for 5 min under 1 M salt or no salt conditions. Generally, the cloudiness of the salt groups is relatively higher than the no salt groups, suggesting a higher mAb precipitation yield for the salt groups. Meanwhile, the cloudiness increases from O4 to O16 in accordance with the yield trend shown in **Figure 5-8 B**. The results here demonstrated that the increase of the linker length can simultaneously improve the mAb binding efficiency of the ligand molecules as well as the precipitation efficiency of the mAb-IF complex. Although O36 shows the best mAb precipitation yields in all conditions, O16 is more desirable in terms of the synthesis yield and material cost and was selected for the subsequent experiments.

5.4.4 Optimization of mAb Precipitation under No Salt Conditions

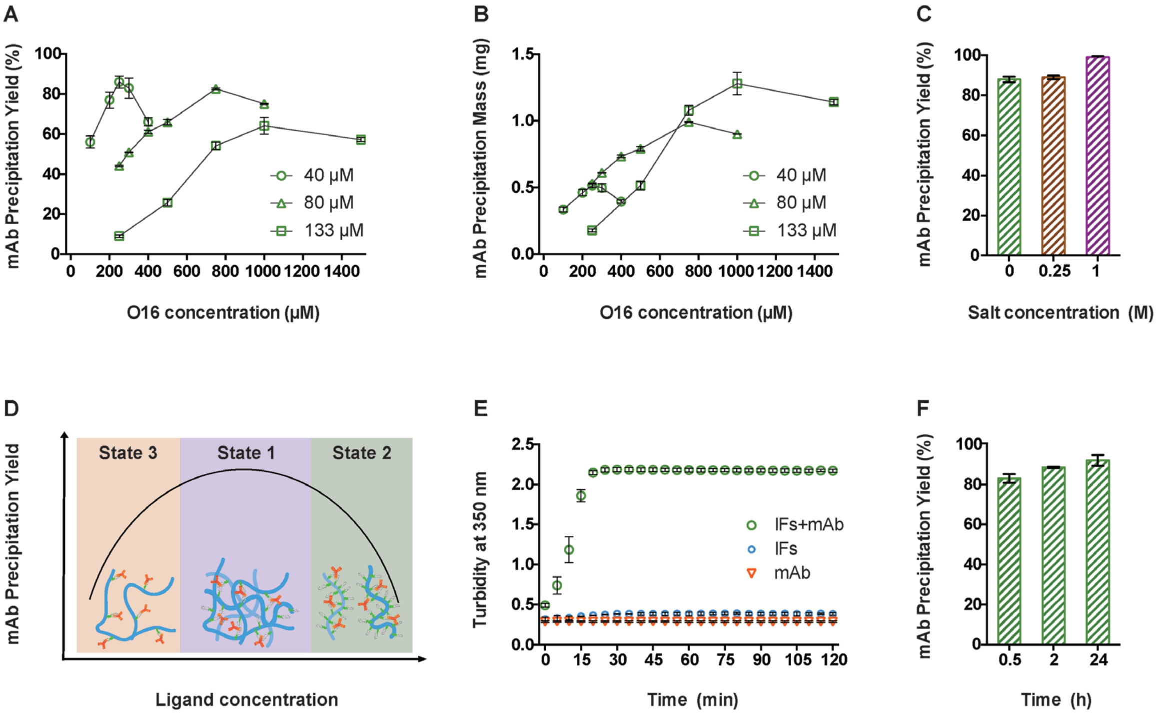

Figure 5-9. Optimization of mAb precipitation yield. The (**A**) yield and (**B**) mass of mAb precipitation for 100 µL mAb1 at 40 µM (0.6 mg), 80 µM (1.2 mg), and 133 µM (2 mg) incubated with IFs at various O16 concentrations. (**C**) Comparison of mAb precipitation yield for 40 µM mAb1 incubated with optimized IFs (2.5 mM filler, 250 µM O16) at different salt concentrations. (**D**) Proposed mechanism of mAb-IF agglomeration as the ligand concentration increases for a fixed mAb concentration. mAbs at **States 3**, **State 1**, and **State 2** are dominant at low, medium, and high ligand concentrations, respectively. (**E**) Turbidity of 40 µM mAb with optimized IFs (2.5 mM filler, 250 µM O16) in 2 hours. (**F**) The effect of binding time on the mAb precipitation yield for 40 µM mAb1 incubated with optimized IFs (2.5 mM filler, 250 µM O16). All experiments were performed in triplicate and the data is shown as mean ± standard deviation.

In Chapter 4, the ligand:mAb molar ratio was shown to play the most significant role in the mAb precipitation yield. To optimize the mAb precipitation yield under no salt conditions and investigate whether the O16 IF system could be efficiently applied to high mAb concentrations, mAb1 at three concentrations, 40 μM (6 mg/mL), 80 μM (12 mg/mL), 133 μM (20 mg/mL), was incubated with IFs formed by 2.5 mM filler molecule and O16 ligand molecule at various concentrations in 100 μL PBS. **Figure 5-9 A** and **B** show the plots of mAb precipitation yield and mass versus O16 concentration, respectively, and an optimal point was observed at a ligand:mAb molar ratio between 6:1 to 9:1 for all three mAb concentrations. These optimal ratios were much higher than the theoretical binding ratio (2:1). A better understanding in the precipitation mechanism under no salt conditions would inspire a more efficient IF design to improve the ligand utilization rate. At the optimal O16 concentration, the mAb precipitation yields for 40 and 80 μM mAb were around 85%, while only about 65% mAb was precipitated for 133 μM mAb, showing a decrease in the IF performance when scaling up for high mAb concentrations. To better understand the salt effect on mAb precipitation yield, parallel experiments were carried out for 40 μM mAb with the optimal IFs (2.5 mM filler, 250 μM O16) at different salt concentrations (**Figure 5-9 C**). More than 99% mAb1 was precipitated when 1 M salt was present, indicating a complete capture of mAb1 onto IFs. However, only 88% mAb1 was precipitated for 0 M salt group, which was attributed to the insufficient IF precipitation that may be caused by the limited IF crosslinking. This could be an inherent limitation of the IF system under no salt conditions and deserves further exploration in the future. Moreover, adding a little bit of salt (0.25 M) was found to play a minimal role in promoting the mAb precipitation yield.

To understand the trend for mAb precipitation yield observed in **Figure 5-9 A-B**, I propose that **States 3**, **State 1**, and **State 2** are dominant at low, medium, and high ligand concentrations, respectively (**Figure 5-9 D**). At low ligand concentration, all ligands are saturated by the excessive mAbs with little left for the binding of the second Fc site (**State 3**). The initial yield increase could be attributed to the increase in dual site mAb binding for IF crosslinking (**State 1)** as the ligand concentration increases. After the optimal operating point, further increasing ligand concentration resulted in a yield decline which could be caused by a decrease in the crosslinking efficiency. Since chances for mAbs to bind to two Z33 from the same IF (**State 2**) would be much higher with decreased spacing of O16 ligands on IFs surfaces.

To gain insight into the kinetics of the agglomeration, the turbidity of a mixture of 40 μM mAb1 and the optimized IFs (2.5 mM filler, 250 μM O16) was monitored by the absorbance at 350 nm for 24 h. As shown in **Figure 5-9 E**, the turbidity increases with time and plateaus within 30 min, suggesting rapid initial agglomeration. To correlate the solution turbidity to the mAb precipitation yield, the supernatant for 30 min, 2 h, and 24 h were analyzed (**Figure 5-9 F)**. Consistent with the turbidity study, the mAb-IF binding and agglomeration could nearly complete within 30 min to reach a high precipitation yield of 83%. Although a slight yield increase was seen for 2h (88%) and 24 h (92%), which was not revealed by the lower-sensitivity turbidity study, it sacrificed the time efficiency of the mAb precipitation process.

5.4.5 Sequential Precipitation and mAb Elution

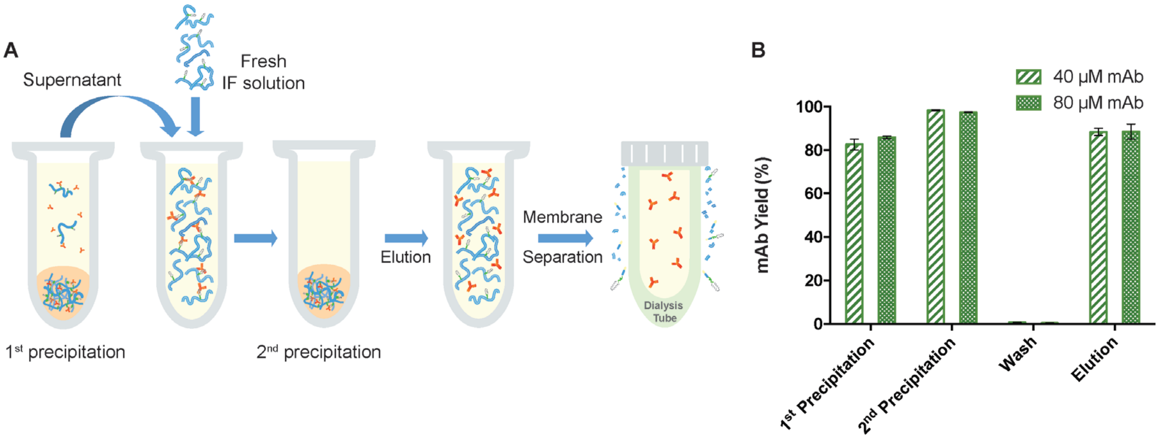

Figure 5-10. Sequential precipitation and mAb purification. (**A**) Schematic illustration of the mAb purification process using IFs. (**B**) mAb precipitation yield, yield loss at wash step, elution yield for 40 μM and 80 μM pure mAb1 after two sequential precipitations under no salt conditions. All experiments were performed in triplicate and the data is shown as mean ± standard deviation.

To further improve the mAb precipitation yield, I proposed to conduct two-step sequential precipitation to precipitate the remaining mAbs. As depicted in **Figure 5-10 A,** the supernatant from the first precipitation step was added into fresh IF solution. A wash step was then carried out using PBS to remove the non-specifically bound impurities in the precipitates from the two precipitation steps. To resuspend the precipitated mAbs, elution buffer (40 mM sodium acetate, pH 3.7) was added to dissociate the mAb-IF complexes.

As a proof of concept, the sequential precipitation was carried out with pure mAb1 at 40 μM and 80 μM. For the first precipitation, 40 μM (6 mg/mL) and 80 μM (12 mg/mL) mAb1 were incubated with IFs containing 250 μM and 750 μM O16, respectively, the optimized condition indicated by **Figure 5-9 A**. More than 82% mAb1 was precipitated for both groups while 8~20 μM mAb1 remained in the supernatant (**Figure 5-10 B)**. Based on another set of O16 concentration optimization in **Figure 5-11**, IFs containing 200 μM O16 was used for the second precipitation step. Eventually, a final precipitation yield of greater than 97% and ~88% elution yield were achieved for both mAb concentration with little yield loss during the wash step (**Figure 5-10 B**). To fully recover the eluted mAbs, a membrane separation step using a 50 kDa cut-off membrane will be conducted in future work to separate the mAb1 (~144 kDa) and dissociated IFs (monomeric size <6 kDa) (**Figure 5-10 A)**. With the promising precipitation and elution yield obtained by the two-step sequential precipitation, future work will focus on the mAb purification process in bio-relevant conditions under no salt conditions and the assessment of the purity level and quality of the final mAb product.

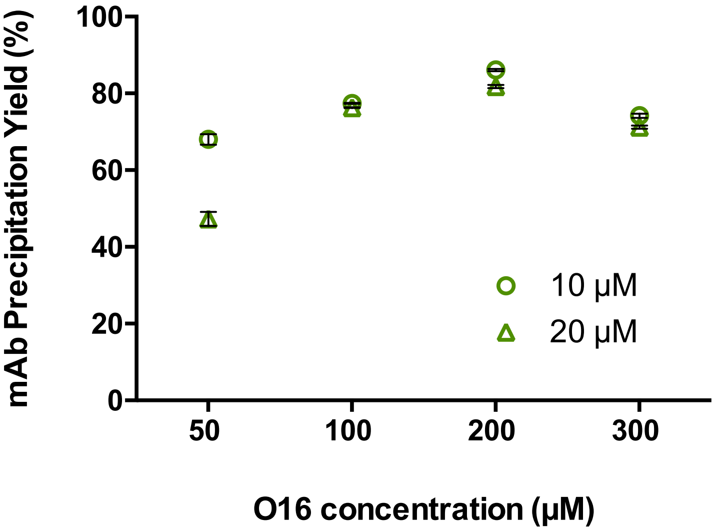

Figure 5-11. mAb precipitation yields for 100 μL mAb1 at 10 μM and 20 μM after an incubation with 100 μL IFs at various O16 concentrations. IFs with 200 μM O16 gave the best mAb precipitation yield for both mAb concentrations.

5.5 Conclusion

In conclusion, I have designed and constructed a series of supramolecular IF systems containing OEG (or PEG) linkers and demonstrated the great impact of epitope topography in the radial direction of IFs on the IF bioactivity. The results reveal that increasing the linker length to OEG16 can simultaneously improve the mAb binding and precipitation efficiency when no additional salt is added. However, too long a linker has an adverse impact on the function of the resultant supramolecular polymers. Importantly, the mAb precipitation yield under no salt conditions could be efficiently optimized by tuning the ligand concentration to reach desired mAb binding states. The mAb-IF binding and agglomeration is a quick process that could nearly complete within 30 min. Further increasing binding time can improve the mAb precipitation yield, but only to a small extent. Moreover, I demonstrated the promising precipitation and elution yield of mAbs using the sequential precipitation strategy. I believe that the strategy of engineering linkers for better epitope presentation will shed important light on the design of supramolecular polymers for specific molecular recognition and targeted drug delivery. I also envision that after further optimizing the operational process, the supramolecular IF system can potentially serve as an efficient alternative for the purification of mAbs and other proteins of interest.

6 Conclusions and Future Work

6.1 Conclusions

Supramolecular polymers represent an important class of polymeric materials formed by self-assembly of molecular building units through non-covalent interactions for their use in various biomedical applications. This dissertation aims to develop a peptide-based supramolecular polymer system, namely immunofibers (IFs), for efficient capture and purification of monoclonal antibodies, which could potentially serve as an alternative to the conventional protein A-based affinity chromatography.

In Chapter 2, I discovered that the alkylation strategy, including the the number and length of the alkyl chains, plays an important role in preserving the α-helical conformation of the mAb-binding peptides within its supramolecular filamentous assemblies. With the knowledge gained in Chapter 2, I successfully incorporated a high affinity mAb-binding peptide, Z33, into self-assembling immuno-amphiphile (IA) in Chapter 3 *via* the direct conjugation of the Z33 peptide to one or two short linear hydrocarbons. I demonstrated that the resulting IA can effectively associate under physiological conditions into supramolecular IFs while preserving the native α-helical conformation and mAb binding affinity of the Z33 peptide.

To reduce the steric hindrance among tightly packed ligands with the self-assembled IFs and promote mAb precipitation, I developed a co-assembled IF system in Chapter 4 formed by a mAb-binding ligand molecule, containing Z33, and a rationally designed filler molecule to modulate the distribution of the Z33 peptide on IF surfaces. I found that the composition of IFs and the molar ratio of ligand to proteins contribute significantly to the mAb capture efficiency. With the help of ammonium sulfate, these co-assembled IFs can specifically capture mAbs with a precipitation yield greater than 99%, leading to an overall mAb recovery yield of >94%. I also demonstrated the feasibility of capturing and recovering two mAbs from clarified cell culture harvest. In Chapter 5, I designed and developed a more advanced IF system containing various OEG (or PEG) linkers to optimize the radial arrangement of the Z33 peptide on the IF surfaces. My results reveal that the mAb-IF interactions were significantly improved as the linker length is increased; however, too long a linker has an adverse impact on the function of the resultant IFs. I demonstrated that this IF system is able to form large complexes upon mAb binding and precipitate mAbs with a promising mAb precipitation and elution yield when no additional salt is added. The use of a sequential precipitation strategy can increase the precipitation yield to greater than 97%. Through rational molecular design and continuous optimization, the resultant IF system exhibits promising performance in mAb capture and precipitation, with great potential for mAb purification from cell culture harvest without the help of additional salt.

6.2 Future Work

While the peptide-based supramolecular immunofiber system has been successfully established in this dissertation for efficient capture and purification of monoclonal antibodies, further efforts are needed to improve current constructs and optimize the purification process in bio-relevant conditions. First, current IF system requires 6~9 Z33 to precipitate one mAb molecule, which was much higher than the theoretical ratio (2:1). A better understanding in the mAb binding and precipitation mechanism, such as the required linker length for mAb to crosslink different IFs and the ideal ligand spacing on IFs to prevent a mAb molecule from binding to adjacent ligands on the same IF, would inspire a more efficient IF design to improve the ligand utilization rate. Next, a more thorough mAb purification process needs to be set up in bio-relevant conditions with the correlations among yield, purity, and mAb functionality established. Future work will seek to evaluate process scalability and robustness and analyze the overall process cost, time, efficiency, and product quality. Currently the building units of the IF system are produced by solid phase peptide synthesis and only for single use in the purification process. The development of a large-scale IF production process using microorganisms or mammalian cells as well as a process for IF recycling will help in reducing material costs. Furthermore, this IF system could be conveniently applied to the capture and purification of other product of interest by incorporating customized binding pairs into the system design.

References

1. Ecker, D. M.; Jones, S. D.; Levine, H. L. *mAbs* **2015,** *7*, 9-14.
2. Grilo, A. L.; Mantalaris, A. *Trends Biotechnol.* **2019,** *37*, 9-16.
3. Udpa, N.; Million, R. P. *Nat. Rev. Drug Discovery* **2016,** *15*, 13-14.
4. Schneider, C. K.; Kalinke, U. *Nat. Biotechnol.* **2008,** *26*, 985-990.
5. Xu, J. L.; Rehmann, M. S.; Xu, X. K.; Huang, C.; Tian, J.; Qian, N. X.; Li, Z. J. *mAbs* **2018,** *10*, 488-499.
6. Gronemeyer, P.; Ditz, R.; Strube, J. *Bioengineering* **2014,** *1*, 188-212.
7. Gronemeyer, P.; Ditz, R.; Strube, J. *Bioengineering (Basel)* **2014,** *1*, 188-212.
8. Rader, R. A.; Langer, E. S. *BioProcess Int.* **2015**, 10-13.
9. Bolton, G. R.; Mehta, K. K. *Biotechnol. Prog.* **2016,** *32*, 1193-1202.
10. Rathore, A. S.; Kumar, D.; Kateja, N. *Biotechnol. Lett.* **2018,** *40*, 895-905.
11. Gagnon, P. *J. Chromatogr. A* **2012,** *1221*, 57-70.
12. Li, Y.; Stern, D.; Lock, L. L.; Mills, J.; Ou, S. H.; Morrow, M.; Xu, X.; Ghose, S.; Li, Z. J.; Cui, H. *Acta Biomater.* **2019**.
13. dos Santos, R.; Carvalho, A. L.; Roque, A. C. A. *Biotechnol. Adv.* **2017,** *35*, 41-50.
14. Arnold, L.; Chen, R. *Biotechnol. Bioeng.* **2014,** *111*, 413-417.
15. Roque, A. C. A.; Silva, C. S. O.; Taipa, M. A. *J. Chromatogr. A* **2007,** *1160*, 44-55.
16. Hilbrig, F.; Freitag, R. *J. Chromatogr. B: Anal. Technol. Biomed. Life Sci.* **2003,** *790*, 79-90.
17. Floss, D. M.; Schallau, K.; Rose-John, S.; Conrad, U.; Scheller, J. *Trends Biotechnol.* **2010,** *28*, 37-45.
18. Swartz, A. R.; Xu, X. K.; Traylor, S. J.; Li, Z. J.; Chen, W. *Biotechnol. Bioeng.* **2018,** *115*, 423-432.
19. Sheth, R. D.; Madan, B.; Chen, W.; Cramer, S. M. *Biotechnol. Bioeng.* **2013,** *110*, 2664-2676.
20. Janoschek, L.; von Roman, M. F.; Berensmeier, S. *J. Chromatogr. B: Anal. Technol. Biomed. Life Sci.* **2014,** *965*, 72-78.
21. Handlogten, M. W.; Stefanick, J. F.; Alves, N. J.; Bilgicer, B. *Anal. Chem.* **2013,** *85*, 5271-5278.
22. Acar, H.; Srivastava, S.; Chung, E. J.; Schnorenberg, M. R.; Barrett, J. C.; LaBelle, J. L.; Tirrell, M. *Adv. Drug Delivery Rev.* **2017,** *110*, 65-79.
23. Su, H.; Zhang, W.; Wang, H.; Wang, F.; Cui, H. *J. Am. Chem. Soc.* **2019**.
24. Wang, J.; Cooper, D. L.; Zhan, W.; Wu, D.; He, H.; Sun, S.; Lovett, S. T.; Xu, B. *Angew. Chem., Int. Ed. Engl.* **2019**.
25. Hernandez-Garcia, A.; Alvarez, Z.; Simkin, D.; Madhan, A.; Pariset, E.; Tantakitti, F.; Vargas-Dorantes, O. D.; Lee, S. S.; Kiskinis, E.; Stupp, S. I. *Adv. Sci.* **2019,** *6*.

26. Barrett, J. C.; Ulery, B. D.; Trent, A.; Liang, S.; David, N. A.; Tirrell, M. V. *ACS Biomater. Sci. Eng.* **2017,** *3*, 144-152.
27. Webber, M. J.; Langer, R. *Chem. Soc. Rev.* **2017,** *46*, 6600-6620.
28. Majumder, P.; Baxa, U.; Walsh, S. T. R.; Schneider, J. P. *Angew. Chem., Int. Ed.* **2018,** *57*, 15040-15044.
29. Gao, J.; Zhan, J.; Yang, Z. *Adv. Mater.* **2019**, e1805798.
30. Fenton, O. S.; Olafson, K. N.; Pillai, P. S.; Mitchell, M. J.; Langer, R. *Adv. Mater.* **2018,** *30*.
31. Hartgerink, J. D.; Beniash, E.; Stupp, S. I. *Science* **2001,** *294*, 1684-1688.
32. Wang, H. M.; Feng, Z. Q. Q.; Xu, B. *J. Am. Chem. Soc.* **2019,** *141*, 7271-7274.
33. Wang, H. M.; Feng, Z. Q. Q.; Xu, B. *Angew. Chem., Int. Ed.* **2019,** *58*, 5567-5571.
34. Boekhoven, J.; Stupp, S. I. *Adv. Mater.* **2014,** *26*, 1642-1659.
35. Moore, A. N.; Silva, T. L. L.; Carrejo, N. C.; Marmolejo, C. A. O.; Li, I. C.; Hartgerink, J. D. *Biomaterials* **2018,** *161*, 154-163.
36. Zhang, P. C.; Cui, Y. G.; Anderson, C. F.; Zhang, C. L.; Li, Y. P.; Wang, R. F.; Cui, H. G. *Chem. Soc. Rev.* **2018,** *47*, 3490-3529.
37. Ulijn, R. V.; Jerala, R. *Chem. Soc. Rev.* **2018,** *47*, 3391-3394.
38. Wang, W.; Hu, Z. *Adv. Mater.* **2018**, e1804827.
39. Matson, J. B.; Zha, R. H.; Stupp, S. I. *Curr. Opin. Solid State Mater. Sci.* **2011,** *15*, 225-235.
40. Cui, H. G.; Webber, M. J.; Stupp, S. I. *Biopolymers* **2010,** *94*, 1-18.
41. Webber, M. J.; Tongers, J.; Renault, M. A.; Roncalli, J. G.; Losordo, D. W.; Stupp, S. I. *Acta Biomater.* **2010,** *6*, 3-11.
42. Aida, T.; Meijer, E. W.; Stupp, S. I. *Science* **2012,** *335*, 813-817.
43. Freeman, R.; Stephanopoulos, N.; Alvarez, Z.; Lewis, J. A.; Sur, S.; Serrano, C. M.; Boekhoven, J.; Lee, S. S.; Stupp, S. I. *Nat. Commun.* **2017,** *8*, 15982.
44. Cui, H.; Webber, M. J.; Stupp, S. I. *Biopolymers* **2010,** *94*, 1-18.
45. Trent, A.; Marullo, R.; Lin, B.; Black, M.; Tirrell, M. *Soft Matter* **2011,** *7*, 9572-9582.
46. Webber, M. J.; Appel, E. A.; Meijer, E. W.; Langer, R. *Nat. Mater.* **2016,** *15*, 13-26.
47. Korevaar, P. A.; Newcomb, C. J.; Meijer, E. W.; Stupp, S. I. *J. Am. Chem. Soc.* **2014,** *136*, 8540-8543.
48. Lin, Y. Y.; Penna, M.; Thomas, M. R.; Wojciechowski, J. P.; Leonardo, V.; Wang, Y.; Pashuck, E. T.; Yarovsky, I.; Stevens, M. M. *ACS Nano* **2019,** *13*, 1900-1909.
49. Pashuck, E. T.; Stupp, S. I. *J. Am. Chem. Soc.* **2010,** *132*, 8819-8821.
50. Marciel, A. B.; Srivastava, S.; Tirrell, M. V. *Soft Matter* **2018,** *14*, 2454-2464.
51. Mart, R. J.; Osborne, R. D.; Stevens, M. M.; Ulijn, R. V. *Soft Matter* **2006,** *2*, 822-835.
52. Zhou, Y.; Li, B.; Li, S.; Ardona, H. A. M.; Wilson, W. L.; Tovar, J. D.; Schroeder, C. M. *ACS Cent. Sci.* **2017,** *3*, 986-994.
53. Dias, A. M. G. C.; Roque, A. C. A. *Biotechnol. Bioeng.* **2017,** *114*, 481-491.
54. I.F. Pinto; M.R. Aires-Barros; Azevedo, A. M. *Pharm. Bioprocess.* **2015,** *3*, 263-279.

55. Khoury, G. E.; Khogeer, B.; Chen, C.; Ng, K. T.; Jacob, S. I.; Lowe, C. R. *Pharm. Bioprocess* **2015,** *3*, 139-152.

56. Pina, A. S.; Lowe, C. R.; Roque, A. C. A. *Biotechnol. Adv.* **2014,** *32*, 366-381.

57. Guan, D.; Chen, Z. *Biotechnol. Lett.* **2014,** *36*, 1391-1406.

58. Khanal, O.; Singh, N.; Traylor, S. J.; Xu, X. K.; Ghose, S.; Li, Z. J.; Lenhoff, A. M. *Biotechnol. Bioeng.* **2018,** *115*, 1938-1948.

59. Franzreb, M.; Siemann-Herzberg, M.; Hobley, T. J.; Thomas, O. R. T. *Appl. Microbiol. Biotechnol.* **2006,** *70*, 505-516.

60. Sheth, R. D.; Jin, M.; Bhut, B. V.; Li, Z. J.; Chen, W.; Cramer, S. M. *Biotechnol. Bioeng.* **2014,** *111*, 1595-1603.

61. Lin, Z.; Zhao, Q.; Xing, L.; Zhou, B.; Wang, X. *Biotechnol. J.* **2015,** *10*, 1877-1886.

62. Freitag, R. *Biotechnol. J.* **2010,** *5*, 1111-1111.

63. Ayyar, B. V.; Arora, S.; Murphy, C.; O'Kennedy, R. *Methods* **2012,** *56*, 116-129.

64. Ishihara, T.; Kadoya, T.; Yoshida, H.; Tamada, T.; Yamamoto, S. *J. Chromatogr. A* **2005,** *1093*, 126-138.

65. Roque, A. C. A.; Lowe, C. R.; Taipa, M. A. *Biotechnol. Prog.* **2004,** *20*, 639-654.

66. Lee, S. C.; Park, K.; Han, J.; Lee, J. j.; Kim, H. J.; Hong, S.; Heu, W.; Kim, Y. J.; Ha, J. S.; Lee, S. G.; Cheong, H. K.; Jeon, Y. H.; Kim, D.; Kim, H. S. *Proc. Natl. Acad. Sci. U. S. A.* **2012,** *109*, 3299-3304.

67. Zhang, J.; Siva, S.; Caple, R.; Ghose, S.; Gronke, R. *Biotechnol. Prog.* **2017,** *33*, 708-715.

68. Tustian, A. D.; Laurin, L.; Ihre, H.; Tran, T.; Stairs, R.; Bak, H. *Biotechnol. Prog.* **2018,** *34*, 650-658.

69. Dransart, B.; Wheeler, A.; Hong, T.; Tran, C.; Abalos, R.; Quezada, A.; Wang, S.; Kluck, B.; Sanaie, N. *BioProcess Int.* **2018**, 14-19.

70. Ghose, S.; Allen, M.; Hubbard, B.; Brooks, C.; Cramer, S. M. *Biotechnol. Bioeng.* **2005,** *92*, 665-673.

71. Detmers, F.; Hermans, P.; Jiao, J. A.; McCue, J. T. *BioProcess Int.* **2010,** *8*, 50-54.

72. Reinhart, D.; Weik, R.; Kunert, R. *J. Immunol. Methods* **2012,** *378*, 95-101.

73. Löfblom, J.; Feldwisch, J.; Tolmachev, V.; Carlsson, J.; Ståhl, S.; Frejd, F. Y. *FEBS Lett.* **2010,** *584*, 2670-2680.

74. Wållberg, H.; Löfdahl, P.-Å.; Tschapalda, K.; Uhlén, M.; Tolmachev, V.; Nygren, P.-Å.; Ståhl, S. *Protein Expression Purif.* **2011,** *76*, 127-135.

75. Du, K.; Dan, S. *J. Chromatogr. A* **2018,** *1548*, 37-43.

76. Liu, X.-C. *Chin. J. Chromatogr.* **2006,** *24*, 73-80.

77. Chen, C.; Khoury, G. E.; Lowe, C. R. *J. Chromatogr. B: Anal. Technol. Biomed. Life Sci.* **2014,** *969*, 171-180.

78. El Khoury, G.; Lowe, C. R. *J. Mol. Recognit.* **2013,** *26*, 190-200.

79. Haigh, J. M.; Hussain, A.; Mimmack, M. L.; Lowe, C. R. *J. Chromatogr. B: Anal. Technol. Biomed. Life Sci.* **2009,** *877*, 1440-1452.

80. Qian, J.; El Khoury, G.; Issa, H.; Al-Qaoud, K.; Shihab, P.; Lowe, C. R. *J. Chromatogr. B: Anal. Technol. Biomed. Life Sci.* **2012,** *898*, 15-23.

81. Yang, H.; Gurgel, P. V.; Carbonell, R. G. *J. Pept. Res.* **2008,** *66*, 120-137.

82. Yang, H.; Gurgel, P. V.; Williams, D. K.; Bobay, B. G.; Cavanagh, J.; Muddiman, D. C.; Carbonell, R. G. *J. Mol. Recognit.* **2009,** *23*, 271-282.

83. Menegatti, S.; Hussain, M.; Naik, A. D.; Carbonell, R. G.; Rao, B. M. *Biotechnol. Bioeng.* **2013,** *110*, 857-870.

84. Dogan, A.; Ozkara, S.; Sari, M. M.; Uzun, L.; Denizli, A. *J. Chromatogr. B Analyt. Technol. Biomed. Life Sci.* **2012,** *893-894*, 69-76.

85. Forier, C.; Boschetti, E.; Ouhammouch, M.; Cibiel, A.; Duconge, F.; Nogre, M.; Tellier, M.; Bataille, D.; Bihoreau, N.; Santambien, P.; Chtourou, S.; Perret, G. *J. Chromatogr. A* **2017,** *1489*, 39-50.

86. Walter, J. G.; Stahl, F.; Scheper, T. *Eng. Life Sci.* **2012,** *12*, 496-506.

87. Smuc, T.; Ahn, I. Y.; Ulrich, H. *J. Pharm. Biomed. Anal.* **2013,** *81-82*, 210-217.

88. Perret, G.; Boschetti, E. *Biochimie* **2018,** *145*, 98-112.

89. Wood, D. W. *Curr. Opin. Struct. Biol.* **2014,** *26*, 54-61.

90. Caroccia, K. E.; Estephan, R.; Cohen, L. S.; Arshava, B.; Hauser, M.; Zerbe, O.; Becker, J. M.; Naider, F. *Biopolymers* **2011,** *96*, 757-771.

91. Wood, D. W. *Sep. Sci. Technol. (Philadelphia, PA, U. S.)* **2010,** *45*, 2245-2257.

92. Hsu, M.-F.; Yu, T.-F.; Chou, C.-C.; Fu, H.-Y.; Yang, C.-S.; Wang, A. H. J. *PLoS One* **2013,** *8*, e56363-e56363.

93. Periasamy, A.; Shadiac, N.; Amalraj, A.; Garajová, S.; Nagarajan, Y.; Waters, S.; Mertens, H. D. T.; Hrmova, M. *Biochim. Biophys. Acta, Biomembr.* **2013,** *1828*, 743-757.

94. Zhao, X.; Li, G.; Liang, S. *J. Anal. Methods Chem.* **2013,** *2013*, 581093-581093.

95. Moon, J.-M.; Kim, G.-Y.; Rhim, H. *Biotechnol. Lett.* **2012,** *34*, 1841-1846.

96. Zou, X.; Yang, F.; Sun, X.; Qin, M.; Zhao, Y.; Zhang, Z. *Nanoscale Res. Lett.* **2018,** *13*, 165-165.

97. Bernier, S. C.; Cantin, L.; Salesse, C. *Protein Expression Purif.* **2018,** *152*, 92-106.

98. van den Berg, D. L. C.; Snoek, T.; Mullin, N. P.; Yates, A.; Bezstarosti, K.; Demmers, J.; Chambers, I.; Poot, R. A. *Cell Stem Cell* **2010,** *6*, 369-381.

99. Schembri, L.; Dalibart, R.; Tomasello, F.; Legembre, P.; Ichas, F.; De Giorgi, F. *Nat. Methods* **2007,** *4*, 107-108.

100. Asher, W. B.; Bren, K. L. *Protein Sci.* **2010,** *19*, 1830-1839.

101. Zhao, W.; Liu, L.; Du, G.; Liu, S. *J. Biotechnol.* **2018,** *283*, 1-10.

102. Schmidt, T. G. M.; Batz, L.; Bonet, L.; Carl, U.; Holzapfel, G.; Kiem, K.; Matulewicz, K.; Niermeier, D.; Schuchardt, I.; Stanar, K. *Protein Expression Purif.* **2013,** *92*, 54-61.

103. Nguyen, A. N.; Song, J.-A.; Nguyen, M. T.; Do, B. H.; Kwon, G. G.; Park, S. S.; Yoo, J.; Jang, J.; Jin, J.; Osborn, M. J.; Jang, Y. J.; Thi Vu, T. T.; Oh, H.-B.; Choe, H. *Sci. Rep.* **2017,** *7*, 16139-16139.

104. Wu, W.-Y.; Miller, K. D.; Coolbaugh, M.; Wood, D. W. *Protein Expression Purif.* **2011,** *76*, 221-228.

105. Coolbaugh, M. J.; Wood, D. W., Purification of E. Coli Proteins Using a Self-Cleaving Chitin-Binding Affinity Tag. In *Protein Affinity Tags*, Giannone, R.; Dykstra, A., Eds. Humana Press: New York, NY, 2014; Vol. 1177, pp 47-58.
106. Gottschalk, U.; Curling, J. *BioPharm Int.* **2007,** *20*, 70-83.
107. Wang, C.; Lacy, S.; Huelsman, R. Novel Purification of Non-Human Antibodies Using Protein a Affinity Chromatography. US 13/898,984, 2014.
108. Fekete, S.; Beck, A.; Veuthey, J. L.; Guillarme, D. *J. Pharm. Biomed. Anal.* **2015,** *113*, 43-55.
109. Yamamoto, S.; Nakanishi, K.; Matsuno, R.; Kamijubo, T. *Biotechnol. Bioeng.* **1983,** *25*, 1373-1391.
110. Fekete, S.; Veuthey, J. L.; Beck, A.; Guillarme, D. *J. Pharm. Biomed. Anal.* **2016,** *130*, 3-18.
111. Hemstrom, P.; Irgum, K. *J. Sep. Sci.* **2006,** *29*, 1784-1821.
112. Boschetti, E.; Judd, D.; Schwartz, W. E.; Tunon, P. *Genet. Eng.* **2000,** *20*.
113. Herigstad, M. O.; Rich, L. E.; Lu, S. M.-t.; Ramasubramanyan, N. Purification of Antibodies Using Hydrophobic Interaction Chromatography. US 9,249,182 B2, 2016.
114. Liu, T.; Lin, D. Q.; Wang, C. X.; Yao, S. J. *J. Sep. Sci.* **2016,** *39*, 3130-3136.
115. Wang, Q.; Wu, H.; Peng, K.; Jin, H.; Shao, H.; Wang, Y.; Crommen, J.; Jiang, Z. *Anal. Chim. Acta* **2018,** *999*, 184-189.
116. Zhao, G.; Dong, X. Y.; Sun, Y. *J. Biotechnol.* **2009,** *144*, 3-11.
117. Halan, V.; Maity, S.; Bhambure, R.; Rathore, A. S. *Curr. Protein Pept. Sci.* **2017**.
118. Kallberg, K.; Johansson, H. O.; Bulow, L. *Biotechnol. J.* **2012,** *7*, 1485-1495.
119. Oehme, F.; Peters, J. *BioPharm Int.* **2010**, 12-19.
120. Singh, N.; Arunkumar, A.; Peck, M.; Voloshin, A. M.; Moreno, A. M.; Tan, Z.; Hester, J.; Borys, M. C.; Li, Z. J. *mAbs* **2017,** *9*, 350-364.
121. Khanal, O.; Xu, X. K.; Singh, N.; Traylor, S. J.; Huang, C.; Ghose, S.; Li, Z. J.; Lenhoff, A. M. *J. Membr. Sci.* **2019,** *570*, 464-471.
122. Nguyen, H. C.; Langland, A. L.; Amara, J. P.; Dullen, M.; Kahn, D. S.; Costanzo, J. A. *Biotechnol. J.* **2018,** *0*, 1700771.
123. Baker, R. W., Overview of Membrane Science and Technology. In *Membrane Technology and Applications*, Third edition ed.; Baker, R. W., Ed. John Wiley & Sons, : 2012; pp 1-14.
124. Rosenberg, E.; Hepbildikler, S.; Kuhne, W.; Winter, G. *J. Membr. Sci.* **2009,** *342*, 50-59.
125. Polyakov, Y. S.; Zydney, A. L. *J. Membr. Sci.* **2013,** *434*, 106-120.
126. Baek, Y.; Singh, N.; Arunkumar, A.; Borys, M.; Li, Z. J.; Zydney, A. L. *Biotechnol. Bioeng.* **2017,** *114*, 2057-2065.
127. Lutz, H.; Arias, J.; Zou, Y. *Biotechnol. Prog.* **2016,** *33*, 113-124.
128. Luo, M.-L.; Zhao, J.-Q.; Tang, W.; Pu, C.-S. *Appl. Surf. Sci.* **2005,** *249*, 76-84.
129. Qiu, X.; Yu, H.; Karunakaran, M.; Pradeep, N.; Nunes, S. P.; Peinemann, K.-V. *ACS Nano* **2013,** *7*, 768-776.

130. Metreveli, G.; Wågberg, L.; Emmoth, E.; Belák, S.; Strømme, M.; Mihranyan, A. *Adv. Healthcare Mater.* **2014,** *3*, 1546-1550.
131. Sadeghi, I.; Kronenberg, J.; Asatekin, A. *ACS Nano* **2018,** *12*, 95-108.
132. Singh, N.; Arunkumar, A.; Chollangi, S.; Tan, Z. G.; Borys, M.; Li, Z. J. *Biotechnol. Bioeng.* **2016,** *113*, 698-716.
133. Juckes, I. R. M. *Biochim. Biophys. Acta* **1971,** *229*, 535-546.
134. Sim, S. L.; He, T.; Tscheliessnig, A.; Mueller, M.; Tan, R. B. H.; Jungbauer, A. *Biotechnol. Bioeng.* **2012,** *109*, 736-746.
135. Sim, S. L.; He, T.; Tscheliessnig, A.; Mueller, M.; Tan, R. B. H.; Jungbauer, A. *J. Biotechnol.* **2012,** *157*, 315-319.
136. Sommer, R.; Tscheliessnig, A.; Satzer, P.; Schulz, H.; Helk, B.; Jungbauer, A. *Biochem. Eng. J.* **2015,** *93*, 200-211.
137. Oelmeier, S. A.; Ladd-Effio, C.; Hubbuch, J. *J. Chromatogr. A* **2013,** *1319*, 118-126.
138. Sommer, R.; Satzer, P.; Tscheliessnig, A.; Schulz, H.; Helk, B.; Jungbauer, A. *Process Biochem.* **2014,** *49*, 2001-2009.
139. Hammerschmidt, N.; Hobiger, S.; Jungbauer, A. *Process Biochem.* **2016,** *51*, 325-332.
140. Grosshans, S.; Wang, G.; Fischer, C.; Hubbuch, J. *J. Chromatogr. A* **2018,** *1533*, 66-76.
141. Hofmann, M.; Winzer, M.; Weber, C.; Gieseler, H. *J. Pharm. Pharmacol.* **2018,** *70*, 648-654.
142. Fahie-Wilson, M.; Halsall, D. *Ann. Clin. Biochem.* **2008,** *45*, 233-235.
143. Kayitmazer, A. B.; Seeman, D.; Minsky, B. B.; Dubin, P. L.; Xu, Y. S. *Soft Matter* **2013,** *9*, 2553-2583.
144. Kurinomaru, T.; Shiraki, K. *Int. J. Biol. Macromol.* **2017,** *100*, 11-17.
145. Xu, Y. S.; Liu, M. M.; Faisal, M.; Si, Y.; Guo, Y. C. *Adv. Colloid Interface Sci.* **2017,** *239*, 158-167.
146. McDonald, P.; Victa, C.; Carter-Franklin, J. N.; Fahrner, R. *Biotechnol. Bioeng.* **2009,** *102*, 1141-1151.
147. Ma, J. F.; Hoang, H.; Myint, T.; Peram, T.; Fahrner, R.; Chou, J. H. *J. Chromatogr. B: Anal. Technol. Biomed. Life Sci.* **2010,** *878*, 798-806.
148. Sieberz, J.; Stanislawski, B.; Wohlgemuth, K.; Schembecker, G. *Sep. Purif. Technol.* **2014,** *127*, 165-173.
149. Sieberz, J.; Cinar, E.; Wohlgemuth, K.; Schembecker, G. *Biochem. Eng. J.* **2017,** *122*, 60-70.
150. Matsuda, A.; Mimura, M.; Maruyama, T.; Kurinomaru, T.; Shiuhei, M.; Shiraki, K. *J. Pharm. Sci.* **2018,** *107*, 2713-2719.
151. Meyer, D. E.; Chilkoti, A. *Nat. Biotechnol.* **1999,** *17*, 1112-1115.
152. Meyer, D. E.; Trabbic-Carlson, K.; Chilkoti, A. *Biotechnol. Prog.* **2001,** *17*, 720-728.
153. Fong, B. A.; Gillies, A. R.; Ghazi, I.; LeRoy, G.; Lee, K. C.; Westblade, L. F.; Wood, D. W. *Protein Sci.* **2010,** *19*, 1243-1252.
154. Fan, Y. M.; Miozzi, J. M.; Stimple, S. D.; Han, T. C.; Wood, D. W. *Polymers* **2018,** *10*, 468.

155. Coolbaugh, M. J.; Tang, M. J. S.; Wood, D. W. *Anal. Chim. Acta* **2017,** *516*, 65-74.
156. Xu, W. H.; Zhao, Q.; Xing, L.; Lin, Z. L. *Sci. Rep.* **2016,** *6*.
157. Liu, F.; Tsai, S. L.; Madan, B.; Chen, W. *Biotechnol. Bioeng.* **2012,** *109*, 2829-2835.
158. Kim, J. Y.; Mulchandani, A.; Chen, W. *Biotechnol. Bioeng.* **2005,** *90*, 373-379.
159. Madan, B.; Chaudhary, G.; Cramer, S. M.; Chen, W. *J. Biotechnol.* **2013,** *163*, 10-16.
160. Swartz, A. R.; Sun, Q.; Chen, W. *Biomacromolecules* **2017,** *18*, 1654-1659.
161. van Eldijk, M. B.; Smits, F. C.; Thies, J. C.; Mecinovic, J.; van Hest, J. C. *J. Biotechnol.* **2014,** *179*, 32-41.
162. Arnold, L.; Chen, R. *Biotechnol. Bioeng.* **2014,** *111*, 413-417.
163. Mattiasson, B.; Kumar, A.; Ivanov, A. E.; Galaev, I. Y. *Nat. Protoc.* **2007,** *2*, 213-220.
164. Chen, J. P.; Hoffman, A. S. *Biomaterials* **1990,** *11*, 631-634.
165. Branco, M. C.; Schneider, J. P. *Acta Biomater* **2009,** *5*, 817-31.
166. Du, X.; Zhou, J.; Shi, J.; Xu, B. *Chem Rev* **2015,** *115*, 13165-307.
167. Mart, R. J.; Osborne, R. D.; Stevens, M. M.; Ulijn, R. V. *Soft Matter* **2006,** *2*, 822.
168. Bellomo, E. G.; Wyrsta, M. D.; Pakstis, L.; Pochan, D. J.; Deming, T. J. *Nat. Mater.* **2004,** *3*, 244-248.
169. Haines-Butterick, L.; Rajagopal, K.; Branco, M.; Salick, D.; Rughani, R.; Pilarz, M.; Lamm, M. S.; Pochan, D. J.; Schneider, J. P. *Proc. Natl. Acad. Sci. U. S. A.* **2007,** *104*, 7791-7796.
170. Nowak, A. P.; Breedveld, V.; Pakstis, L.; Ozbas, B.; Pine, D. J.; Pochan, D.; Deming, T. J. *Nature* **2002,** *417*, 424-428.
171. Zhao, F.; Ma, M. L.; Xu, B. *Chem. Soc. Rev.* **2009,** *38*, 883-891.
172. Trent, A.; Ulery, B. D.; Black, M. J.; Barrett, J. C.; Liang, S.; Kostenko, Y.; David, N. A.; Tirrell, M. V. *AAPS J.* **2015,** *17*, 380-388.
173. Lin, Y. A.; Cheetham, A. G.; Zhang, P. C.; Ou, Y. C.; Li, Y. G.; Liu, G. S.; Hermida-Merino, D.; Hamley, I. W.; Cui, H. G. *ACS Nano* **2014,** *8*, 12690-12700.
174. Rudra, J. S.; Sun, T.; Bird, K. C.; Daniels, M. D.; Gasiorowski, J. Z.; Chong, A. S.; Collier, J. H. *ACS Nano* **2012,** *6*, 1557–1564.
175. Su, H.; Koo, J. M.; Cui, H. G. *J. Controlled Release* **2015,** *219*, 383-395.
176. Wang, Y.; Cheetham, A. G.; Angacian, G.; Su, H.; Xie, L. S.; Cui, H. G. *Adv. Drug Delivery Rev.* **2017,** *110*, 112-126.
177. Abbas, M.; Zou, Q. L.; Li, S. K.; Yan, X. H. *Adv. Mater.* **2017,** *29*.
178. Zou, Q. L.; Abbas, M.; Zhao, L. Y.; Li, S. K.; Shen, G. Z.; Yan, X. H. *J. Am. Chem. Soc.* **2017,** *139*, 1921-1927.
179. Lock, L. L.; Li, Y.; Mao, X.; Chen, H.; Staedtke, V.; Bai, R.; Ma, W.; Lin, R.; Li, Y.; Liu, G.; Cui, H. *ACS Nano* **2017,** *11*, 797-805.
180. Anderson, C. F.; Cui, H. G. *Ind. Eng. Chem. Res.* **2017,** *56*, 5761-5777.
181. Li, Y.; Wang, F. H.; Cui, H. G. *Bioeng. Transl. Med.* **2016,** *1*, 306-322.
182. Chow, L. W.; Wang, L. J.; Kaufman, D. B.; Stupp, S. I. *Biomaterials* **2010,** *31*, 6154-6161.
183. Niece, K. L.; Hartgerink, J. D.; Donners, J. J.; Stupp, S. I. *J. Am. Chem. Soc.* **2003,** *125*, 7146-7147.

184. Cui, H. G.; Cheetham, A. G.; Pashuck, E. T.; Stupp, S. I. *J. Am. Chem. Soc.* **2014,** *136*, 12461-12468.

185. Moyer, T. J.; Finbloom, J. A.; Chen, F.; Toft, D. J.; Cryns, V. L.; Stupp, S. I. *J. Am. Chem. Soc.* **2014,** *136*, 14746-14752.

186. Silva, G. A.; Czeisler, C.; Niece, K. L.; Beniash, E.; Harrington, D. A.; Kessler, J. A.; Stupp, S. I. *Science* **2004,** *303*, 1352-1355.

187. Chu-Kung, A. F.; Bozzelli, K. N.; Lockwood, N. A.; Haseman, J. R.; Mayo, K. H.; Tirrell, M. V. *Bioconjugate Chem.* **2004,** *15*, 530-535.

188. Chu-Kung, A. F.; Nguyen, R.; Bozzelli, K. N.; Tirrell, M. *J. Colloid Interface Sci.* **2010,** *345*, 160-167.

189. Lockwood, N. A.; Haseman, J. R.; Tirrell, M. V. *Biochem. J.* **2004,** *378*, 93-103.

190. Missirlis, D.; Farine, M.; Kastantin, M.; Ananthanarayanan, B.; Neumann, T.; Tirrell, M. *Bioconjugate Chem.* **2010,** *21*, 465-475.

191. Kokkoli, E.; Mardilovich, A.; Wedekind, A.; Rexeisen, E. L.; Garg, A.; Craig, J. A. *Soft Matter* **2006,** *2*, 1015-1024.

192. Ulijn, R. V.; Smith, A. M. *Chem. Soc. Rev.* **2008,** *37*, 664-675.

193. Marqusee, S.; Robbins, V. H.; Baldwin, R. L. *Proc. Natl. Acad. Sci. U. S. A.* **1989,** *86*, 5286-5290.

194. Nelson, J. W.; Kallenbach, N. R. *Proteins: Struct., Funct., Bioinf.* **1986,** *1*, 211-217.

195. Korevaar, P. A.; Newcomb, C. J.; Meijer, E. W.; Stupp, S. I. *J. Am. Chem. Soc.* **2014,** *136*, 8540-8543.

196. Takahashi, Y.; Ueno, A.; Mihara, H. *Bioorg. Med. Chem.* **1999,** *7*, 177-185.

197. Löwik, D. W.; Garcia-Hartjes, J.; Meijer, J. T.; van Hest, J. C. *Langmuir* **2005,** *21*, 524-526.

198. Forns, P.; Lauer-Fields, J. L.; Gao, S.; Fields, G. B. *Biopolymers* **2000,** *54*, 531-546.

199. Cheetham, A. G.; Zhang, P.; Lin, Y.-A.; Lock, L. L.; Cui, H. *J. Am. Chem. Soc.* **2013,** *135*, 2907-2910.

200. Luo, Z.; Zhao, X.; Zhang, S. *PLoS One* **2008,** *3*, e2364.

201. Greenfield, M. A.; Hoffman, J. R.; de la Cruz, M. O.; Stupp, S. I. *Langmuir* **2010,** *26*, 3641-7.

202. Beniash, E.; Hartgerink, J. D.; Storrie, H.; Stendahl, J. C.; Stupp, S. I. *Acta biomaterialia* **2005,** *1*, 387-397.

203. McClendon, M. T.; Stupp, S. I. *Biomaterials* **2012,** *33*, 5713-22.

204. Choe, S.; Veliceasa, D.; Bond, C. W.; Harrington, D. A.; Stupp, S. I.; McVary, K. T.; Podlasek, C. A. *Acta Biomater* **2016,** *32*, 89-99.

205. Lin, B. F.; Megley, K. A.; Viswanathan, N.; Krogstad, D. V.; Drews, L. B.; Kade, M. J.; Qian, Y.; Tirrell, M. V. *Journal of Materials Chemistry* **2012,** *22*, 19447.

206. Black, K. A.; Lin, B. F.; Wonder, E. A.; Desai, S. S.; Chung, E. J.; Ulery, B. D.; Katari, R. S.; Tirrell, M. V. *Tissue Eng Part A* **2015,** *21*, 1333-42.

207. Walsh, G. *Nature Biotechnology* **2014,** *32*.

208. Pagels, R. F.; Prud'homme, R. K. *J Control Release* **2015,** *219*, 519-35.

209. Carter, P. J. *Exp Cell Res* **2011,** *317*, 1261-9.

210. Benjamin Leader, Q. J. B. a. D. E. G. *Nature Reviews Drug Discovery* **2008,** *7*, 21-39.

211. Frokjaer, S.; Otzen, D. E. *Nat Rev Drug Discov* **2005,** *4*, 298-306.

212. Deisenhofer, J. *Biochemistry* **1981,** *20*, 2361-2370.

213. Moks, T.; ABRAHMSÉN, L.; NILSSON, B.; Hellman, U.; SJÖQUIST, J.; Uhlen, M. *Eur. J. Biochem.* **1986,** *156*, 637-643.

214. Braisted, A. C.; Wells, J. A. *Proc. Natl. Acad. Sci. U. S. A.* **1996,** *93*, 5688-5692.

215. Nilsson, B.; Moks, T.; Jansson, B.; Abrahmsén, L.; Elmblad, A.; Holmgren, E.; Henrichson, C.; Jones, T. A.; Uhlén, M. *Protein Eng.* **1987,** *1*, 107-113.

216. Starovasnik, M. A.; Braisted, A. C.; Wells, J. A. *Proc. Natl. Acad. Sci. U. S. A.* **1997,** *94*, 10080-10085.

217. Olszewski, K. A.; Kolinski, A.; Skolnick, J. *Proteins* **1996,** *25*, 286-299.

218. Boutelje, J.; Karlström, A. R.; Hartmanis, M. G.; Holmgren, E.; Sjögren, A.; Levine, R. L. *Arch. Biochem. Biophys.* **1990,** *283*, 141-149.

219. Cedergren, L.; Andersson, R.; Jansson, B.; Uhlen, M.; Nilsson, B. *Protein Eng.* **1993,** *6*, 441-448.

220. Zhou, J.; Li, J.; Du, X. W.; Xu, B. *Biomaterials* **2017,** *129*, 1-27.

221. Palmer, L. C.; Stupp, S. I. *Acc. Chem. Res.* **2008,** *41*, 1674–1684.

222. Sahoo, J. K.; Nazareth, C.; VandenBerg, M. A.; Webber, M. J. *Biomater. Sci.* **2017,** *5*, 1526-1530.

223. Paramonov, S. E.; Jun, H. W.; Hartgerink, J. D. *J. Am. Chem. Soc.* **2006,** *128*, 7291-7298.

224. Zhang, P. C.; Cheetham, A. G.; Lin, Y. A.; Cui, H. *ACS Nano* **2013,** *7*, 5965-5977.

225. Missirlis, D.; Chworos, A.; Fu, C. J.; Khant, H. A.; Krogstad, D. V.; Tirrell, M. *Langmuir* **2011,** *27*, 6163-6170.

226. Gore, T.; Dori, Y.; Talmon, Y.; Tirrell, M.; Bianco-Peled, H. *Langmuir* **2001,** *17*, 5352-5360.

227. Bitton, R.; Schmidt, J.; Biesalski, M.; Tu, R.; Tirrell, M.; Bianco-Peled, H. *Langmuir* **2005,** *21*, 11888-11895.

228. Lock, L. L.; Reyes, C. D.; Zhang, P.; Cui, H. *J. Am. Chem. Soc.* **2016,** *138*, 3533-3540.

229. Marullo, R.; Kastantin, M.; Drews, L. B.; Tirrell, M. *Biopolymers* **2013,** *99*, 573-581.

230. Henchey, L. K.; Jochim, A. L.; Arora, P. S. *Curr. Opin. Chem. Biol.* **2008,** *12*, 692-697.

231. Lin, R.; Cheetham, A. G.; Zhang, P.; Lin, Y. A.; Cui, H. *Chem. Commun. (Cambridge, U. K.)* **2013,** *49*, 4968-4970.

232. Stuart, M. C.; van de Pas, J. C.; Engberts, J. B. *J. Phys. Org. Chem.* **2005,** *18*, 929-934.

233. Nilsson, B.; Moks, T.; Jansson, B.; Abrahmsen, L.; Elmblad, A.; Holmgren, E.; Henrichson, C.; Jones, T. A.; Uhlen, M. *Protein Eng.* **1987,** *1*, 107-113.

234. Lock, L. L.; LaComb, M.; Schwarz, K.; Cheetham, A. G.; Lin, Y.-a.; Zhang, P.; Cui, H. *Faraday Discuss.* **2013,** *166*, 285-301.

235. Greenfield, N. J.; Fasman, G. D. *Biochemistry* **1969,** *8*, 4108-4116.

236. Biancalana, M.; Koide, S. *Biochim. Biophys. Acta* **2010,** *1804*, 1405-1412.

237. Hudson, S. A.; Ecroyd, H.; Kee, T. W.; Carver, J. A. *FASEB J.* **2009,** *276*, 5960-5972.

238. Chothia, C.; Levitt, M.; Richardson, D. *J. Mol. Biol.* **1981,** *145*, 215-250.
239. Richmond, T. J.; Richards, F. M. *J. Mol. Biol.* **1978,** *119*, 537-555.
240. Nelson, R.; Sawaya, M. R.; Balbirnie, M.; Madsen, A. Ø.; Riekel, C.; Grothe, R.; Eisenberg, D. *Nature* **2005,** *435*, 773-778.
241. Benzinger, T. L.; Gregory, D. M.; Burkoth, T. S.; Miller-Auer, H.; Lynn, D. G.; Botto, R. E.; Meredith, S. C. *Proc. Natl. Acad. Sci. U. S. A.* **1998,** *95*, 13407-13412.
242. Xu, H.; Wang, J.; Han, S.; Wang, J.; Yu, D.; Zhang, H.; Xia, D.; Zhao, X.; Waigh, T. A.; Lu, J. R. *Langmuir* **2008,** *25*, 4115-4123.
243. Leung, C.-Y.; Palmer, L. C.; Qiao, B. F.; Kewalramani, S.; Sknepnek, R.; Newcomb, C. J.; Greenfield, M. A.; Vernizzi, G.; Stupp, S. I.; Bedzyk, M. J. *ACS Nano* **2012,** *6*, 10901-10909.
244. Hartgerink, J. D.; Beniash, E.; Stupp, S. I. *Proc. Natl. Acad. Sci. U. S. A.* **2002,** *99*, 5133-5138.
245. Tanford, C. *The Hydrophobic Effect: Formation of Micelles and Biological Membranes 2d Ed*; John Wiley & Sons: New York, 1980; p A246.
246. Yu, Y.-C.; Tirrell, M.; Fields, G. B. *J. Am. Chem. Soc.* **1998,** *120*, 9979-9987.
247. Fields, G. B.; Lauer, J. L.; Dori, Y.; Forns, P.; Yu, Y. C.; Tirrell, M. *Biopolymers* **1998,** *47*, 143-151.
248. Friess, W. *Eur. J. Pharm. Biopharm.* **1998,** *45*, 113-136.
249. Tossi, A.; Sandri, L.; Giangaspero, A. *Biopolymers* **2000,** *55*, 4-30.
250. Zana, R.; Talmon, Y. *Nature* **1993,** *362*, 228-230.
251. Bates, F. S.; Hillmyer, M. A.; Lodge, T. P.; Bates, C. M.; Delaney, K. T.; Fredrickson, G. H. *Science* **2012,** *336*, 434-440.
252. Lodge, T. P. *Macromol. Chem. Phys.* **2003,** *204*, 265-273.
253. Frederix, P.; Scott, G. G.; Abul-Haija, Y. M.; Kalafatovic, D.; Pappas, C. G.; Javid, N.; Hunt, N. T.; Ulijn, R. V.; Tuttle, T. *Nat. Chem.* **2015,** *7*, 30-37.
254. Hamley, I. W. *Chem. Commun.* **2015,** *51*, 8574-8583.
255. Jonker, A. M.; Lowik, D.; van Hest, J. C. M. *Chem. Mater.* **2012,** *24*, 759-773.
256. Smith, D. J.; Brat, G. A.; Medina, S. H.; Tong, D. D.; Huang, Y.; Grahammer, J.; Furtmuller, G. J.; Oh, B. C.; Nagy-Smith, K. J.; Walczak, P.; Brandacher, G.; Schneider, J. P. *Nat. Nanotechnol.* **2016,** *11*, 95-102.
257. Pashuck, E. T.; Duchet, B. J. R.; Hansel, C. S.; Maynard, S. A.; Chow, L. W.; Stevens, M. M. *ACS Nano* **2016,** *10*, 11096-11104.
258. Tantakitti, F.; Boekhoven, J.; Wang, X.; Kazantsev, R. V.; Yu, T.; Li, J. H.; Zhuang, E.; Zandi, R.; Ortony, J. H.; Newcomb, C. J.; Palmer, L. C.; Shekhawat, G. S.; de la Cruz, M. O.; Schatz, G. C.; Stupp, S. I. *Nat. Mater.* **2016,** *15*, 469-476.
259. Chow, L. W.; Armgarth, A.; St-Pierre, J. P.; Bertazzo, S.; Gentilini, C.; Aurisicchio, C.; McCullen, S. D.; Steele, J. A. M.; Stevens, M. M. *Adv. Healthc. Mater.* **2014,** *3*, 1381-1386.
260. Altunbas, A.; Lee, S. J.; Rajasekaran, S. A.; Schneider, J. P.; Pochan, D. J. *Biomaterials* **2011,** *32*, 5906-5914.

261. Zhou, J.; Du, X. W.; Yamagata, N.; Xu, B. *J. Am. Chem. Soc.* **2016,** *138*, 3813-3823.

262. Cheetham, A. G.; Zhang, P. C.; Lin, Y. A.; Lock, L. L.; Cui, H. G. *J. Am. Chem. Soc.* **2013,** *135*, 2907-2910.

263. Ma, W.; Cheetham, A. G.; Cui, H. G. *Nano Today* **2016,** *11*, 13-30.

264. Chakroun, R. W.; Zhang, P. C.; Lin, R.; Schiapparelli, P.; Quinones-Hinojosa, A.; Cui, H. G. *Wiley Interdiscip. Rev.: Nanomed. Nanobiotechnol.* **2018,** *10*.

265. Su, H.; Zhang, P. C.; Cheetham, A. G.; Koo, J. M.; Lin, R.; Masood, A.; Schiapparelli, P.; Quinones-Hinojosa, A.; Cui, H. G. *Theranostics* **2016,** *6*, 1065-1074.

266. Lin, R.; Cui, H. G. *Curr. Opin. Chem. Eng.* **2015,** *7*, 75-83.

267. Mlinar, L. B.; Chung, E. J.; Wonder, E. A.; Tirrell, M. *Biomaterials* **2014,** *35*, 8678-8686.

268. Black, M.; Trent, A.; Kostenko, Y.; Lee, J. S.; Olive, C.; Tirrell, M. *Adv. Mater.* **2012,** *24*, 3845-3849.

269. Chung, E. J.; Mlinar, L. B.; Nord, K.; Sugimoto, M. J.; Wonder, E.; Alenghat, F. J.; Fang, Y.; Tirrell, M. *Adv. Healthc. Mater.* **2015,** *4*, 367-376.

270. Lock, L. L.; Reyes, C. D.; Zhang, P. C.; Cui, H. G. *J. Am. Chem. Soc.* **2016,** *138*, 3533-3540.

271. Herpoldt, K. L.; Artzy-Schnirman, A.; Christofferson, A. J.; Makarucha, A. J.; de la Rica, R.; Yaroysky, I.; Stevens, M. M. *Chem. Mater.* **2015,** *27*, 7187-7195.

272. Yu, Y. C.; Berndt, P.; Tirrell, M.; Fields, G. B. *J. Am. Chem. Soc.* **1996,** *118*, 12515-12520.

273. Yu, Y. C.; Tirrell, M.; Fields, G. B. *J. Am. Chem. Soc.* **1998,** *120*, 9979-9987.

274. Ramakers, B. E. I.; Bode, S. A.; Killaars, A. R.; van Hest, J. C. M.; Lowik, D. *J. Mat. Chem. B* **2015,** *3*, 2954-2961.

275. van den Heuvel, M.; Prenen, A. M.; Gielen, J. C.; Christianen, P. C. M.; Broer, D. J.; Lowik, D.; van Hest, J. C. M. *J. Am. Chem. Soc.* **2009,** *131*, 15014-15017.

276. Fleming, S.; Debnath, S.; Frederix, P.; Tuttle, T.; Ulijn, R. V. *Chem. Commun.* **2013,** *49*, 10587-10589.

277. Li, Y.; Wang, Y. Z.; Ou, S. H.; Lock, L. L.; Xu, X. K.; Ghose, S.; Li, Z. J.; Cui, H. G. *Biomacromolecules* **2017,** *18*, 3611-3620.

278. Forns, P.; Lauer-Fields, J. L.; Gao, S.; Fields, G. B. *Biopolymers* **2000,** *54*, 531-546.

279. Low, D.; O'Leary, R.; Pujar, N. S. *J. Chromatogr. B Analyt. Technol. Biomed. Life Sci.* **2007,** *848*, 48-63.

280. Shukla, A. A.; Hubbard, B.; Tressel, T.; Guhan, S.; Low, D. *J. Chromatogr. B Analyt. Technol. Biomed. Life Sci.* **2007,** *848*, 28-39.

281. Jaenicke, L. *Anal. Biochem.* **1974,** *61*, 623-627.

282. Kawashima, R.; Abei, M.; Fukuda, K.; Nakamura, K.; Murata, T.; Wakayama, M.; Seo, E.; Hasegawa, N.; Mizuguchi, H.; Obata, Y.; Hyodo, I.; Hamada, H.; Yokoyama, K. K. *Int. J. Cancer* **2011,** *129*, 1244-1253.

283. Kickhoefer, V. A.; Han, M.; Raval-Fernandes, S.; Poderycki, M. J.; Moniz, R. J.; Vaccari, D.; Silvestry, M.; Stewart, P. L.; Kelly, K. A.; Rome, L. H. *ACS Nano* **2008,** *3*, 27-36.

284. Hober, S.; Nord, K.; Linhult, M. *J. Chromatogr. B Analyt. Technol. Biomed. Life Sci.* **2007,** *848*, 40-47.

285. Huse, K.; Böhme, H.-J.; Scholz, G. H. *J. Biochem. Biophys. Methods* **2002,** *51*, 217-231.

286. Berndt, P.; Fields, G. B.; Tirrell, M. *J. Am. Chem. Soc.* **1995,** *117*, 9515-9522.

287. Li, J.; Du, X. W.; Hashim, S.; Shy, A.; Xu, B. *J. Am. Chem. Soc.* **2017,** *139*, 71-74.

288. Wiseman, T.; Williston, S.; Brandts, J. F.; Lin, L.-N. *Anal. Biochem.* **1989,** *179*, 131-137.

289. Demers, J.-P.; Mittermaier, A. *J. Am. Chem. Soc.* **2009,** *131*, 4355-4367.

290. Lund, L. N.; Christensen, T.; Toone, E.; Houen, G.; Staby, A.; St Hilaire, P. M. *J. Mol. Recognit.* **2011,** *24*, 945-952.

291. Freire, E.; Kawasaki, Y.; Velazquez-Campoy, A.; Schön, A., Characterisation of Ligand Binding by Calorimetry. In *Biophysical Approaches Determining Ligand Binding to Biomolecular Targets: Detection, Measurement and Modelling*, Podjarny, A.; Dejaegere, A.; Kieffer, B., Eds. RSC: Cambridge, UK, 2011; pp 275-299.

292. Guatrecasas, P. *J. Biol. Chem.* **1970,** *245*, 3059-3065.

293. Freeman, R.; Han, M.; Alvarez, Z.; Lewis, J. A.; Wester, J. R.; Stephanopoulos, N.; McClendon, M. T.; Lynsky, C.; Godbe, J. M.; Sangji, H.; Luijten, E.; Stupp, S. I. *Science* **2018,** *362*, 808-813.

294. Su, H.; Zhang, W.; Wang, H.; Wang, F.; Cui, H. *J. Am. Chem. Soc.* **2019**, 11997-12004.

295. Wang, J.; Cooper, D. L.; Zhan, W.; Wu, D.; He, H.; Sun, S.; Lovett, S. T.; Xu, B. *Angew. Chem., Int. Ed. Engl.* **2019**, 10741-10744.

296. Hernandez-Garcia, A.; Alvarez, Z.; Simkin, D.; Madhan, A.; Pariset, E.; Tantakitti, F.; Vargas-Dorantes, O. D.; Lee, S. S.; Kiskinis, E.; Stupp, S. I. *Adv. Sci.* **2019,** *6*, 1801458.

297. Li, J. H.; He, Y. P.; Wang, W. D.; Wu, C.; Hong, C.; Hammond, P. T. *Angew. Chem., Int. Ed. Engl.* **2017,** *56*, 13709-13712.

298. Majumder, P.; Baxa, U.; Walsh, S. T. R.; Schneider, J. P. *Angew. Chem., Int. Ed. Engl.* **2018,** *57*, 15040-15044.

299. Fenton, O. S.; Olafson, K. N.; Pillai, P. S.; Mitchell, M. J.; Langer, R. *Adv. Mater.* **2018,** *30*, 1705328.

300. MacKay, J. A.; Chen, M. N.; McDaniel, J. R.; Liu, W. G.; Simnick, A. J.; Chilkoti, A. *Nat. Mater.* **2009,** *8*, 993-999.

301. Lueckheide, M.; Vieregg, J. R.; Bologna, A. J.; Leon, L.; Tirrell, M. V. *Nano Lett.* **2018,** *18*, 7111-7117.

302. Loynachan, C. N.; Soleimany, A. P.; Dudani, J. S.; Lin, Y. Y.; Najer, A.; Bekdemir, A.; Chen, Q.; Bhatia, S. N.; Stevens, M. M. *Nat. Nanotechnol.* **2019,** *14*, 883-890.

303. Pochan, D. J.; Schneider, J. P.; Kretsinger, J.; Ozbas, B.; Rajagopal, K.; Haines, L. *J. Am. Chem. Soc.* **2003,** *125*, 11802-11803.

304. Zimenkov, Y.; Dublin, S. N.; Ni, R.; Tu, R. S.; Breedveld, V.; Apkarian, R. P.; Conticello, V. P. *J. Am. Chem. Soc.* **2006,** *128*, 6770-6771.

305. Carrick, L. M.; Aggeli, A.; Boden, N.; Fisher, J.; Ingham, E.; Waigh, T. A. *Tetrahedron* **2007,** *63*, 7457-7467.

306. Navon, Y.; Bitton, R. *Isr. J. Chem.* **2016,** *56*, 581-589.

307. Bhattacharyya, J.; Bellucci, J. J.; Weitzhandler, I.; McDaniel, J. R.; Spasojevic, I.; Li, X. H.; Lin, C. C.; Chi, J. T. A.; Chilkoti, A. *Nat. Commun.* **2015,** *6*, 7939.

308. Guo, H.; Lee, C.; Shah, M.; Janga, S. R.; Edman, M. C.; Klinngam, W.; Hamm-Alvarez, S. F.; MacKay, J. A. *J. Controlled Release* **2018,** *292*, 183-195.

309. Li, Y.; Stern, D.; Lock, L. L.; Mills, J.; Ou, S. H.; Morrow, M.; Xu, X.; Ghose, S.; Li, Z. J.; Cui, H. *Acta Biomater.* **2019**, 73-90.

310. Li, Y.; Lock, L. L.; Wang, Y. Z.; Ou, S. H.; Stern, D.; Schon, A.; Freire, E.; Xu, X. K.; Ghose, S.; Li, Z. J.; Cui, H. G. *Biomaterials* **2018,** *178*, 448-457.

311. Inostroza-Brito, K. E.; Collin, E.; Siton-Mendelson, O.; Smith, K. H.; Monge-Marcet, A.; Ferreira, D. S.; Rodriguez, R. P.; Alonso, M.; Rodriguez-Cabello, J. C.; Reis, R. L.; Sagues, F.; Botto, L.; Bitton, R.; Azevedo, H. S.; Mata, A. *Nat. Chem.* **2015,** *7*, 897-904.

312. Makam, P.; Gazit, E. *Chem. Soc. Rev.* **2018,** *47*, 3406-3420.

313. Nagy-Smith, K.; Beltramo, P. J.; Moore, E.; Tycko, R.; Furst, E. M.; Schneider, J. P. *ACS Cent. Sci.* **2017,** *3*, 586-597.

314. Chin, S. M.; Synatschke, C. V.; Liu, S. P.; Nap, R. J.; Sather, N. A.; Wang, Q. F.; Alvarez, Z.; Edelbrock, A. N.; Fyrner, T.; Palmer, L. C.; Szleifer, I.; de la Cruz, M. O.; Stupp, S. I. *Nat. Commun.* **2018,** *9*, 2395.

315. Storrie, H.; Guler, M. O.; Abu-Amara, S. N.; Volberg, T.; Rao, M.; Geiger, B.; Stupp, S. I. *Biomaterials* **2007,** *28*, 4608-4618.

316. Guler, M. O.; Hsu, L.; Soukasene, S.; Harrington, D. A.; Hulvat, J. F.; Stupp, S. I. *Biomacromolecules* **2006,** *7*, 1855-1863.

317. Hudalla, G. A.; Sun, T.; Gasiorowski, J. Z.; Han, H. F.; Tian, Y. F.; Chong, A. S.; Collier, J. H. *Nat. Mater.* **2014,** *13*, 829-836.

318. Behanna, H. A.; Donners, J. J. J. M.; Gordon, A. C.; Stupp, S. I. *J. Am. Chem. Soc.* **2005,** *127*, 1193-1200.

319. Sahoo, J. K.; VandenBerg, M. A.; Ruiz Bello, E. E.; Nazareth, C. D.; Webber, M. J. *Nanoscale* **2019,** *11*, 16534-16543.

320. Raspa, A.; Saracino, G. A. A.; Pugliese, R.; Silva, D.; Cigognini, D.; Vescovi, A.; Gelain, F. *Adv. Funct. Mater.* **2014,** *24*, 6317-6328.

321. Baldwin, R. L. *Biophys. J.* **1996,** *71*, 2056-2063.

322. Choe, W.; Durgannavar, T. A.; Chung, S. J. *Materials* **2016,** *9*, 994.

323. Ellis, R. J. *Trends Biochem. Sci.* **2001,** *26*, 597-604.

324. Zhou, H. X.; Rivas, G.; Minton, A. P. *Annu. Rev. Biophys.* **2008,** *37*, 375-397.

325. Adelizzi, B.; Van Zee, N. J.; de Windt, L. N. J.; Palmans, A. R. A.; Meijer, E. W. *Journal of the American Chemical Society* **2019,** *141*, 6110-6121.

326. Aida, T.; Meijer, E. W. *Israel Journal of Chemistry* **2020,** *60*, 33-47.

327. Stupp, S. I.; Clemons, T. D.; Carrow, J. K.; Sai, H.; Palmer, L. C. *Israel Journal of Chemistry* **2020,** *60*, 124-131.

328. Webber, M. J.; Appel, E. A.; Meijer, E. W.; Langer, R. *Nature Materials* **2016,** *15*, 13-26.

329. Shy, A. N.; Kim, B. J.; Xu, B. *Matter* **2019,** *1*, 1127-1147.

330. Sato, K.; Hendricks, M. P.; Palmer, L. C.; Stupp, S. I. *Chemical Society Reviews* **2018,** *47*, 7539-7551.

331. Acar, H.; Srivastava, S.; Chung, E. J.; Schnorenberg, M. R.; Barrett, J. C.; LaBelle, J. L.; Tirrell, M. *Advanced Drug Delivery Reviews* **2017,** *110*, 65-79.

332. Su, H.; Wang, F. H.; Ran, W.; Zhang, W. J.; Dai, W. B.; Wang, H.; Anderson, C. F.; Wang, Z. Y.; Zheng, C.; Zhang, P. C.; Li, Y. P.; Cui, H. G. *Proceedings of the National Academy of Sciences of the United States of America* **2020,** *117*, 4518-4526.

333. Wang, H. M.; Feng, Z. Q. Q.; Xu, B. *Theranostics* **2019,** *9*, 3213-3222.

334. Moore, A. N.; Hartgerink, J. D. *Accounts of Chemical Research* **2017,** *50*, 714-722.

335. VandenBerg, M. A.; Sahoo, J. K.; Zou, L.; McCarthy, W.; Webber, M. J. *ACS Nano* **2020**.

336. Wang, F. H.; Xu, D. Q.; Su, H.; Zhang, W. J.; Sun, X. R.; Monroe, M. K.; Chakroun, R. W.; Wang, Z. Y.; Dai, W. B.; Oh, R.; Wang, H.; Fan, Q.; Wan, F. Y.; Cui, H. G. *Science Advances* **2020,** *6*.

337. Chen, C. H.; Palmer, L. C.; Stupp, S. I. *Nano Letters* **2018,** *18*, 6832-6841.

338. Du, X. W.; Zhou, J.; Xu, B. *Chemistry-an Asian Journal* **2014,** *9*, 1446-1472.

339. Sur, S.; Tantakitti, F.; Matson, J. B.; Stupp, S. I. *Biomaterials Science* **2015,** *3*, 520-532.

340. Cheetham, A. G.; Zhang, P. C.; Lin, Y. A.; Lock, L. L.; Cui, H. G. *Journal of the American Chemical Society* **2013,** *135*, 2907-2910.

341. Mullerpatan, A.; Chandra, D.; Kane, E.; Karande, P.; Cramer, S. *Journal of Biotechnology* **2020,** *309*, 59-67.

342. Venkiteshwaran, A.; Heider, P.; Teyssevre, L.; Belfort, G. *Biotechnology and Bioengineering* **2008,** *101*, 957-966.

343. Fausnaugh, J. L.; Pfannkoch, E.; Gupta, S.; Regnier, F. E. *Anal Biochem* **1984,** *137*, 464-72.

344. Baldwin, R. L. *Biophysical Journal* **1996,** *71*, 2056-2063.

345. Majumdar, R.; Manikwar, P.; Hickey, J. M.; Samra, H. S.; Sathish, H. A.; Bishop, S. M.; Middaugh, C. R.; Volkin, D. B.; Weis, D. D. *Biochemistry* **2013,** *52*, 3376-3389.

346. Swartz, A. R.; Xu, X. K.; Traylor, S. J.; Li, Z. J.; Chen, W. *Biotechnology and Bioengineering* **2018,** *115*, 423-432.

347. Harris, J. M.; Chess, R. B. *Nature Reviews Drug Discovery* **2003,** *2*, 214-221.

348. Webber, M. J.; Appel, E. A.; Vinciguerra, B.; Cortinas, A. B.; Thapa, L. S.; Jhunjhunwala, S.; Isaacs, L.; Langer, R.; Anderson, D. G. *Proceedings of the National Academy of Sciences of the United States of America* **2016,** *113*, 14189-14194.

349. Accardo, A.; Ringhieri, P.; Palumbo, R.; Morelli, G. *Biopolymers* **2014,** *102*, 304-312.

Curriculum Vitae

Education

Ph.D.

Aug. 2015 – Aug. 2020	Johns Hopkins University, Baltimore, MD Department of Chemical and Biomolecular Engineering Advisor: Dr. Honggang Cui

B.Eng.

Sept. 2011 – July 2015	Tsinghua University, Beijing, China Department of Chemical Engineering

Professional Appointments

Teaching Assistant, Department of Chemical and Biomolecular Engineering

2018	Course EN.540.628 Supramolecular Materials and Nanomedicine
2017	Course EN.540.301 Kinetic Processes
2016	Course EN.540.301 Kinetic Processes

Peer Reviewed Publications

1. **Li, Y.**; Lock, L.L.; Stern, D.; Mills, J.; Morrow, M.; Xu, X.; Ghose, S.; Li, Z.J.; Cui, H. Manipulation of Epitope Radial Topography in High-Affinity Supramolecular Polymers for Binding-Triggered Antibody Precipitation, to be submitted.
2. **Li, Y.**; Lock, L.L.; Mills, J.; Ou, S.-H.; Morrow, M.; Stern, D.; Xu, X.; Ghose, S.; Li, Z.J.; Cui, H. Selective Capture and Recovery of Monoclonal Antibodies by Self-Assembling Supramolecular Polymers of High Affinity for Protein Binding, ***Nano Letters***. In revision.
3. **Li, Y.**; Stern, D.; Lock, L.L.; Mills, J.; Ou, S.-H.; Morrow, M.; Xu, X.; Ghose, S.; Li, Z.J.; Cui, H. Emerging Biomaterials for Downstream Manufacturing of Therapeutic Proteins, ***Acta Biomaterialia***, **2019**, 95, 73-90.

4. **Li, Y.**; Lock, L. L.; Wang, Y.; Ou, B.; Stern, D.; Schön, A.; Freire, E.; Xu, X.; Li, Z. J.; Ghose, S.; Cui, H. Bioinspired Supramolecular Engineering of Self-Assembling Immunofibers for High Affinity Binding of Immunoglobulin G, ***Biomaterials***, **2018**, 178, 448-457.
5. **Li, Y.**; Wang, Y.; Ou, S.-H.; Lock, L. L.; Xu, X.; Ghose, S.; Li, Z. J.; Cui, H. Conformation Preservation of Alpha-Helical Peptides within Supramolecular Filamentous Assemblies, ***Biomacromolecules***, **2017**, 18, 3611-3620.
6. Lock, L. L.; Li, Y.; Mao, X.; Chen, H.; Staedtke, V.; Bai, R.; Ma, W.; Lin, R.; **Li, Y.**; Liu, G.; Cui, H., One-Component Supramolecular Filament Hydrogels as Theranostic Label-Free Magnetic Resonance Imaging Agents, ***ACS Nano***, **2017**, 11, 797–805.
7. **Li Y.**; Wang F.; Cui, H. Peptide-Based Supramolecular Hydrogels for Delivery of Biologics, ***Bioengineering & Translational Medicine***, **2016**, 1, 306-322.

Patents

1. **JHU/BMS Patent**: Cui, H.; **Li, Y.**; Xu, X.; Lock, L.L.; Li. Z.J. "A supramolecular high affinity protein-binding system for purification of biomacromolecules." U.S. Patent Application 16/498675, filed February 27, **2020**.
2. **JHU/BMS Patent**: Cui, H.; **Li, Y.**; Xu, X.; Lock, L.L.; Li. Z.J. "Supramolecular filamentous assemblies for protein purification." WO/2019/036631, filed February 21, **2019**.

Conferences & Presentations

1. **Li, Y.**; Lock, L.L.; Mills, J.; Ou, S.-H.; Stern, D.; Morrow, M.; Xu, X.; Ghose, S.; Cui, H. Protein A-Inspired Supramolecular Engineering of Co-Assembling Immunofibers for Effective Purification of Monoclonal Antibodies. **Oral presentation** at: 8th International Conference on Bioengineering and Nanotechnology: Biomolecular Engineering. May 28-31, **2019**; Baltimore, MD.
2. **Li, Y.**; Lock, L.L.; Mills, J.; Ou, S.-H.; Stern, D.; Morrow, M.; Xu, X.; Ghose, S.; Cui, H. Affinity Precipitation of Monoclonal Antibodies for Non-Chromatography Purification by Co-Assembled Protein A Mimicking Peptide Immunofibers. **Oral**

presentation at: 257th American Chemical Society National Meeting & Exposition: Molecular Recognition & Self-Assembly. March 31- April 4, **2019**; Orlando, FL.

3. **Li, Y.**; Lock, L.L.; Xu, X. IgG Capture and Purification Using Co-Assembled Protein A Mimicking Peptide Immunofibers. Summer intern **oral presentation**, August 13, **2018**; Bristol-Myers Squibb, Devens, MA.
4. **Li, Y.**; Lock, L. L.; Wang, Y.; Xu, X.; Li, Z. J.; Cui, H. Co-Assembled Protein A Mimicking Peptide Immunofibers for Affinity Precipitation of Monoclonal Antibodies. **Poster** presented at: 12th Annual Nano-Bio Symposium. May 4, **2018**; Johns Hopkins University, Baltimore, MD.
5. **Li, Y.**; Lock, L. L.; Wang, Y.; Xu, X.; Li, Z. J.; Cui, H. A Biomimetic Approach to Engineering High Affinity Protein-Binding Supramolecular Nanofibers. **Poster** presented at: 11th Annual Nano-Bio Symposium. May 5, **2017**; Johns Hopkins University, Baltimore, MD.
6. **Li, Y.**; Lock, L. L.; Wang, Y.; Xu, X.; Li, Z. J.; Cui, H. A Biomimetic Approach to Engineering High Affinity Protein-Binding Supramolecular Nanofibers. **Poster** presented at: 253rd American Chemical Society National Meeting & Exposition: Joint PMSE/POLY Session. April 2-6, **2017**; San Francisco, CA.
7. **Li Y.**; Lock L. L.; Mao X.; Cui, H. Peptide-Based Capsules for Protein Delivery. **Poster** presented at: 252nd American Chemical Society National Meeting & Exposition: Division of Medicinal Chemistry. August 21-25, **2016**; Philadelphia, PA.

Honors and Awards

2014	Academic Excellence Scholarship (Heng Da Scholarship) Tsinghua University
2013	Academic Excellence Scholarship (Guang Hua Scholarship) Tsinghua University
2012	3rd Prize of National Undergraduate Physics Contest

Work Experience

May 2018 - Sept. 2018	Bristol-Myers Squibb, Devens, MA (Summer Intern)